The convective instability of the boundary-layer flow over families of rotating spheroids

This dissertation is submitted to the University of Leicester

for the degree of Doctor of Philosophy

by

Abdul Samad

Department of Mathematics

University of Leicester

October 2010

This thesis is dedicated to the memory of my grandparents

Mr & Mrs Khyber Khan.

Declaration

This thesis describes research carried out in the Department of Mathematics, University of Leicester from November 2006 to October 2010. No part of the work contained herein has been submitted to this or any other university for any degree, diploma or other qualification. This thesis is the result of my own work, except where explicitly stated in the text.

Abdul Samad

Department of Mathematics

University of Leicester

October 2010

Acknowledgements

I would like to thank my supervisor, Dr. Stephen J. Garrett, for his excellent supervision and patience throughout my time at Leicester and also for proof-reading this thesis. I am grateful to Dr. Jeremy Levesley for helping me in the early stages of this work, and to Dr. Alexander Gorban for his advice in my early work. Without naming each, I am thankful to all my housemates and colleagues who made my days enjoyable at Leicester. I would also like to thank each member of my family for their continued support and patience. Financial support is acknowledged from University of Peshawar, Pakistan.

The convective instability of the boundary-layer flow over families of rotating spheroids:

by Abdul Samad

Abstract

The majority of this work is concerned with the *local*-linear convective instability analysis of the incompressible boundary-layer flows over prolate spheroids and oblate spheroids rotating in otherwise still fluid. The laminar boundary layer and the perturbation equations have been formulated by introducing two distinct orthogonal coordinate systems. A cross-sectional eccentricity parameter e is introduced to identify each spheroid within its family. Both systems of equations reduce exactly to those already established for the rotating sphere boundary layer. The effects of viscosity and streamline-curvature are included in each analysis.

We predict that for prolate spheroids at low to moderate latitudes, increasing eccentricity has a strong stabilizing effect. However, at high latitudes of $\theta \geq 60$, increasing eccentricity is seen to have a destabilizing effect. For oblate spheroids, increasing eccentricity has a stabilizing effect at all latitudes. Near the pole of both types of spheroids, the critical Reynolds numbers approach that for the rotating disk boundary layer. However, in prolate spheroid case near the pole for very large values of e, the critical Reynolds numbers exceed that for the rotating disk. We show that high curvature near the pole of prolate spheroids is responsible for the increase in critical Reynolds number with increasing eccentricity.

For both types of spheroids at moderate eccentricity, we predict that the most amplified modes travel at approximately 76% of the surface speed at all latitudes.

This is consistent with the existing studies of boundary-layer flows over the related rotating-disk, -sphere and -cone geometries. However, for large values of eccentricity, the traveling speed of the most amplified modes increases up to approximately 90% of the surface speed of oblate spheroids and up to 100% in the prolate spheroid case.

Key Words

Laminar flow in three-dimensional boundary layers, Convective instabilities, transition to turbulence, rotating prolate spheroids and oblate spheroids.

Contents

Chapter 1

Introduction

For practical and theoretical reasons, rotating-disk flow has served as the foremost model problem for studying transition in fully 3D incompressible boundary layers for over six decades and has a huge body of associated literature (see Theodorsen & Regier (1945); Smith (1947); Gregory, Stuart & Walker (1955); Reed & Saric (1989); Saric, Reed & White (2003); Wimmer (1988); Owen & Rogers (1989); Malik (1986); Lingwood (1995a), for example). The rotating-disk flow owes its practical importance to the fact that the transition of its boundary layer shares many similarities with transition over swept wings (Reed & Saric (1989); Saric, Reed & White (2003); Wimmer (1988)) and many types of rotating machinery (Owen & Rogers (1989)). However, continuing developments in spinning projectiles, aerofoils and aeroengines has led to the need to understand the onset of laminar-turbulent transition of the boundary-layer flows over rotating cones and spheroids as objects in their own right.

Although numerous flow-visualization studies led by Kohama and Kobayashi have been published (Kohama & Kobayashi (1983); Kobayashi & Arai (1990); Kohama (1985); Kobayashi, Kohama, & Kurosawa (1983); Kobayashi, & Izumi (1983);

Taniguchi, Kobayashi & Fukunishi (1998); Kohama (2000)), which demonstrate an apparent similarity to the rotating-disk flow as seen in Figure 1.1, other geometries received only little attention theoretically prior to 2002 when Garrett & co-workers commenced a series of studies of the boundary-layer flow over rotating cones and spheres (Garrett (2002); Garrett & Peake (2002, 2004, 2007); Garrett, Hussain & Stephen (2009a,b); Garrett (2010a,b,c)). This thesis should be considered as a generalization of Garrett's previous work on rotating-sphere boundary layers to two different types of spheroids rotating in otherwise still fluid. The general family of spheroids can be divided into two distinct types, these are identified as (a) the family of rotating prolate spheroids (these represent more practically significant rotating convex nose cones) and (b) the family of rotating oblate spheroids (these represent when the sphere is flattened). We will see that the laminar flow and stability characteristics of both types of the rotating spheroids flow is closely related to the rotating-sphere flow, indeed the sphere is a particular case of spheroids with zero cross-sectional eccentricity. It is therefore instructive to show a review of the existing work on the boundary-layer flow over a rotating sphere, whilst we begin this study for the two families of spheroids as mentioned above.

The first theoretical studies on the rotating-sphere flow were by Taniguchi *et al.*(1998) and Garrett & Peake (2002, 2004) who performed local convective and absolute instability analyses of the boundary-layer flow over a sphere rotating both in and out of enforced axial flows. The studies focused on the calculation of the critical Reynolds numbers at the onset of instabilities at each latitude. The work was a natural extension of the previous theoretical work into the basic-flow profiles within that boundary layer (see Howarth (1951); Banks (1965); Manohar (1967); Banks (1976)) and the stability analyses of the rotating-disk flow due to, for example,

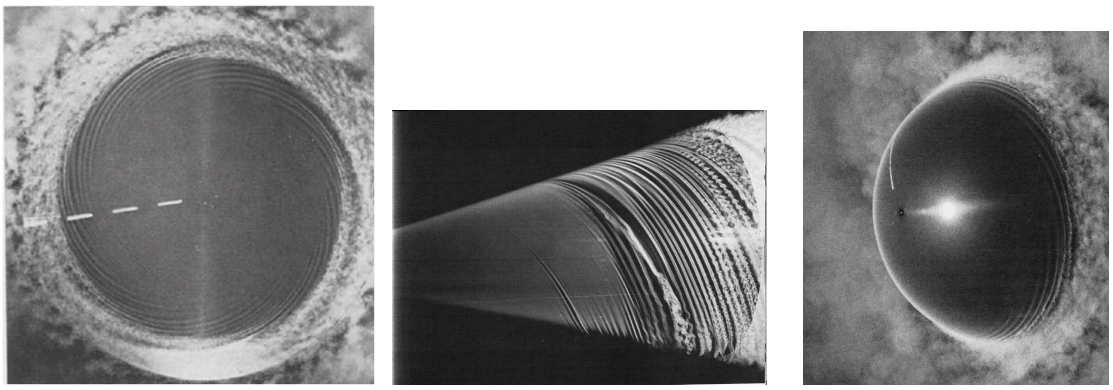

Figure 1.1: Boundary-layer flow visualizations over a rotating disk, cone and sphere due to Kohoma, Kobayashi and co-workers. Note that for each geometry, as one moves away from the pole the flow first remains laminar, then spiral vortices appear before the turbulent region is entered after the vortices have broken down. Increasing the rotation rate of each body acts to move the transitional region closer to the pole.

Malik (1986) and Lingwood (1995a,b). Garrett (2002); Garrett & Peake (2002, 2004) began their study of the rotating-sphere boundary layer by first computing the laminar flow profiles using the series-solution method due to Howarth (1951); Nigam (1954); Banks (1965) and then proceeded by using a more accurate numerical solution. It is therefore natural that we proceed in a similar way for the two types of spheroids. To our knowledge the only published work on the laminar boundary layer over a rotating spheroid is due to Fadnis (1954) who extended the Nigham series solution for the rotating sphere. However, Banks has since showed a flaw in Nigham's solution and this follows through into Fadnis's work. Indeed, the formulation used is such that the results cannot be verified against the laminar-flow profiles already established for a rotating sphere, which is a particular case of spheroid. In §§2.1 & 5.1 we formulate the governing partial differential equations (PDEs) for the laminar flow within the boundary-layer flow over the rotating prolate spheroids and oblate spheroids respectively. Distinct coordinate systems are used for each spheroidal

family (prolate and oblate) and we define an eccentricity parameter to distinguish particular bodies within each family. The governing PDEs for each type of spheroids are solved using an extension of the method originally developed by Banks for the rotating sphere. The resulting flow profiles are compared with direct numerical solutions of the PDEs obtained using a commercially available routine. A discussion of the resulting laminar flows is given in §§2.4 & 5.3 with particular emphasis on the implications for their hydrodynamic stability.

Garrett & Peake found that local convective-instability analyses could be used to predict successfully the onset of spiral vortices at each latitude, and that the onset of absolute instability appears to be related to the onset of turbulence (at least for low to moderate latitudes). As with rotating disks and broad cones, modes of type I (crossflow) and II (streamline curvature) were found to dictate the convective instability at all latitudes over the rotating sphere, and modes of type I and III the absolute instability. Further information on these instability modes within the related boundary layers can be found in Lingwood (1995a); Garrett (2002); Garrett & Peake (2002, 2004, 2007); Garrett, Hussain & Stephen (2009a,b); Garrett (2010a,b,c). In §§3.1 & 6.1 we formulate the perturbation equations that govern the stability problem for the prolate spheroids and oblate spheroids respectively. A linear convective instability analysis is the first step in the study of transition of boundary-layer flows and engineering applications can require knowledge of the exact critical parameters at which the convective instability can occur. Therefore, in this thesis, we focus on the convective instability analyses for each type of spheroid. The absolute instability analysis will be dealt in the future after completion of this thesis.

As mentioned by Kohama (2000), the major transition process is led by the ap-

pearance of stationary vortices. This is generally accepted by many scientists as in practical situations, naturally occurring roughness elements leads to stationary vortices. Therefore, we begin with *a priori* assumption that the spiral vortices rotate with the surface of each spheroid. In §§3.4 & 6.3 the convective instability analyses for stationary vortices at all latitudes for various values of the cross-sectional eccentricity are presented for the prolate spheroids and oblate spheroids respectively. In each case viscous and streamline curvature effects are included and local convective instability analyses are conducted between latitudes of 10°-70°. In the limit of zero eccentricity, results of existing rotating-sphere investigations are reproduced at all latitudes. The effect of increasing eccentricity over the convective instability is discussed in detail.

However, an interesting experimental observation made by Kobayashi & Arai (1990) was that the co-rotating spiral vortices were fixed on the sphere surface when the rotation rate was large (and transition occurred at low to moderate latitudes), whilst they moved relative to the sphere surface when the rotation rate was smaller (and transition occurred at high latitudes). The relative speed of the slow vortices was always around 76% of the local surface speed of the sphere. This observation was unique to this set of experiments, i.e. slow vortices had not been observed by Sawatzki (1970) or Kohama & Kobayashi (1983), and also had not been observed in rotating-disk and cone experiments (see Kobayashi, Kohama, & Kurosawa (1983); Kobayashi, & Izumi (1983); Kohama (1985), for example). Garrett & Peake originally attempted to clarify the appearance of slow vortices using a method of investigation since denoted *method 1* in Garrett (2010a). This method involves calculating the critical parameters of a set of neutral curves, each pertaining to a different fixed azimuthal wavenumber of disturbance; the azimuthal phase velocity

of disturbances, c, is then calculated from the globally-critical parameters and associated with the vortex speed. This approach predicts stationary vortices ($c = 1$) at all latitudes below 66°, where the type I mode dominates. Above this latitude an apparent point of inflection (rather than a global minimum) was found in the distribution of critical Reynolds number with azimuthal wavenumber. Garrett & Peake concluded that the onset of the slow vortices was related to the earlier onset of the type II mode and the appearance of the inflection point, although they were unable to determine a theoretical speed to compare to the observed $c = 0.76$. By artificially fixing $c = 0.76$ (using *method 2* as denoted in Garrett (2010a)), they were able to correctly predict properties of the slow vortices, i.e. critical Reynolds number, vortex number and angle of orientation.

Garrett (2010c) recently revisited the problem of vortex-speed selection within the rotating-sphere boundary layer and was able to predict theoretically a selection speed of 75% for a sphere rotating in otherwise still fluid. He also demonstrated that this speed increases slightly with incident axial flow. These predictions were obtained by extending the *method 2* approach to consider the linear amplification rates within the region of convective instability. The results demonstrated that, although the type II mode had larger amplification rates than the type I mode for large values of c, the globally maximum amplification rates throughout the convectively unstable region occurred for the type I mode at $c = 0.75$. This suggests that Garrett & Peake's earlier observation of slow vortices at the position of streamline-curvature dominance was merely coincidental. Garrett (2010a,b) performed similar analyses of the boundary-layer flows over the family of rotating cones (including the disk at the limiting half-angle) and again found that type I modes travelling at 75% were the most amplified. Although naturally occurring surface roughness is known to

prohibit the selection of travelling modes, Garrett's collection of work leads to the prediction that slow vortices travelling at a local speed of 75% would be selected over perfectly smooth disks, cones and spheres. A similar analysis is performed here for both types of the rotating spheroids (see §§4.1 & 6.4).

A parallel-flow approximation is used in the stability analyses of the rotating prolate spheroids and rotating oblate spheroids boundary layers presented in Chapters 3, 4 and 6, and so we are restricted to the local stability characteristics of each flow. The parallel-flow approximation is described by Davies & Carpenter (2001) as "when the real spatially inhomogeneous flow is approximated by a spatially homogenous flow". This approximation leads to inaccuracies, however, we assume that these will not be large enough to affect the general characteristics of our results presented in this thesis. We will discuss this in the relevant chapters in detail.

We are unaware of explicit experimental studies into the stability and transition of rotating-spheroid boundary layers. We are also unaware of any existing theoretical studies of the stability of rotating-spheroid flows. Our study therefore represents the first stability analysis in these geometries and, unfortunately, we will not be able to compare our results to existing observations or results. However, we will see that our formulation is consistent with existing investigations into the rotating-sphere and -disk boundary layers and we will find favourable comparisons with those when appropriate parameter values are used. Although, we present the conclusion of related results at the end of each chapter, but we make overall general conclusion in §7.1. In §7.2, we suggest further work that can be performed in the light of this thesis.

Chapter 2

Laminar boundary-layer over families of rotating prolate spheroids

This chapter is concerned with the derivation of the steady boundary-layer equations that give the laminar flow profiles over the outer surface of a general family of prolate spheroids rotating in otherwise still fluid. Garrett (2002); Garrett & Peake (2002, 2004) performed stability analyses of the rotating-sphere boundary-layer and began by first computing the laminar flow profiles using the series-solution method due to Banks (1965), Nigham (1954) and then proceeded by using a more accurate numerical solution. It is therefore natural that we proceed in a similar way.

In §2.1 we formulate the governing partial differential equations (PDEs) for the laminar boundary-layer flow over rotating prolate spheroids. The prolate spheroidal coordinate system is introduced and we define an eccentricity parameter to distinguish particular bodies within the family of prolate spheroids. In §2.2.1 the governing PDEs of laminar boundary-layer flow are solved using an extension of the

method originally developed by Banks for the rotating sphere. The resulting flow profiles are compared with direct numerical solutions of the PDEs obtained using a commercially available routine in §2.2.2. A discussion of the resulting flows is given in §2.4. This chapter is based on the paper Samad & Garrett (2010).

2.1 Formulation of laminar boundary-layer equations over rotating prolate spheroids

A Cartesian frame of reference is used that is fixed in space and has origin located at the center of the body. The prolate spheroid rotates with constant angular velocity $\Omega^\star$ about the z-axis. We introduce a prolate spheroidal coordinate system $(\eta^\star, \theta, \phi)$ defined relative to the Cartesian coordinates as

$$x^\star = \sqrt{\eta^{\star 2} - d^{\star 2}}\sin\theta\cos\phi,$$
$$y^\star = \sqrt{\eta^{\star 2} - d^{\star 2}}\sin\theta\sin\phi,$$
$$z^\star = \eta^\star\cos\theta,$$

where $0 \leq \theta \leq \pi$ and $0 \leq \phi \leq 2\pi$. A sketch of prolate spheroidal coordinate system is shown in Figure 2.1. The quantity $\eta^\star$ is the distance from the origin of the prolate spheroidal coordinate system and normal to the body surface at a particular latitude θ and azimuth ϕ. In fact $\eta^\star$ makes the angles θ and ϕ with the horizontal and vertical planes through the z-axis respectively. Furthermore, $d^\star$ is the distance of the focus from the centre of the cross-sectional ellipse formed by the prolate spheroid. Note that asterisks denote dimensional quantities. Obviously the major axis of each cross-sectional ellipse formed from the prolate family are along the axis of rotation of the body. This coordinate system is consistent with that discussed by Morse (1953)

and we have confirmed that this 3D-system $(\theta, \phi, \eta^\star)$ is orthogonal, we also note that it reduces to the spherical coordinate system as $d^\star \to 0$. In Appendix A.1 we derive the Navier-Stokes and continuity equations in general orthogonal curvilinear coordinates (see equations (A.19)–(A.22)). These equations are then transformed into prolate spheroidal coordinate system in Appendix A.1.1.

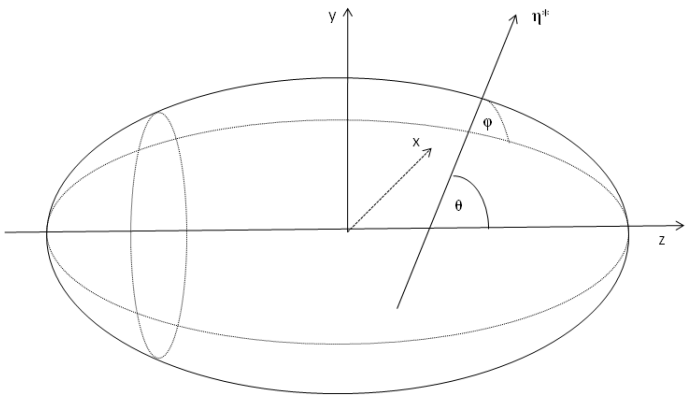

Figure 2.1: Sketch of the prolate spheroidal coordinate system.

We introduce $e = d_0^\star/\eta_0^\star \in [0, 1]$, which defines the constant eccentricity of the cross-sectional ellipse of a particular prolate spheroid. The quantity $d_0^\star$ is the constant distance of the focus from the centre of that particular prolate with surface points defined by $\eta_0^\star(\theta, \phi)$. Obviously $\eta_0^\star$ is equal in length to the semi-major axis of that particular prolate. Following the same procedure of transformation in Appendix A.1.1, we apply Prandtl's boundary-layer assumptions to the Navier-Stokes equations and replace $\eta^\star$ by constant $\eta_0^\star$ in equations (A.19)–(A.22) to obtain the dimensional boundary layer equations that govern the laminar flow. These equations

are ,

$$\frac{\sqrt{\eta_0^{\star 2}-d_0^{\star 2}}}{\sqrt{\eta_0^{\star 2}-d_0^{\star 2}\cos^2\theta}}W^\star\frac{\partial U^\star}{\partial \eta^\star}+\frac{1}{\sqrt{\eta_0^{\star 2}-d_0^{\star 2}\cos^2\theta}}\left(U^\star\frac{\partial U^\star}{\partial\theta}-V^{\star 2}\cot\theta\right)$$
$$=\nu^\star\frac{\eta_0^{\star 2}-d_0^{\star 2}}{\eta_0^{\star 2}-d_0^{\star 2}\cos^2\theta}\frac{\partial^2 U^\star}{\partial\eta^{\star 2}}, \tag{2.1}$$

$$\frac{\sqrt{\eta_0^{\star 2}-d_0^{\star 2}}}{\sqrt{\eta_0^{\star 2}-d_0^{\star 2}\cos^2\theta}}W^\star\frac{\partial V^\star}{\partial \eta^\star}+\frac{1}{\sqrt{\eta_0^{\star 2}-d_0^{\star 2}\cos^2\theta}}\left(U^\star\frac{\partial V^\star}{\partial\theta}+U^\star V^\star\cot\theta\right)$$
$$=\nu^\star\frac{\eta_0^{\star 2}-d_0^{\star 2}}{\eta_0^{\star 2}-d_0^{\star 2}\cos^2\theta}\frac{\partial^2 V^\star}{\partial\eta^{\star 2}}, \tag{2.2}$$

$$\frac{\sqrt{\eta_0^{\star 2}-d_0^{\star 2}}}{\sqrt{\eta_0^{\star 2}-d_0^{\star 2}\cos^2\theta}}\frac{\partial W^\star}{\partial \eta^\star}+\frac{1}{\sqrt{\eta_0^{\star 2}-d_0^{\star 2}\cos^2\theta}}\frac{\partial U^\star}{\partial\theta}$$
$$+\left(\frac{d_0^{\star 2}\cos\theta\sin\theta}{(\eta_0^{\star 2}-d_0^{\star 2}\cos^2\theta)^{3/2}}+\frac{\cot\theta}{\sqrt{\eta_0^{\star 2}-d_0^{\star 2}\cos^2\theta}}\right)U^\star=0, \tag{2.3}$$

where $U^\star$, $V^\star$ & $W^\star$ are the dimensional velocities in the θ, ϕ and $\eta^\star$ directions respectively. These equations are derived by assuming steady-state incompressible flow with the assumption $\delta^\star/\eta_0^\star \ll 1$. Further, we have applied the boundary-layer assumptions that $W^\star \sim O(\delta^\star)$, $U^\star \sim O(1)$, $V^\star \sim O(1)$ and $(\partial/\partial\theta) \sim O(1)$, where $\delta^\star = (\nu^\star/\Omega^\star)^{1/2}$ is the boundary-layer thickness and $\nu^\star$ is the coefficient of kinematic viscosity. Using these in the continuity equation we can find that $\partial/\partial\eta^\star \sim O(\delta^{\star -1})$, and in the normal component of Navier–Stokes equations we find $P^\star = P^\star(\theta)$. Since, the prolate spheroid is rotating in otherwise still fluid, $P^\star = constant$. In the fixed frame of reference equations (2.1)–(2.3) are subject to the boundary conditions

$$\begin{aligned} U^\star = \quad W^\star = \quad V^\star - a^\star\Omega^\star\sin\theta = 0 \quad & \text{on } \eta^\star = \eta_0^\star, \\ U^\star = \quad V^\star = \quad 0 \qquad\qquad\qquad\quad & \text{as } \eta^\star \to \infty. \end{aligned} \tag{2.4}$$

In order to obtain the non-dimensional boundary-layer equations we scale the velocities on the equatorial surface speed of the prolate, as in equation (2.5). This is consistent with Garrett & Peake's formulation of the rotating sphere.

$$U = \tfrac{U^\star}{\Omega^\star a^\star}, \qquad V = \tfrac{V^\star}{\Omega^\star a^\star}, \qquad W = \tfrac{W^\star}{(\nu^\star\Omega^\star)^{1/2}}. \tag{2.5}$$

Here $U(\eta,\theta;e)$, $V(\eta,\theta;e)$ and $W(\eta,\theta;e)$ are the scaled velocities in the θ-, ϕ- and η–directions respectively. Note that $a^\star$ is the equatorial radius of the body defined for the prolate spheroid as $a^\star = \eta_0^\star\sqrt{1-e^2}$. Further, η is the distance in the normal direction from the surface of the prolate spheroid, scaled on the boundary-layer thickness, such that $\eta = (\Omega^\star/\nu^\star)^{1/2}\,(\eta^\star - \eta_0^\star)$. For the prolate family of spheroids, the resulting non-dimensional laminar-flow equations are

$$W\frac{\partial U}{\partial \eta} + U\frac{\partial U}{\partial \theta} - V^2\cot\theta = \sqrt{\frac{1-e^2}{1-e^2\cos^2\theta}}\frac{\partial^2 U}{\partial \eta^2}, \tag{2.6}$$

$$W\frac{\partial V}{\partial \eta} + U\frac{\partial V}{\partial \theta} + UV\cot\theta = \sqrt{\frac{1-e^2}{1-e^2\cos^2\theta}}\frac{\partial^2 V}{\partial \eta^2}, \tag{2.7}$$

$$\frac{\partial W}{\partial \eta} + \frac{\partial U}{\partial \theta} + \left(\frac{e^2\cos\theta\sin\theta}{1-e^2\cos^2\theta} + \cot\theta\right)U = 0, \tag{2.8}$$

We note that the limit $e = 0$ reduces the laminar-flow equations to those for the rotating sphere as found in the literature (see Garrett & Peake (2002); Banks (1965), for example). The boundary conditions are given by

$$U = W = V - \sin\theta = 0 \text{ on } \eta = 0, \tag{2.9}$$

$$U = V = 0 \text{ as } \eta \to \infty, \tag{2.10}$$

which represent the non-slip boundary condition on the prolate spheroid surface and the quiescent fluid condition at the edge of the boundary layer.

2.2 Solution methods for the laminar flow over prolate spheroids

2.2.1 Series solution

In order to solve equations (2.6)–(2.8) at particular latitudes for a given eccentricity, a series expansion solution in powers of θ is sought of the form

$$U(\eta; e) = \theta F_1 + \theta^3 F_3 + \ldots, \tag{2.11}$$

$$V(\eta; e) = \theta G_1 + \theta^3 G_3 + \ldots, \tag{2.12}$$

$$W(\eta; e) = H_1 + \theta^2 H_3 + \ldots. \tag{2.13}$$

Here F_n, G_n and H_n are functions of the non-dimensional variable η and parameter e, and $n = 1, 3, 5, \ldots$. This is consistent with the series solution originally proposed by Howarth (1951) and Banks (1965) where $e = 0$. The boundary conditions (2.9)–(2.10) can then be written as

$$F_n(0) = H_n(0) = G_n(0) - \frac{1}{n!}(-1)^{(n-1)/2} = 0, \tag{2.14}$$

$$F_n(\infty) = G_n(\infty) = 0. \tag{2.15}$$

After substituting the above series expansions into equations (2.6)–(2.8) we obtain a set of non-linear ODEs involving terms up to and including $n = 7$. These are stated in Appendix B.1 as equations (B.1)–(B.12).

It is interesting to note that the leading-order equations (B.1), (B.5) and (B.9) in the prolate case give the von Kármán equations (von Kármán (1921)) in an inertial frame of reference, but with modified boundary conditions arising from scaling on the equatorial surface speed. We therefore see that the flow close to the nose of the rotating prolate spheroid is very similar to that over the rotating disk. This is to be

expected as the spheroids are locally flat in that region.

The solution of equations (B.1)–(B.12) subject to conditions (2.14)–(2.15) represents a two-point boundary value problem which is solved using a shooting method that incorporates a fourth order Runge–Kutta integrator over a suitably large domain. To decide upon the domain size that accurately approximates infinity, the shooting method was used over a variety of domain sizes until the solution converged. A domain of integration between $\eta = 0$ and 20 was found to be sufficiently large for all $e \leq 0.7$ considered. Indeed numerous programs are available to solve such BVPs efficiently, for example bvp4c in matlab and this was used here.

If we exclude the equatorial region (close to $\theta = 90°$), we find that the series solutions are everywhere convergent for all values of $e \leq 0.7$. As a check of the numerical code we note that the same values as calculated by Garrett and Banks were obtained for the first four quantities of $F_n'(0)$, $G_n'(0)$, $H_n(\infty)$ when $e = 0$ (note that a prime denotes differentiation with respect to η). These values, together with values at $e = 0$–0.7, are given in Appendix B.2. For the prolate spheroid, we note that the leading-order ($n = 1$) boundary values are identical for all e. This reflects that e does not appear in the governing ODEs at this order. This does not happen in the oblate case which will be discussed in §5.1.

The resulting flow profiles are discussed in §2.3 where they are compared with those arising from the numerical method of §2.2.2. The computational advantage of the series-solution approximation is that only one run of the code is required for each e: storing the resulting $F_n(\eta; e)$, $G_n(\eta; e)$, $H_n(\eta; e)$ enables the velocity components at each latitude to be obtained from the construction in equations (2.11)–(2.13). However, the series solution becomes increasingly inaccurate as the latitude increases and this is discussed in §2.3.

2.2.2 Numerical Solutions

Manohar (1967) and Banks (1976) solve the special case of equations (2.6)–(2.8) with $e = 0$ using finite difference techniques to produce accurate basic flow profiles at each latitude. We extend these by computing solutions in the general case of $e \leq 0.7$ for prolate family of spheroids. The spatial discretization is performed using the Keller box scheme Keller (1970) and the method of lines Berzins & Furzeland (1989) is employed to reduce the PDEs to a system of ODEs in θ at each mesh point. The resulting system is solved at each latitude by marching from a given complete solution at $\theta = 5^\circ$ towards the equator at $\theta = 90^\circ$ in one degree increments. At each latitude a backward differentiation formula method is used over a grid of 2000 data points between $\eta = 0$ and $\eta = 20$. The initial solution at $\theta = 5^\circ$ is found using the series solutions of §2.2.1. The computational routine used is commercially available from NAG as D03PEF.

The resulting profiles for $e = 0$ have been compared to the results of Banks (1976) and Garrett & Peake and complete agreement is found up to the equator. These profiles can be seen in Figure 1 of Garrett & Peake (2002), for example.

2.3 Results

In this section we present the flow profiles obtained from the numerical method and comparisons with the profiles obtained from the series-solution approximation are made. Experimental observations of the boundary-layer flow over rotating spheres have noted that the boundary layer erupts at latitudes close to the equator (see Sawatzki (1970); Kohama & Kobayashi (1983), for example) and it is assumed that this will be the case for spheroids of all eccentricities. Theoretical profiles for

latitudes above 80° are therefore not considered.

Figure 2.2 demonstrates laminar-flow profiles obtained from the numerical solution with increasing eccentricity at two different locations. At $\theta = 10°$, when increasing e from 0 (the sphere) in increments of 0.1 we find that there is almost negligible effect on the velocity components. Further over the body (at $\theta = 70°$, for example) the variation in flow profile is slightly more pronounced, although manifests mostly in the normal velocity component. As discussed in §3.4, this has limited implications for the stability of the flow. We also note that Figure 2.2 shows that the magnitude of the reverse flow is decreased with e at these high latitudes.

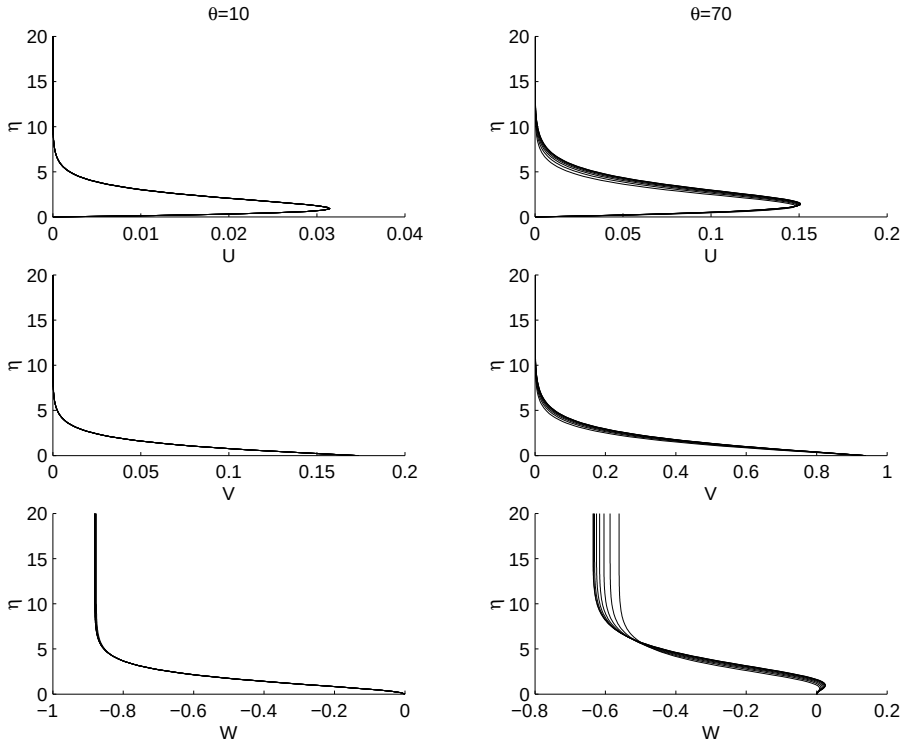

Figure 2.2: Prolate spheroid velocity profiles at latitudes $\theta = 10°$ and 70° with increasing $e = 0$–0.7 in increments of 0.1 (right to left for U,V and left to right for W in each frame).

In order to understand the development of the flow over prolate spheroids, Figure

2.3 shows the flow components for $e = 0.3$ and 0.7 at all latitudes up to $\theta = 80°$. Note that the latitudinal velocity is inflectional at all latitudes and eccentricities which implies that it is unstable to crossflow instabilities according to Rayleigh's theorem. We also note that fluid is entrained into the boundary layer at all latitudes through the negative W-component, but has a region of reverse flow close to the surface which first appears at a particular latitude between $\theta = 64°$–$66°$ depending on the value of e. The rate of inflow into the boundary layer is decreasing with increasing latitude for all values of e. This has a major implication for the convective instability of the flow and we will discuss this in §3.5.

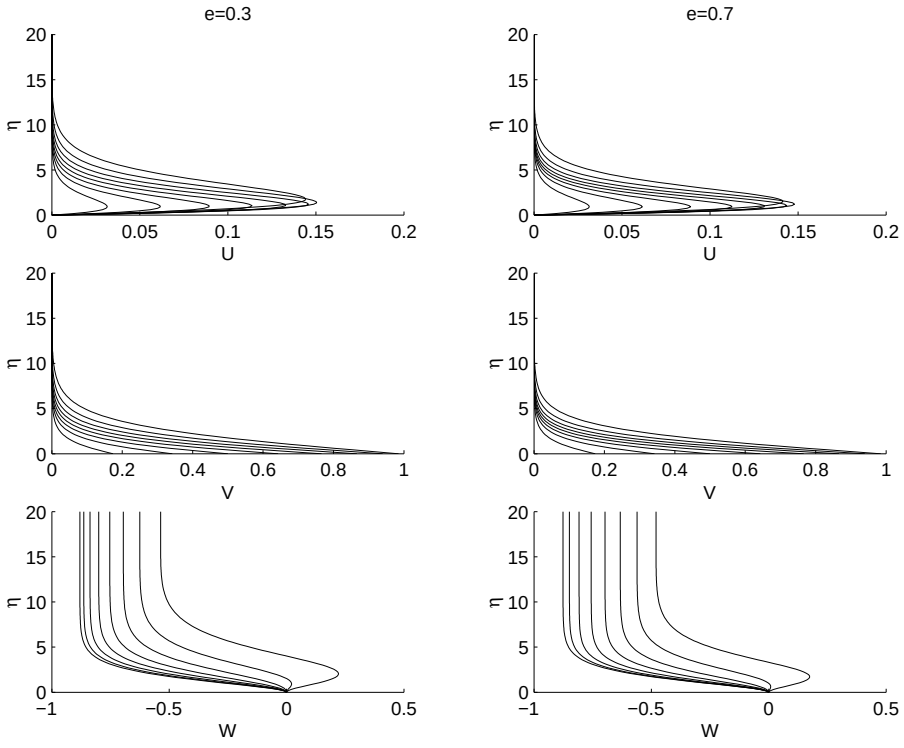

Figure 2.3: Prolate spheroid velocity profiles at $\theta = 10°$–$80°$ in increments of $10°$ (left to right in each frame) for $e = 0.3$ and 0.7.

The profiles arising from the series-solution approximation are compared to the numerical solutions at various latitudes and eccentricities in Figures 2.4–2.7 (similar

comparisons at various other latitudes and eccentricities are shown in Appendix B.3 Figures B.1–B.4). From these a purely visual comparison can be made and we observe that the series solutions match the numerical solutions very well at low latitudes, however discrepancies arise at higher latitudes which are exaggerated with increased eccentricity. For $e = 0.7$ we see qualitatively different behavior from the series solution at sufficiently high latitudes. Further investigation shows that visually such a major discrepancy is not found at lower to moderate latitudes for $e < 0.7$.

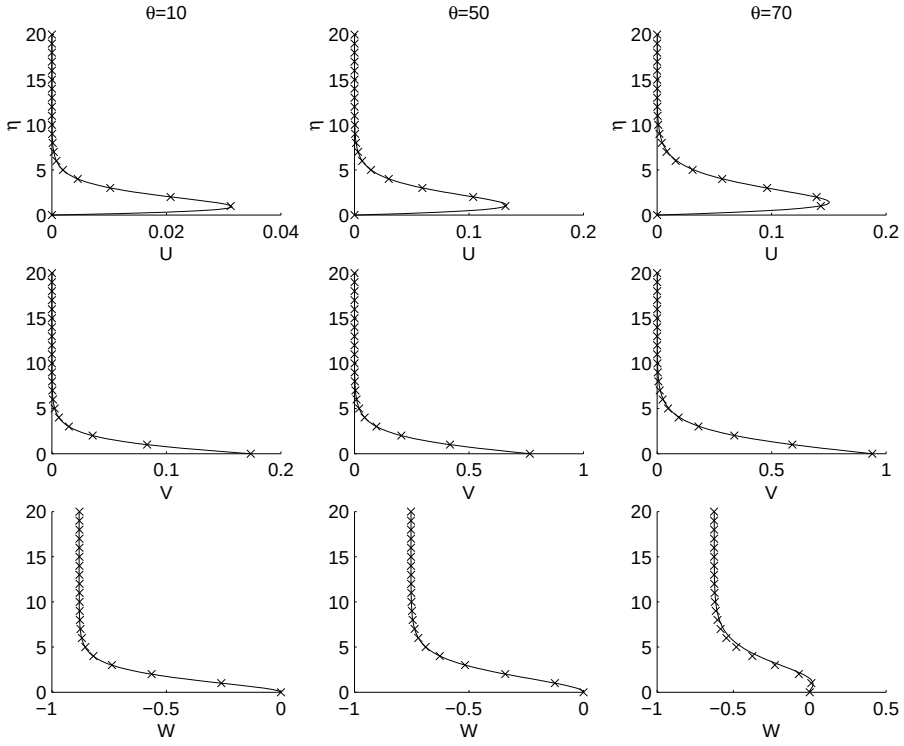

Figure 2.4: Comparison of the numerical (solid line) and series solutions (cross points) at $\theta = 10°$, $50°$ $70°$ for $e = 0.3$.

A better measure of the accuracy of the series solution with respect to the nu-

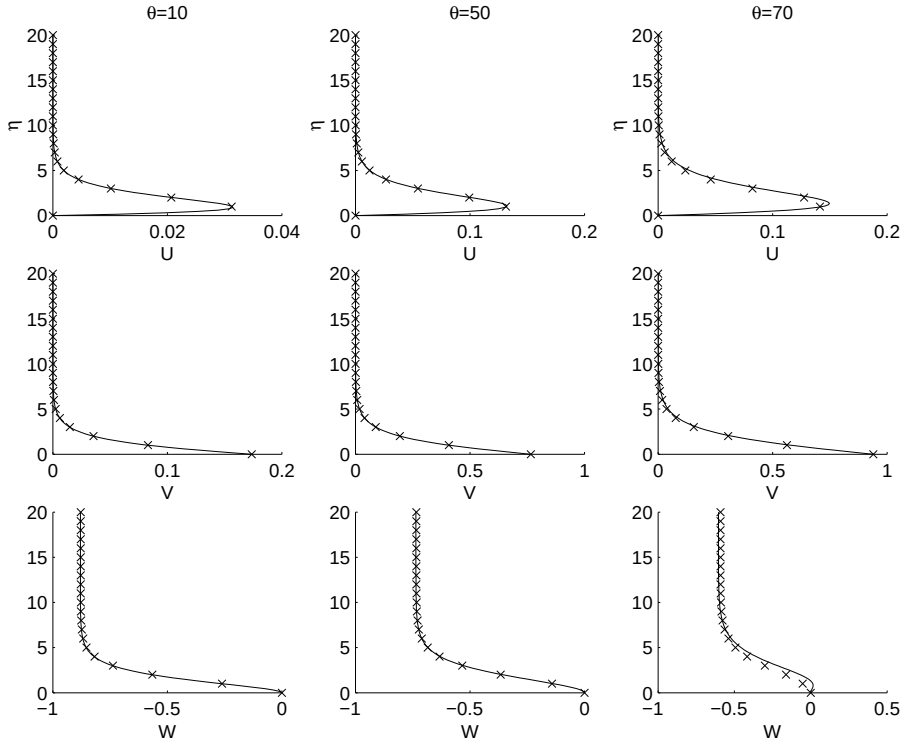

Figure 2.5: Comparison of the numerical (solid line) and series solutions (cross points) at $\theta = 10°$, $50°$ $70°$ for $e = 0.5$.

merical solution can be obtained from the root mean square error

$$E_{X,e} = \sqrt{\frac{\sum_{j=1}^{N} |X_{\mathrm{Num}}(\eta_j; e) - X_{\mathrm{Ser}}(\eta_j; e)|^2}{N}}.$$

Here $X = U, V, W$ indicates a velocity component and η_i is a discretized point on $\eta \in [0, 20]$. The subscripts Num and Ser indicate the numerical or series-solution velocity profiles, respectively.

Tables 2.1–2.5 give the values of $E_{X,e}$ computed at $\theta = 10°$, $30°$, $50°$, $60°$ and $70°$ at a range of eccentricities, with $N = 2000$. From these we see that the accuracy of the series solution reduces with increased latitude and eccentricity, as expected from the visual inspections. The implications of these error values is discussed in

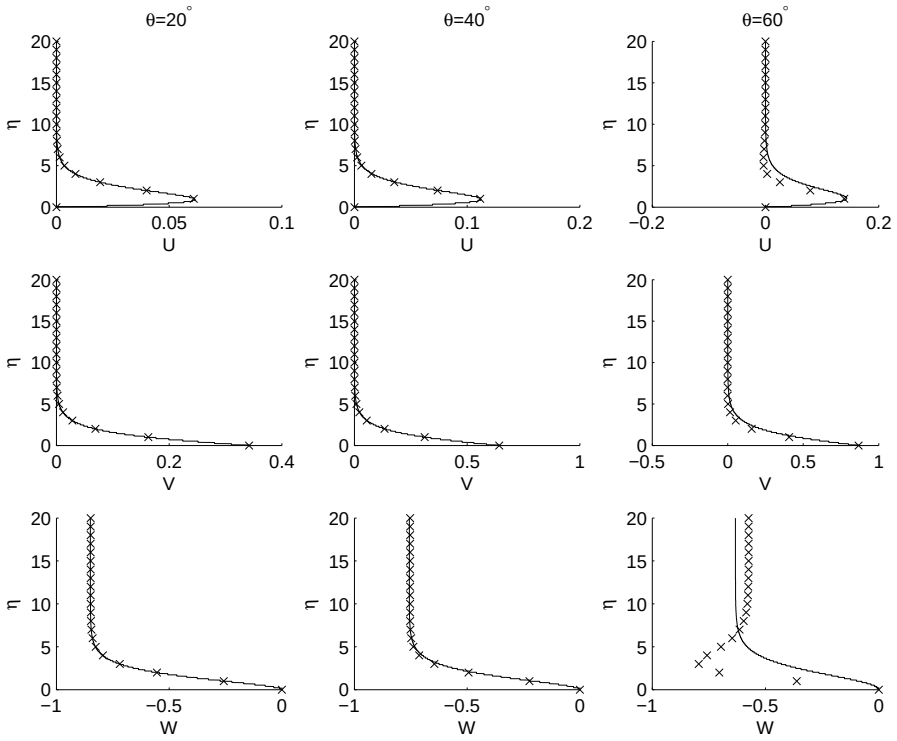

Figure 2.6: Comparison of the numerical (solid line) and series solutions (cross points) at $\theta = 20°$, $40°$, $60°$ for $e = 0.7$.

§2.4.

2.4 Conclusion

In this chapter we have derived the governing PDEs for the laminar flow within the boundary-layer flow over rotating prolate spheroids. The system is seen to limit to the known equations for the rotating sphere by setting $e = 0$. Two methods are used to solve the governing equations for general e: a series-solution approximation and an accurate numerical solution. We note that the flow is related to that over a rotating disk as the latitude is reduced to the pole. The series-solution method can therefore be thought of as successive modifications to von-Kármán-type profiles

e	$E_{U,e}$	$E_{V,e}$	$E_{W,e}$
0.0	4.28580651e-004	1.02571773e-003	4.64335505e-003
0.1	4.28523644e-004	1.02572095e-003	4.66467955e-003
0.3	4.26852032e-004	1.02541285e-003	4.66108975e-003
0.5	4.28045004e-004	1.02730166e-003	4.69179986e-003
0.6	4.28804415e-004	1.02799610e-003	4.69440232e-003
0.7	4.29641804e-004	1.02822675e-003	4.69972570e-003

Table 2.1: RMS error of the series-solution approximation at $\theta = 10^\circ$ on the prolate spheroid.

e	$E_{U,e}$	$E_{V,e}$	$E_{W,e}$
0.0	1.18616171e-003	2.87019127e-003	4.10868859e-003
0.1	1.18641710e-003	2.87103386e-003	4.10966227e-003
0.3	1.18444856e-003	2.87796789e-003	4.12698548e-003
0.5	1.19420562e-003	2.90240668e-003	4.16571560e-003
0.6	1.20198860e-003	2.92209213e-003	4.18988895e-003
0.7	1.21505060e-003	2.95117223e-003	4.33890863e-003

Table 2.2: RMS error of the series-solution approximation at $\theta = 30^\circ$ on the prolate spheroid.

e	$E_{U,e}$	$E_{V,e}$	$E_{W,e}$
0.0	1.65136257e-003	4.12585180e-003	3.31639009e-003
0.1	1.65231425e-003	4.12894867e-003	3.31517144e-003
0.3	1.65617800e-003	4.15577277e-003	3.33587432e-003
0.5	1.69700396e-003	4.24025179e-003	4.43999447e-003
0.6	1.84203276e-003	4.45163542e-003	1.06666069e-002
0.7	3.36205733e-003	6.79584999e-003	4.51212468e-002

Table 2.3: RMS error of the series-solution approximation at $\theta = 50^\circ$ on the prolate spheroid.

e	$E_{U,e}$	$E_{V,e}$	$E_{W,e}$
0.0	1.71982519e-003	4.44895486e-003	4.98776671e-003
0.1	1.72117695e-003	4.45408096e-003	4.94239089e-003
0.3	1.72902206e-003	4.50236668e-003	4.77133691e-003
0.5	1.93656440e-003	4.89513770e-003	1.15706002e-002
0.6	3.42021406e-003	7.31978921e-003	3.72764449e-002
0.7	1.23694821e-002	2.34902790e-002	1.57428897e-001

Table 2.4: RMS error of the series-solution approximation at $\theta = 60^\circ$ on the prolate spheroid.

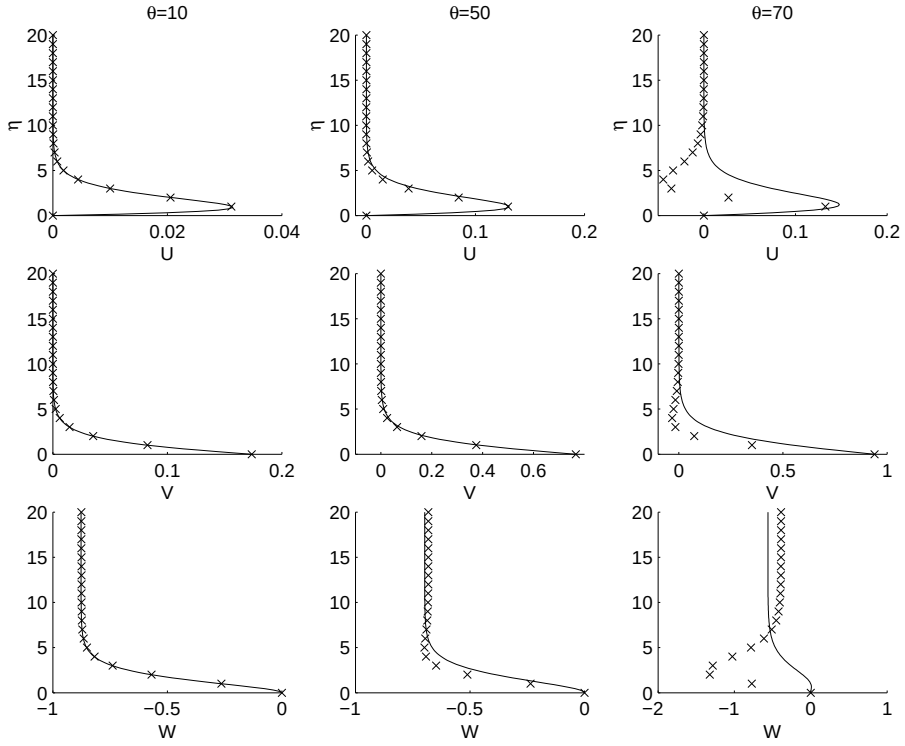

Figure 2.7: Comparison of the numerical (solid line) and series solutions (cross points) at $\theta = 10°$, $50°$ $70°$ for $e = 0.7$.

with latitude. Indeed versions of the von Kármán equations appear at leading order in the series solutions ODEs. The implication of this for the numerical solution is that profiles related to the von Kármán flow could be used as the initial profile if the integration were to start at a sufficiently low latitude, say $\theta = 1°$. These would be obtained from the leading-order series-solution ODEs. This avoids the need to run the higher-order series approximations at, say $\theta = 5°$, as was done here. The effect of increasing eccentricity over basic flow profiles at lower to moderate latitudes is negligible, however at larger latitudes the profiles pronounce noticeably with increasing e.

From visual inspections and calculation of RMS errors of the resulting series-solution profiles with respect to the numerical solutions, we see that the series so-

e	$E_{U,e}$	$E_{V,e}$	$E_{W,e}$
0.0	1.77024796e-003	4.89055591e-003	1.87557079e-002
0.1	1.77037567e-003	4.90776160e-003	1.85930635e-002
0.3	1.74378990e-003	5.12010242e-003	1.77107446e-002
0.5	3.06503473e-003	8.25161013e-003	3.65534125e-002
0.6	9.95096091e-003	2.08045536e-002	1.10611765e-001
0.7	4.08463646e-002	7.85181478e-002	4.44902646e-001

Table 2.5: RMS error of the series-solution approximation at $\theta = 70^\circ$ on the prolate spheroid.

lution is very accurate at low latitudes for all $e \leq 0.7$. However, as the latitude is increased the discrepancy between the two increases and this is exaggerated with increasing eccentricity. At $\theta = 70^\circ$ significantly different qualitative behaviour for the flow is found with large eccentricity.

Now that the governing ODEs for the series solutions of the general family of prolate spheroids are available in Appendix B.1, the method is considerably easier to use in engineering applications than the numerical method on grounds of cost and required expertise. However, the decision of which method to use should be taken with the required accuracy levels kept in mind.

We note that the normal velocity profile W which represents the rate of inflow into the boundary layer, decreases with increasing eccentricity. This decrease with the increase in eccentricity exaggerates at high latitudes of prolate spheroids. In Chapter 5 we perform similar analysis on the laminar flow within the boundary layer over the family of rotating oblate spheroids, where we observe a counter effect of increasing e over the normal velocity profile. In §5.2 we compare the laminar

velocity profiles for both cases of spheroids. In Chapter 3 we conduct convective instability analyses on the resulting flow profiles for rotating prolate spheroids (in a similar manner to Garrett (2002); Garrett & Peake (2002, 2004)) where the implications of increasing eccentricity and the extent of the usefulness of series solution over neutral curves of convective instability are presented in detail. Clearly we are concerned with the use of the flow profiles within a stability analysis, however, other applications may require different conclusions about the applicability of the series-solution approximations. We will return to this in §3.5.

Chapter 3

The convective instability of the boundary-layer flow over rotating prolate spheroids

We investigate theoretically the convective instability mechanisms within the three-dimensional boundary-layer flow over the outer surface of a general family of prolate spheroids rotating in otherwise still fluid. This is an extension of Garrett & Peake (2002) convective instability analyses of the rotating-sphere boundary layer. Viscous and streamline curvature effects are included, and local convective instability analyses are conducted between latitudes of 10°–70° from the axis of rotation in 10° increments.

We use the prolate-spheroidal coordinate system discussed in Chapter 2. The unsteady perturbation equations for the convective instability problem of rotating prolate spheroids are derived in §3.1 where each particular prolate spheroid is identified by its eccentricity parameter e. In §3.2 the perturbation equations of rotating prolate spheroids are solved. The methods of solution described here will also be used

in the solution of the set of perturbation equations for rotating oblate spheroids presented in Chapter 6. The results of local convective instability analysis are presented in §3.4 at each latitude for particular values of eccentricity between $0 \leq e \leq 0.7$. In practical situations, surface roughness acts to select stationery modes. We therefore explicitly assume stationary vortices with respect to the rotating-body surface. Travelling modes are considered in Chapter 4. In the limit of zero eccentricity, results of existing rotating-sphere investigations are reproduced at all latitudes. The effects of increasing eccentricity over the parameters of convective instabilities are discussed in detail at each latitude and comparisons are made with the results of other related geometries.

3.1 Derivation of the perturbation equations

In this section we formulate the stability problem. The prolate spheroidal coordinate system $(\theta, \phi, \eta^\star)$ defined in §2.1 is used to derive the set of perturbation equations which govern the stability of the boundary-layer flow over the surface of rotating prolate spheroids.

In Appendix A.1.1 we derived the steady continuity equation and full 3D Navier-Stokes equations in prolate spheroidal coordinate system as (A.26)–(A.29). Assume that $U^\star$, $V^\star$, $W^\star$ are the steady basic flow velocity components in the θ-, ϕ- and $\eta^\star$-directions respectively and $P^\star$ is the constant pressure. For the stability analysis we impose infinitesimally small perturbations on the steady basic flow at a particular latitude on the rotating prolate spheroid boundary layer. The perturbation variables (denoted by lower case hatted quantities) are assumed to have the normal-mode form,

$$\left(\hat{u}^\star, \hat{v}^\star, \hat{w}^\star, \hat{p}^\star\right) = \left(u^\star(\eta), v^\star(\eta), w^\star(\eta), p^\star(\eta)\right) e^{\mathrm{i}\left(\alpha^\star \int_0^\theta ds + \beta^\star r_0^\star \phi - \gamma^\star t^\star\right)}. \tag{3.1}$$

Here $ds = \sqrt{\eta_0^{\star 2} - d_0^{\star 2}\cos^2\theta}\, d\theta$ is an element of arc length in the latitudinal direction, such that $\int_0^\theta ds$ is the arc length from the pole to the particular latitude under consideration; $d_0^\star$ is the constant distance of the focus from the centre of the prolate spheroid; and $r_0^\star = \sqrt{\eta_0^{\star 2} - d_0^{\star 2}}\sin\theta$ is the local surface radius of the body. The quantities $\alpha^\star$ and $\beta^\star$ are wavenumbers in the θ- and ϕ- directions respectively, and $\gamma^\star$ is the frequency. Note that an asterisk denotes a dimensional quantity. The dimensional velocity components and pressure of the perturbed flow are formed by adding the perturbation quantities into the steady basic flow quantities. These are denoted by bared upper-case quantities,

$$(\bar{U}^\star, \bar{V}^\star, \bar{W}^\star, \bar{P}^\star) = (U^\star + \hat{u}^\star, V^\star + \hat{v}^\star, W^\star + \hat{w}^\star, P^\star + \hat{p}^\star). \tag{3.2}$$

As discussed in the beginning that in practical applications roughness elements on the surface of rotating prolate spheroid will act to select stationary vortices and here we explicitly assume this. Traveling vortices are considered separately in Chapter 4. If the roughness elements on the surface are large enough, then the mean velocity profiles may significantly be distorted by sufficiently growing vortices which can cause secondary instabilities (Kohama (1984b); Lingwood (1995a)). Throughout this thesis it is assumed that the surface roughness and the free stream disturbances are both small enough for the transition process to be controlled by the mean velocity profiles rather than secondary instabilities. Mathematically, we assume the perturbating quantities to be sufficiently small so that products can be ignored and a linear analysis conducted.

To derive the dimensional perturbation equations we substitute the dimensional

perturbed flow variables (3.2) into dimensional continuity and Navier-Stokes equations (A.26)–(A.29). Using the flow variables (3.1) and after linearization we find the second-order perturbation equations which govern the stability of the boundary-layer over rotating prolate spheroids. These are presented in Appendix C.1 as equations (C.1)–(C.4). We non-dimensionalize (C.1)–(C.4) using the boundary-layer thickness $\delta^\star$ as the length scale; the maximum rotation speed of the spheroid surface $a^\star\Omega^\star$ as the velocity scale; and $\rho^\star(a^\star\Omega^\star)^2$ as the pressure scale, where $a^\star$ is the equatorial radius of the prolate spheroid; $\Omega^\star$ is the constant angular velocity and $\rho^\star$ is the fluid density. This is consistent with the non-dimensionalization of the mean-flow variables in §2.1, and this means that the non-dimensional perturbing quantities can be written as

$$\begin{aligned} &u = u^\star/a^\star\Omega^\star, && v = v^\star/a^\star\Omega^\star, && w = w^\star/a^\star\Omega^\star, \\ &\alpha = \alpha^\star\delta^\star, && \beta = \beta^\star\delta^\star, && \gamma = \gamma^\star\delta^\star/a^\star\Omega^\star, \\ &p = p^\star/\rho^\star(a^\star\Omega^\star)^2, && \delta_1 = \delta^\star/a^\star = 1/R, && l = 1/(1+\sqrt{1-e^2}\,\eta/R). \end{aligned} \tag{3.3}$$

where R is the Reynolds number defined as,

$$R = \frac{\delta^\star a^\star\Omega^\star}{\nu^\star} = \frac{\delta^\star\eta_0^\star\Omega^\star\sqrt{1-e^2}}{\nu^\star}, \tag{3.4}$$

We note that $a^\star = \eta_0^\star\sqrt{1-e^2}$; e is the eccentricity of the cross-sectional ellipse of a particular prolate spheroid and η is the non-dimensional distance in the normal direction from the surface of the prolate spheroid, scaled on the boundary-layer thickness $\delta^\star$. Indeed we have defined these in detail in §2.1.

For a general spatio-temporal analysis the latitudinal wavenumber, α, and frequency, γ, are complex quantities; we write these quantities as $\alpha = \alpha_r + \mathrm{i}\alpha_i$ and $\gamma = \gamma_r + \mathrm{i}\gamma_i$. This will permit both convective and absolute instability studies, although only convective modes are studied in this thesis. In contrast, β is real

to ensure periodicity around the azimuth of the spheroid. The integer number of complete cycles of the disturbance round the azimuth is

$$n = \beta R \sin\theta. \tag{3.5}$$

The angle that the phase fronts make with a cross-section parallel to the equator of the prolate spheroid is denoted by ϵ and is found from

$$\epsilon = \tan^{-1}\left(\beta/\alpha_r\right). \tag{3.6}$$

Later in this chapter, we will identify ϵ and n as being the angle and number of spiral vortices on the prolate spheroid surface.

Note that the Reynolds number is interpreted as a measure of the equatorial rotation speed of the spheroid, with the location of the analysis given by the particular θ under consideration. This is in contrast to previous studies of rotating disks Lingwood (1995a); Garrett (2010a) and rotating cones Garrett *et al* .(2007,2009a,b) where the Reynolds number is interpreted as a measure of the radial location of the analysis for a particular rotation rate. As R depends on e, care must be taken in any direct comparison between spheroids of different eccentricities. The Reynolds number R is used in the formulation and derivation of the perturbation equations for consistency with previous analyses on the rotating sphere, however an alternative Reynolds number will be used in the discussion of the results which removes the dependence on e and enables comparisons of different bodies rotating with the same angular rate, $\Omega^\star$.

After neglecting $O(R^{-2})$ terms the non-dimensional perturbation equations are,

$$\begin{aligned} M\,\frac{dw}{d\eta} + \delta_1 l \frac{(2-e^2(1+\cos^2\theta))}{(1-e^2\cos^2\theta)^{3/2}}\,w = \\ -l\left[\left(\delta_1 M\left(\frac{e^2\sin\theta\cos\theta}{1-e^2\cos^2\theta}+\cot\theta\right)+\mathrm{i}\alpha\right)u+\mathrm{i}\beta v\right] \end{aligned} \tag{3.7}$$

$$M\delta_1 W\frac{du}{d\eta}+\left[\mathrm{i}\left(l(\alpha U+\beta V)-\gamma\right)+\delta_1 l\,M\frac{\partial U}{\partial\theta}\right]u$$
$$-2\delta_1 l\,M\cot\theta\,V\,v+\left(M\frac{\partial U}{\partial\eta}+\frac{M^2\delta_1\,l}{\sqrt{1-e^2\cos^2\theta}}U\right)w=$$
$$-\mathrm{i}l\alpha p+\frac{1}{R}\left[M^2\frac{d^2u}{d\eta^2}-l^2(\alpha^2+\beta^2)\,u\right] \tag{3.8}$$

$$M\delta_1 W\frac{dv}{d\eta}+\left[\mathrm{i}\left(l(\alpha U+\beta V)-\gamma\right)+\delta_1 l\,M\cot\theta\,U\right]v+$$
$$\delta_1 l\,M\left(cot\theta\,V+\frac{\partial V}{\partial\theta}\right)u+\left(M\frac{\partial V}{\partial\eta}+\frac{\delta_1\,l\,V}{\sqrt{1-e^2\cos^2\theta}}\right)w=$$
$$-\mathrm{i}l\,\beta p+\frac{1}{R}\left[M^2\frac{d^2v}{d\eta^2}-l^2(\alpha^2+\beta^2)\,v\right] \tag{3.9}$$

$$M\delta_1 W\frac{dw}{d\eta}+\left[\mathrm{i}\left(l(\alpha U+\beta V)-\gamma\right)+\delta_1\left(M\frac{\partial W}{\partial\eta}+l\frac{e^2M\sin\theta\cos\theta}{1-e^2\cos^2\theta}U\right)\right]w$$
$$-2\delta_1 l\frac{M^2\,U}{\sqrt{1-e^2\cos^2\theta}}u-\frac{2\delta_1 l\,V}{\sqrt{1-e^2\cos^2\theta}}\,v=$$
$$-M\frac{dp}{d\eta}+\frac{1}{R}\left[M^2\frac{d^2w}{d\eta^2}-l^2(\alpha^2+\beta^2)w\right] \tag{3.10}$$

where

$$M=\sqrt{\frac{1-e^2}{1-e^2\cos^2\theta}} \tag{3.11}$$

Factors $1/(1+\sqrt{1-e^2}\;\eta/R)$ appear multiplying terms in the perturbation equations which are set to unity in an approximation similar to the parallel-flow approximation. This approximation limits the analysis to a local analysis at each value of θ, and its validity at low and high latitudes for a fixed value of e will be discussed in §3.5. Note also that the equations have terms multiplied by R and δ_1, these factors indicate terms arising from viscous and streamline curvature effects respectively. Following Lingwood (1995a,b); Garrett (2002); Garrett & Peake (2002, 2004, 2007), the perturbation equations (3.7)–(3.10) can be written as a set of six first-order ordinary differential equations using the transformed variables

$$\phi_1(\eta,\alpha,\beta,\gamma;\theta,R,e)=\alpha_1 u+\beta v,$$

$$\phi_2(\eta,\alpha,\beta,\gamma;\theta,R,e)=\alpha_1 u'+\beta v',$$

$$\phi_3(\eta,\alpha,\beta,\gamma;\theta,R,e) = w,$$

$$\phi_4(\eta,\alpha,\beta,\gamma;\theta,R,e) = p,$$

$$\phi_5(\eta,\alpha,\beta,\gamma;\theta,R,e) = \alpha_1 v - \beta u,$$

$$\phi_6(\eta,\alpha,\beta,\gamma;\theta,R,e) = \alpha_1 v' - \beta u',$$

these equations are

$$\phi_1' = \phi_2 \tag{3.12}$$

$$\begin{aligned}\left[\frac{M^2\phi_2'}{R}\right]_v =& \frac{1}{R}\Big(\left[\alpha^2+\beta^2\right]_v + \mathrm{i}R\left(\alpha U+\beta V-\gamma\right)\Big)\phi_1 + \left[\frac{MW\phi_2}{R}\right]_s \\ &+\Bigg(M\left(\alpha_1 U'+\beta_1 V'\right) + \left[\frac{M^2\alpha_1 U+\beta V}{R\sqrt{1-e^2\cos^2\theta}}\right]_s\Bigg)\phi_3 + \mathrm{i}\Bigg(\alpha^2+\beta^2 \\ &-\left[\frac{\mathrm{i}M\alpha}{R}\left(\frac{e^2\sin\theta\cos\theta}{1-e^2\cos^2\theta}+\cot\theta\right)\right]_s\Bigg)\phi_4 - \left[\frac{M\cot\theta V\phi_5}{R}\right]_s \\ &+\frac{M}{R}\left[\left(\alpha_1\frac{\partial U}{\partial\theta}+\beta\frac{\partial V}{\partial\theta}\right)u - \left(\alpha_1 V-\beta U\right)\cot\theta v\right]_s\end{aligned} \tag{3.13}$$

$$M\phi_3' = -\,\mathrm{i}\phi_1 - \left[\frac{2-e^2(1+\cos^2\theta)}{R(1-e^2\cos^2\theta)^{3/2}}\phi_3\right]_s \tag{3.14}$$

$$\begin{aligned}M\phi_4' =& \left[\frac{\mathrm{i}W\phi_1}{R}\right]_s - \left[\frac{\mathrm{i}M\phi_2}{R}\right]_v + \left[\frac{2\left(M^2U\,u+Vv\right)}{R\sqrt{1-e^2\cos^2\theta}}\right]_s \\ &-\frac{1}{R}\Bigg(\left[\alpha^2+\beta^2\right]_v + \mathrm{i}R\Big(\alpha U+\beta V-\gamma\Big) \\ &+\left[M\left(W'+\frac{e^2\cos\theta\sin\theta}{(1-e^2\cos^2\theta)}U\right)\right]_s\Bigg)\phi_3\end{aligned} \tag{3.15}$$

$$\phi_5' = \phi_6 \tag{3.16}$$

$$\begin{aligned}\left[\frac{M^2\phi_6'}{R}\right]_v =& \left[\frac{V\cot\theta\phi_1}{R}\right]_s + \Bigg(M\left(\alpha_1 V'-\beta U'\right) \\ &+\left[\frac{1}{R}\left(\frac{\alpha_1 V}{\sqrt{1-e^2\cos^2\theta}}-\frac{M\,\beta U}{(1-e^2\cos^2\theta)}\right)\right]_s\Bigg)\phi_3 \\ &+\left[\frac{\beta M}{R}\left(\frac{e^2\cos\theta\sin\theta}{1-e^2\cos^2\theta}+\cot\theta\right)\phi_4\right]_s + \frac{1}{R}\Bigg(\left[\alpha^2+\beta^2\right]_v \\ &+\mathrm{i}R\left(\alpha U+\beta V-\gamma\right)\Bigg)\phi_5 + \left[\frac{M\,W\phi_6}{R}\right]_s \\ &+\left[\frac{M}{R}\left(\left(\alpha_1\frac{\partial V}{\partial\theta}-\beta\frac{\partial U}{\partial\theta}\right)u+\cot\theta\left(\alpha_1 U+\beta V\right)v\right)\right]_s\end{aligned} \tag{3.17}$$

Where a prime denotes differentiation with respect to the normal η (spatial variable), and $\alpha_1 = \alpha - \left[\frac{\mathrm{i}M}{R}\right]_s \left(\frac{e^2 \sin\theta\cos\theta}{1-e^2\cos^2\theta} + \cot\theta\right)$, where M is defined in equation (3.11).

Equations (3.12)–(3.17) are the perturbation equations upon which convective and absolute instability analyses of the boundary-layer over rotating prolate spheroids can be performed for a fixed value of e, however we are analyzing only the convective modes (of types I & II) in this chapter, while the linear growth rates of these convective modes will be investigated in subsequent chapters. The subscripts v and s in the perturbation equations (3.12)–(3.17) indicate which of the $O(R^{-1})$ terms arise from viscous and streamline-curvature effects, respectively. Coriolis terms do not appear since a fixed frame of reference is used. Note that the perturbation velocities u and v still appear explicitly, but can be expressed in terms of ϕ_1 and ϕ_2 via

$$u = \frac{1}{\alpha_1^2+\beta^2}\left(\alpha_1\phi_1 - \beta\phi_5\right), \qquad v = \frac{1}{\alpha_1^2+\beta^2}\left(\alpha_1\phi_5 + \beta\phi_1\right).$$

By neglecting the $O(R^{-1})$ streamline-curvature terms we obtain the Orr–Sommerfeld equation for the rotating prolate spheroid in the form

$$\begin{aligned}&\frac{\mathrm{i}}{R}\left(M^3\phi_3'''' - 2M\left(\alpha^2+\beta^2\right)\phi_3'' + \frac{1}{M}\left(\alpha^2+\beta^2\right)^2\phi_3\right)\\ &\quad + \left(\alpha U + \beta V - \gamma\right)\left(M\phi_3'' - \frac{(\alpha^2+\beta^2)}{M}\phi_3\right) - M\left(\alpha U'' + \beta V''\right)\phi_3 = 0\end{aligned} \tag{3.18}$$

Further, neglecting both streamline-curvature and viscous terms leads to Rayleigh's equation (3.19). By doing this we assume that viscosity has a negligible effect on the instability of the boundary-layer;

$$\left(\alpha\,U + \beta\,V - \gamma\right)\left(M\phi_3'' - \frac{1}{M}\left(\alpha^2+\beta^2\right)\phi_3\right) - M\left(\alpha\,U'' + \beta\,V''\right)\phi_3 = 0 \tag{3.19}$$

This study presents an analysis of the full system of perturbation equations and these comparisons are made only to demonstrate the consistency of the full system

with the standard equations of stability theory. We also note that in the particular case of $e = 0$, the perturbation equations reduce to those derived by Garrett *et al.* (2002, 2004) for the rotating sphere.

3.2 Solution of the perturbation equations

The system defined by (3.12)–(3.17) represents an eigenvalue problem, with the homogenous boundary conditions

$$\begin{aligned} \phi_i &= 0 \quad \text{on} \quad \eta = 0, \\ \phi_i &\to 0 \quad \text{as} \quad \eta \to \infty, \end{aligned} \tag{3.20}$$

where $i = 1, 2 \ldots 6$. In this section we solve these equations by extending the techniques used by Garrett (2002) and Lingwood (1995b) in their analyses of related geometries.

The system represents a sixth-order differential equation system at each latitude for fixed value of e and permits six independent solutions for each transformed variable solution. These are denoted by $\phi_i^j(\eta; \alpha, \beta, \gamma; R, \theta)$ with the superscript j indicating one of the six independent solutions of the transformed variable solutions denoted by i.

At the outer edge of the boundary layer $U \to 0$, $V \to 0$ and $W \to W_\infty$ (some fixed value). So when $\eta \to \infty$ the perturbation equations (3.12)–(3.17) therefore become,

$$\phi_1' = \phi_2, \tag{3.21}$$

$$\begin{aligned} \frac{M^2 \phi_2'}{R} =& \frac{1}{R}\left(\alpha^2 + \beta^2 - \mathrm{i}R\gamma\right)\phi_1 + \frac{MW_\infty \phi_2}{R} + \mathrm{i}\Bigg(\alpha^2 + \beta^2 - \\ & \frac{\mathrm{i}\alpha M}{R}\left(\frac{e^2 \sin\theta\cos\theta}{1 - e^2\cos^2\theta} + \cot\theta\right)\Bigg)\phi_4, \end{aligned} \tag{3.22}$$

$$M\phi_3' = -\mathrm{i}\phi_1 - \frac{2 - e^2(1-\cos^2\theta)}{R(1-e^2\cos^2\theta)^{3/2}}\phi_3, \tag{3.23}$$

$$M\phi_4' = \frac{\mathrm{i}W_\infty}{R} - \frac{\mathrm{i}M}{R}\phi_2 - \frac{1}{R}\left(\alpha^2+\beta^2-\mathrm{i}R\gamma\right)\phi_3, \tag{3.24}$$

$$\phi_5' = \phi_6, \tag{3.25}$$

$$\frac{M^2\phi_6'}{R} = \frac{\beta M}{R}\left(\frac{e^2\sin\theta\cos\theta}{1-e^2\cos^2\theta}+\cot\theta\right)\phi_4 + \frac{1}{R}\left(\alpha^2+\beta^2-\mathrm{i}R\gamma\right)\phi_5 + \frac{MW_\infty\phi_6}{R}. \tag{3.26}$$

Equations (3.21)–(3.26) permit solutions in the form

$$\phi_i^j(\eta\to\infty;\alpha,\beta,\gamma;R) = c_i^j e^{\kappa_j\eta} \tag{3.27}$$

Where the coefficients c_i^j and exponent κ_j are constants with respect to η, and can be found by substituting (3.27) into (3.21)–(3.26). After ignoring $O(R^{-2})$ terms we find the exponents to be

$$\kappa_{1,2} = \frac{W_\infty}{2M} \mp \frac{1}{M}\left[\left(\frac{W_\infty}{2}\right)^2+\alpha^2+\beta^2-\mathrm{i}R\gamma\right]^{1/2} \tag{3.28}$$

$$\kappa_{3,4} = \frac{W_\infty}{2M} \mp \frac{1}{M}\left[\left(\frac{W_\infty}{2}\right)^2+\alpha^2+\beta^2-\mathrm{i}R\gamma\right]^{1/2} \tag{3.29}$$

$$\kappa_{5,6} = \mp\left[\alpha^2+\beta^2-\frac{\mathrm{i}\alpha M}{R}\left(\frac{e^2\sin\theta\cos\theta}{1-e^2\cos^2\theta}+\cot\theta\right)\right]^{1/2} \tag{3.30}$$

where the real parts of complex square-roots are taken to be positive.

From the second boundary condition of (3.20), as $\eta\to\infty$ all perturbations must decay, therefore only the j=1,3 and 5 solutions are relevant. The required coefficients in (3.27) for the transformed variables with j=1, 3 and 5 are found to be

$$c_1^1 = 1 \qquad c_1^3 = 0 \qquad c_1^5 = \mathrm{i}\kappa_5,$$

$$c_2^1 = \kappa_1 \qquad c_2^3 = 0 \qquad c_2^5 = \mathrm{i}\kappa_5^2,$$

$$c_3^1 = -\mathrm{i}/M\kappa_1 \qquad c_3^3 = 0 \qquad c_3^5 = M,$$

$$
\begin{aligned}
c_4^1 &= 0 & c_4^3 &= 0 & c_4^5 &= \frac{[\mathrm{i}R\gamma - W_\infty\kappa_5]}{MR\kappa_5}, \\
c_5^1 &= 0 & c_5^3 &= 1 & c_5^5 &= 0, \\
c_6^1 &= 0 & c_6^3 &= \kappa_3 & c_6^5 &= 0.
\end{aligned} \tag{3.31}
$$

As $\eta \to \infty$ there are six independent solutions for each transformed variable solution denoted by i, but only three are decaying which are relevant. Each transformed variable solution is formed by a linear combination of these with coefficients of $C_{1,3,5}$. These coefficients can be calculated from the boundary conditions of the transformed variables at $\eta = 0$. So we can write,

$$
\begin{pmatrix} \phi_1(0) \\ \phi_3(0) \\ \phi_5(0) \end{pmatrix} = \begin{pmatrix} \phi_1^1(0) & \phi_1^3(0) & \phi_1^5(0) \\ \phi_3^1(0) & \phi_3^3(0) & \phi_3^5(0) \\ \phi_5^1(0) & \phi_5^3(0) & \phi_5^5(0) \end{pmatrix} \begin{pmatrix} C_1 \\ C_3 \\ C_5 \end{pmatrix} = \begin{pmatrix} 0 \\ 0 \\ 0 \end{pmatrix}. \tag{3.32}
$$

This matrix equation has a non-trivial solution only when the determinant of the coefficient matrix is zero. We call the determinant D and require

$$
D(\alpha, \beta, \gamma; R, \theta, e) = 0. \tag{3.33}
$$

This is the dispersion relation for the rotating prolate spheroid at a latitude θ for a given value of $e \in [0, 1]$ and allows an unknown parameter (α, β or γ) to be calculated given the others at each R. The dispersion relation is satisfied when the coefficient matrix is singular, and allows $C_{1,3,5}$ to be determined from singular value decomposition.

In particular, for the prolate spheroid defined by eccentricity e, the system is solved for certain combinations of α, β, γ, R at a particular latitude θ and fixed value of e. The perturbation equations (3.12)–(3.17) are numerically integrated down towards the prolate spheroid surface from each of the initial solutions defined

by (3.27)–(3.31) at the edge of the boundary layer. As with the basic flow, the outer edge of the boundary layer is approximated by $\eta = 20$ and a double-precision fixed-step-size fourth-order Runge–Kutta integrator is used. The integrations result in nine independent solutions over the domain of integration from which the coefficient matrix of equation (3.32) can be formed. The independent solutions denoted by $j = 1$ and 3 grow much more rapidly than the solution denoted by $j = 5$ as the integration proceeds towards the prolate spheroid surface. The round-off error of the numerical integration follows the most rapidly growing solution and so it becomes difficult to preserve the linear independence of the independent solutions when simply integrating the equations. To maintain linear independence Gram–Schmidt orthonormalization is applied each time the solutions loose their independence, and details of this technique can be found in Nicholson (1995), for example.

To calculate the spatial branches for a fixed value of e at each θ and R for a given frequency γ, the wavenumber β is varied and a second-order Newton–Raphson search method is used to find the complex value of α that produces a singular coefficient matrix, i.e. satisfies the dispersion relation. To calculate the temporal branches for a fixed value of e at each θ and R for a given wavenumber β and imaginary part of the frequency γ_i, the real part of the frequency is varied and α is calculated in the same way. However, in what follows we are concerned with spatial modes only. The numerical code used is based on that provided by S. J. Garrett (personal communication, 2008), and the subroutines of the code originate from Press, Teukolshy, Vetterling & Flannery (1992).

Although (3.12)–(3.17) are specific to the boundary-layer of the rotating prolate spheroids, the methods discussed here are common to the rotating oblate spheroids stability analysed conducted in this thesis. Only slight modifications are needed

when dealing with the stability analysis of rotating oblate spheroids, and these will be discussed in the relevant chapter for rotating oblate spheroids.

3.3 Convective instability analysis

In this section we solve the perturbation equations (3.12)–(3.17) subject to the homogeneous boundary conditions (3.20) with the aim of occurring only convective instabilities. In a system that is free of absolute instabilities we can assume that the amplitude of the external disturbances decay in time at any particular location but grow in space leading to convective instabilities. It follows that in the Briggs-Bers procedure we can assume excitations at only real frequencies i.e imaginary part of frequency, $\gamma_i = 0$. Taniguchi *et al.* (1998) in their temporal analysis on rotating-sphere, followed a procedure taking different fixed values of the vortex angles, so that β is known in terms of α from (3.6). In another approach, we insist that the vortices rotate with some fixed multiple of the body surface velocity. We follow this approach computing the neutral curves of convective instabilities of rotating spheroids. As the non-dimensional speed of the surface of the rotating spheroid is $\sin\theta$, vortices traveling at speed c relative to the spheroid surface can be modelled by equating $c\sin\theta$ with the disturbance phase velocity in the same (azimuthal) direction, γ_r/β, leading to

$$\gamma_r = c\beta\sin\theta, \tag{3.34}$$

this results in the dispersion relation $D(\alpha, \beta, \gamma; R, \theta; e) = D(\alpha, \beta; R, c, \theta; e) = 0$. This approach has been denoted *method 2* by Garrett (2010a). Solving the dispersion relation enables an investigation into the spatial branches within the convectively unstable region prior to their pinching and the occurrence of local absolute instability

at some higher critical Reynolds number. An analysis of the local absolute instability of the flows is however not presented in this thesis. As mentioned in §3.1, throughout in this chapter we explicitly assume stationary vortices that rotate with the spheroid surface and so we take $c = 1$.

3.4 Results

In this section we present the neutral curves of convective instability by solving the dispersion relation $D(\alpha, \beta; R, c, \theta; e) = 0$ with the constraint that c=1 using the numerical methods explained in §3.2. The analysis involve solving D for α whilst marching through β at a particular set of R and θ for a fixed value of e. Neutral curves of convective instability are determined at $\alpha_i = 0$. We note that the basic flow equations (2.6)–(2.8) presented in §2.1 were solved using the accurate numerical method of §2.2.2 and we use these solutions for the basic flow profiles in solving the full perturbation equations for prolate spheroids. However, the accuracy of the series solution of the basic flow in the convective instability analysis is presented in §3.4.4.

3.4.1 Spatial branches

Spatial branches have been calculated at $\theta = 10°$–$70°$ in $10°$ increments for $e = 0.0$–0.7. As with the analyses of related geometries by Lingwood (1995a) and Garrett *et al.*, two spatial branches are found to determine the convective-instability characteristics at all latitudes and Reynolds numbers. Branch 1 arises from a crossflow-instability mode (type I) and branch 2 arises from streamline-curvature effects (type II). This can be shown in the analysis of the Orr-Sommerfeld equation (3.18) where branch 2 is not found, which is consistent of the existing work

on related geometries (for example see Garrett (2002, 2010a,c)).

In the complex α-plane, a branch lying below the α_r-axis indicates convective instability. Figures 3.1 shows the two spatial branches at $\theta = 10^\circ$ and $R = 2300$ for $e = 0.6$ where we see that the convective instability is determined only from branch 1. Further increasing R at the same latitude we find that an exchange of modes occurs at a particular R and branch 1 is seen showing two minimums below the α_r-axis. Figure 3.2 shows the two branches at $R = 2420$ where the modified branch 1 with large region under α_r-axis indicates convective instability due to crossflow-mode and the smaller region under α_r-axis indicates the convective instability due to streamline-curvature mode. Increasing the value of R causes the two minima on branch 1 under the α_r-axis to move further downward and the points where the branch 1 crosses the α_r-axis move apart, hence widening the region of instability and mapping out two lobes of the neutral curve. Above a certain value of R the smaller peak on branch 1 moves below the α_r–axis as shown in Figure 3.3 and further increases in R produce the upper and lower branches of the neutral curve.

This characteristic of the two branches is typical at all latitudes below $\theta = 60^\circ$–66° depending on the value of e. At $\theta \geq 66^\circ$ for all values of e and $\theta \geq 60^\circ$ for $e > 0.6$ we note that the two branches do not behave as described, and no branch exchange occurs between the two branches at a particular R. In the neutral curves for $\theta \geq 66^\circ$ for all values of e, the two lobed structure has disappeared and the convective instability is caused only from branch 1 while a kink is shown by branch 2. However, we note that the kink in branch 2 is caused when the streamline-curvature effects dominate over the crossflow effects. This can be seen in Figure 3.4 where at $\theta = 60^\circ$ and $e = 0.6$ the streamline-curvature effects become dominant and the convective instability is caused after the two spatial branches exchange but the

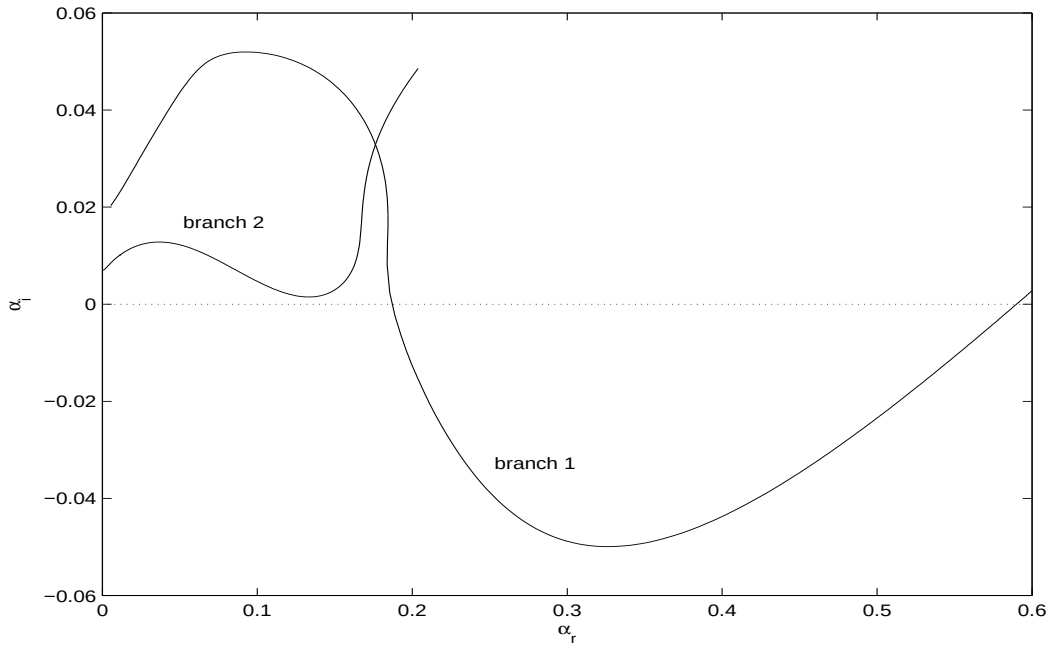

Figure 3.1: The two spatial branches for $e = 0.6$ at $\theta = 10^\circ$ and $R = 2300$ showing convective instability from branch 1 only.

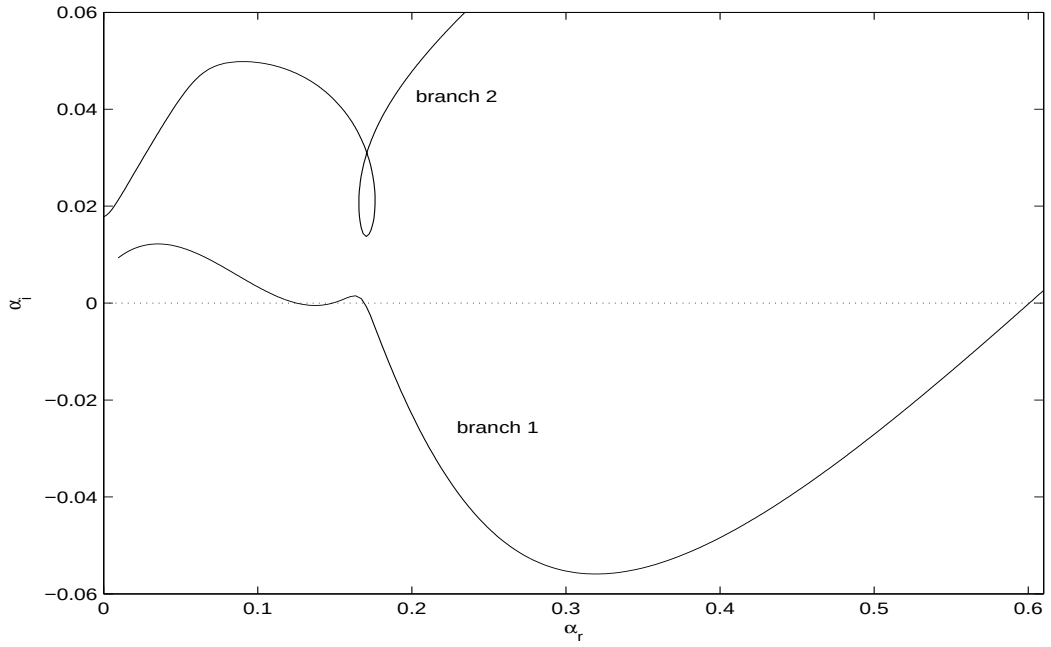

Figure 3.2: The two spatial branches after the exchange for $e = 0.6$ at $\theta = 10^\circ$ and $R = 2420$ showing regions of both streamline-curvature and crossflow instabilities.

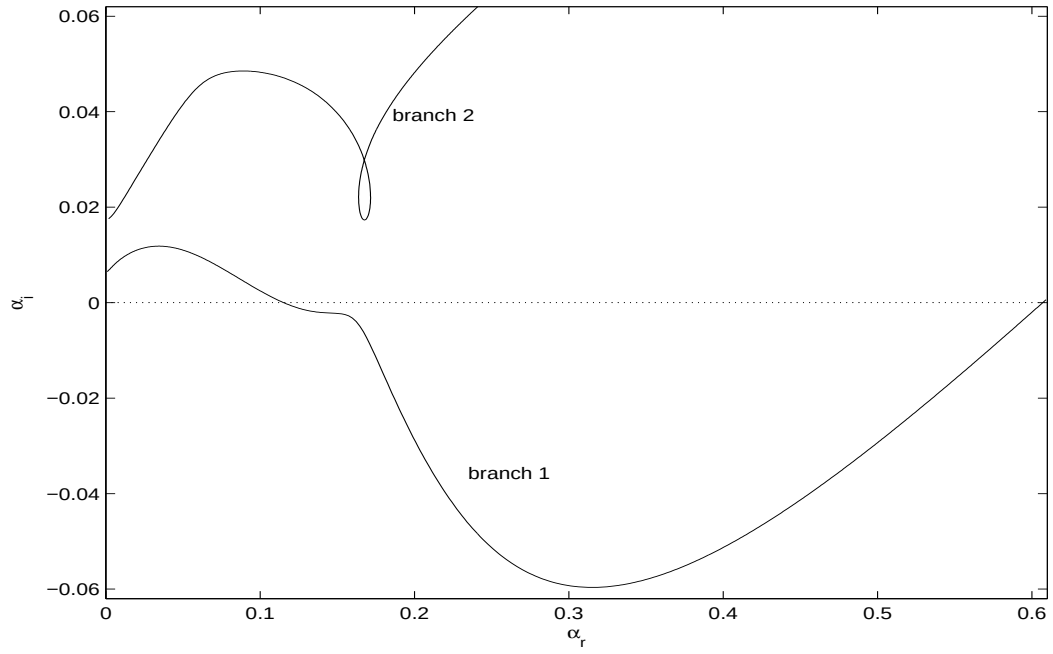

Figure 3.3: The two spatial branches after the exchange for $e = 0.6$ at $\theta = 10°$ and $R = 2500$ showing combined region of streamline-curvature and crossflow instabilities.

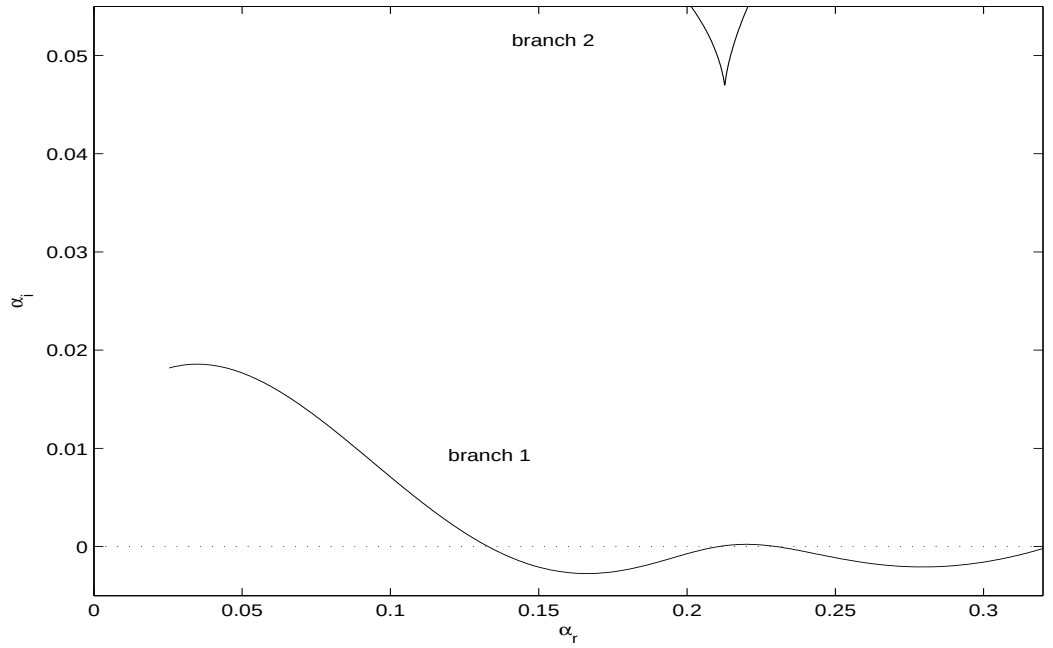

Figure 3.4: The two spatial branches after the exchange showing regions of streamline-curvatute and crossflow instability for $e = 0.6$ at $\theta = 60°$ and $R = 163$.

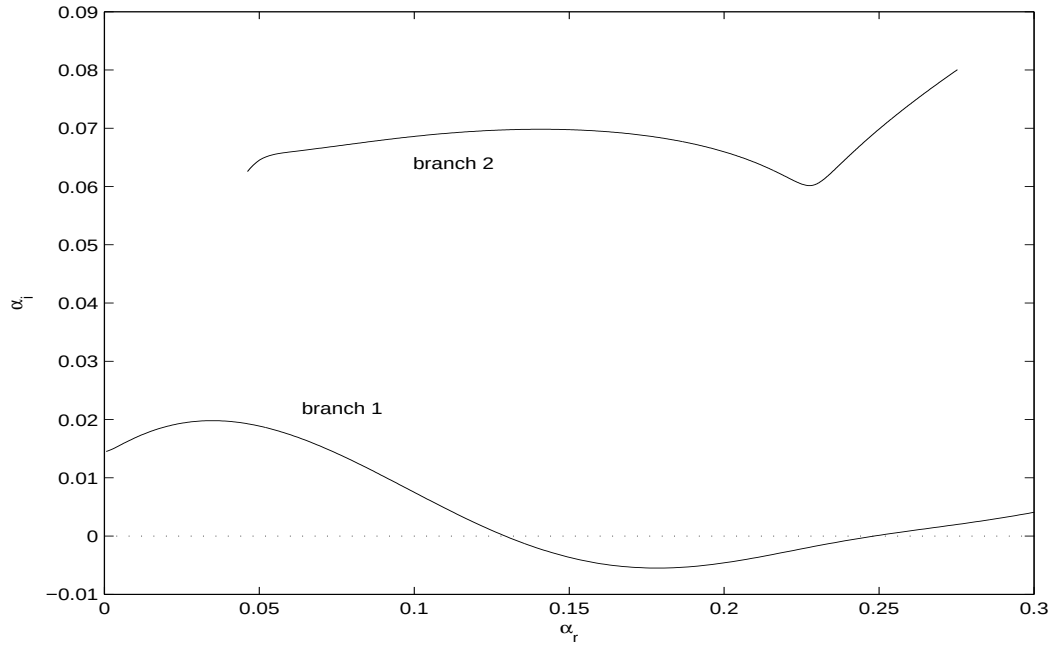

Figure 3.5: For $e = 0.7$ at $\theta = 60°$ and $R = 140$ the convective instability is caused only from branch 1 and branch 2 shows a kink.

minimum of the region showing streamline curvature instability has moved lower than the minimum of the region showing crossflow instability. In Figure 3.5 at $\theta = 60°$ and $e = 0.7$ the two lobed structure has disappeared and the convective instability is caused by branch 1 where, as expected, a kink is appeared in branch 2.

3.4.2 The neutral curves

The Reynolds number R introduced in equation (6.2) is based on the equatorial rotation speed of the body and so is dependent on e. A comparison of the stability characteristics at a fixed latitude across bodies with different eccentricities rotating at the same *angular* rate is therefore difficult to interpret when using this Reynolds

number. However, expressing the results in terms of a Reynolds number defined as

$$Re = \frac{R}{\sqrt{1-e^2}}, \tag{3.35}$$

enables the direct comparison of different bodies rotating at the same angular rate (and with equal semi-major axis lengths) at a particular value of Re. This Reynolds number was used by Garrett in the stability analysis of rotating sphere boundary-layer and we will call this as *the spherical Reynolds number*. Henceforth, *the spherical Reynolds number* Re is interpreted as a measure of the angular rotation rate, $\Omega^\star$.

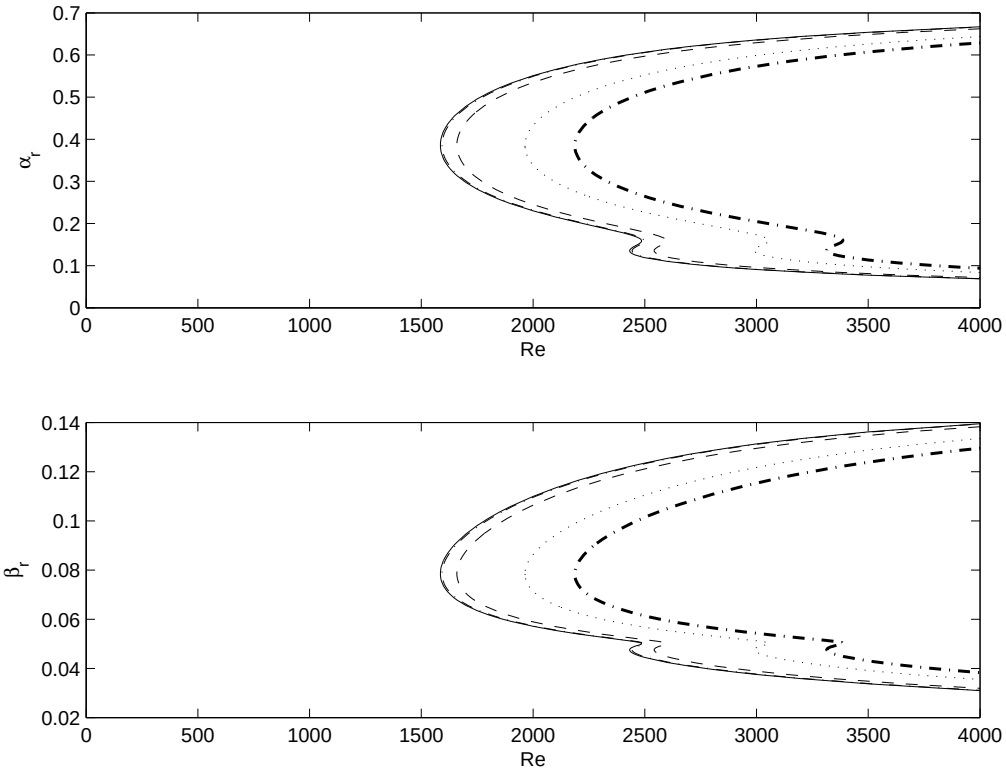

Figure 3.6: Neutral curves in the (Re, α)- and (Re, β)-planes at latitude 10° for $e = 0$ (–), 0.1 (-.), 0.3(−−), 0.6 $(\cdots)$ & 0.7 (**-.**).

The stability characteristics of the rotating sphere boundary-layer (i.e. when $e = 0$) were discussed in detail by Garrett & Peake and Garrett; where they compared

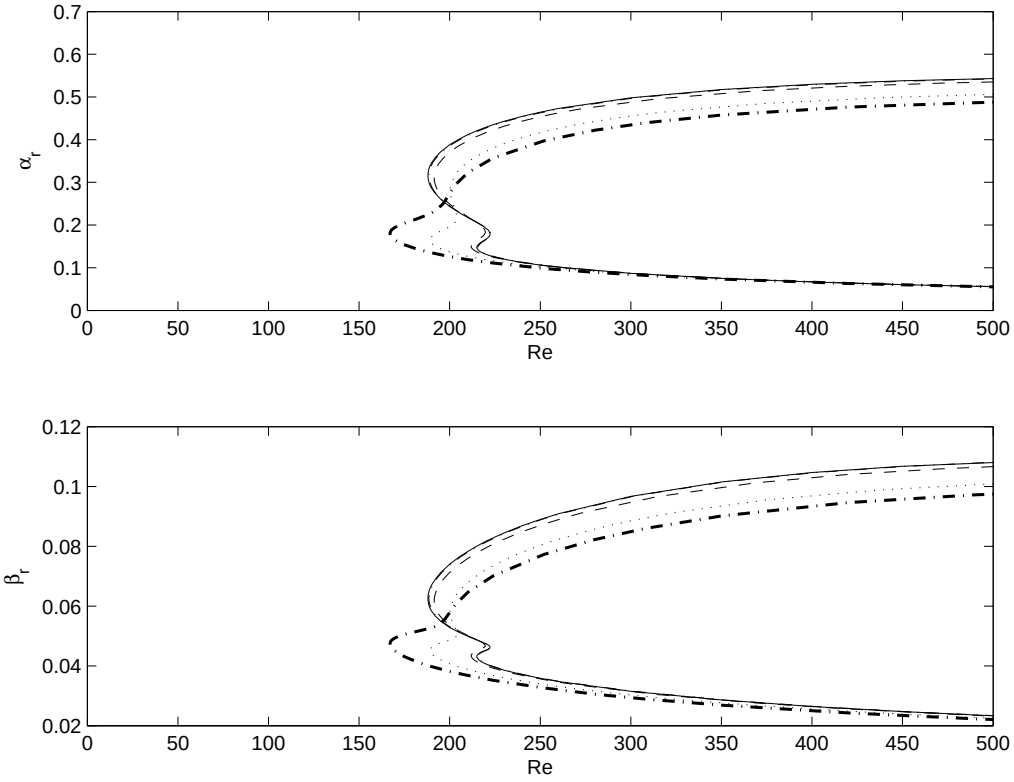

Figure 3.7: Neutral curves in the (Re, α)- and (Re, β)-planes at latitude 60° for $e = 0$ (–), 0.1 (-.), 0.3(−−), 0.6 $(\cdots)$ & 0.7 (**-.**).

the results with other existing theoretical and experimental results. In this current analysis our focus is on the effects of eccentricity on convective instability as the body is deformed from a sphere to a rotating prolate spheroid. Neutral curves in the (Re, α_r)- and (Re, β)-planes are shown in Figures 3.6 & 3.7 at $\theta = 10°$ and 60° for $0 \leq e \leq 0.7$. Furthermore, neutral curves at latitudes to $\theta = 70°$ (in 10° increments) are sketched in Figure 3.8 for $e = 0.0$, 0.3 and 0.7 in the (Re, α_r)-plane only. Each curve encloses a region that is convectively unstable, and we see the characteristic two-lobed structure for low to moderate latitudes which is also seen in other analysis of related geometries. The larger lobe, characterized by higher wavenumbers arises from the behaviour of the type I branch; and the smaller

lobe, characterized by smaller wavenumbers, from the type II branch. However, we note that at higher latitudes and eccentricities the larger lobe either disappears or becomes less dangerous, indicating a dominance of streamline curvature effects as we discuss now.

Critical Reynolds numbers in terms of R and R_S for the onset of both modes are listed at all latitudes for $0 \leq e \leq 0.7$ (in increments of 0.1) in Appendix C.3 Tables C.1–C.8. Note that R can be converted in terms of Re using the relation (3.35) and R_S is called the spin Reynolds number discussed in §3.4.3. From Figures 3.6–3.8 and Tables C.1–C.8 it is clear that the effect of increasing eccentricity on the relative importance of the type I mode is small at low θ. This reflects the dependence on e in the perturbation equations at $O(1/R)$ only (the order at which type II [streamline curvature] effects occur), and so the stability characteristics at leading order are determined by the steady flows alone, which have been shown to be insensitive to e for low θ. However, we also see that eccentricity acts to increase the relative importance of the type II mode as the latitude is increased. For $\theta \leq 50°$, the type I mode remains the most dangerous (in the sense of lowest critical Reynolds number) at each e considered; at $\theta = 60°$, the type II becomes the most dangerous for sufficiently high e between 0.3 and 0.7; and for $\theta = 70°$, the type II lobe is seen to be most dangerous for all eccentricities. All neutral curves shown were calculated using the full perturbation equations (3.12)–(3.17). Neutral curves calculated using the Orr–Somerfeld equation (3.18) were found to be single-lobed at each latitude, with critical Reynolds numbers lower than the most dangerous modes arising from the full system. However, this is shown only at $\theta = 20°$ for $e = 0.7$ in Figure 3.9. The neutral curves calculated from the full system and the Orr–Somerfeld equation are found to be consistent for large Re for all parameter sets $\{\theta, e\}$.

Considering the effect of increasing eccentricity at a particular latitude, Figure 3.8 demonstrates that increasing e increases the critical Reynolds numbers for the onset of both modes at latitudes $10^\circ \leq \theta \leq 40^\circ$, i.e. eccentricity acts as a stabilizing effect at low to moderate latitudes. However, at latitudes $\theta \geq 50^\circ$ the type II mode is seen to become increasingly dangerous with increased e, eventually becoming dominant over the type I mode. Eccentricity therefore has a de-stabilizing effect at high latitudes[1]. At all latitudes the neutral curves for $e = 0$ are as calculated by Garrett & Peake (2002) for the rotating sphere. Furthermore, we predicted that the neutral curves for the Orr-Sommerfeld equations are also stabilizing for increasing e at moderate to lower latitudes, however this is shown only at $\theta = 20^\circ$ for $e = 0.1$ and 0.7 in Figure 3.10.

Taking into account the interpretation of Re as a measure of the angular rotation rate, we interpret the results as follows: rotating prolate spheroids with higher eccentricity first become convectively unstable at high latitudes for lower angular rotation rates than is required for lower eccentricities, however for instability to manifest at lower latitudes, a higher angular rotation rate is required for bodies with larger eccentricity. Eccentricity is therefore interpreted as a de-stabilizing influence at high latitudes and stabilizing for moderate to low latitudes.

3.4.3 Comparison of results with other related Geometries

In the investigation of rotating disk boundary-layer flow, Malik (1986) and Lingwood (1995a) used a Reynolds number which is based on the local disk velocity at

[1]We note that increasing e acts to slightly narrow the region of convectively unstable parameters at all latitudes and so could be interpreted as a stabilizing effect in this sense. However, for high latitudes the reduced critical Reynolds number is expected to be the dominant characteristic.

the radius under investigation and the local-boundary-layer thickness. The equivalent Reynolds number in our investigation is written as $R_D = Re \sin\theta$. Although not shown here, when our results are expressed in terms of this Reynolds number we find that for values of $e \leq 0.5$, the neutral curves become very similar to that for convective instability of the rotating-disk boundary layer (due to Malik (1986), for example) as θ tends towards the pole. This behaviour at smaller latitude is consistent with that discussed by Garrett & Peake (2002) in the case of rotating sphere. This is of no surprise as the region close to the pole is locally flat, particularly for small eccentricities, and so limits to a small rotating disk. Figures 3.11 & 3.12 show that the critical Reynolds number for both crossflow and streamline curvature effects approach those of the rotating-disk as θ tends toward the pole . However, we note that for large values of e, at lower latitudes of prolate spheroids the critical Reynolds numbers exceed that of rotating-disk boundary-layer. We suspect this due to curvature having a stabilizing effect at lower latitude. We explain this further in §3.5.

Taniguchi *et al.*(1998) and Kohama *et al.*(1983) present their results for the rotating sphere in the (R_S, n)- and (R_S, ϵ)-planes. Here R_S is the spin Reynolds number and is defined in terms of spherical Reynolds number as $R_S = \eta_0^{\star 2}\Omega^\star/\nu^\star = Re^2$. Note that n is the number of vortices defined in (3.5) and ϵ is vortex angle from (3.6). Garrett (2002) showed the results for the special case of $e = 0$ in these planes and compared the results with those theoretical and experimental results of Taniguchi *et al.* and Kohama *et al.* respectively. He found that his results were consistent with the experimental observations of Kohama *et al.*. We sketch the neutral curves of convective instability for prolate spheroids at latitudes of 10°– 70° in (R_S, n)- and (R_S, ϵ)-planes for various values of e in Appendix C.2 as Figures C.1–

C.7. We note that as the latitude decreases the number of vortices n at the onset of instability increases for all values of e, and this is consistent with the experimental observation of Kohama *et al.*. We note that at low to moderate latitudes eccentricity has apparently no effect on the number of spiral vortices at the onset of instabilities. However, at high latitudes the number of vortices n slightly decrease with increasing e. At lower latitude 10°, the number of vortices at the onset of crossflow mode is tending to approximately 22. This is consistent with that calculated by Malik (1986) for the rotating disk. At low to moderate latitudes of $\theta = 40°$ for all values of e, we find that at the onset of instability the stationary vortices were predicted to have roughly the same vortex angle for each mode, the values found being $\epsilon \approx 11.4°$ and 19.4° at the onset of crossflow instabilities and streamline-curvature instabilities respectively. However, as the latitude is increased above 40° we predict that the vortex angle at the onset of crossflow instability decreases slightly, whilst the vortex angle at the onset of streamline-curvature instability increases slightly; this is further exaggerated with increasing e. However, at high latitudes where the crossflow effects do not dominate we note that the vortex angle decreases with increasing e.

3.4.4 Accuracy of series-solution method in convective instability analysis

We compare the neutral curves obtained from the full perturbation equations using the two different solution methods (i.e the series solution method and numerical method) of the steady flow equations (2.6)–(2.8) of §2.1. We intend to show the exact limits of latitudes for different values of e up to which the series solution of the basic flow can be used to study convective instability in this geometry. As explained in Chapter 2, the series solution has major benefits in terms of computational power

required.

In §2.3 we have shown the comparison between the basic flow profiles of prolate spheroids for the two different solution methods (series solution method and numerical solution method) at various latitudes for $e \in [0, 1]$. These comparisons were shown through visual inspection as well as root mean square (RMS) errors of the basic flow profiles at various latitudes for $e \leq 0.7$. We observed that at lower latitudes the series solution was very accurate at low to moderate latitudes for all $e \leq 0.7$, but as the latitude was increased the discrepancy between the two solutions also increased. This was further exaggerated with increasing e. We observe that this discrepancy between the basic flow solutions is consistent with the discrepancy found between neutral curves of convective instabilities for the two different basic flow solutions. In Figures 3.13 & 3.14 comparison between the neutral curves for two solutions of basic flow are shown at two latitudes of 10° and 60° for various values of e. From these visual inspections we see that the discrepancy between the neutral curves at lower latitude is negligible for all values of $e \leq 0.7$, but as the latitude is increased the discrepancy is increased. This is exaggerated with increasing e. We do not show this comparison at other latitudes, but the discrepancy between the two different solutions of the basic flow is reflected in the same way in the convective instability characteristics. Indeed the discrepancy between the neutral curves (calculated for the two types of basic flow) is increased when W-profile of the basic flow has root mean square error of $O(e^{-2})$ magnitude (see Tables 2.1–2.5). Therefore, the series solution of the basic flow can capture the parameters and characteristics of the convective instability very accurately at latitudes of $\theta \leq 40^\circ$ for all values of e, 50° for $e \leq 0.5$ and 60° for $e \leq 0.3$.

3.5 Conclusion

In this chapter we have formulated the perturbation equations that govern the stability of the boundary-layer over the family of rotating prolate spheroids, and convective instability analyses were conducted in detail. This chapter should be viewed as a generalization of Garrett & Peake (2002) previous work through the consideration of the more general class of prolate spheroids which includes the sphere at $e = 0$, as a special case. Our results for $e = 0$ reproduce those for the rotating sphere. As mentioned at the beginning, only stationary vortices were considered in this chapter.

Analysis of spatial branches from the full perturbation equations shows that two spatial branches (type I and type II) arise to determine the characteristics of convective instability at each latitude and Reynolds number. The streamline-curvature mode (type II) does not arise in the analysis of the Orr-Sommerfeld equation. This is consistent with the anlyses by Lingwood and Garrett on the related geometries.

The convective instability of the boundary-layer over the family of rotating prolate spheroids is dependent on the steady flow of the boundary-layer. At higher latitudes, the rate of inflow into the boundary layer was less than that at lower latitudes, and this influenced the boundary layer by moving instabilities from higher latitudes towards lower latitudes with increasing Reynolds number i.e. the rotation rate. For increasing eccentricity at a fixed latitude our results suggest that eccentricity has a de-stabilizing effect at high latitudes, i.e. lower rotation rates are required for the flow to first become convectively unstable at higher latitudes for bodies with larger e. However, in contrast, eccentricity is seen to be stabilizing at moderate to low latitudes, i.e. higher rotation rates are then required to move the transition region closer to the pole for bodies with larger e. As increasing e is equivalent to

increasing curvature of the prolate spheroid, this is therefore convenient to conclude that increasing curvature has a stabilizing effect on the boundary-layer over rotating prolate spheroids. This was also evident at lower latitude 10° where the critical Reynolds number R_D for both types (I & II) for large values of e exceeded the critical Reynolds number of the rotating-disk flow. However, with increasing latitude from the pole towards the equator, curvature decreases. Therefore, at high latitudes we find a combination of two destabilizing effects to the boundary-layer. These two destabilizing effects at high latitudes are due to (i) decreasing curvature due to increasing latitude and (ii) decreasing rate of inflow (W-profile) into the boundary layer at higher latitudes which exaggerates with increasing e compared to that at lower latitudes. Therefore these two destabilizing effects combine to overcome the stabilizing effect of curvature (due to increasing e) at moderate latitudes between 50°–60°. This is evident from the fact that the values of critical R_D are nearly the same at these moderate latitudes for all e. As the latitude is increased above 60°, the combination of these two destabilizing effects aggregates and consequently we predict a counter effect i.e. destabilizing effect of increasing e at latitudes $\theta \leq 60°$. Indeed the destabilizing effect of e at high latitudes is observed due to the faster decrease in the rate of inflow into the boundary layer with increasing e (note that decrease in the rate of inflow into the boundary layer has a destabilizing effect). It is acknowledged here that we are unaware of any experimental investigations into the rotating prolate spheroid flows considered here, which means that we are currently unable to compare our results for $e > 0$ with experiments as was done by Garrett & Peake and Garrett for $e = 0$.

The convective instability analysis shows that crossflow instabilities dominate below $\theta = 60°$–$66°$ depending on the value of e. The number of spiral vortices at the

onset of instability for each fixed value of e are predicted to increase with decreasing latitude and this is consistent with the experimental observation of Kohama & Kobayashi in the special case when $e = 0$. As the analysis moves towards the pole we predict that the number of spiral vortices approaches $n \approx 22$, which is the same predicted theoretically for rotating disk (Malik (1986)). At the onset of instability the stationary spiral vortices have roughly the same vortex angles at low to moderate latitudes for each value of e, these are $\epsilon \approx 11.5^\circ$ and 19.5° at the onset of crossflow and streamline curvature instabilities, respectively. These values were also predicted by Garrett (2002) in the analysis of rotating sphere and agree well with those predicted on the rotating disk. However, at $\theta = 50^\circ$ and above the vortex angles at the onset of instabilities begin to reduce slightly. At $\theta = 60^\circ$ and above, the predicted value of ϵ approaches 14° at the onset of streamline curvature instabilities for each value of e, which is in good agreement to the experimental observation of Kohama (1984b). Our theoretical predictions suggest that the spiral vortex angle at the onset of transition is slightly varying with latitude for the rotating prolate spheroids at each value of e. At higher latitudes, this is further exaggerated with e. However, Kohama and Kobayashi have reported vortex angle $\epsilon = 14^\circ$ at the onset of instabilities at all latitudes of the rotating sphere boundary-layer and we will discuss this in detail in the subsequent chapter.

In the derivations of the governing equations, factors $1/(1 + \sqrt{1 - e^2}\ \eta/R)$ that multiplied terms in the perturbation equations have been replaced by unity. This approximation is similar to the parallel-flow approximation found in many other boundary-layer investigations and means that the perturbation equations solved here are not rigorous at $O(1/R)$. As discussed by Garrett & Peake (in the case that $e = 0$), the thickening of the boundary layer, together with the fact that the critical

Reynolds numbers decrease with latitude, means that the approximation is less valid for higher latitudes. However, increasing e acts to counteract this slightly, and the approximation is more valid for higher eccentricities and low latitudes. In any event, it is our opinion that any inaccuracies introduced through this assumption are not sufficiently large to affect the conclusions of this work. It is also acknowledged that this work consists of a linear analysis and so would be inaccurate in situations where the growth rates are large and non-linear effects would occur.

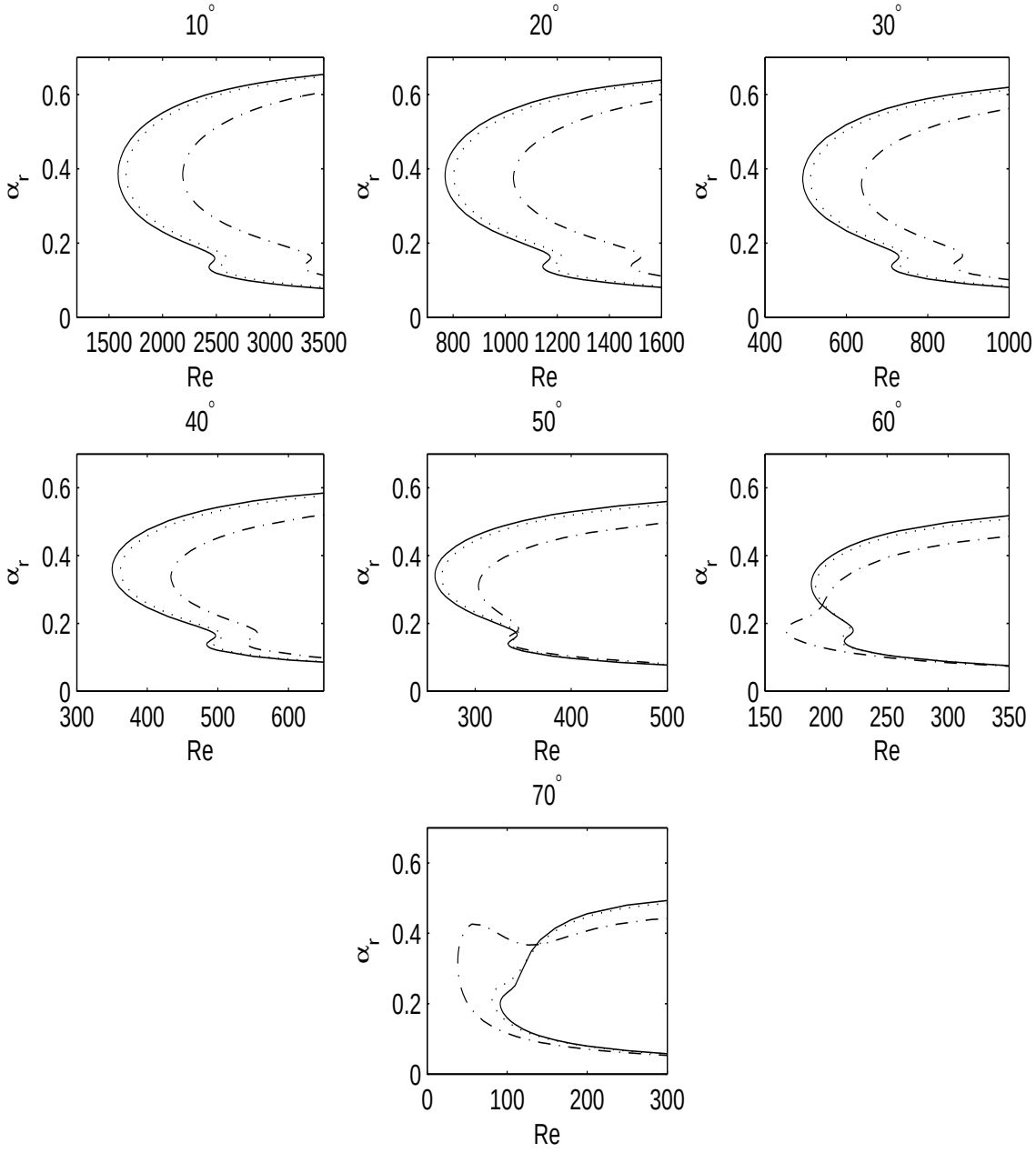

Figure 3.8: Neutral curves in the (Re, α)-plane at all latitudes for $e = 0.0$ (–), 0.3 $(\cdots)$ & 0.7 (-.).

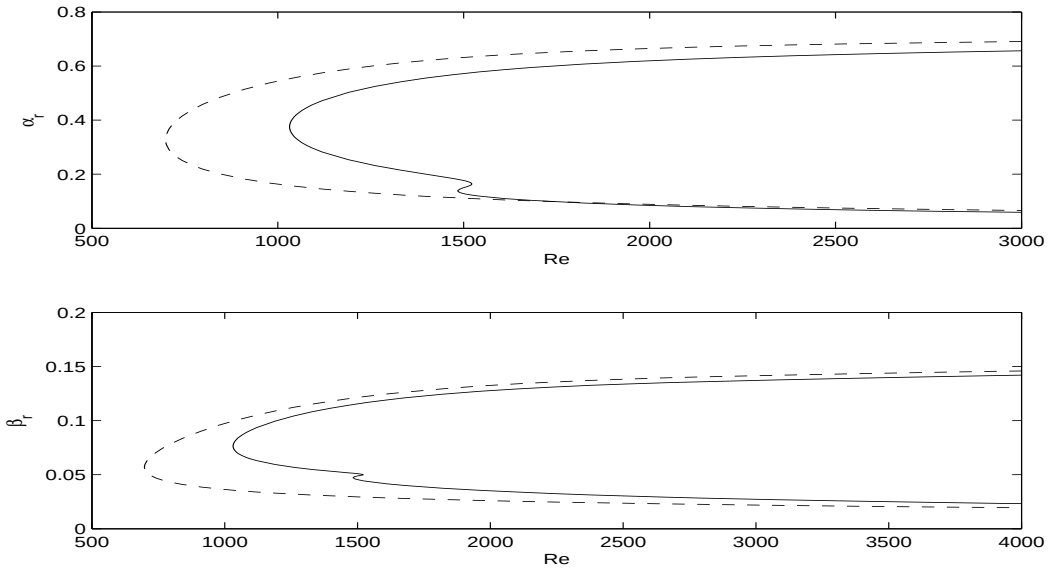

Figure 3.9: A comparison between both neutral curves in Re, α_r & Re, β-planes calculated from the full perturbation equations (–) and Orr–Sommerfeld equations (−−) at $\theta = 20°$ for $e = 0.7$.

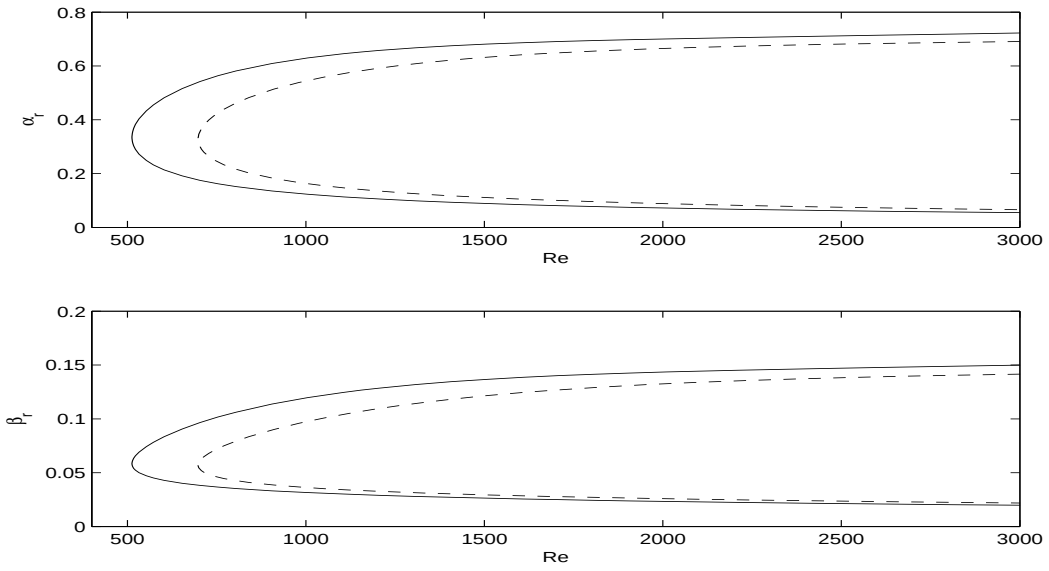

Figure 3.10: A comparison between neutral curves calculated from the Orr–Sommerfeld equations at $\theta = 20°$ for $e = 0.1$ (–) & 0.7 (−−).

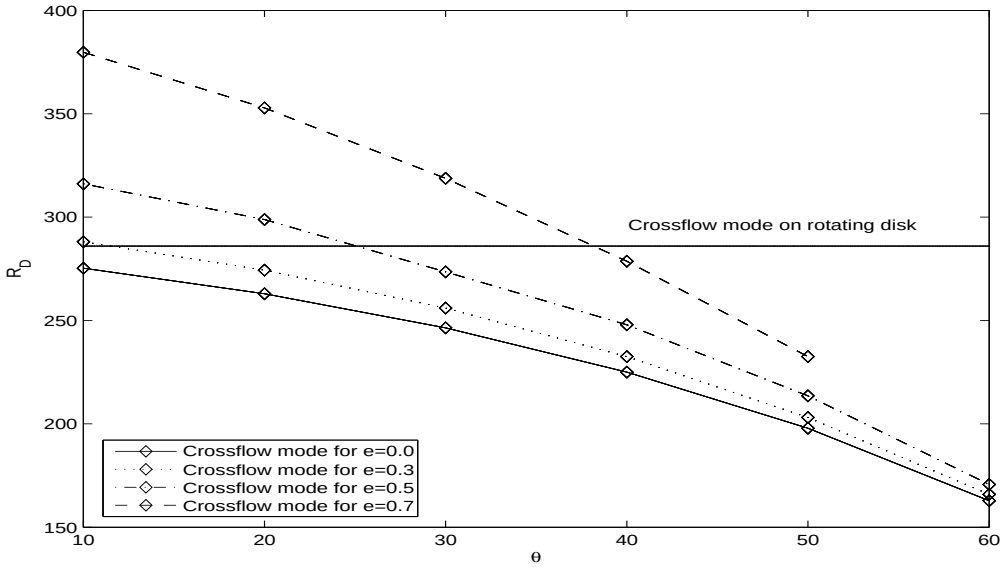

Figure 3.11: A comparison of the critical R_D values for convective instability due to crossflow effects at each latitude with those of the Malik (1986) for the rotating disk (horizontal line).

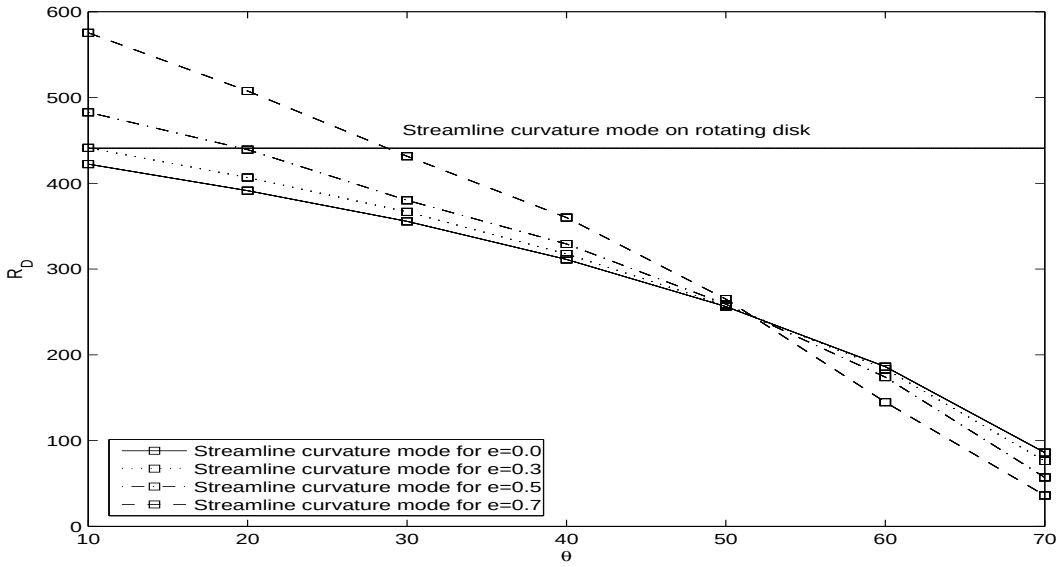

Figure 3.12: A comparison of the critical R_D values for convective instability due to streamline curvature mode at each latitude with those of the Malik (1986) for the rotating disk (horizontal line).

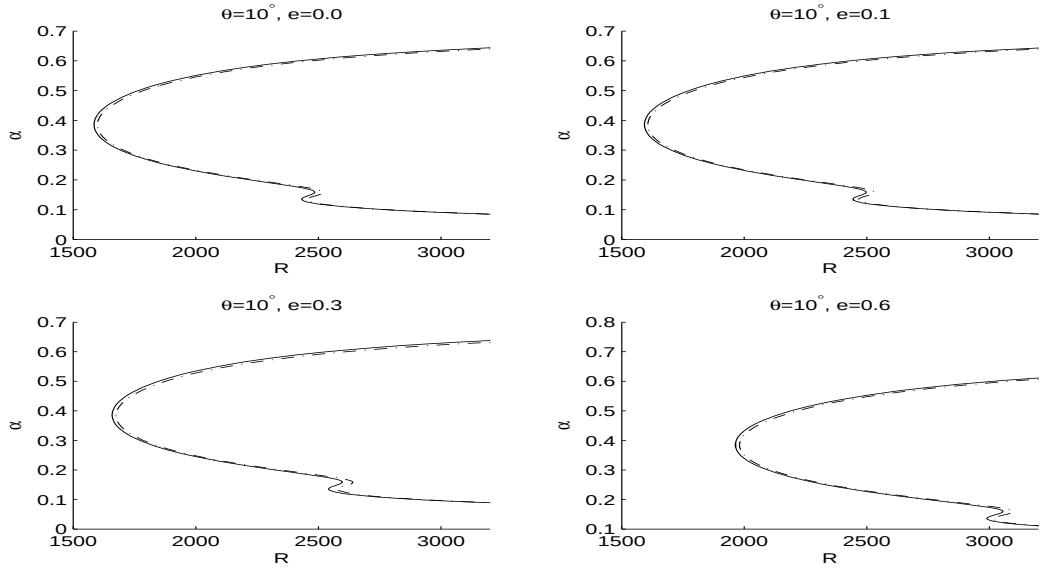

Figure 3.13: Neutral curves in the (Re, α)-plane for numerical solution (–) and series solution method (-.) at latitude 10° for $e = 0, 0.1, 0.3, 0.6$.

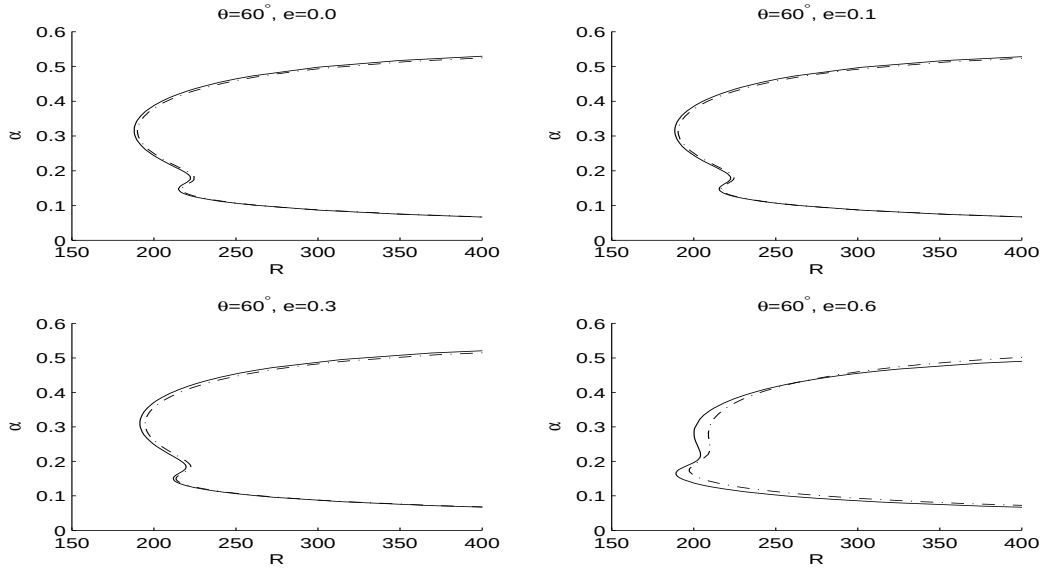

Figure 3.14: Neutral curves in the (Re, α)-plane for numerical solution (–) and series solution method (-.) at latitude 60° for $e = 0, 0.1, 0.3, 0.6$.

Chapter 4

Vortex-speed selection within the boundary-layer flow over prolate spheroids rotating in still fluid

In this chapter we extend the convective instability mechanisms within the boundary-layer flow over a family of rotating prolate spheroids presented in Chapter 3 and investigate the amplification rates within the convectively-unstable region. We use the same perturbation equations and numerical techniques for the prolate spheroid case presented in §§3.1 & 3.2. This work is indeed a generalization of the rotating-sphere boundary-layer by Garrett (2010c) where he associated the onset of convective instability with the experimentally observed onset of spiral vortices reported in the literature. In §4.1 we show the spatial amplification rates for stationary as well as traveling vortices at different speeds with respect to the prolate spheroid surface at various latitudes for a number of values of eccentricity. Where possible, we compare our results with those theoretical and experimental results observed for the rotating sphere. A discussion on the results is presented in §4.2.

4.1 Growth rates of stationary and traveling disturbances

In §3.4 we solved the dispersion relation $D(\alpha, \beta; R, c, \theta; e) = 0$ with the constraint that c=1. In this section we solve the same dispersion relation for a set of values of $c = 0.6$–2 using the numerical methods explained in §3.2. Physically the spatial growth rate for a fixed value of e is determined by a range of disturbance waves at a particular location (determined by θ) and rotation rate (determined by R). Indeed, the spatial growth rate is determined by the imaginary part of latitudinal wave number i.e. α_i at a particular θ and Re. We sketch the neutral curve of convective instability at a particular location in the (Re, α_r)-plane, and absolute values of α_i are plotted as the third dimension. This determines the spatial growth rate.

Garrett (2002) has shown that the rotating-sphere boundary layer is absolutely unstable at particular Reynolds numbers and beyond this the flow becomes turbulent. Absolute instability is the spatio-temporal instability and so the region of absolute instability contained within the region of convective instability is irrespective of c. In the rotating-sphere case, Garrett (2010c) considered the convective growth rates through the convectively unstable region bounded by the critical Reynolds numbers of absolute instability. Note that in producing plots of the spatial growth rates shown in Figure 4.1 it is only possible to consider the convective instability over a finite distance in Re before a region of absolute instability is entered. Although we are able to consider the convective instability beyond this critical value by avoiding parameters within the region of absolute instability, eventually the position of maximum growth rate coincides with the location of a pinch point. At this point the characteristic branch exchange between the type I and type III branches occurs

and the maximum spatial growth rate in the convective sense is undefined. How far the convective instability analysis for maximum growth rates can be extended for each c, θ and e is determined by the occurrence of a pinch point in the absolutely unstable region with $\gamma = c\beta \sin\theta$.

4.1.1 Growth rates and vortex speed selection

In order to visualize the growth rates for stationary disturbances, Figure 4.1 plots the spatial branches of the type I and II modes through the convectively unstable region at various locations over the surface of prolate spheroid for a particular value of $e = 0.3$. We note that the growth rates of each mode are unchanged as the analysis moves over the surface of the prolate spheroid. At each latitude the type I mode has significantly larger growth rate. Further investigation shows that this analysis does not change with changing values of e. This analysis is consistent with the rotating sphere (i.e. $e = 0$) by Garrett (2010c). From this we conclude that the amplification of the two convectively unstable modes is unchanged at different points on the prolate spheroid for each value of e and the type I mode is likely the most amplified at all Reynolds numbers (rotation rates) in otherwise still fluid.

Disturbance speeds have been considered in the range $c = 0.5$–2 for each parameter set and neutral curves computed as in §3.4. Figures 4.2 & 4.3 show the neutral curves at $\theta = 10^\circ$ & $\theta = 60^\circ$ for $e = 0.3$ in terms of α_r, β, n, and ϵ for $c = 0.7$, 0.8, 0.9, 1 and 2. Similar neutral curves at $\theta = 10^\circ$ & $\theta = 60^\circ$ for $e = 0.6$ are also shown in Appendix C.4 for $c = 0.7$, 0.8, 0.9 and 1 in Figures C.8 & C.9 respectively. Note that n and ϵ are observable quantities in experiments which motivates their use here. Recall that $c = 0.7$ corresponds to disturbances traveling at 70% of the local spheroid surface speed, and $c = 1.5$ and 2 correspond to disturbances travelling

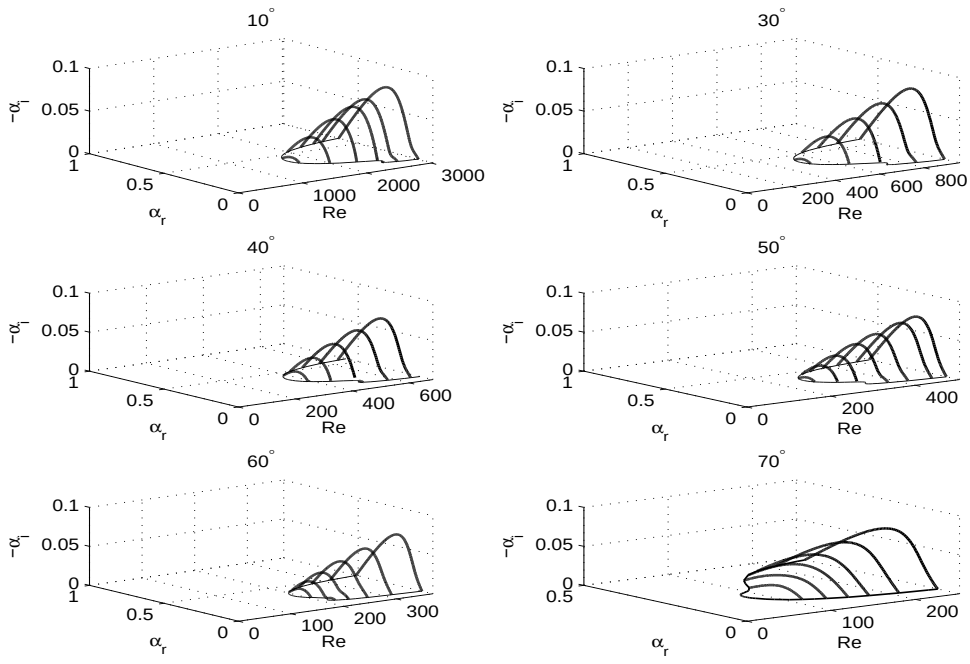

Figure 4.1: Linear convective growth rates for stationary disturbances through the convectively unstable region at various θ for $e = 0.3$.

at speeds greater than the prolate spheroid surface. At these latitudes and eccentricities, and indeed all considered, we find that the lobe arising from the type II mode is sensitive to the disturbance speed. In particular, the type II lobe is quickly eliminated for $c < 1$ and exaggerated for $c > 1$. The result that quickly travelling type II modes are the most dangerous (in the sense of lowest critical Re) is consistent with the previous theoretical results on the related geometries Balakumar & Malik (1991); Faller (1991); Turkyilmazoglu & Gajjar (1998); Garrett (2010a,b,c). However, it is important to note that the range of waveangles and vortex numbers predicted to be unstable to quickly travelling modes is narrowed with increased c. In a sense this is a stabilizing effect because only a very narrow range of vortex parameters can be selected, and is much more significant than the slight narrowing mentioned in footnote 1 of §3.4.2.

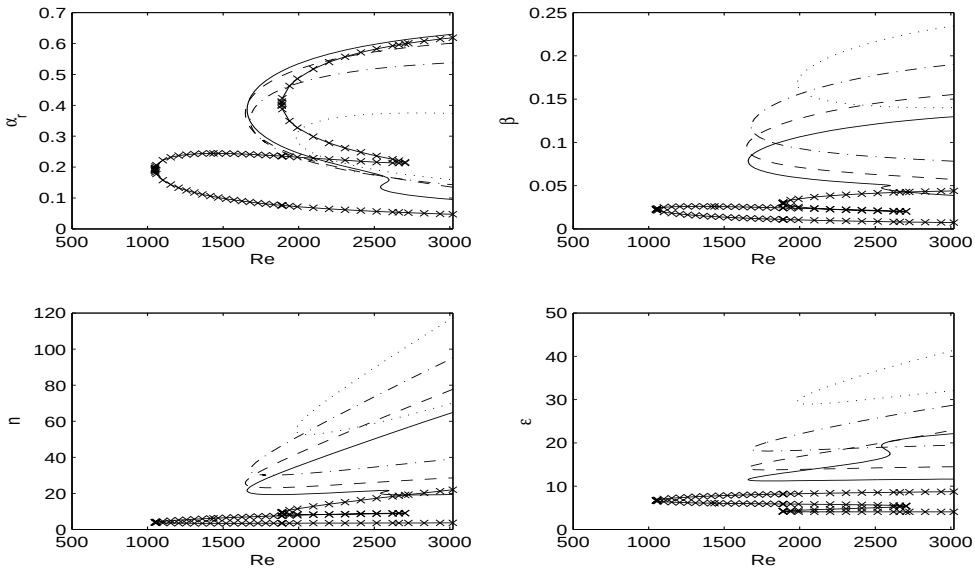

Figure 4.2: Neutral curves for traveling disturbances with c=0.7 ($\cdots$), 0.8 (-.), 0.9 ($--$), 1.0 (–), 2.0 (**-x**) at $\theta = 10^\circ$ for $e = 0.3$.

We therefore have two competing factors in the vortex-speed selection process over all prolate spheroids: the critical Reynolds numbers for the onset of the type II mode reduce with increased c, but the range of parameter values that the corresponding vortices can exist at becomes increasingly narrow, thereby prohibiting selection. In order to clarify the process we follow Garrett (2010a,b,c) and consider the linear growth rates for travelling modes through the region of convective instability. The results of this at $\theta = 10^\circ$ & 60° for $e = 0.3$ are given in Figures 4.4 & 4.5 respectively, where plots of the spatial branches at different values of c are presented in order to visualize the growth rates. We see that the growth rates within the type II lobe increase relative to the type I mode as c increases. However, more importantly, we note that the globally maximum growth rates are for the type I mode, and these peak between $c = 0.7$ and $c = 0.8$. Similar results of growth rates are also shown at $\theta = 10^\circ$ & 60° for $e = 0.6$ in Figures C.10 & C.11 for $c = 0.7$, 0.8,

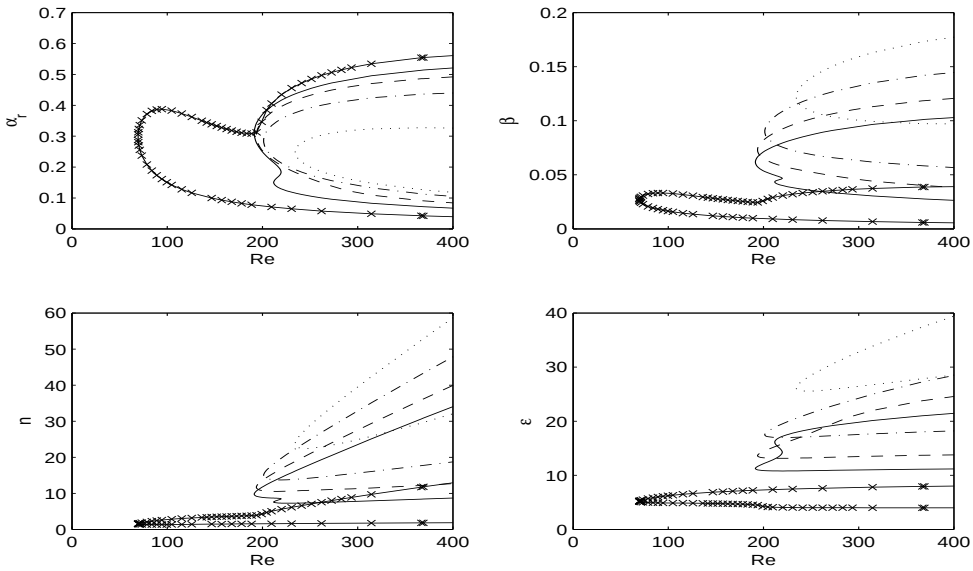

Figure 4.3: Neutral curves for traveling disturbances with c=0.7 ($\cdots$), 0.8 (-.), 0.9 ($--$), 1.0 (–), 2.0 (**-x**) at $\theta = 60^\circ$ for $e = 0.3$.

0.9 and 1.0.

Figures 4.6 & 4.7 demonstrate that the growth rates are maximized for $c = 0.76$. Although the figures demonstrate this at latitude $\theta = 10^\circ$ for two values of e, this is found for all values of e and $\theta \leq 60^\circ$. It is not shown here, but the growth rates maximized for $c \geq 0.76$ at latitudes $\theta \geq 70^\circ$ for values of $e \geq 0.1$. It is therefore most likely that $c = 0.76$ is the preferred vortex speed over rotating prolate spheroids for all eccentricities at $\theta \leq 60^\circ$ where roughness elements are not present enabling the existence of travelling modes. It is interesting to note that this is entirely consistent with the results of Garrett (2010a,b,c) where similar analyses are presented for the related geometries and travelling modes of type I with $c = 0.75$ are found to be the most amplified. However, further investigation shows that for larger values of e and $\theta \geq 70^\circ$, the preferred vortex speed increases towards $c \approx 1.0$.

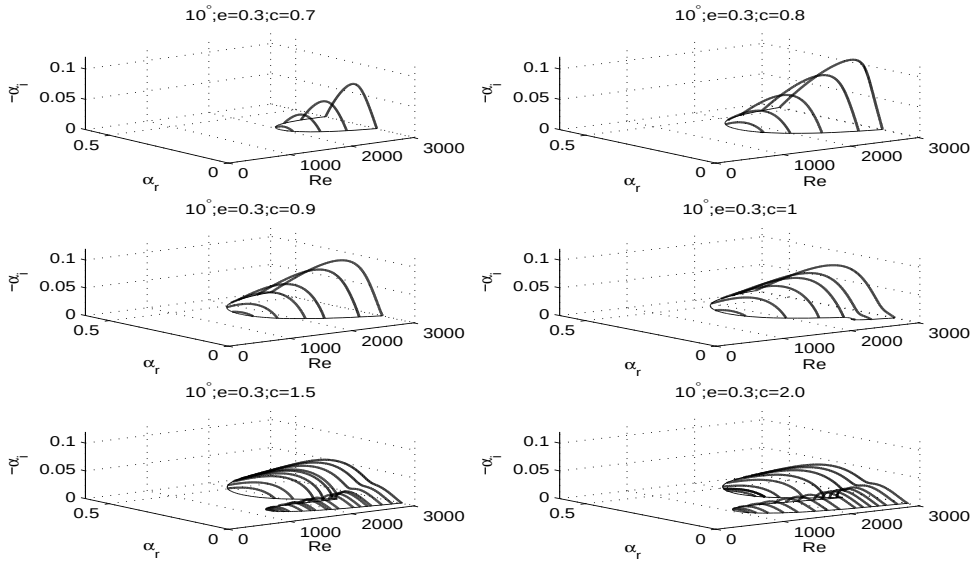

Figure 4.4: Linear convective growth rates for travelling-mode disturbances with $c = 0.7$–2 for $\theta = 10°, e = 0.3$.

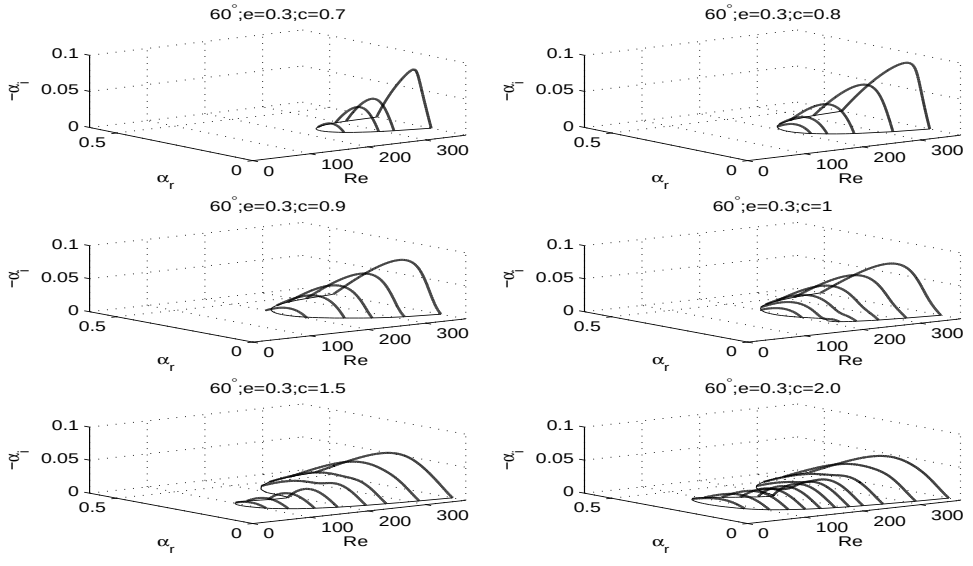

Figure 4.5: Linear convective growth rates for travelling-mode disturbances with $c = 0.7$–2 for $\theta = 60°, e = 0.3$.

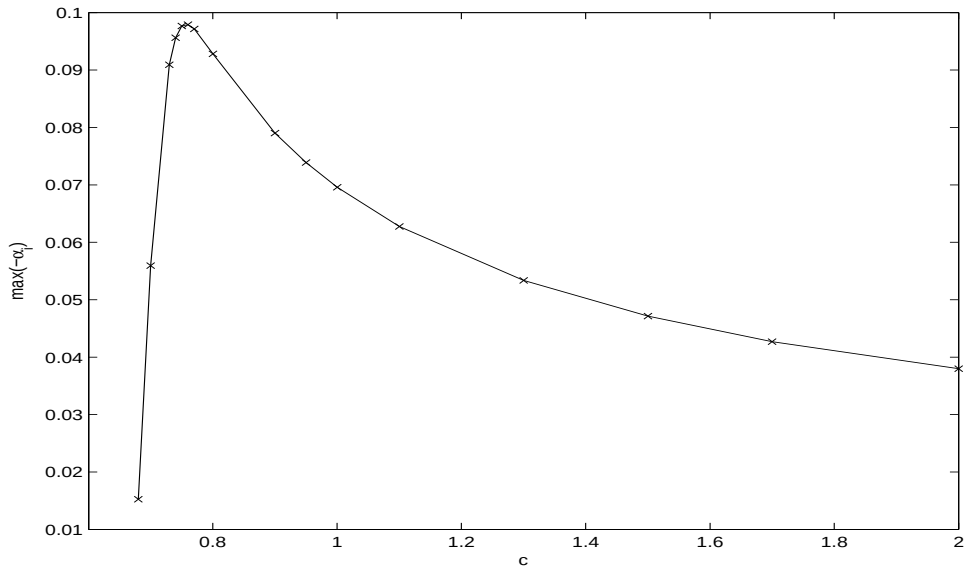

Figure 4.6: Maximum linear convective growth rates at $\theta = 10^\circ$ for $e = 0.3$ at $Re = 2880$.

4.1.2 Vortex angle and effect of eccentricity on neutral curves

In the experimental investigation on rotating sphere, Kohama & Kobayashi (1983) reported the vortex angle $\epsilon \approx 14^\circ$ at the onset of instability at each latitude. In our theoretical investigation, Figures 4.2, 4.3, C.8 & C.9 demonstrate that the vortex angle $\epsilon \approx 14^\circ$ at the onset of convective instability for $c \approx 0.9$. Further investigation shows that this is the same at all latitudes up to $\theta = 60^\circ$ for all values of e. Although, at high latitudes of $\theta \geq 70^\circ$ and for all values of e, we find that the vortex speed is slightly increased in order to have $\epsilon \approx 14^\circ$ at the onset of instability and further exaggerates towards $c \approx 1.0$ for large values of e. This shows a discrepancy with that reported for the rotating sphere by Kohama & Kobayashi, that the vortex angle is 14° at the onset of instability and the preferred vortex speed is $c = 0.76$. We return to discuss this in §4.2.

Figures 4.8 & 4.9 shows that the neutral curves of convective instabilities at

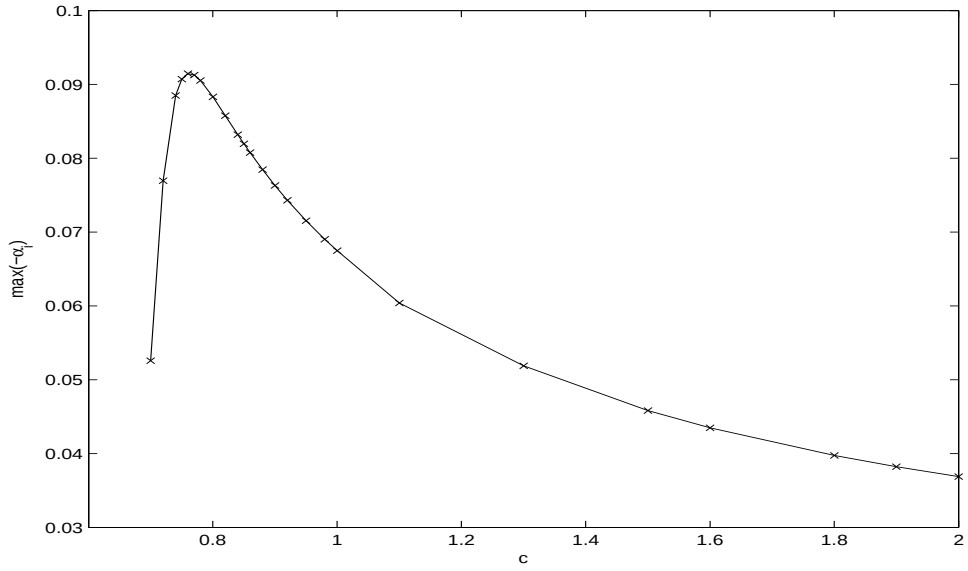

Figure 4.7: Maximum linear convective growth rates at $\theta = 10^\circ$ for $e = 0.6$ at $Re = 3350$.

each particular location for traveling disturbances are stabilizing with increasing eccentricity. Further investigation shows that for $c < 1.0$, increasing values of e has a stabilizing effect on the neutral curves of convective instabilities at all latitudes. However, for larger values of $c \geq 1.0$ and $\theta \geq 60^\circ$ the type II effects become most dangerous and at these high latitudes increasing e has a destabilizing effect on the neutral curves in terms of the decreasing critical Reynolds numbers.

4.2 Conclusion

We have shown that *slowly rotating* vortices are the most amplified and are likely to be selected in experiments where perfectly smooth prolate spheroids are used. The growth rates were maximized for vortices that rotate at around 76% of the prolate spheroid surface speed at all $\theta \leq 60^\circ$ for all values of e, and this speed increases slightly at $\theta \geq 70^\circ$ which exaggerates further at least up to 100% of the

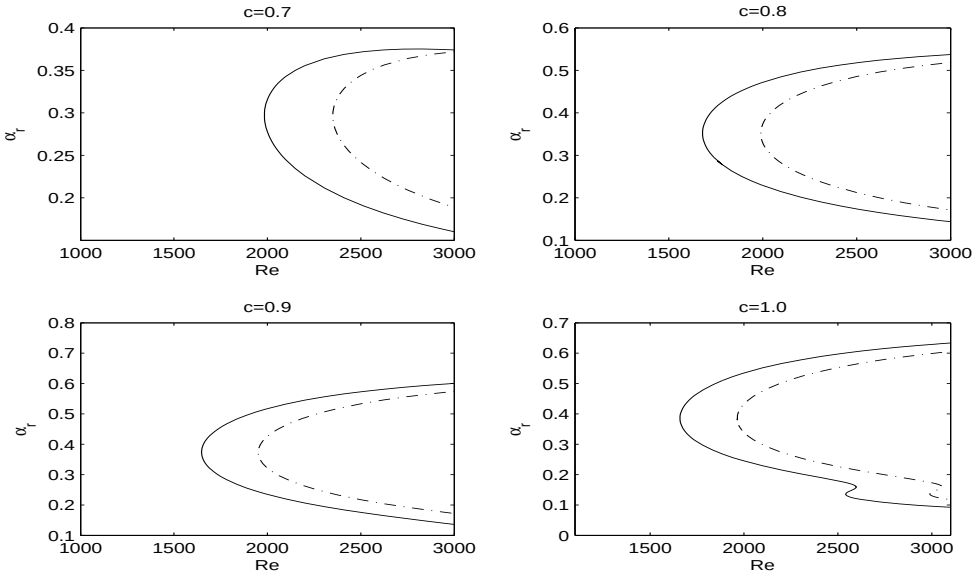

Figure 4.8: Neutral curves for traveling disturbances with $c = 0.7, 0.8, 0.9, 1.0$ at $\theta = 10^\circ$ for $e = 0.3$ (–) & $e = 0.6$ (-.-).

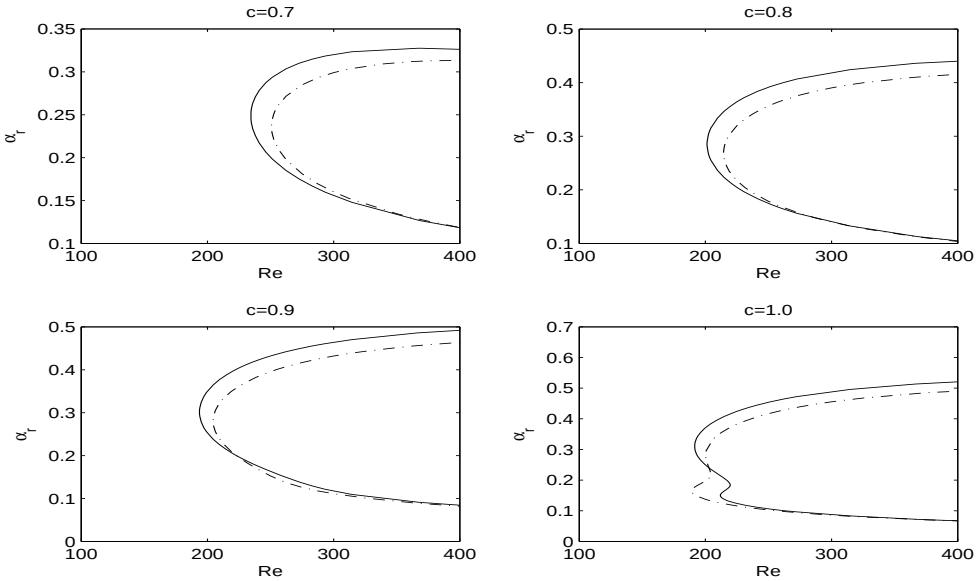

Figure 4.9: Neutral curves for traveling disturbances with $c = 0.7, 0.8, 0.9, 1.0$ at $\theta = 60^\circ$ for $e = 0.3$ (–) & $e = 0.6$ (-.-).

equatorial surface speed for large values of e. Although this is unlikely to be the case in most practical applications where surface roughness would be unavoidable and stationary vortices selected, the discovery is consistent with the unusual observation by Kobayashi & Arai (1990) of vortices traveling at 76% of the sphere surface in particular conditions. It is interesting to note that the same vortex-speed selection process has been demonstrated in the boundary-layer flow over rotating disks and cones by Garrett (2010a,b). Although experiments on smooth rotating disks have been reported by Corke and co-workers (1998) where non-stationary modes have been observed, their results cannot be interpreted in terms of a particular vortex speed. Further experiments similar to Kobayashi & Arai (1990) are therefore required for all geometries to test these theoretical predictions.

Our results show that the vortex angle of 14° at the onset of instability at each location does not necessarily coincide with the maximum growth rates for all e and θ, however the vortex angle is 14° for $c \approx 0.9$ at the onset of instability for all values of e and $\theta \leq 60°$. The vortex speed slightly increases in order to have the same vortex angle of 14° at the onset of instability at $\theta \geq 70°$ and this exaggerates further towards $c \approx 1.0$ with increasing e. This discrepancy in the case of rotating sphere where Kohama & Kobayashi reported the vortex speed at 76% of the surface speed and the vortex angle of 14° at the onset of instability at each location, is perhaps due to the use of few different spheres used in their experiments. In our opinion, they might have observed the vortex speed on one sphere with perfect smoothness and the vortex angle on another sphere with slightly less smoothness. Therefore, we suggest further experiments to investigate the accuracy of our theoretical results in these geometries.

The effect of increasing eccentricity at each location for traveling vortices is sta-

bilizing over prolate spheroids. However, for vortices rotating at high speeds, when the type II effects become most dangerous, eccentricity has a destabilizing effect at high latitudes. Therefore, we conclude that for slow rotating vortices, increasing eccentricity is delaying the convective instability at all latitudes for rotating prolate spheroids.

It is acknowledged that an approximation similar to the parallel flow approximation which was discussed in detail in §3.5, will lead to inaccuracies in the predicted results, however, this is our opinion that these will be small and will not affect the conclusions of this work. We also acknowledge that this work consists of a linear analysis and so would be inaccurate in situations where the growth rates are large and non-linear effects would occur. However, we have predicted the selection of slow vortices from the very onset of convective instability where growth rates are small; it is therefore expected that non-linearity would affect the breakdown of the slow vortices in situations where the onset of absolute instability is severely delayed, but not their initial selection.

Chapter 5

Laminar boundary-layer over families of rotating oblate spheroids

This chapter furthers the work of Chapter 2 by investigating the laminar boundary-layer flow over the outer surface of a general family of oblate spheroids rotating in otherwise still fluid, and has appeared in the literature as Samad & Garrett (2010). In §5.1 we introduce the oblate spheroidal coordinate system and the governing laminar boundary layer equations over rotating oblate spheroids are derived. An eccentricity parameter is defined to distinguish particular bodies within the family of oblate spheroids. The governing partial differential equations (PDEs) of laminar boundary-layer flow over rotating oblate spheroids for fixed values of eccentricity are solved in §5.1 using two methods: the series solution approximation of §2.2.1 and an accurate numerical method of §2.2.2. We note that setting the eccentricity to zero the governing PDEs produce those established for a rotating sphere in still fluid which is same to the prolate case discussed in §2.1. In §5.2 we present the results

obtained from the two methods and the flow profiles of rotating oblate spheroids are compared to that of rotating prolate spheroids of §2.2.2. The implication of increasing eccentricity over the laminar flow profiles of oblate spheroids and the usefulness of series-solutions are discussed in detail in §5.3.

5.1 Formulation and solution methods

We formulate the steady laminar-flow equations for the family of oblate spheroids rotating in otherwise still fluid by extending the same procedure of §2.1. Indeed, rotating an ellipse about its minor-axis produces an oblate spheroid and rotating the same ellipse about its major-axis produce a prolate spheroid. Hence, the eccentricity of the cross-sectional ellipse defined for prolate spheroid is also the same for oblate spheroid. The oblate spheroid rotates with constant angular velocity $\Omega^\star$ about the z-axis. For the oblate spheroid we introduce an oblate spheroidal coordinate system defined relative to cartesian coordinates as

$$x^\star = \eta^\star \sin\theta \cos\phi,$$

$$y^\star = \eta^\star \sin\theta \sin\phi,$$

$$z^\star = \sqrt{\eta^{\star 2} - d^{\star 2}} \cos\theta.$$

where $0 \leq \theta \leq \pi$ and $0 \leq \phi \leq 2\pi$. The quantity $\eta^\star$ is the distance from the origin of the system and normal to the body surface at a particular latitude θ and azimuth ϕ. A sketch of the oblate spheroidal coordinate system is shown in Figure 5.1 where $\eta^\star$ makes the angles θ and ϕ with the horizontal and vertical planes through the z-axis respectively. Furthermore, $d^\star$ is the distance of the focus from the center of the cross-sectional ellipse formed by the oblate spheroid. Obviously the minor axis of each cross-sectional ellipse formed from the oblate family are along

the axis of rotation of the body. We have confirmed that this 3D-system $(\theta, \phi, \eta^\star)$ is an orthogonal coordinate system and is consistent with that discussed by Morse (1953). In Appendix A.1.2 we apply transformation to equations (A.19)–(A.22) and

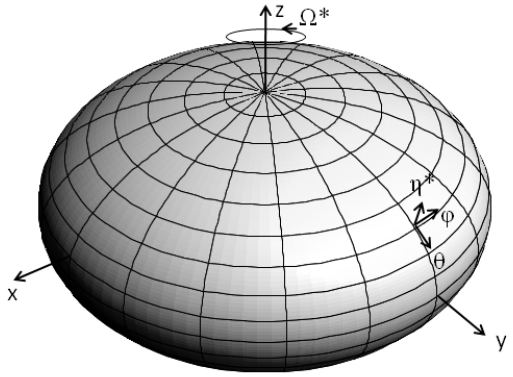

Figure 5.1: Sketch of the oblate spheroidal coordinate system. This is sketched with a free software called 3D-XplorMath-J.exe

full 3D Navier-Stokes equations and steady continuity equation in the above oblate spheroidal coordinate system are obtained (see equations (A.33)–(A.36)). Following the same procedure of transformation of Appendix A.1.2 and replacing $\eta^\star$ by $\eta_0^\star$ in equations (A.19)–(A.22), we apply the same boundary-layer assumptions of Chapter 2 to the resulting equations and obtain the dimensional boundary-layer equations that govern the laminar flow over the family of oblate spheroids rotating in otherwise still fluid. These equations are written as,

$$\frac{\sqrt{\eta_0^{\star 2}-d_0^{\star 2}}}{\sqrt{\eta_0^{\star 2}-d_0^{\star 2}\sin^2\theta}}W^\star\frac{\partial U^\star}{\partial \eta^\star}+\frac{1}{\sqrt{\eta_0^{\star 2}-d_0^{\star 2}\sin^2\theta}}\left(U^\star\frac{\partial U^\star}{\partial\theta}-V^{\star 2}\cot\theta\right)$$
$$=\nu^\star\frac{\eta_0^{\star 2}-d_0^{\star 2}}{\eta_0^{\star 2}-d_0^{\star 2}\sin^2\theta}\frac{\partial^2 U^\star}{\partial\eta^{\star 2}}, \tag{5.1}$$

$$\frac{\sqrt{\eta_0^{\star 2}-d_0^{\star 2}}}{\sqrt{\eta_0^{\star 2}-d_0^{\star 2}\sin^2\theta}}W^\star\frac{\partial V^\star}{\partial \eta^\star}+\frac{1}{\sqrt{\eta_0^{\star 2}-d_0^{\star 2}\sin^2\theta}}\left(U^\star\frac{\partial V^\star}{\partial\theta}+U^\star V^\star\cot\theta\right)$$
$$=\nu^\star\frac{\eta_0^{\star 2}-d_0^{\star 2}}{\eta_0^{\star 2}-d_0^{\star 2}\sin^2\theta}\frac{\partial^2 V^\star}{\partial\eta^{\star 2}}, \tag{5.2}$$

$$\frac{\sqrt{\eta_0^{\star 2}-d_0^{\star 2}}}{\sqrt{\eta_0^{\star 2}-d_0^{\star 2}\sin^2\theta}}\frac{\partial W^\star}{\partial \eta^\star}+\frac{1}{\sqrt{\eta_0^{\star 2}-d_0^{\star 2}\sin^2\theta}}\frac{\partial U^\star}{\partial\theta}$$
$$+\left(\frac{-d_0^{\star 2}\cos\theta\sin\theta}{(\eta_0^{\star 2}-d_0^{\star 2}\sin^2\theta)^{3/2}}+\frac{\cot\theta}{\sqrt{\eta_0^{\star 2}-d_0^{\star 2}\sin^2\theta}}\right)U^\star=0, \tag{5.3}$$

In a fixed frame of reference equations (5.1)–(5.3) are subject to the same boundary conditions as in equation (2.4). The quantity $a_0^\star$ in the equations of boundary conditions represent the length of the semi-major axis of the cross-sectional ellipse of a particular oblate spheroid and is defined as $a_0^\star=\eta_0^\star$ which is defined differently for prolate spheroid. Indeed $a_0^\star$ is the equatorial radius for both types of spheroid: prolate and oblate. For consistency with the analysis on prolate spheroids and those on spheres by Garrett (2002); Banks (1965), we scale the velocity components in equations (5.1)–(5.3) on the equatorial surface speed as shown in equation (2.5) of §2.1. For the oblate family of spheroids, the resulting non-dimensional laminar-flow equations are,

$$W\frac{\partial U}{\partial\eta}+\frac{1}{\sqrt{1-e^2}}\left(U\frac{\partial U}{\partial\theta}-V^2\cot\theta\right)=\sqrt{\frac{1-e^2}{1-e^2\sin^2\theta}}\frac{\partial^2 U}{\partial\eta^2}, \tag{5.4}$$

$$W\frac{\partial V}{\partial\eta}+\frac{1}{\sqrt{1-e^2}}\left(U\frac{\partial V}{\partial\theta}+UV\cot\theta\right)=\sqrt{\frac{1-e^2}{1-e^2\sin^2\theta}}\frac{\partial^2 V}{\partial\eta^2}, \tag{5.5}$$

$$\sqrt{1-e^2}\frac{\partial W}{\partial\eta}+\frac{\partial U}{\partial\theta}+\left(\cot\theta-\frac{e^2\cos\theta\sin\theta}{1-e^2\sin^2\theta}\right)U=0. \tag{5.6}$$

We note that when setting $e=0$, the laminar flow equations for both oblate and prolate reduces to those for the already established equations of rotating sphere. This is

because the cross-sectional ellipse becomes a circle for $e = 0$ in both types of spheroid (oblate and prolate). The boundary conditions in (2.4) are non-dimensionalized in the same way and are written here for completeness as,

$$U = W = V - \sin\theta = 0 \text{ on } \eta = 0, \tag{5.7}$$

$$U = V = 0 \text{ as } \eta \to \infty, \tag{5.8}$$

In order to solve equations (5.4)–(5.6) subject to conditions (5.7)–(5.8) we again use the two solution methods: series solution approximation of §2.2.1 and an accurate numerical method of §2.2.2. From the series solution method we obtain a set of non-linear ODEs for oblate spheroid containing general e, involving terms up to and including n=7. These are stated in Appendix D.1 as equations (D.1)–(D.12). Excluding the equatorial region (close to $\theta = 90°$), we find that the series solutions are everywhere convergent for all values of $e \leq 0.8$ for a domain of integration between $\eta = 0$ and 20. The values obtained for the quantities $F_n'(0)$, $G_n'(0)$, $H_n(\infty)$ at $e = 0 - 0.8$ (in increments of 0.1) are given in Appendix D.2 and again we obtain very similar values of these quantities when $e = 0$ as calculated by Garrett (2002); Banks (1965). We note that the leading-order boundary values (for $n = 1$) are not identical at all values of e, unlike the prolate case, and this is because powers of $(1 - e^2)$ are appearing in the leading-order equations (D.1), (D.5) and (D.9).

5.2 Results

As the boundary-layer flow is assumed to erupt near equator we do not consider theoretical profiles arising for latitudes above 80°. The development of flow over oblate spheroids for fixed e is found to be generally similar to that over prolate spheroids and the equivalent plot to Figure 2.3 is not shown here. The latitudinal

velocity is again inflectional at all latitudes and eccentricities. We also note that fluid is entrained into the boundary layer at all latitudes through a negative W-component and has a region of reverse flow close to the surface for sufficiently high latitudes between $\theta = 60°$–$64°$ depending on the value of e. Figures 5.2 & 5.3 demonstrate laminar-flow profiles obtained from the numerical solution at four different locations.

At all latitudes, when increasing e from 0 (the sphere) we find that there is almost

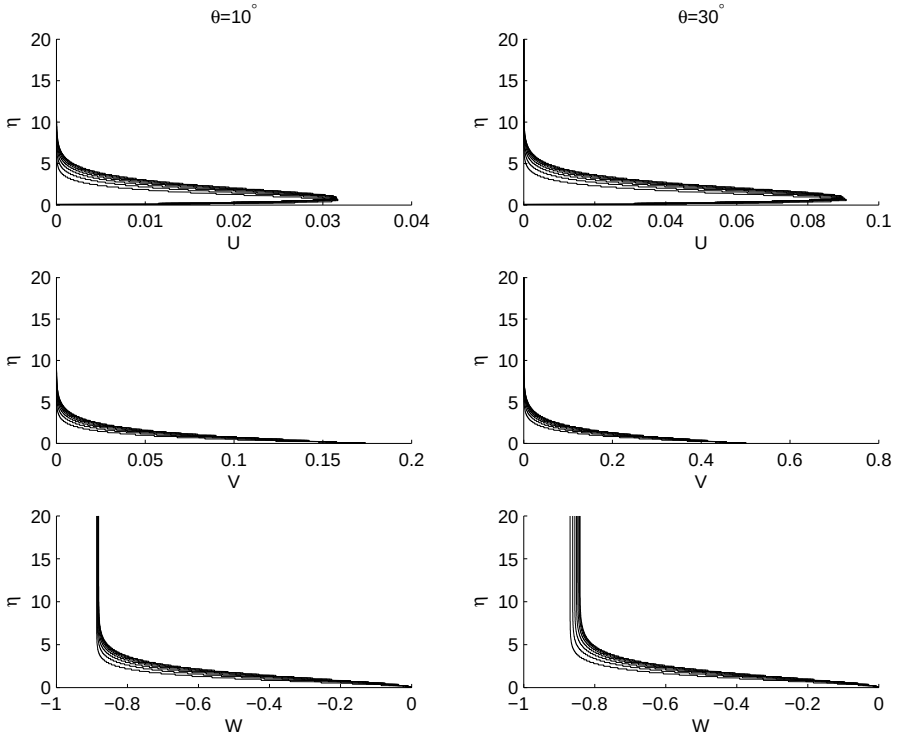

Figure 5.2: Oblate spheroid velocity profiles at latitudes $\theta = 10°$ and $30°$ with increasing $e = 0.1$–0.8 in increments of 0.1 (right to left in each frame).

the same variation in the latitudinal and azimuthal velocity components. However, over the body (at $\theta = 70°$, for example) the variation in normal velocity component is slightly more pronounced. Further, the effect of increasing the eccentricity at any particular location is seen to have the opposite effect on the normal velocity by

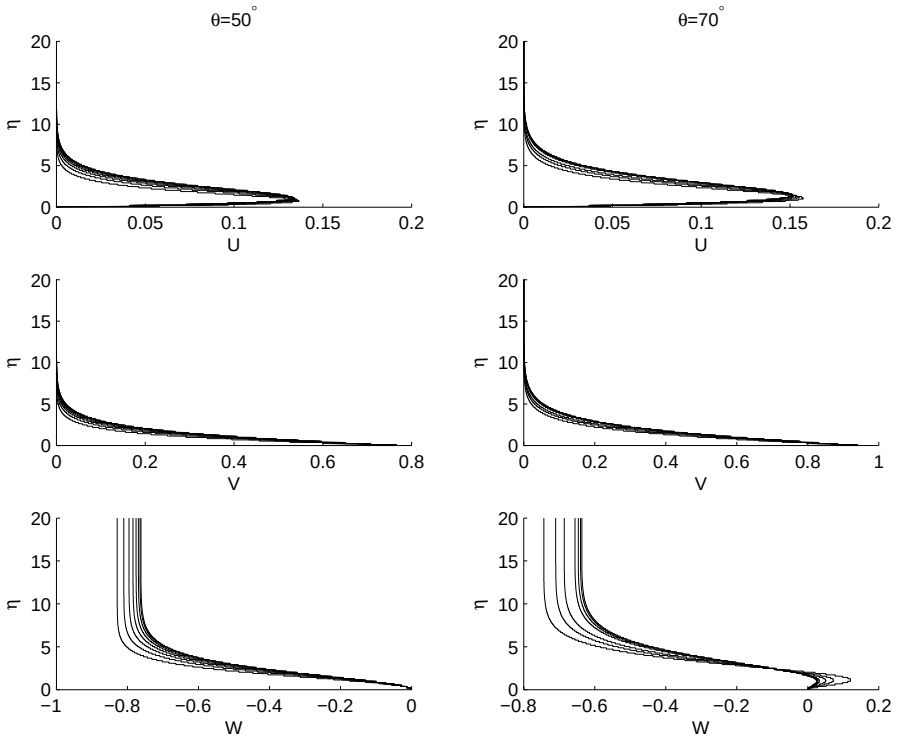

Figure 5.3: Oblate spheroid velocity profiles at latitudes $\theta = 50°$ and $70°$ with increasing $e = 0.1$–0.8 in increments of 0.1 (right to left in each frame).

moving the profiles in the opposite direction, entraining more fluid into the boundary layer. It is also seen to increase the magnitude of the reverse flow that appears close to the surface at sufficiently high latitudes. This is more clearly seen in Figure 5.4 where the flow profiles for both cases of spheroids: prolate and oblate, at $e = 0.7$ are compared against those for the rotating sphere ($e = 0$) at low and high latitudes. At each latitude we see that the W-profile limits to an equal distance either side of the sphere limit. The small region of reverse flow in the normal direction is seen to be greater for the oblate case. We also note that the latitudinal and azimuthal flows in the oblate case are more sensitive to eccentricity at low latitudes, this is reflected from e appearing in the leading order equations of the series solution ODEs (D.1)–

(D.12). However, as the latitude increases, the U- and V-components for prolate and oblate spheroids become indistinguishable at any particular e.

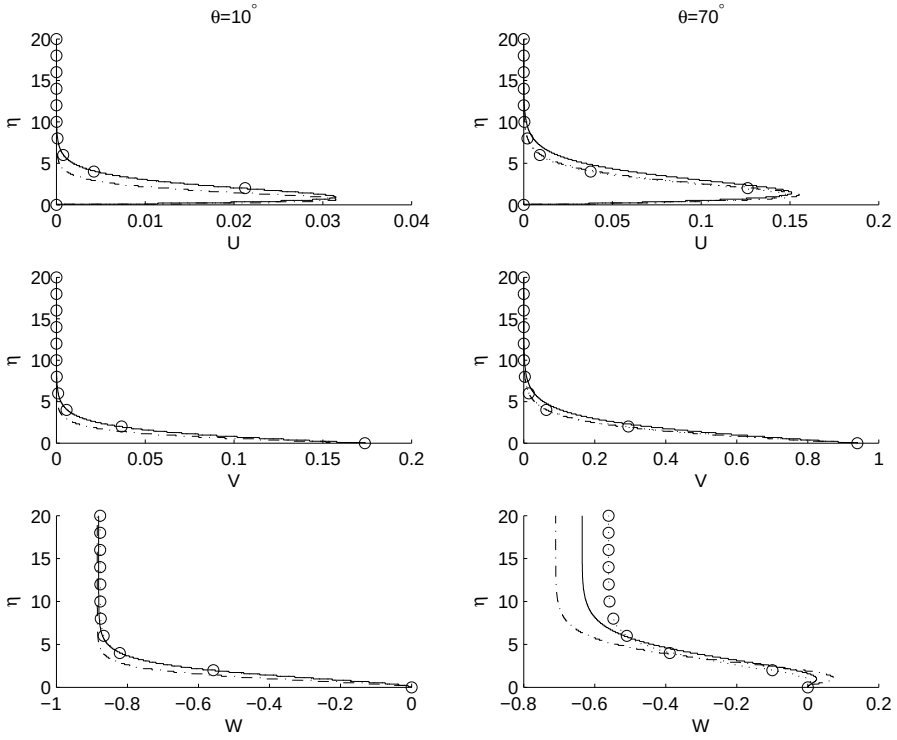

Figure 5.4: A comparison of flow profiles at $\theta = 10°$ and $70°$ for the rotating sphere (–), prolate spheroid with $e = 0.7$ (-o-) and oblate spheroid with $e = 0.7$ (-.).

Figures 5.5–5.8 show a visual comparison between flow profiles arising from the series-solution approximation and numerical solutions at various latitudes and eccentricities. Similar visual comparisons at various other latitudes and eccentricities are shown in Appendix D.3 as Figures D.1–D.6. The measure of the accuracy of the series solution with respect to the numerical solution is obtained from the root mean square error $E_{X,e}$ which is defined in §2.3. Tables 5.1–5.5 give the values of $E_{X,e}$ computed at $\theta = 10°$, $30°$, $50°$, $60°$ and $70°$ for a range of eccentricities. From these we note that the accuracy of the series solution reduces with increased latitude

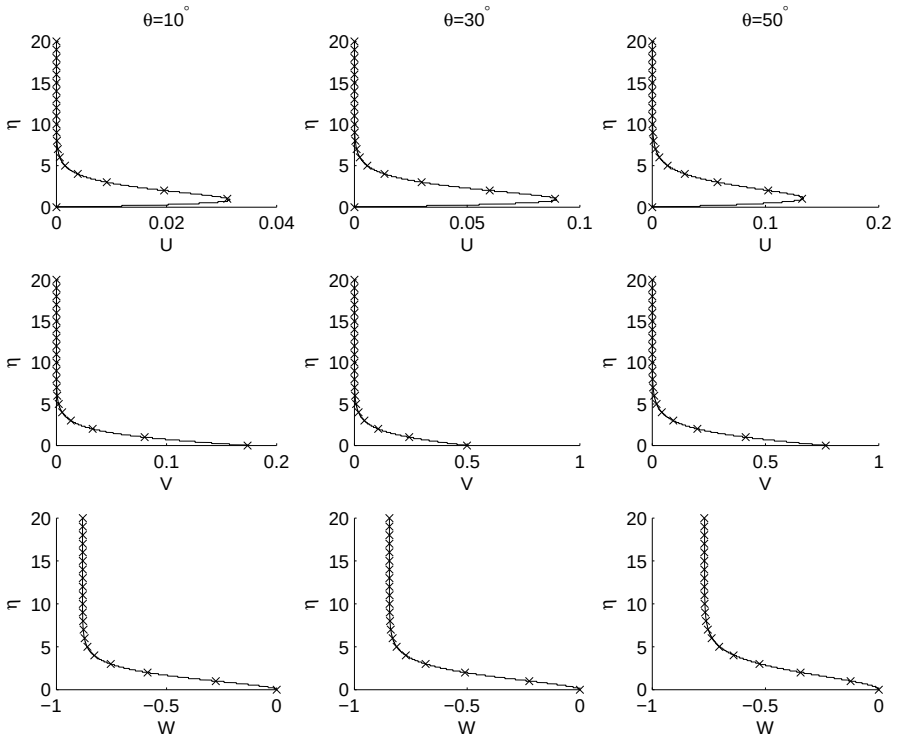

Figure 5.5: Comparison of the numerical (solid line) and series solutions (cross points) at $\theta = 10°$, $30°$ $50°$ for $e = 0.3$.

and eccentricity, as expected from the visual inspections. We will discuss this and its implications for the convective instability analysis in §6.3.

5.3 Conclusion

In this chapter we derived the governing PDEs for the laminar flow within the boundary-layer over rotating oblate spheroids in otherwise still fluid. Similarly to the prolate case, the system of PDEs for oblate spheroid also reduces to the known equations for the rotating sphere as $e \to 0$. Two methods of solution are used to solve the governing equations for general e. We note that modified versions of von Kaḿań equations also appear at leading order in the series solution ODEs,

e	$E_{U,e}$	$E_{V,e}$	$E_{W,e}$
0.1	4.28951895e-004	1.02863645e-003	4.68266896e-003
0.3	4.37325695e-004	1.05015059e-003	4.77669201e-003
0.5	4.58443020e-004	1.10010825e-003	5.02727164e-003
0.6	4.78885173e-004	1.14513675e-003	5.24108957e-003
0.7	5.08797092e-004	1.21168921e-003	5.58064799e-003
0.8	5.58589632e-004	1.32029533e-003	6.26230416e-003

Table 5.1: RMS error of the series-solution approximation at $\theta = 10^\circ$ on the prolate spheroid.

e	$E_{U,e}$	$E_{V,e}$	$E_{W,e}$
0.1	1.16925494e-004	6.75722482e-005	7.07251784e-004
0.3	1.36264716e-004	7.58854146e-005	3.95294496e-004
0.5	1.99320339e-004	1.12700616e-004	1.78993094e-003
0.6	2.67542404e-004	1.59007669e-004	3.59885263e-003
0.7	3.66839606e-004	2.54556190e-004	6.48213098e-003
0.8	5.23661964e-004	3.75836568e-004	9.91872357e-003

Table 5.2: RMS error of the series-solution approximation at $\theta = 30^\circ$ on the prolate spheroid.

e	$E_{U,e}$	$E_{V,e}$	$E_{W,e}$
0.1	1.34316665e-004	8.75939095e-005	7.39709767e-004
0.3	2.20519410e-004	1.87083080e-004	2.23667052e-003
0.5	5.31269082e-004	5.35959892e-004	7.12184623e-003
0.6	8.31484486e-004	8.47762112e-004	1.19901252e-002
0.7	1.25126879e-003	1.30929833e-003	1.96843202e-002
0.8	1.83687989e-003	1.93786194e-003	3.21181121e-002

Table 5.3: RMS error of the series-solution approximation at $\theta = 50^\circ$ on the prolate spheroid.

e	$E_{U,e}$	$E_{V,e}$	$E_{W,e}$
0.1	1.30660119e-004	4.00731564e-004	4.34827643e-003
0.3	2.57368684e-004	6.11464028e-004	6.51873510e-003
0.5	8.41537847e-004	1.30007085e-003	1.31344462e-002
0.6	1.36892748e-003	1.86564394e-003	1.93137272e-002
0.7	2.05032719e-003	2.58362794e-003	2.90435431e-002
0.8	2.92193292e-003	3.51407359e-003	4.61615396e-002

Table 5.4: RMS error of the series-solution approximation at $\theta = 60^\circ$ on the prolate spheroid.

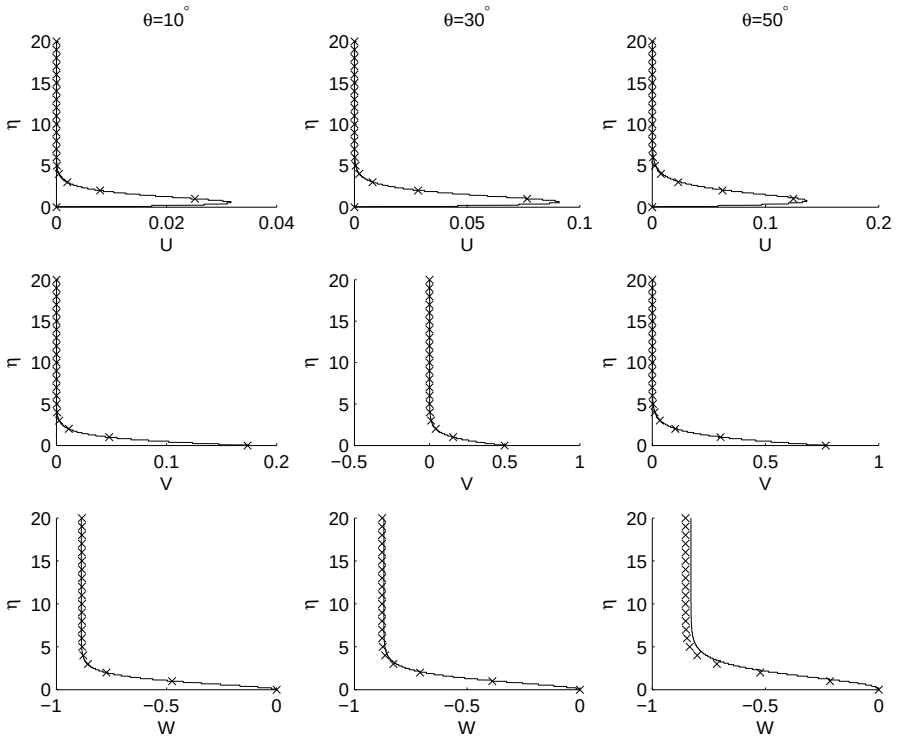

Figure 5.6: Comparison of the numerical (solid line) and series solutions (cross points) at $\theta = 10°$, $30°$, $50°$ for $e = 0.8$.

however factors of $(1 - e^2)$ appear in these leading-order equations and this is not seen in the prolate case. The formulation used here has led to flow profiles in the latitudinal and azimuthal directions that behave in the same way in both the prolate and oblate cases at fixed value of eccentricity. However, at lower latitudes in the oblate case, the latitudinal and azimuthal profiles are more sensitive to variation in e but at higher latitudes almost coincide with those of the prolate case for a fixed e. Further, a significant difference in the normal component is found in that the profiles asymptote to equal distances either side of the rotating-sphere profiles.

From visual inspections and calculations of RMS errors, we see that the discrepancies resulting from the series solution profiles with respect to numerical solutions

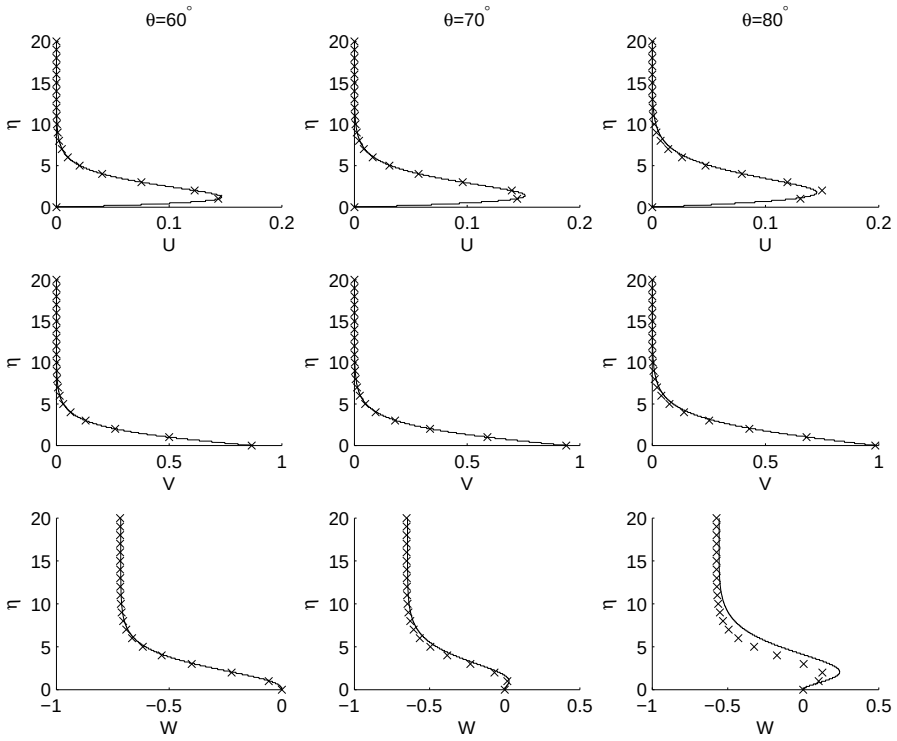

Figure 5.7: Comparison of the numerical (solid line) and series solutions (cross points) at $\theta = 60°$, $70°$ $80°$ for $e = 0.3$.

are very similar to those calculated for the prolate case. We note that the series solution is very accurate at low latitudes for all $e \leq 0.8$. However, as the latitude is increased the discrepancy between the two solutions increases and this is exaggerated with increasing eccentricity. At $\theta = 80°$ we find a significantly different qualitative behaviour for the flow with large eccentricity. Keeping in mind the RMS errors of the series solution profiles with respect to the numerical solutions, the governing ODEs for the series solution of the general oblate spheroid available in Appendix D.1 are more easy to use in engineering applications than the numerical method on ground of cost and required expertise.

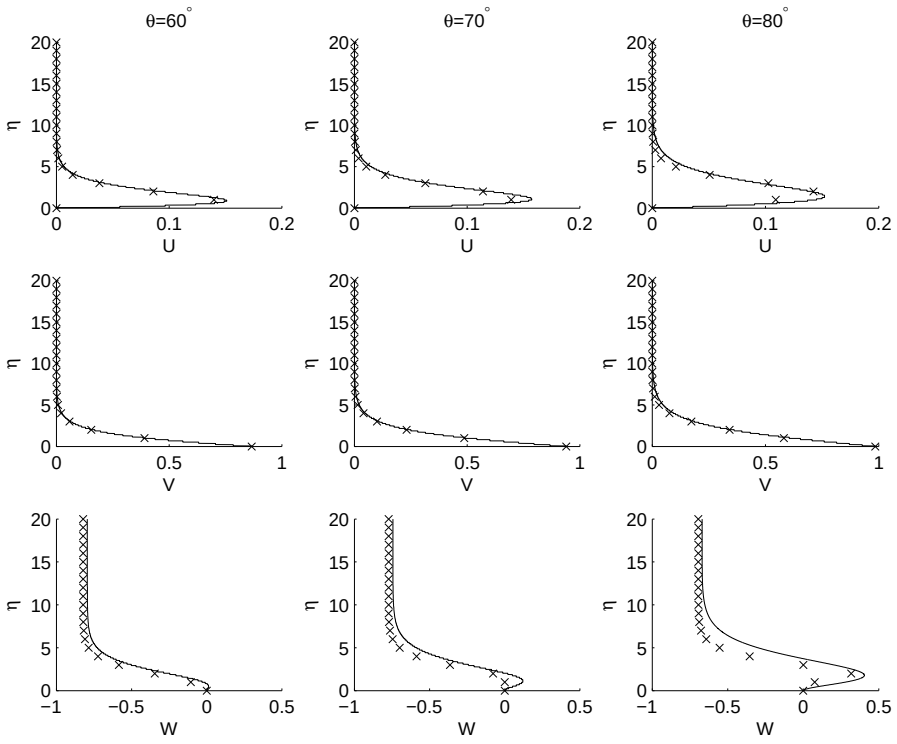

Figure 5.8: Comparison of the numerical (solid line) and series solutions (cross points) at $\theta = 60°$, $70°$ $80°$ for $e = 0.8$.

e	$E_{U,e}$	$E_{V,e}$	$E_{W,e}$
0.1	6.65103503e-004	1.99939545e-003	1.89122611e-002
0.3	6.02835535e-004	2.36906675e-003	2.20993173e-002
0.6	2.18099333e-003	4.48352864e-003	3.67230584e-002
0.7	3.19035224e-003	5.29314061e-003	4.59978351e-002
0.8	4.24762359e-003	6.03269672e-003	6.61689359e-002

Table 5.5: RMS error of the series-solution approximation at $\theta = 70°$ on the prolate spheroid.

Chapter 6

The convective instability of the boundary-layer flow over rotating oblate spheroids

This chapter is concerned with the convective instability mechanisms within the boundary-layer flow over the outer surface of a general family of oblate spheroids rotating in otherwise still fluid. This is an extension of Chapter 3 where we carried out' convective instability analyses of the boundary-layer flow over rotating prolate spheroids. Again, viscous and streamline-curvature effects are included and local convective instability analysis are conducted at latitudes 10°–80° from the axis of rotation in 10° increments for a range of particular oblate spheroids.

We use the oblate spheroidal coordinate system discussed in Chapter 5. In §6.1 we derive the unsteady perturbation equations that govern the stability problem of the general family of rotating oblate spheroids. An eccentricity parameter e is introduced to identify each particular oblate spheroid within its family. Similar to the prolate case of §3.4 in the limit of zero eccentricity, the perturbation equations for

oblate spheroids also produce those already established in the literature for rotating-sphere boundary layer.

We solve these perturbation equations for oblate spheroids in §6.2 by extending the techniques presented in §§3.2 & 3.3. Stationary convective modes are considered in §6.3. The effect of eccentricity at each latitude on the neutral curves is discussed and the results are compared to other related geometries. In §6.4 we consider traveling modes in particular, and the linear convective growth rates of disturbances traveling at different azimuthal phase speeds. In §6.5 we compare the results of the two different types of spheroids i.e. the oblate spheroids and the prolate spheroids with appropriate parameters. Conclusions are drawn in §6.6.

6.1 Derivation of the perturbation equations

In this section we use the oblate spheroidal coordinate system $(\theta, \phi, \eta^\star)$ defined in §5.1 to derive the set of perturbation equations that govern the stability of the boundary-layer flow over the surface of rotating oblate spheroids.

In Appendix A.1.2 we have derived the continuity equation and the full 3D unsteady Navier-Stokes equations in oblate spheroidal coordinate system as equations (A.33)–(A.36). We use these equations to derive the perturbation equations by assuming that $U^\star$, $V^\star$, $W^\star$ are the steady basic flow velocity components in the θ-, ϕ- and $\eta^\star$- directions respectively and $P^\star$ is the constant pressure. We impose infinitesimally small perturbations on the steady basic flow at a particular latitude on the rotating prolate spheroid boundary layer. The perturbation variables (denoted by lower case hatted quantities) are assumed to have the normal-mode form

$$\left(\hat{u}^\star, \hat{v}^\star, \hat{w}^\star, \hat{p}^\star\right) = \Big(u^\star(\eta), v^\star(\eta), w^\star(\eta), p^\star(\eta)\Big) e^{\mathrm{i}\left(\alpha^\star \int_0^\theta ds + \beta^\star r_0^\star \phi - \gamma^\star t^\star\right)}. \tag{6.1}$$

Here $ds = \sqrt{\eta_0^{\star 2} - d_0^{\star 2}\sin^2\theta}\,d\theta$ is an element of arc length in the latitudinal direction, such that $\int_0^\theta ds$ is the arc length from the pole to the particular latitude under consideration; $d_0^\star$ is the constant distance of the focus from the centre of the prolate spheroid; and $r_0^\star = \eta_0^\star \sin\theta$ is the local surface radius of the body. Note that $\eta_0^\star$ is equal in length to the equatorial radius of a particular oblate spheroid. We follow §3.1 and the dimensional velocity components and pressure of the perturbed flow are formed in the same way as in (3.2). We substitute these dimensional variables of the perturbed flow into the steady continuity and unsteady Navier-Stokes equations (A.33)–(A.36). We assume that perturbating quantities are small enough so that products can be ignored and a linear analysis conducted. For details of derivation of perturbation equations, the interested reader is referred to §3.1. Using the perturbation variables (6.1) and after linearization we obtained the dimensional perturbation equations that govern the stability of the general family of rotating oblate spheroids. These equations are shown in Appendix E as equations (E.1)–(E.4). These equations are non-dimensionalized on the typical length, velocity, time and pressure scales: $\delta^\star$, $\eta_\circ^\star\Omega^\star$, $\delta^\star/\eta_\circ^\star\Omega^\star$ and $\rho^\star(\eta_\circ^\star\Omega^\star)^2$ respectively, where $\rho^\star$ is the fluid density. The resulting non-dimensional equations are linearized by neglecting $O(R^{-2})$ terms, where

$$Re = \frac{\delta^\star a^\star \Omega^\star}{\nu^\star} = \frac{\delta^\star \eta_0^\star \Omega^\star}{\nu^\star}, \tag{6.2}$$

is the Reynolds number. Note that the Reynolds number is interpreted as a measure of the equatorial rotation speed of the spheroid, with the location of the analysis given by the particular θ under consideration. This is in contrast to previous studies of rotating disks and cones where the Reynolds number is interpreted as a measure of the radial location of the analysis for a particular rotation rate. Moreover, unlike to the prolate case in §3.1, here the Reynolds number Re does not depend on

eccentricity parameter e. We recall that this Reynolds number in §3.4.2 was called the spherical Reynolds number, and was used by Garrett & Peake (2002) in the stability analysis over rotating-sphere boundary-layer. The basic flow velocities are non-dimensionlized in a similar way as in §5.1. The quantities $\alpha^\star$, $\beta^\star$ and $\gamma^\star$ are explained in detail in §3.1. The non-dimensionalized perturbation equations for general family of oblate spheroids are written as,

$$N\frac{dw}{d\eta} + N\delta_1 l\frac{(2-e^2(1+\sin^2\theta))}{(1-e^2\sin^2\theta)}w = - l\left[\left(\delta_1\left(\frac{-e^2\sin\theta\cos\theta}{(1-e^2\sin^2\theta)^{3/2}} + \frac{\cot\theta}{\sqrt{1-e^2\sin^2\theta}}\right) + \mathrm{i}\alpha\right)u + \mathrm{i}\beta v\right] \tag{6.3}$$

$$N\delta_1 W\frac{du}{d\eta} + \left[\mathrm{i}\left(l(\alpha U+\beta V)-\gamma\right) + \frac{\delta_1 l}{\sqrt{1-e^2\sin^2\theta}}\frac{\partial U}{\partial\theta}\right]u - \frac{2\delta_1 l\cot\theta}{\sqrt{1-e^2\sin^2\theta}}V\,v + \left(N\frac{\partial U}{\partial\eta} + \frac{N\delta_1 l}{(1-e^2\sin^2\theta)}U\right)w = - \mathrm{i}l\alpha p + \frac{1}{Re}\left[N^2\frac{d^2u}{d\eta^2} - l^2(\alpha^2+\beta^2)\,u\right] \tag{6.4}$$

$$N\delta_1 W\frac{dv}{d\eta} + \left[\mathrm{i}\left(l(\alpha U+\beta V)-\gamma\right) + \frac{\delta_1 l\cot\theta}{\sqrt{1-e^2\sin^2\theta}}U\right]v + \delta_1 l\left(\frac{cot\theta V}{\sqrt{1-e^2\sin^2\theta}} + \frac{1}{\sqrt{1-e^2\sin^2\theta}}\frac{\partial V}{\partial\theta}\right)u + \left(N\frac{\partial V}{\partial\eta} + \frac{\delta_1 l\,V}{\sqrt{1-e^2\sin^2\theta}}\right)w = -\mathrm{i}l\,\beta p + \frac{1}{Re}\left[N^2\frac{d^2v}{d\eta^2} - l^2(\alpha^2+\beta^2)\,v\right] \tag{6.5}$$

$$N\delta_1 W\frac{dw}{d\eta} + \left[\mathrm{i}\left(l(\alpha U+\beta V)-\gamma\right) + \delta_1\left(N\frac{\partial W}{\partial\eta} - l\frac{e^2\sin\theta\cos\theta}{(1-e^2\sin^2\theta)^{3/2}}U\right)\right]w - 2\delta_1 l\frac{N\,U}{(1-e^2\sin^2\theta)}u - 2\delta_1 N l\,V\,v = - N\frac{dp}{d\eta} + \frac{1}{Re}\left[N^2\frac{d^2w}{d\eta^2} - l^2(\alpha^2+\beta^2)w\right] \tag{6.6}$$

where

$$N = \sqrt{\frac{1-e^2}{1-e^2\sin^2\theta}} \tag{6.7}$$

Factors $l = 1/(1+\eta/Re)$ appear multiplying terms in these perturbation equa-

tions which are set to unity in an approximation similar to the parallel flow approximation. Its validity at low and high latitudes will be discussed in §6.6. The equations have terms multiplied by Re and δ_1, these factors indicate terms due to viscous and streamline curvature effects.

Using the transformed variables of §3.1, these perturbation equations (6.3)–(6.6) for oblate spheroids, can be written as a set of six first order ordinary differential equations and are given as,

$$\phi_1' = \phi_2 \tag{6.8}$$

$$\begin{aligned}\left[\frac{N^2\phi_2'}{Re}\right]_v =& \frac{1}{Re}\Big(\left[\alpha^2+\beta^2\right]_v + \mathrm{i}Re\left(\alpha U+\beta V-\gamma\right)\Big)\phi_1 + \left[\frac{NW\phi_2}{Re}\right]_s \\ &+\Bigg(N\left(\alpha_1 U'+\beta_1 V'\right)+\left[\frac{1}{Re}\left(N\alpha_1 U+\frac{\beta V}{\sqrt{1-e^2\sin^2\theta}}\right)\right]_s\Bigg)\phi_3 \\ &+\mathrm{i}\Bigg(\alpha^2+\beta^2-\left[\frac{\mathrm{i}\alpha}{Re}\left(\frac{-e^2\sin\theta\cos\theta}{(1-e^2\sin^2\theta)^{3/2}}+\frac{\cot\theta}{\sqrt{1-e^2\sin^2\theta}}\right)\right]_s\Bigg)\phi_4 \\ &-\left[\frac{\cot\theta V\phi_5}{Re\sqrt{1-e^2\sin^2\theta}}\right]_s+\frac{1}{Re\sqrt{1-e^2\sin^2\theta}}\Bigg[\left(\alpha_1\frac{\partial U}{\partial\theta}+\beta\frac{\partial V}{\partial\theta}\right)u \\ &-\big(\alpha_1 V-\beta U\big)\cot\theta\, v\Bigg]_s\end{aligned} \tag{6.9}$$

$$N\phi_3' = -\mathrm{i}\phi_1-\left[\frac{N(2-e^2\sin^2\theta)}{Re(1-e^2\sin^2\theta)}\phi_3\right]_s \tag{6.10}$$

$$\begin{aligned}N\phi_4' =& \left[\frac{\mathrm{i}W\phi_1}{Re}\right]_s-\left[\frac{\mathrm{i}N\phi_2}{Re}\right]_v+\left[\frac{2N}{Re}\left(\frac{U\,u}{(1-e^2\sin^2\theta)}+V\,v\right)\right]_s \\ &-\frac{1}{Re}\Bigg(\left[\alpha^2+\beta^2\right]_v+\mathrm{i}Re\Big(\alpha U+\beta V-\gamma\Big) \\ &+\left[NW'-\frac{e^2\sin\theta\cos\theta}{(1-e^2\sin^2\theta)^{3/2}}U\right]_s\Bigg)\phi_3\end{aligned} \tag{6.11}$$

$$\phi_5' = \phi_6 \tag{6.12}$$

$$\left[\frac{N^2\phi_6'}{Re}\right]_v = \left[\frac{V\cot\theta\phi_1}{Re\sqrt{1-e^2\sin^2\theta}}\right]_s+\Big(N\left(\alpha_1 V'-\beta U'\right)$$

$$+\left[\frac{1}{Re}\left(\frac{\alpha_1 V}{\sqrt{1-e^2\sin^2\theta}}-\frac{N\,\beta U}{(1-e^2\sin^2\theta)}\right)\right]_s\Bigg)\phi_3$$
$$+\left[\frac{\beta}{Re}\left(\frac{-e^2\cos\theta\sin\theta}{(1-e^2\sin^2\theta)^{3/2}}+\frac{\cot\theta}{\sqrt{1-e^2\sin^2\theta}}\right)\phi_4\right]_s+\frac{1}{Re}\Bigg(\left[\alpha^2+\beta^2\right]_v$$
$$+\mathrm{i}Re\left(\alpha U+\beta V-\gamma\right)\Bigg)\phi_5+\left[\frac{N\,W\phi_6}{Re}\right]_s$$
$$+\left[\frac{1}{Re\sqrt{1-e^2\sin^2\theta}}\left(\left(\alpha_1\frac{\partial V}{\partial\theta}-\beta\frac{\partial U}{\partial\theta}\right)u+\cot\theta\left(\alpha_1 U+\beta V\right)v\right)\right]_s \tag{6.13}$$

Where a prime denotes differentiation with respect to the normal η (spatial variable), and $\alpha_1=\alpha-\left[\frac{\mathrm{i}\,N}{Re}\right]_s\left(\frac{-e^2\sin\theta\cos\theta}{(1-e^2\sin^2\theta)^{3/2}}+\frac{\cot\theta}{\sqrt{1-e^2\sin^2\theta}}\right)$, where N is defined in equation (6.7).

Equations (6.8)–(6.13) are the perturbation equations for oblate spheroids upon which the convective and absolute instability analyses can be performed. However, we only perform convective instability analyses over oblate spheroids for various values of eccentricity parameter e. The subscripts v and s in the perturbation equations indicate terms arising from viscous and streamline curvature effects respectively. Coriolis terms do not appear since a fixed frame of reference was used. The perturbation velocities u and v in the perturbation equations can be written explicitly in terms of ϕ_1 and ϕ_2 and are similar to those defined in the prolate spheroid case. The Orr-Sommerfeld and Rayleigh's equation for oblate spheroids are similar to that for prolate spheroids presented in equations (3.18) & (3.19) respectively, except the constant M is replaced by N, where N is defined in (6.7). Note that the perturbation equations (6.8)–(6.13) for the oblate spheroids reduce to those of the rotating sphere boundary-layer established in the literature Garrett & Peake (2002, 2004) for $e=0$.

6.2 Solution of the perturbation equations

The solution methods for solving the perturbation equations for oblate spheroids are the same as described in §3.2. However, we discuss the small amendments to solve the eigenvalue problem defined by equations (6.8)–(6.13) subject to the boundary conditions (3.20). For a particular oblate spheroid defined by a value of $e \in [0, 1]$, the eigenvalue problem will be solved for a certain combinations of values of α, β and γ at each Reynolds number and each particular value of θ. We form a dispersion relation $D(\alpha, \beta, \gamma; Re, \theta, e) = 0$, for rotating oblate spheroids, with the aim of calculating the convective instability branches.

As explained in §3.2, we assume that at the outer edge of the boundary-layer $U \to 0$, $V \to 0$ and $W \to W_\infty$ as $\eta \to \infty$. An approximate solution at the outer edge of the boundary-layer can be found by solving the perturbation equations (6.8)–(6.13) at the outer edge of the boundary-layer, we obtain,

$$\phi_1' = \phi_2, \tag{6.14}$$

$$\frac{N^2\phi_2'}{Re} = \frac{1}{Re}\left(\alpha^2+\beta^2-\mathrm{i}Re\,\gamma\right)\phi_1 + \frac{NW_\infty\phi_2}{Re} + \mathrm{i}\Bigg(\alpha^2+\beta^2 - \frac{\mathrm{i}\alpha}{Re}\left(\frac{-e^2\sin\theta\cos\theta}{(1-e^2\sin^2\theta)^{3/2}} + \frac{\cot\theta}{\sqrt{1-e^2\sin^2\theta}}\right)\Bigg)\phi_4, \tag{6.15}$$

$$N\phi_3' = -\mathrm{i}\phi_1 - \frac{N(2-e^2\sin^2\theta)}{Re(1-e^2\sin^2\theta)}\phi_3, \tag{6.16}$$

$$N\phi_4' = \frac{\mathrm{i}W_\infty}{Re} - \frac{\mathrm{i}N}{Re}\phi_2 - \frac{1}{Re}\left(\alpha^2+\beta^2-\mathrm{i}Re\,\gamma\right)\phi_3, \tag{6.17}$$

$$\phi_5' = \phi_6, \tag{6.18}$$

$$\frac{N^2\phi_6'}{Re} = \frac{\beta}{Re}\left(\frac{-e^2\sin\theta\cos\theta}{(1-e^2\sin^2\theta)^{3/2}} + \frac{\cot\theta}{\sqrt{1-e^2\sin^2\theta}}\right)\phi_4 + \frac{1}{Re}\left(\alpha^2+\beta^2-\mathrm{i}Re\,\gamma\right)\phi_5 + \frac{NW_\infty\phi_6}{Re}. \tag{6.19}$$

Equations (6.14)–(6.19) permits solutions of the form $c_i^j e^{\kappa_j \eta}$ and following the meth-

ods of §3.2, the numerical solution for k_j are obtained for each j. Note that as we require an exponentially decaying solution we use only the solution with $k_j < 0$. Extensive experimentation with the maximum value of η has shown that the eigenvalues are independent of the domain as long as it allows the fully developed basic flow components of velocity to be used, i.e. $\eta > 15$. Therefore, we form an approximate numerical solution of the perturbation equations at $\eta = 20$ for each of the transformed variables defined by i. We numerically integrate the full perturbation equations from these initial solutions down towards $\eta = 0$ enables the correct eigenvalues to be calculated. Details of this process are given in detail in §3.2.

6.3 The convective instability analysis for stationary vortices

In this section we solve the perturbation equations (6.8)–(6.13) with the aim of studying the occurrence of convective instabilities. Since, we are supposing that the flow is not absolutely unstable, in the Briggs-Bers procedure we can reduce the imaginary part of the frequency down to zero, so that $\gamma_i = 0$. For computing the neutral curves of convective instabilities of rotating oblate spheroids, we assume that the vortices rotate with some fixed multiple of the body surface. This procedure is identical to that described in §3.2. Following this procedure, vortices traveling with speed c relative to the oblate spheroid surface can be modeled by the same relation in equation (3.34). Note that the perturbation equations for oblate spheroids contain the laminar flow profiles U, V and W and these have been already solved numerically in §5.2. In this section, we discuss stationary modes, that is when the vortices rotate with the spheroid surface. The traveling disturbances in the range of $c \in [0, 2]$ are

considered in §6.4.

6.3.1 The neutral curves

As discussed in §3.1, naturally occurring surface roughness is known to select stationary modes in the boundary-layer flows over related rotating geometries, we therefore begin by making the *a priori* assumption that spiral vortices rotate with the oblate spheroid surface. As with the analyses of the prolate spheroids in §3.4.1 and other related geometries Lingwood (1995a); Garrett (2002); Garrett & Peake (2002, 2004, 2007); Garrett, Hussain & Stephen (2009a,b); Garrett (2010a,b,c), two spatial branches are found to determine the convective-instability characteristics at all latitudes and Reynolds numbers. These arise from the crossflow (type I) and the streamline-curvature (type II) effects. Spatial branches have been calculated at $\theta = 10°$–$70°$ for the oblate spheroids for $e = 0.0$–0.8. The detailed behaviour of the branches is not discussed here, however these spatial branches are consistent with those found for prolate spheroids described in §3.4.1.

The boundary-layer eruption close to the equator of the rotating spheroids disrupts the flow beyond $\theta = 80°$, therefore we do not consider latitudes beyond $\theta = 70°$. Neutral curves in the (Re, α_r)-, (Re, β)-planes are shown in Figures 6.1 and 6.2 at $\theta = 10°$ and $60°$ for $0 \leq e \leq 0.8$. Furthermore, neutral curves at latitudes to $\theta = 70°$ (in $10°$ increments) are shown in Figure 6.3 for $e = 0.0$, 0.3, 0.6 and 0.8 in the (Re, α_r)-plane only. Each curve encloses a region that is convectively unstable, and we see the characteristic two-lobed structure for latitudes $\theta \leq 60°$ for all values of e and for $\theta = 70°$ for $e \geq 0.6$ which is also seen in the analysis of related geometries. The larger lobe, characterized by higher wavenumbers arises from the behaviour of the type I branch with Reynolds number; and the smaller lobe, characterized by

smaller wavenumbers, from the type II branch. Note that the two lobed structure in the prolate case was disappeared for large values of e at $\theta = 60°$ and for $\theta = 70°$ for all values of e. However, in the oblate spheroid case the two lobe structure only disappears at 70° for small values of $e \leq 0.5$.

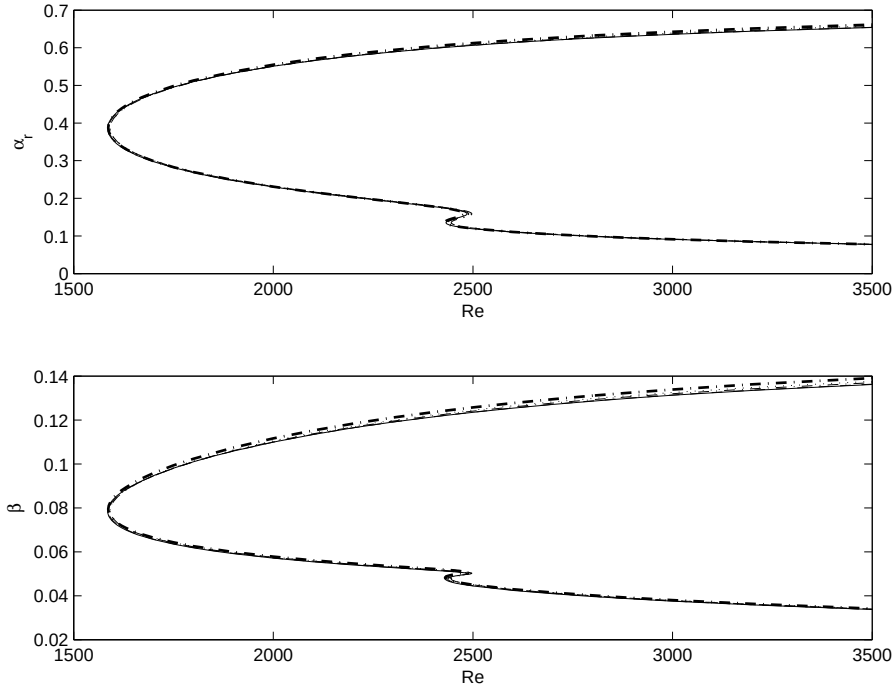

Figure 6.1: Neutral curves in the (Re, α)- and (Re, β)-planes at latitude 10° for $e = 0$ (–), 0.3 (−−), 0.6 (-.), 0.7 $(\cdots)$ & 0.8 (**-.**).

All neutral curves shown were calculated using the full perturbation equations (6.8)–(6.13). Neutral curves calculated using the Orr–Somerfeld equation for oblate spheroids are not shown here, however they were found to be single-lobed at each latitude similar to that for prolate spheroids, with critical Reynolds numbers lower than the most dangerous modes arising from the full system. Moreover, similar to the prolate case, the neutral curves calculated from the full system and the Orr–Somerfeld equation for oblate spheroids are also found to be consistent for large Re

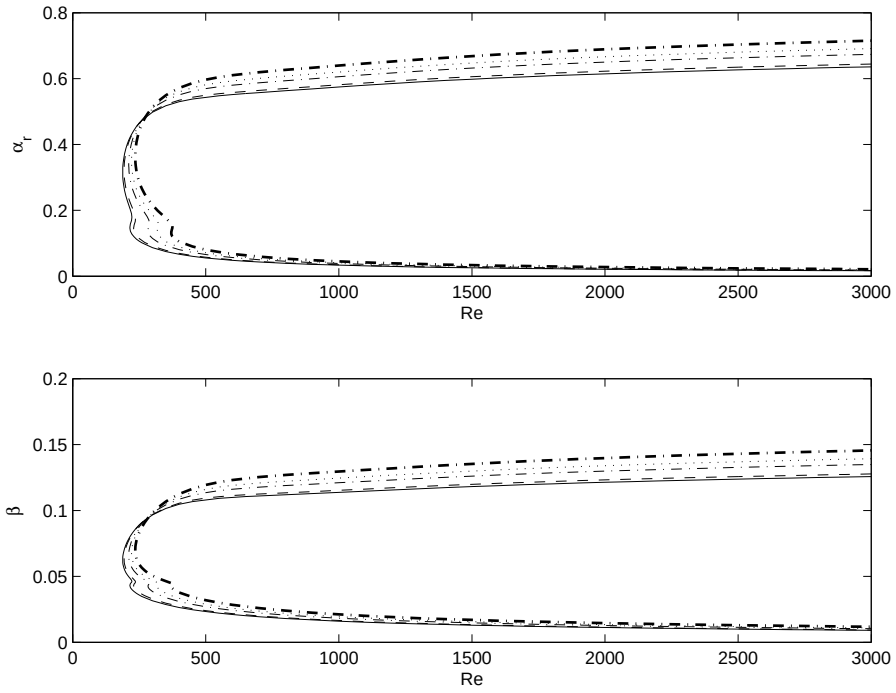

Figure 6.2: Neutral curves in the (Re, α)- and (Re, β)-planes at latitude 60° for $e = 0$ (–), 0.3 (−−), 0.6 (-.), 0.7 $(\cdots)$ & 0.8 (**-.**).

for all parameter sets $\{\theta, e\}$.

At all latitudes the neutral curves for $e = 0$ are as calculated by Garrett & Peake (2002) and this is to be expected as in the limiting case of $e = 0$ the full perturbation equations in both cases of spheroids become exactly those already established for rotating sphere. From Figures 6.1–6.3, it is clear that type I remains as the most dangerous (in the sense of lower critical Reynolds number) at all $\theta \leq 60°$ for all values of e; the type II effects become the most dangerous at $\theta \geq 70°$ for small values of $e \leq 0.5$. However, for large values of $e > 0.5$ the type I effects become the most dangerous at this high latitude.

The critical Reynolds numbers for the onset of convective instability for both modes, are listed in Appendix E.2 Tables E.1–E.9 in terms of spherical Reynolds

number Re and the spin Reynolds numbers R_S for $0 \leq e \leq 0.8$ (in increments of 0.1) at each latitude (the spin Reynolds number has been explained in §3.4.3). We note from Figure 6.1 that there is almost negligible effect of increasing e over the neutral curves at low $\theta = 10^\circ$. However close numerical inspection from Tables E.1–E.9 shows that for increasing e, the critical Reynolds number for both type I [viscous effects] & type II [streamline curvature effects] increases but swiftly start decreasing for higher values of $e \geq 0.7$. Figure 6.3 demonstrates that except at $\theta = 10^\circ$ at all other latitudes the effect of increasing e increases the critical Reynolds numbers for the onset of both modes, i.e. eccentricity has a stabilizing effect at all latitudes except near to the pole[1]. Near to the pole (at $\theta \leq 10^\circ$), increasing e has a stabilizing effect, however for very large values of $e \geq 0.7$, this stabilizing effect of e reverses slightly. Eccentricity therefore has a stabilizing effect at all latitudes except for very large values of e near to the pole. We note that as the latitude increases, the stabilizing effect of eccentricity also increases. Furthermore, the neutral curves calculated for the Orr-Sommerfeld equations of the oblate spheroids are also stabilizing for increasing e at all latitudes, although we do not show it here.

Interpreting the Reynolds number Re as a measure of the angular rotation rate, we can interpret the results as follows: neglecting the unusual behavior for large values of eccentricity near to the pole, rotating oblate spheroids with higher eccentricity become convectively unstable at all latitudes for higher rotation rates than is required for lower eccentricities. However, for instability to manifest near to the pole of the bodies is affected negligibly with eccentricity. Eccentricity is therefore

[1] We note that increasing e acts to slightly expand the region of convectively unstable parameters at all latitudes and so could be interpreted as a destabilizing effect in this sense. However, for all latitudes the increased critical Reynolds number is expected to be the dominant characteristic in many engineering applications.

interpreted as a stabilizing influence at all latitudes for the oblate spheroids rotating in otherwise still fluid.

The neutral curves obtained from the full perturbation equations for oblate spheroids were compared for the two different solutions of the steady basic flow profiles obtained from equations (5.4)–(5.6) of §5.1 which were obtained by using the two different solution methods (i.e. the series solution method and numerical method). The intention is to calculate the exact limits of latitudes for different values of e up to which the series solution method is appropriate to study the convective instability analyses over oblate spheroids. In §5.2, the root mean square errors (RMS) were calculated to measure the numerical errors between the series solution and the numerical solution of the steady basic flow for oblate spheroids. These (RMS) errors are shown at various latitudes in Tables 5.1–5.5 for a range of eccentricities. We note that as the latitude increases the discrepancy between the two solutions of the steady basic flow increases which is further exaggerated with increasing e. Although, we do not show it here, it is observed that the discrepancy between the basic flow solutions is consistent with that predicted between the neutral curves of convective instabilities for oblate spheroids when the perturbation equations were solved for the two different solutions of the basic flow. In §3.4.4, similar observations were made in the prolate spheroid case where we showed the visual difference between the neutral curves for the two solutions of the basic flow in Figures 3.13 & 3.14 at two latitudes for various values of e. The discrepancy between the neutral curves is increased when the W-profile of the steady flow for oblate spheroids has RMS error of $\mathrm{O}(e^{-2})$ magnitude (see Tables 5.1–5.5). Therefore, it is sufficient to use the series solution to capture accurately the characteristics of convective instabilities for oblate spheroids at latitudes of $\theta \leq 30^{\circ}$ for all values

of e, 40° for $e \leq 0.6$, 50° for $e \leq 0.5$ and 60° for $e \leq 0.4$. The series solution method is easy to use in terms of computational power and technical expertise required.

6.3.2 Comparison of results with other related geometries

In §3.4.3 we compared the results for prolate spheroids using the Reynolds number used by Malik (1986); Lingwood (1995a) in their investigation of rotating disk boundary layer and the spin Reynolds number used in the investigation of rotating sphere boundary layer by Taniguchi *et al.*(1998) and Kohama *et al.*(1983). We also follow this for comparing the results of the oblate spheroids. The purpose is to show the consistency of our results in the appropriate parameters with the related theoretical and experimental results.

As mentioned in §3.4.3, the Reynolds number used by Malik and Lingwood is based on the local radius of the rotating disk and is written as $R_D = Re \sin\theta$. When our results are expressed in terms of this Reynolds number at latitudes near to the pole, however not shown here, we find that the neutral curves for all values of e become very similar to those for rotating disk boundary layer presented by Malik (1986). This is because the oblate spheroid is locally flat near the pole for all values of e and so limits to a small rotating disk. This prediction is consistent with that discussed in §3.4.3 for prolate spheroids. Figures 6.4 & 6.5 show that the critical Reynolds number for both crossflow and streamline curvature instabilities approach those of the rotating disk as θ tends towards the pole and this occurs for all values of e. However, as the latitude is increased the difference between the critical Reynolds numbers at each latitude for increasing e increases. From this we suspect that increasing the curvature has a stabilizing effect over instabilities. Note that increasing latitude from the pole of oblate spheroids increases the curvature.

Moreover increasing the value of e also increases the curvature at a particular location above moderate latitudes of oblate spheroids. The large increase in critical Reynolds numbers for both crossflow and streamline curvature instabilities at each location (from moderate to high latitudes) with increasing e reflects that curvature has a stabilizing effect. Note that at low latitudes of oblate spheroids, the curvature decreases for increasing e, but strong inflow with increasing e has strong stabilizing effect which dominates the destabilizing effect of low curvature. Further note that in the prolate spheroid case, the critical Reynolds number for both crossflow flow and streamline curvature effects for large values of e at lower latitude near the pole exceeded the critical Reynolds number of rotating disk. We will again discuss this in detail in §6.5.

As discussed in §3.4.3, the angle that the phase fronts make with a circle parallel to the equator is denoted by ϵ, and is found from $\epsilon = \arctan(\beta/\alpha_r)$. The integer number of complete cycles of the disturbance round the azimuth is $n = \beta Re \sin\theta$. We identify ϵ and n as being the angle and number of spiral vortices on the spheroid surface, respectively. Taniguchi *et al.*(1998) and Kohama *et al.*(1983) presented their results for the rotating sphere in the (R_S, n)- and (R_S, ϵ)-planes. Here R_S is called the spin Reynolds number and is defined in terms of spherical Reynolds number as $R_S = \eta_0^{\star 2}\Omega^\star/\nu^\star = Re^2$. In Appendix E.3, Figures E.1–E.7 show the neutral curves of convective instabilities in the (R_S, n)- and (R_S, ϵ)-planes for oblate spheroids at latitudes 10°–70° for various values of e. We note that for decreasing latitude, the number of spiral vortices n at the onset of convective instability increases for all values of e, and this is consistent with the experimental observation of Kohama *et al.* in their investigation over rotating sphere. At latitude 10°, the number of spiral vortices at the onset of crossflow instability tend to approximately 22 for all values of

e. This is consistent with that calculated for rotating disk by Malik (1986). We also note that from low to moderate latitudes eccentricity has no effect on the number of spiral vortices, however above moderate latitudes n slightly increase with e at the onset of both crossflow instability and streamline curvature instability. This is in contrast to that predicted for the prolate spheroids.

Figures E.1–E.7 also demonstrate that at low to moderate latitudes up to 40°, the stationary vortices are predicted to have the same vortex angle at the onset of instabilities for all values of e. The values found being $\epsilon \approx 11.4°$ and 19.4° at the onset of crossflow instability and streamline curvature instability respectively. However, as the latitude increases above 40°, we note that the vortex angle at the onset of streamline curvature instability increases slightly with increase in e, although apparently remains the same at the onset of crossflow instability.

6.4 Growth rates and vortex speed selection

In this section we follow the techniques of §4.1 and investigate the growth rates of stationary and traveling disturbances for oblate spheroids at each latitude for various values of e. The disturbance relation is solved for disturbance speeds in the range $c = 0.6 - 2.0$ for each parameter set and neutral curves are computed as in §6.3.1. As discussed in detail in §4.1, the spatial growth rate is determined from the range of absolute values of α_i at particular vortex speed. We also note that in producing the plots for spatial growth rates as shown in Figure 6.6, it is only possible to consider a finite distance in Re before a region of absolute instability is entered (for detail on this the interested reader is referred to §4.1).

In Figure 6.6, we visualized the growth rates for type I & II modes for stationary

vortices through the convectively unstable region at various latitudes over oblate spheroid for a particular value of $e = 0.6$. We note that the growth rates for both modes at each location over oblate spheroid does not change as the analysis moves over the surface of oblate spheroid. At each location the type I mode has significantly larger growth rate. Moreover, this analysis remains the same for each value of e. This is also consistent with such analysis over prolate spheroids. From this we conclude that the amplifications of the two convectively unstable modes are unchanged at equal distances in Re at all locations on both types of spheroids, and that type I mode is likely the most amplified at all Reynolds numbers. Figures 6.7 & 6.8 show the neutral curves at $\theta = 20^\circ$ for $e = 0.3$ and $\theta = 60^\circ$ for $e = 0.7$ in (Re, α_r), (Re, β), (Re, n), (Re, ϵ)–planes for c=0.7, 0.8, 0.9, 1.0 and 2.0 respectively. Note that the quantities n and ϵ are the quantities through which we associate the results with the experimental observations of Kohama & Kobayashi (1983). At these latitudes and indeed all considered, we find that similar to previous analysis on related geometries, the type II mode is sensitive to the vortex speed. The type II mode is quickly eliminated for $c < 1$ and exaggerated for $c > 1$. Indeed, the type II modes are the most dangerous for quickly traveling modes (in the sense of lower critical Reynolds number) and this is consistent with the results predicted for prolate spheroids.

In Figures 6.9 & 6.10, we show the growth rates at $\theta = 20^\circ$ for $e = 0.3$ and $\theta = 60^\circ$ for $e = 0.7$ in order to visualize the growth rates of the linear spatial branches at different values of c. We see that type I mode has the globally maximum growth rates for all values of c considered, and these peak between c=0.7 & c=0.8. Further investigation shows that these predictions are the same for all latitudes and small values of $e \in [0, 0.6]$. However, at high latitudes and for $e \geq 0.7$, the peek of growth

rates occurred for slightly above c=0.8.

Figure 6.11 demonstrates that the growth rate is maximized for $c = 0.75$ at $\theta = 20^\circ$ for $e = 0.3$. Further investigation shows that the growth rates are maximized for the same value of $c = 0.75$ at all latitudes for small values of $e \leq 0.6$. However, as the eccentricity is increased we note that at high latitudes of $\theta \geq 60^\circ$, the maximum growth rates are predicted at $c \geq 0.76$. Figure 6.12 demonstrates that the growth rates are maximized for $c = 0.78$ at $\theta = 60^\circ$ for $e = 0.7$. We note that in general these predictions for oblate spheroids that the maximum growth rates at all latitudes and eccentricities occur at $c \approx 0.76$, are fully consistent with already predicted experimental and theoretical results over rotating spheres.

The vortex angle ϵ at the onset of convective instability at lower to moderate latitudes is predicted at $c \approx 0.9$. However, as the latitude increases above 60°, the value of c tends towards 1.0 in order to have the value of $\epsilon \approx 14^\circ$ at the onset of instability. This prediction is consistent with the prolate spheroid case. We note that unlike the prolate spheroid case, in the oblate case for large values of e and high latitudes, the value of $\epsilon = 14^\circ$ at the onset of instability again returns at $c \approx 0.9$. However, as discussed in the prolate spheroid case that Kohama & Kobayashi (1983) reported $\epsilon \approx 14^\circ$ at the onset of instability at each latitude of rotating sphere. In general for all values of e and all latitudes, our theoretical results show that the vortex angle $\epsilon \approx 14^\circ$ at the onset of instability, does not necessarily coincide with the vortex speed ($(c \approx 0.76)$) when the maximum growth rates occur. We will discuss this slight discrepancy of our results with the experimental results further in §6.6.

Figure 6.13 demonstrates that the increasing eccentricity has a stabilizing effect for both type I & II instabilities for various speeds of traveling disturbances, although

it is shown only at $\theta = 60°$. We have predicted that this observation is similar at all other latitudes. From this we conclude that eccentricity has a stabilizing effect on the convective instability of the rotating oblate spheroids for all vortex speeds considered.

6.5 Comparison of the results of oblate spheroids and prolate spheroids

In this section we focus on the main distinctions between the convective instability results for the two different types of spheroids. The prolate spheroids convective instability analyses were performed in Chapters 3 & 4.

In the prolate spheroid case, Figures 3.11 & 3.12 demonstrate that the critical Reynolds numbers at $\theta = 10°$ for $e \geq 0.4$ exceeded the critical Reynolds numbers of crossflow and streamline curvature instabilities of rotating disk. However, in the oblate spheroid case, Figures 6.4 & 6.5 demonstrate that the critical Reynolds numbers for both types I & II instabilities at lower latitude $\theta = 10°$ for all values of e are tending to converge to those critical Reynolds numbers of type I & II predicted for rotating disk boundary layer. Physically, it seems sensible that near the pole, oblate spheroids become more similar in shape to rotating disks than prolate spheroids. As we mentioned in §3.5 that increase in curvature has a stabilizing effect on convective instability for both type I & II instabilities of the boundary layer over rotating prolate spheroids. This observation now also seems justified in the rotating oblate spheroids case. Obviously at lower latitudes near the pole on the surface of prolate spheroids the curvature is larger than that for oblate spheroids. Further, we note that increase in curvature with e near the pole of prolate spheroids

is robust, but the curvature decreases with e near the pole of oblate spheroids. This is, therefore, near the pole on rotating prolate spheroids with increase in e we see a rapid increase in critical Reynolds numbers for both types I & II instabilities. Although this increase in critical Reynolds numbers for the oblate spheroids near the pole is very slow. Note that the stabilizing effect with e, near the pole of the prolate spheroids is happening due to the large increase in curvature. In the oblate spheroids case the slow stabilizing effect near the pole, is due to the increase in the rate of inflow into the boundary layer flow with e. This is also demonstrated in Appendix E.4, Figures E.8–E.12, where the neutral curves for both prolate spheroids and oblate spheroids are sketched in the same planes at $\theta = 10°$–$60°$ for various values of e. It is to be noted that by stabilization of convective instability at a particular location we mean a neutral curve with large critical Reynolds number than another at the same location and eccentricity for the two types of spheroids. These figures also demonstrate that the eccentricity has a strong stabilizing effect on the convective instability for prolate spheroids than those for oblate spheroids up to latitudes $\theta \leq 50°$. We note that eccentricity has a destabilizing effect in terms of critical Reynolds number for prolate spheroids at $\theta \geq 60°$ for $e > 0.3$. However, at $\theta \geq 60°$, eccentricity show a strong stabilizing effect for the convective instability of oblate spheroids. This can be interpreted as the curvature increase with increasing latitude over the surface of oblate spheroids and this exaggerates strongly with eccentricity at high latitudes, therefore, we predict a strong stabilizing effect of eccentricity for oblate spheroids at these high latitudes.

In §§4.1 & 6.4, we predicted that the growth rates for traveling vortices maximized for $c \approx 0.76$ for all values of e at $\theta \leq 60°$ for both types of spheroids but to attain the maximum growth rates at $\theta \geq 60°$ for large values of e, the value of c is

slightly to be increased. However, we note that the increase in value of c to attain the maximum growth rates at high latitudes for large values of e, is comparatively slower for the oblate spheroids than that observed in the prolate spheroids case.

6.6 Conclusion

In this chapter we followed the techniques of Chapter 3 and formulated the perturbation equations that govern the stability of the boundary-layer over the general family of rotating oblate spheroids. The convective instability analyses were performed in detail. The techniques of Chapter 4 were extended to investigate the amplification rates for traveling disturbances. In similar way to the prolate spheroid case, when $e = 0$ our results for the oblate spheroids also reproduce those for the rotating sphere.

In general, our results for the oblate spheroids are consistent with those for the prolate spheroids. Similar to the prolate spheroids case, the convective instability of the boundary layer for oblate spheroids is also dependent on the rate of inflow into the boundary layer. We note that for each value of e, the rate of inflow into the boundary layer over oblate spheroid, was decreasing with increasing latitude and this influenced the convective instability of the boundary layer by decreasing the critical Reynolds number with increasing latitude.

At a fixed latitude, our results suggest that increasing eccentricity has a stabilizing effect i.e. higher rotation rates are required for the boundary layer to become convectively unstable at a fixed latitude with higher value of e. This prediction that eccentricity has a stabilizing effect, is true at all latitudes over oblate spheroids except very near to the pole for very large values of e. However, at lower to mod-

erate latitudes the stabilizing effect of eccentricity is slow compared to that at high latitudes. Near the pole of oblate spheroids, the stabilizing effect of e is almost negligible. This reflects that as there is almost negligible increase in curvature near the pole, which results in negligible increase in critical Reynolds numbers of convective instability near the pole. Although, as the latitude increases, the curvature increases and it further exaggerates with increasing e, we observe that the critical Reynolds numbers also increase with e. At high latitudes, curvature exaggerates more rapidly with e and this results with more rapid increase in critical Reynolds numbers. This effect of e was slightly different in the prolate spheroids case, where e played a strong stabilizing role from low to moderate latitudes and then at high latitudes, the effect of e was reversed into a destabilizing role. From this we conclude that the rotating prolate spheroids are convectively more stable than the rotating oblate spheroids at lower to moderate latitudes for the same value of e θ. However, at high latitudes, oblate spheroids become strongly stable than the prolate spheroids for the same value of e and θ. In the case of traveling vortices, we also concluded that for all speeds of rotating vortices, increasing eccentricity is delaying the convective instability at all latitudes for the rotating oblate spheroids.

The number of spiral vortices for stationary vortices at the onset of instability decreased with decreasing latitude and this is consistent with that predicted in the prolate spheroid case. As the analysis moves towards the pole, the number of spiral vortices for all values of e approaches that predicted for rotating disk by Malik (1986). At the onset of instability the stationary vortices have roughly the same vortex angles at low to moderate latitudes for all values of e and these are identical to those predicted for prolate spheroids.

Similar to the prolate spheroid case we have shown that *slowly rotating* vortices

are the most amplified and are likely to be selected in experiments where perfectly smooth oblate spheroids are used. We predicted that the growth rates were maximized for vortices that rotate at around 75% of the oblate spheroid surface at all $\theta \leq 60^\circ$ for all values of $e \leq 0.6$. However this speed increases slightly for $\theta \geq 60^\circ$ and $e > 0.6$ up to 90% of the equatorial surface speed of the oblate spheroid. The increase in the speed of vortices at maximum growth rates at high latitudes and large values of e for oblate spheroids was comparatively slow than that in the prolate spheroid case. This discovery is consistent with the unusual observation of Kobayashi & Arai (1990) that vortices rotate at 76% of the sphere surface in particular conditions where very smooth surfaces are selected and surface roughness is avoided. This is also consistent with the theoretical predictions of Garrett (2010a,b,c) in his analyses over the boundary layer of rotating disk, cone and sphere. Further experiments similar to Kobayashi & Arai (1990) are suggested to confirm our results at high latitudes and larger eccentricities.

We predicted that the vortex angle of 14° at the onset of instability at each location does not coincide with the the maximum growth rates for all values of e. This is also consistent with the prolate spheroid case. We found that for the rotating oblate spheroids the vortex angle at the onset of instability is 14° for $c \approx 0.9$ at latitudes $\theta \leq 60^\circ$ for all values of e. However, at $\theta \geq 70^\circ$ the vortex speed c slightly exaggerates for the vortex angle to be at 14°, however this is for small values of e at this high latitude. For large values of e and large latitudes, the vortex angle of 14° at the onset of instability again returns to $c \approx 0.9$. This prediction is not consistent with that observed by Kohama *et al.*(1983) and Kobayashi *et al.*(1990) that the vortex angle at each latitude of the rotating sphere is 14° at the onset of instability. As we suggested in §4.2 this discrepancy might be due to their use of different

spheres in experiments. This is our opinion that they might have investigated the vortex angle at the onset of instability on a sphere with larger surface roughness and the vortex speed on another with perfectly smooth surface. We suggest further experiments to clarify our predictions in these geometries.

Factors $1/(1+\eta/Re)$ that multiply terms in the governing perturbation equations for the oblate spheroids have been replaced by unity and is similar to parallel flow approximations found in many other boundary layer investigation. As we discussed in §3.5 that this approximation is less valid at high latitudes. The validity of this approximation is also discussed by Garrett (2002) in detail for $e = 0$. However, this is our opinion that any inaccuracies introduced through this assumption are not large enough to affect the conclusion of this work. It is also acknowledged that our analyses would be inaccurate in situations where the growth rates are large and non-linear effects dominate.

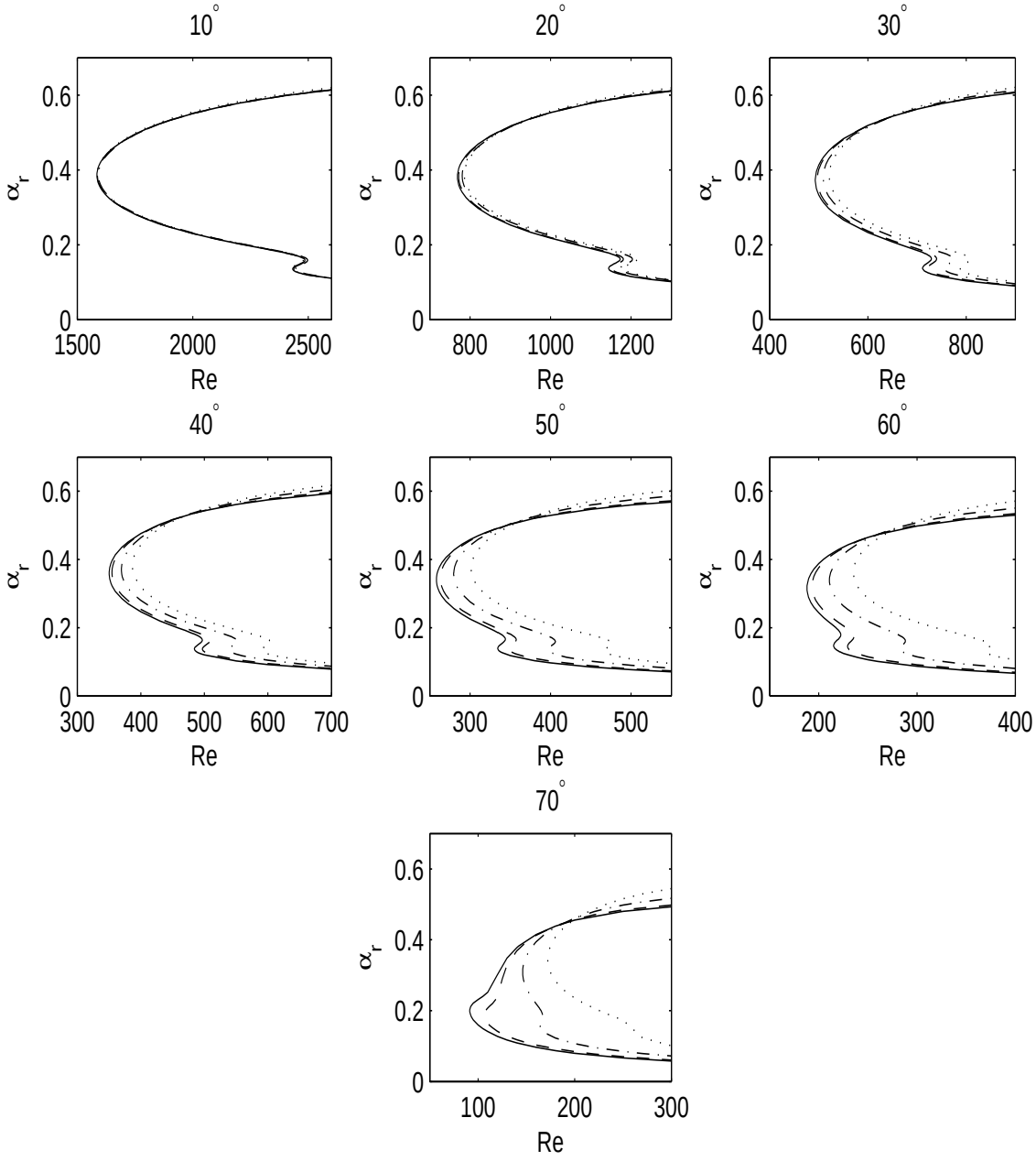

Figure 6.3: Neutral curves in the (Re, α)-plane at all latitudes for $e = 0.0$ (–), 0.3 (––), 0.6 (-.) & 0.8 ($\cdots$).

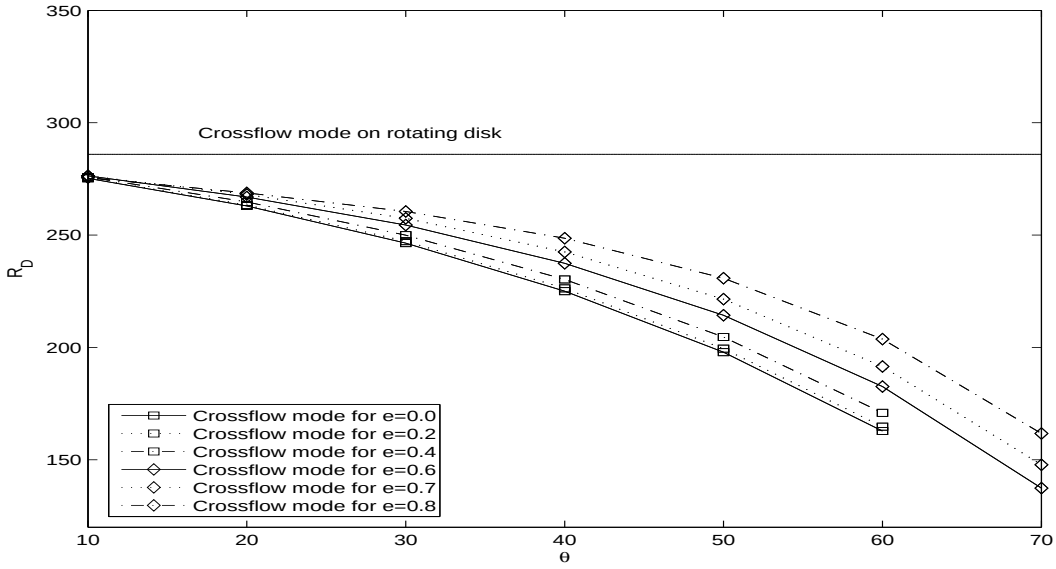

Figure 6.4: A comparison of the critical R_D values for convective instability of oblate spheroids due to crossflow effects at each latitude with those of the Malik (1986) for the rotating disk (horizontal line).

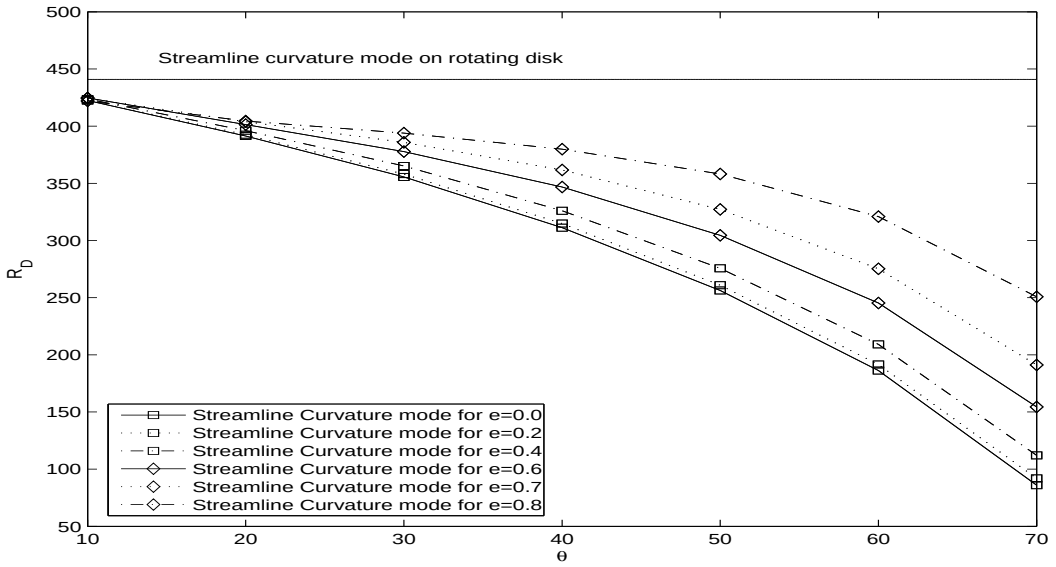

Figure 6.5: A comparison of the critical R_D values for convective instability due to streamline curvature mode of oblate spheroids at each latitude with those of the Malik (1986) for the rotating disk (horizontal line).

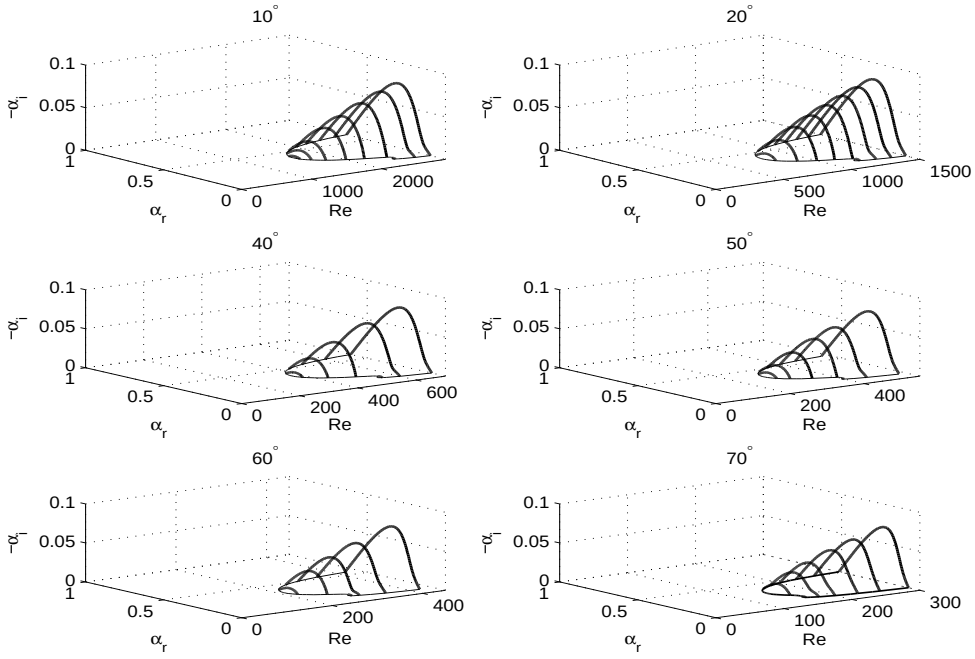

Figure 6.6: Linear convective growth rates for stationary disturbances through the convectively unstable region at various θ for $e = 0.6$.

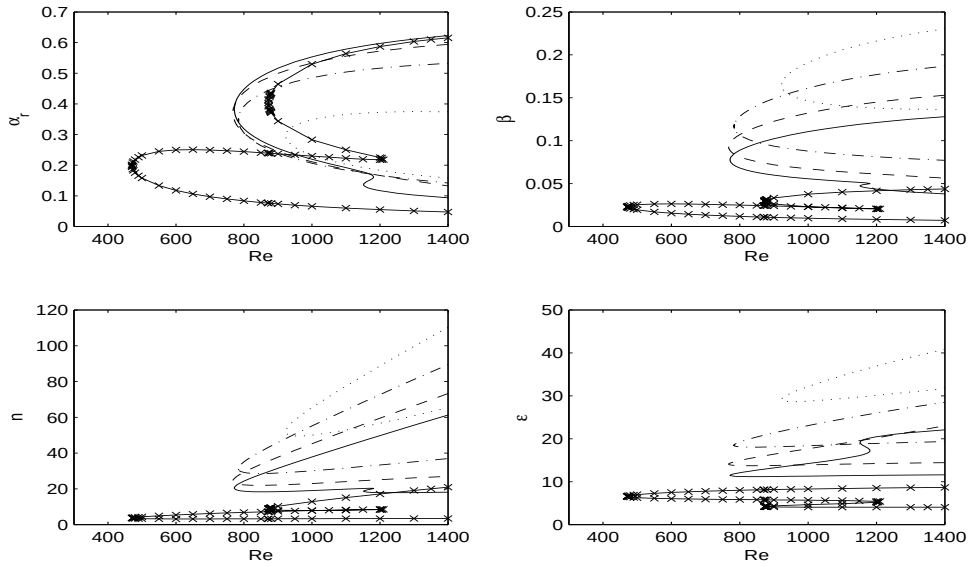

Figure 6.7: Neutral curves for traveling disturbances with c=0.7 ($\cdots$), 0.8 (-.), 0.9 ($--$), 1.0 (–), 2.0 (**-x**) at $\theta = 20°$ for $e = 0.3$.

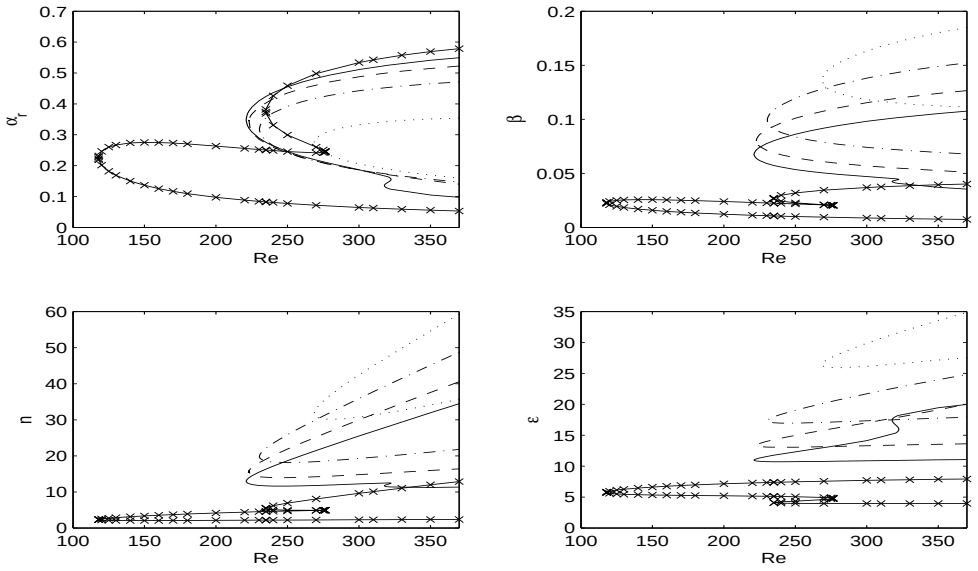

Figure 6.8: Neutral curves for traveling disturbances with c=0.7 ($\cdots$), 0.8 (-.), 0.9 ($--$), 1.0 (–), 2.0 (**-x**) at $\theta = 60°$ for $e = 0.7$.

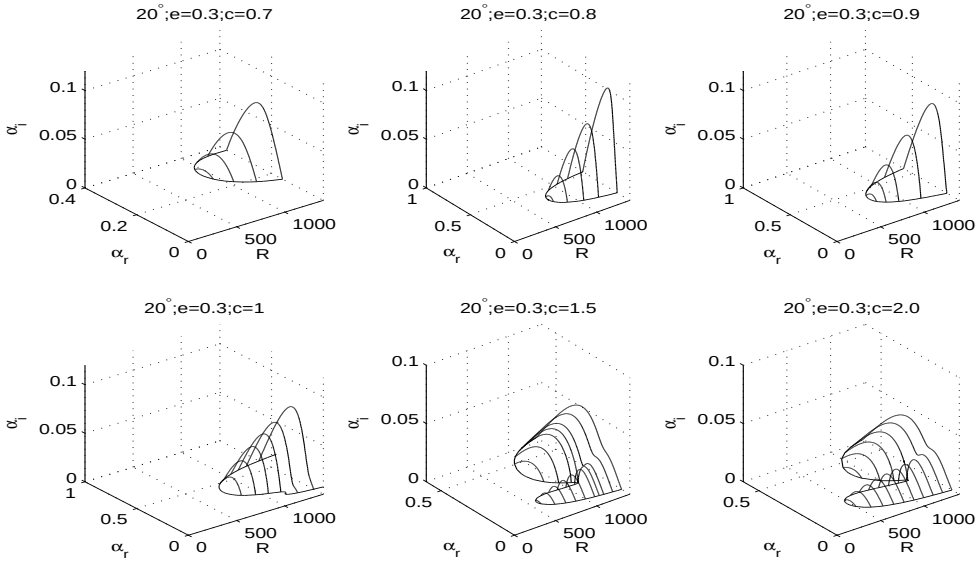

Figure 6.9: Linear convective growth rates for travelling-mode disturbances with $c = 0.7$–2 for $\theta = 20°, e = 0.3$.

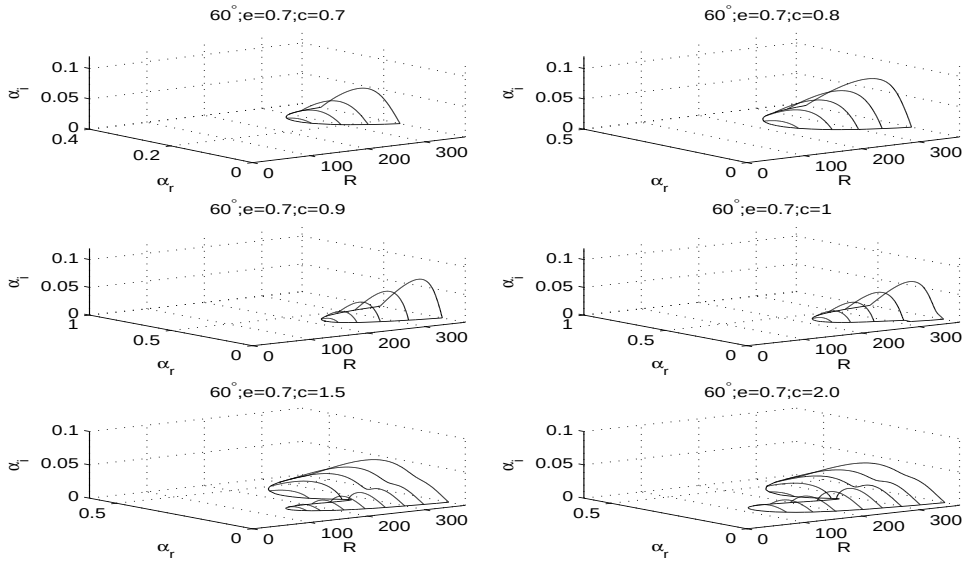

Figure 6.10: Linear convective growth rates for travelling-mode disturbances with $c = 0.7$–2 for $\theta = 60°, e = 0.7$.

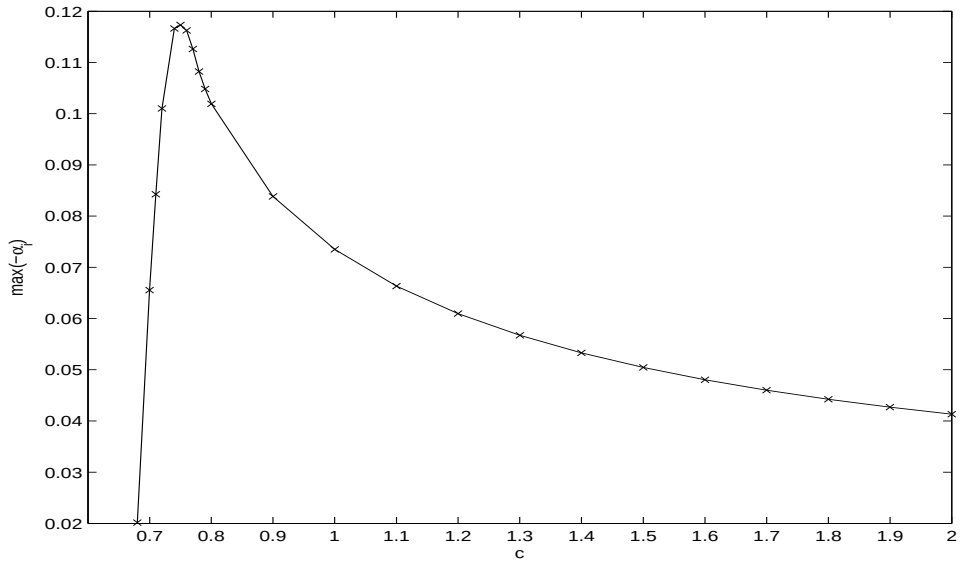

Figure 6.11: Maximum linear convective growth rates at $\theta = 20°$ for $e = 0.3$ at $Re = 1400$.

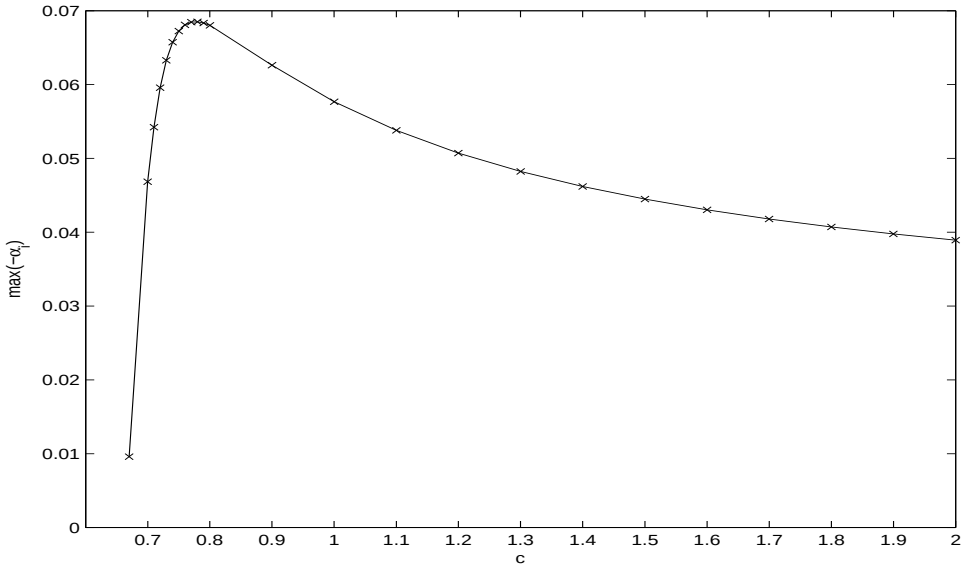

Figure 6.12: Maximum linear convective growth rates at $\theta = 60°$ for $e = 0.7$ at $Re = 370$.

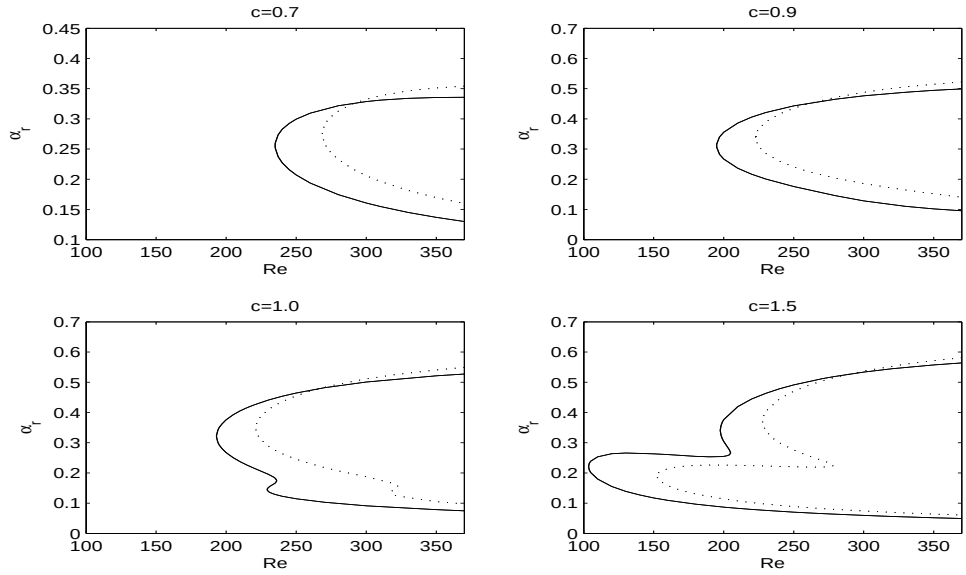

Figure 6.13: Neutral curves for traveling disturbances with $c = 0.7, 0.8, 1.0, 1.5$ at $\theta = 60°$ for $e = 0.3$ (–) & $e = 0.7$ $\cdots$.

Chapter 7

Conclusions

This thesis is concerned with the laminar flow and convective instability within the boundary layer over spheroids rotating in otherwise still fluid. A detailed summary and conclusion drawn from the results of each investigation can be found at the end of the relevant chapters. However, in §7.1 we review the important results and make some general conclusions, and in §7.2 suggestions for further research are made in the light of this thesis.

7.1 Completed work

As in previous stability analyses over other geometries, we began with the laminar flow within the boundary layer and then the stability analyses were performed. We followed this procedure to investigate the stability analysis over the two types of spheroids. We introduced two distinct three-dimensional orthogonal coordinate systems for the prolate spheroids and oblate spheroids. By using these two coordinate systems, the laminar boundary-layer equations have been formulated for each type of spheroids. As discussed in Chapter 1, until now we are unaware of the

laminar flow equations for these two types of spheroids, but indeed these equations are consistent with those established for the rotating sphere in the literature. An eccentricity parameter e appears in each set of the laminar flow equations which identify each particular spheroid within its family. We solved these equations by using the two different solution methods i.e. the series solution method (originally introduced by Banks (1965)) and an accurate numerical method (using the NAG routine D03PEF). The results were compared for increasing eccentricity for each type of spheroid. For $e = 0$, both systems reproduced exactly the same results for the laminar flow over rotating spheres.

The perturbation equations that govern the stability problem have been formulated separately for both types of spheroids. Setting the eccentricity parameter $e = 0$, both systems reproduce the same perturbation equations for the rotating-sphere boundary layer that appeared in the literature Garrett & Peake (2002); Garrett (2010c). This is physically reasonable as for eccentricity equal to zero, both types of spheroids reduce geometrically to a sphere.

We have noticed that as the latitude is increased for each type of spheroid, the normal component of velocity which represents the rate of inflow into the boundary layer, is decreased and this was the same for all values of eccentricity. This reflected a major implication for the stability of the boundary layer over both types of spheroids. We note that for each value of e, as the latitude was increased, the critical Reynolds numbers for convective instability were decreased. This was the same for both types of spheroids. From this we conclude that the convective instability is dependent in general on the laminar flow inside the boundary layer over rotating spheroids, and is influenced essentially by the rate of inflow into the boundary layer. This is consistent with the previous experimental and theoretical observations over rotating

spheres, where we see that keeping in mind the curvature of a sphere is constant, but the boundary layer became convectively unstable at higher latitudes for smaller angular rotation rates than at lower latitudes. This fact was observed for both types of spheroids at each value of eccentricity that the instabilities moved from higher latitudes towards lower latitudes with increasing angular rotation rates i.e. Reynolds numbers.

From above discussion we conclude that the rate of inflow (the W-profile) into the boundary-layer flow over both types of spheroids, influence the convective instability within the boundary-layer flow. For increasing the rate of inflow into the boundary layer flow we predict increase in the critical Reynolds numbers for both types I (cross-flow) & II (streamline curvature) modes and vice versa. Therefore it is reasonable to expect that the increase or decrease in the rate of inflow into the boundary-layer flow due to the variation in e should also influence the critical Reynolds numbers for both types I & II modes. In the oblate spheroid case for increasing e, the rate of inflow into the boundary-layer increases at each latitude. This increase in the rate of inflow has a stabilizing effect on the convective instability within the boundary layer flow over oblate spheroids. At lower latitudes of oblate spheroids, the rate of inflow increases slightly with increasing e and this reflects slight increase in the critical Reynolds numbers for both types I & II modes. However, above moderate latitudes of oblate spheroids, the rate of inflow at a fixed latitude increases strongly with e, which influence the boundary layer flow by strongly increasing the critical Reynolds number at these high latitudes.

On the other hand for the prolate spheroids at each particular latitude, the rate of inflow into the boundary layer flow decreases with increasing e. However, its effect on the stability is not observed as discussed above in the oblate spheroids case.

Conventionally, the decrease in the rate of inflow into the boundary-layer should have a destabilizing effect on the boundary layer flow over any such related geometries. For prolate spheroids at latitudes $\theta \geq 60°$, this convention is in good agreement. This is obvious from the results that at a fixed latitude, critical Reynolds numbers decrease with increasing e at these high latitudes of prolate spheroids. However, this convention does not agree at moderate to lower latitudes of prolate spheroids for increasing eccentricity at a fixed latitude. We see that at lower to moderate latitudes of prolate spheroids, the critical Reynolds numbers increase with increasing eccentricity at a fixed latitude. This increase in critical Reynolds numbers with e exaggerates with decreasing latitude. One possible explanation for this stabilizing effect despite the slight decrease in the rate of inflow with e, is the large local mean curvature at lower latitudes. For prolate spheroids, simple algebra and calculus leads to derive that decreasing latitude, increase the curvature and this exaggerates with increasing e. The type II mode is dependent on the curvature of the body and the neutral curves of instability for prolate spheroids show that, increasing curvature has a stabilizing effect on the type II lobe. At lower latitudes of prolate spheroids, increase in e strongly increase the curvature. Since, the decrease in the rate of inflow with e particularly at lower latitudes for prolate spheroids, is small and its destabilizing effect on the boundary layer should also be small. Although this small destabilize effect is not seen due to the strong curvature effects with increasing e at lower to moderate latitudes. Note that similar phenomenon also happens near the pole of oblate spheroids, where the curvature is very small and that we observe a destabilizing effect at $\theta = 10°$ for $e \geq 0.7$. We suspect moving below $10°$, the effect of e will be more destabilizing. Moreover, at lower to moderate latitudes of oblate spheroid, the stabilizing effect of e is negligible. This is because at lower

to moderate latitude curvature is small and also the rate of inflow slightly increase with e. Consequently, we see slight increase in critical Reynolds numbers at low to moderate latitudes of oblate spheroids.

The results obtained for the laminar flow equations by using the two different solutions methods, were compared visually and numerically by introducing the root mean square (RMS) errors. We found that the RMS errors were increasing with increasing latitudes for both types of spheroids and these errors were exaggerated with increasing eccentricity. The implications of the RMS errors for the stability of the boundary layer for both types of spheroids were consistent with that predicted for the laminar flow over rotating spheroids. We observed that at low to moderate latitudes the series solution produce accurate stability characteristics for both types of spheroids for all values of e. However, the discrepancy for the stability characteristics due to series solution increased at high latitudes, which exaggerated with increasing eccentricity. The interested reader is refereed to the relevant chapters to know the exact limits of latitudes and eccentricity up to which series solutions can be used to capture with accuracy the characteristics of convective instability for both types of spheroids. We note that we are concerned with the use of the flow profiles within the stability analysis and other applications may require different limits about the accuracy of the series solution approximations.

For both types of spheroids, we observed that the *slowly rotating* vortices are the most amplified and are likely to be selected in experiments where perfectly smooth rotating spheroids are used. We predicted that for both types of spheroids, for small values of eccentricity the growth rates were maximized at approximately 76% of the local surface speed of the spheroids. However, this speed slightly increased at high latitudes of 60° and $e \geq 0.6$ up to 90% of the local surface speed of rotating

oblate spheroids. For prolate spheroids, this speed was increased up to 100% of the local surface speed at these high latitudes and large values of eccentricity. This prediction is consistent with the experimental observations of Kohama & Kobayashi (1983) and Kobayashi & Arai (1990) that vortices rotate at 76% of the sphere surface in particular condition where very smooth surfaces are used and surface roughness is avoided. This prediction is also consistent with the theoretical observations of Garrett (2010a,b,c) in the stability analysis of the boundary layer over rotating disk, cone and sphere.

Kohama *et al.*(1983) and Kobyashi *et al.*(1990) reported a vortex angle 14° at the onset of instability over the rotating sphere. We note that the theoretical vortex angle for both types of spheroids is approximately 14° at the onset of instability at all latitudes for the vortex speed at approximately 90% of the surface speed. However, the vortex speed slightly exaggerates with increasing latitude and eccentricity for the vortex angle to be at 14° at the onset of instability. This means that for both types of rotating spheroids, the vortex angle of $\epsilon \approx 14°$ at the onset of instability at all latitudes does not necessarily coincide with the maximum growth rates. This is the same for all values of eccentricity. This is a slight discrepancy between the theoretical and experimental results. We, therefore suggest more such experiments to clarify these theoretical predictions, with greater focus on vortex speed.

7.2 Further work

This thesis must be considered as a preliminary investigation into the boundary layer over rotating spheroids. As this thesis is a natural generalization of the stability analysis over the boundary layer of rotating sphere by Garrett (2002), where

he performed other analyses in addition to the convective instability analyses. In particular, absolute instability analyses and the repetition of these analyses in axial flow. The absolute instability is likely to be linked to transition of the flow into a turbulent flow and is very important in many engineering applications. In the same way, in future we intend to perform the absolute instability analysis over both types of spheroids in still fluid as well as in the uniform axial flow. We note that that in the absolute instability analysis, the perturbation equations for both types of spheroids remain the same. Similarly for the stability analysis of the boundary layer over spheroids rotating in uniform axial flow, we only need to modify the steady laminar flow. We also need to numerically clarify the stability analysis very near to the poles of both types of spheroids. Particularly as in the prolate spheroid case, near to the pole at 10° for large values of eccentricity, the critical Reynolds number exceeded that predicted for the rotating disk. We need to investigate how far these exceed the critical Reynolds number of rotating disk when the latitude is further reduced towards the pole. We also suggest experiments to investigate the stability of the boundary layer of rotating spheroids to clarify our results presented in this thesis.

In the investigation of rotating cone boundary layer, Garrett, Hussain & Stephen (2009a,b) compared their numerical results at large Reynolds numbers with the results obtained through another approach to the boundary-layer problem, called an asymptotic analysis. The asymptotic analysis are rigorous at $(O(1/R))$ and we can also use this approach to compare our results at large Re for the rotating spheroids. The global mode analysis such as found by Pier & Huerre (2001) in the study of wake flows, on rotating disks by Davies & Carpenter (2001); Pier (2002) and rotating sphere by Garrett (2002), can also be extended for rotating spheroids.

We can also include the generalization of such stability analysis over other axisymmetric bodies of revolution like the convex and concave paraboloids, ovals, cylinders and tori etc. We believe these bodies can be modeled in a similar way to the rotating spheroids by choosing some appropriate three dimensional orthogonal coordinate system.

Appendices

Appendix A

3D Navier-Stoke's and Continuity Equations

In this appendix we present the incompressible 3D Navier-Stoke's and continuity equations in two distinct three dimensional coordinate systems that were not shown in the main text of this thesis. In Appendix A.1 we present the derivation of the Navier-Stoke's and continuity equations in 3D general orthogonal curvilinear coordinates. These full 3D Navier-Stoke's and continuity equations in curvilinear coordinates are transformed separately into prolate spheroidal and oblate spheroidal coordinate systems shown in Appendix A.1.1 & Appendix A.1.2 respectively.

A.1 3D General Orthogonal Coordinates

The *Navier Stoke's* equations for fluid flow in the absence of external forces can be written as,

$$\frac{\partial \vec{V}}{\partial t} + \left(\vec{V} \cdot \vec{\nabla}\right) \vec{V} = -\frac{1}{\rho}\vec{\nabla}P + \nu\nabla^2\vec{V} \tag{A.1}$$

Where $\vec{V}$ is the velocity, ρ density and ν the kinematic viscosity of the fluid. Using the following vector identities,

$$(\vec{V}\cdot\vec{\nabla})\vec{V} = -\vec{V}\times(\vec{\nabla}\times\vec{V}) + \vec{\nabla}(\frac{1}{2}V^2)$$

And $$\nabla^2\vec{V} = \vec{\nabla}(\vec{\nabla}\cdot\vec{V}) - \vec{\nabla}\times(\vec{\nabla}\times\vec{V})$$

The Equation (A.1) takes the following form,

$$\frac{\partial\vec{V}}{\partial t} - \vec{V}\times(\vec{\nabla}\times\vec{V}) + \vec{\nabla}(\frac{1}{2}V^2) = -\frac{1}{\rho}\vec{\nabla}P + \nu\big[\vec{\nabla}(\vec{\nabla}\cdot\vec{V}) - \vec{\nabla}\times\vec{\Omega}\big] \tag{A.2}$$

Where $\vec{\Omega} = \nabla\times\vec{V}$ is the vorticity. Let (x_1, x_2, x_3) be the general orthogonal curvilinear coordinates and $\vec{V} = u_1\,\hat{e}_1 + u_2\,\hat{e}_2 + u_3\,\hat{e}_3$ Where $\hat{e}_1$, $\hat{e}_2$, $\hat{e}_3$ are the unit vectors in the direction of increasing x_1, x_2 and x_3 respectively.

The components of a gradient are

$$(\frac{1}{h_1}\frac{\partial}{\partial x_1},\ \frac{1}{h_2}\frac{\partial}{\partial x_2},\ \frac{1}{h_3}\frac{\partial}{\partial x_3})$$

Where the quantities h_1, h_2, h_3 are called the scale factors. Using the gradient and divergence of vector $\vec{V}$ we can write the components of $\vec{\nabla}(\vec{\nabla}\cdot\vec{V})$ as follows,

$$\frac{1}{h_1}\frac{\partial}{\partial x_1}\left(\frac{1}{h_1h_2h_3}\Big(\frac{\partial}{\partial x_1}(h_2h_3u_1) + \frac{\partial}{\partial x_2}(h_3h_1u_2) + \frac{\partial}{\partial x_3}(h_1h_2u_3)\Big)\right) \tag{A.3}$$

$$\frac{1}{h_2}\frac{\partial}{\partial x_2}\left(\frac{1}{h_1h_2h_3}\Big(\frac{\partial}{\partial x_1}(h_2h_3u_1) + \frac{\partial}{\partial x_2}(h_3h_1u_2) + \frac{\partial}{\partial x_3}(h_1h_2u_3)\Big)\right) \tag{A.4}$$

$$\frac{1}{h_3}\frac{\partial}{\partial x_3}\left(\frac{1}{h_1h_2h_3}\Big(\frac{\partial}{\partial x_1}(h_2h_3u_1) + \frac{\partial}{\partial x_2}(h_3h_1u_2) + \frac{\partial}{\partial x_3}(h_1h_2u_3)\Big)\right) \tag{A.5}$$

$$\vec{\Omega} = \vec{\nabla}\times\vec{V} = \frac{1}{h_1h_2h_3}\begin{vmatrix} h_1e_1 & h_2e_2 & h_3e_3 \\ \frac{\partial}{\partial x_1} & \frac{\partial}{\partial x_2} & \frac{\partial}{\partial x_3} \\ h_1u_1 & h_2u_2 & h_3u_3 \end{vmatrix}$$

So the components of $\vec{\Omega}$ can be written as

$$\xi_1 = \frac{1}{h_2 h_3}\left(\frac{\partial}{\partial x_2}(h_3 u_3) - \frac{\partial}{\partial x_3}(h_2 u_2)\right) \tag{A.6}$$

$$\xi_2 = \frac{1}{h_3 h_1}\left(\frac{\partial}{\partial x_3}(h_1 u_1) - \frac{\partial}{\partial x_1}(h_3 u_3)\right) \tag{A.7}$$

$$\xi_3 = \frac{1}{h_1 h_2}\left(\frac{\partial}{\partial x_1}(h_2 u_2) - \frac{\partial}{\partial x_2}(h_1 u_1)\right) \tag{A.8}$$

The components of the vector product $\vec{V} \times \vec{\Omega}$ are

$$\vec{V} \times \vec{\Omega} = \big(u_2\xi_3 - u_3\xi_2\,,\ u_3\xi_1 - u_1\xi_3\,,\ u_1\xi_2 - u_2\xi_1\big) \tag{A.9}$$

The components of $\vec{\nabla}(\frac{1}{2}V^2)$ (after simplification) are

$$\frac{1}{h_1}\left(u_1\frac{\partial u_1}{\partial x_1} + u_2\frac{\partial u_2}{\partial x_1} + u_3\frac{\partial u_3}{\partial x_1}\right) \tag{A.10}$$

$$\frac{1}{h_2}\left(u_1\frac{\partial u_1}{\partial x_2} + u_2\frac{\partial u_2}{\partial x_2} + u_3\frac{\partial u_3}{\partial x_2}\right) \tag{A.11}$$

$$\frac{1}{h_3}\left(u_1\frac{\partial u_1}{\partial x_3} + u_2\frac{\partial u_2}{\partial x_3} + u_3\frac{\partial u_3}{\partial x_3}\right) \tag{A.12}$$

The components of $-\vec{V} \times \vec{\Omega} + \vec{\nabla}(\frac{1}{2}V^2)$ (after simplification) are

$$\frac{u_1}{h_1}\frac{\partial u_1}{\partial x_1} + \frac{u_2}{h_2}\frac{\partial u_1}{\partial x_2} + \frac{u_3}{h_3}\frac{\partial u_1}{\partial x_3} + \frac{u_1 u_2}{h_1 h_2}\frac{\partial h_1}{\partial x_2} - \frac{u_2^2}{h_1 h_2}\frac{\partial h_2}{\partial x_1} + \frac{u_1 u_3}{h_3 h_1}\frac{\partial h_1}{\partial x_3} - \frac{u_3^2}{h_3 h_1}\frac{\partial h_3}{\partial x_1} \tag{A.13}$$

$$\frac{u_1}{h_1}\frac{\partial u_2}{\partial x_1} + \frac{u_2}{h_2}\frac{\partial u_2}{\partial x_2} + \frac{u_3}{h_3}\frac{\partial u_2}{\partial x_3} + \frac{u_2 u_1}{h_2 h_1}\frac{\partial h_2}{\partial x_1} - \frac{u_1^2}{h_1 h_2}\frac{\partial h_1}{\partial x_2} - \frac{u_3^2}{h_2 h_3}\frac{\partial h_3}{\partial x_2} + \frac{u_2 u_3}{h_2 h_3}\frac{\partial h_2}{\partial x_3} \tag{A.14}$$

$$\frac{u_1}{h_1}\frac{\partial u_3}{\partial x_1} + \frac{u_2}{h_2}\frac{\partial u_3}{\partial x_2} + \frac{u_3}{h_3}\frac{\partial u_3}{\partial x_3} - \frac{u_1^2}{h_3 h_1}\frac{\partial h_1}{\partial x_3} + \frac{u_3 u_1}{h_3 h_1}\frac{\partial h_3}{\partial x_1} + \frac{u_3 u_2}{h_2 h_3}\frac{\partial h_3}{\partial x_2} - \frac{u_2^2}{h_2 h_3}\frac{\partial h_2}{\partial x_3} \tag{A.15}$$

The components of $\vec{\nabla} \times \vec{\Omega}$, are the following,

$$\frac{1}{h_2 h_3}\left(\frac{\partial(h_3\xi_3)}{\partial x_2} - \frac{\partial(h_2\xi_2)}{\partial x_3}\right) \tag{A.16}$$

$$\frac{1}{h_1 h_3}\left(\frac{\partial(h_1\xi_1)}{\partial x_3} - \frac{\partial(h_3\xi_3)}{\partial x_1}\right) \tag{A.17}$$

$$\frac{1}{h_1 h_2}\left(\frac{\partial(h_2\xi_2)}{\partial x_1} - \frac{\partial(h_1\xi_1)}{\partial x_2}\right) \tag{A.18}$$

Substituting equations (A.3)–(A.18) in equation (A.2) we write the full Navier Stoke's equations explicitly in general orthogonal curvilinear coordinates as

x_1 component:

$$\begin{aligned}\frac{\partial u_1}{\partial t}+\frac{u_1}{h_1}\frac{\partial u_1}{\partial x_1}+\frac{u_2}{h_2}\frac{\partial u_1}{\partial x_2}+\frac{u_3}{h_3}\frac{\partial u_1}{\partial x_3}+\frac{u_1u_2}{h_1h_2}\frac{\partial h_1}{\partial x_2}-\frac{u_2^2}{h_1h_2}\frac{\partial h_2}{\partial x_1}+\frac{u_1u_3}{h_3h_1}\frac{\partial h_1}{\partial x_3}\\ -\frac{u_3^2}{h_3h_1}\frac{\partial h_3}{\partial x_1}=-\frac{1}{\rho h_1}\frac{\partial P}{\partial x_1}+\nu\Bigg[\frac{1}{h_1}\frac{\partial}{\partial x_1}\Bigg(\frac{1}{h_1h_2h_3}\Big(\frac{\partial}{\partial x_1}(h_2h_3u_1)\\ +\frac{\partial}{\partial x_2}(h_3h_1u_2)+\frac{\partial}{\partial x_3}(h_1h_2u_3)\Big)\Bigg)-\frac{1}{h_2h_3}\left(\frac{\partial(h_3\xi_3)}{\partial x_2}-\frac{\partial(h_2\xi_2)}{\partial x_3}\right)\Bigg]\end{aligned} \tag{A.19}$$

x_2 component:

$$\begin{aligned}\frac{\partial u_2}{\partial t}+\frac{u_1}{h_1}\frac{\partial u_2}{\partial x_1}+\frac{u_2}{h_2}\frac{\partial u_2}{\partial x_2}+\frac{u_3}{h_3}\frac{\partial u_2}{\partial x_3}+\frac{u_2u_1}{h_2h_1}\frac{\partial h_2}{\partial x_1}-\frac{u_1^2}{h_1h_2}\frac{\partial h_1}{\partial x_2}-\frac{u_3^2}{h_2h_3}\frac{\partial h_3}{\partial x_2}\\ +\frac{u_2u_3}{h_2h_3}\frac{\partial h_2}{\partial x_3}=-\frac{1}{\rho h_2}\frac{\partial P}{\partial x_2}+\nu\Bigg[\frac{1}{h_2}\frac{\partial}{\partial x_2}\Bigg(\frac{1}{h_1h_2h_3}\Big(\frac{\partial}{\partial x_1}(h_2h_3u_1)\\ +\frac{\partial}{\partial x_2}(h_3h_1u_2)+\frac{\partial}{\partial x_3}(h_1h_2u_3)\Big)\Bigg)-\frac{1}{h_1h_3}\left(\frac{\partial(h_1\xi_1)}{\partial x_3}-\frac{\partial(h_3\xi_3)}{\partial x_1}\right)\Bigg]\end{aligned} \tag{A.20}$$

x_3 component:

$$\begin{aligned}\frac{\partial u_3}{\partial t}+\frac{u_1}{h_1}\frac{\partial u_3}{\partial x_1}+\frac{u_2}{h_2}\frac{\partial u_3}{\partial x_2}+\frac{u_3}{h_3}\frac{\partial u_3}{\partial x_3}-\frac{u_1^2}{h_3h_1}\frac{\partial h_1}{\partial x_3}+\frac{u_3u_1}{h_3h_1}\frac{\partial h_3}{\partial x_1}+\frac{u_3u_2}{h_2h_3}\frac{\partial h_3}{\partial x_2}\\ -\frac{u_2^2}{h_2h_3}\frac{\partial h_2}{\partial x_3}=-\frac{1}{\rho h_3}\frac{\partial P}{\partial x_3}+\nu\Bigg[\frac{1}{h_3}\frac{\partial}{\partial x_3}\Bigg(\frac{1}{h_1h_2h_3}\Big(\frac{\partial}{\partial x_1}(h_2h_3u_1)\\ +\frac{\partial}{\partial x_2}(h_3h_1u_2)+\frac{\partial}{\partial x_3}(h_1h_2u_3)\Big)\Bigg)-\frac{1}{h_1h_2}\left(\frac{\partial(h_2\xi_2)}{\partial x_1}-\frac{\partial(h_1\xi_1)}{\partial x_2}\right)\Bigg]\end{aligned} \tag{A.21}$$

For incompressible flow the continuity equation in general orthogonal curvilinear coordinates becomes,

$$\frac{1}{h_1h_2h_3}\Big(\frac{\partial}{\partial x_1}(h_2h_3u_1)+\frac{\partial}{\partial x_2}(h_3h_1u_2)+\frac{\partial}{\partial x_3}(h_1h_2u_3)\Big)=0 \tag{A.22}$$

Now that the 3D Navier-Stoke's and continuity equations are available in general orthogonal coordinates, we can easily transform these into any other physical 3D orthogonal coordinate system.

A.1.1 Prolate spheroidal Coordinate System

In this section we show the Navier-Stoke's and continuity equations in prolate spheroidal coordinates. The prolate spheroidal coordinate system has been shown in §2.1. We transform the general orthogonal coordinates presented in §A.1 into prolate spheroidal coordinates and using (A.19)–(A.22) we obtain the continuity and Navier-Stoke's equations in prolate spheroidal coordinates. Where the scale factors were derived as follows ,

$$h_{\eta^\star} = \sqrt{\frac{\eta^{\star 2} - d^{\star 2}\cos^2\theta}{\eta^{\star 2} - d^{\star 2}}}\,, \tag{A.23}$$

$$h_\theta = \sqrt{\eta^{\star 2} - d^{\star 2}\cos^2\theta}\,, \tag{A.24}$$

$$h_\phi = \sqrt{\eta^{\star 2} - d^{\star 2}}\sin\theta\,, \tag{A.25}$$

The continuity equation is,

$$\left(\frac{d^{\star 2}\cos\theta\sin\theta}{(\eta^{\star 2} - d^{\star 2}\cos^2\theta)^{3/2}} + \frac{\cot\theta}{\sqrt{\eta^{\star 2} - d^{\star 2}\cos^2\theta}}\right)U^\star + \frac{1}{\sqrt{\eta^{\star 2} - d^{\star 2}}\sin\theta}\frac{\partial V^\star}{\partial\phi}$$
$$+ \frac{1}{\sqrt{\eta^{\star 2} - d^{\star 2}\cos^2\theta}}\frac{\partial U^\star}{\partial\theta} + \left(\frac{\eta^\star\sqrt{\eta^{\star 2} - d^{\star 2}}}{(\eta^{\star 2} - d^{\star 2}\cos^2\theta)^{3/2}} + \right.$$
$$\left.\frac{\eta^\star}{\sqrt{\eta^{\star 2} - d^{\star 2}\cos^2\theta}\sqrt{\eta^{\star 2} - d^{\star 2}}}\right)W^\star + \sqrt{\frac{\eta^{\star 2} - d^{\star 2}}{\eta^{\star 2} - d^{\star 2}\cos^2\theta}}\frac{\partial W^\star}{\partial\eta^\star} = 0 \tag{A.26}$$

The θ component of the Navier Stokes equations in Prolate Spheroidal coordinates is written as ,

$$\frac{\partial U^\star}{\partial t^\star} + \frac{U^\star}{\sqrt{\eta^{\star 2} - d^{\star 2}\cos^2\theta}}\frac{\partial U^\star}{\partial\theta} + \frac{V^\star}{\sqrt{\eta^{\star 2} - d^{\star 2}}\sin\theta}\frac{\partial U^\star}{\partial\phi}$$
$$+ \frac{W^\star\sqrt{\eta^{\star 2} - d^{\star 2}}}{\sqrt{\eta^{\star 2} - d^{\star 2}\cos^2\theta}}\frac{\partial U^\star}{\partial\eta^\star} - \frac{V^{\star 2}\cot\theta}{\sqrt{\eta^{\star 2} - d^{\star 2}\cos^2\theta}}$$
$$+ \frac{U^\star W^\star\eta^\star\sqrt{\eta^{\star 2} - d^{\star 2}}}{(\eta^{\star 2} - d^{\star 2}\cos^2\theta)^{3/2}} - \frac{W^{\star 2}d^{\star 2}\cos\theta\sin\theta}{(\eta^{\star 2} - d^{\star 2}\cos^2\theta)^{3/2}} =$$

$$
\begin{aligned}
&- \frac{1}{\rho^\star\sqrt{\eta^{\star 2}-d^{\star 2}\cos^2\theta}}\frac{\partial P^\star}{\partial\theta} + \nu^\star\Bigg[\frac{(\eta^{\star 2}-d^{\star 2})}{(\eta^{\star 2}-d^{\star 2}\cos^2\theta)}\frac{\partial^2 U^\star}{\partial\eta^{\star 2}} \\
&+ \frac{1}{(\eta^{\star 2}-d^{\star 2}\cos^2\theta)}\frac{\partial^2 U^\star}{\partial\theta^2} + \frac{\csc^2\theta}{(\eta^{\star 2}-d^{\star 2})}\frac{\partial^2 U^\star}{\partial\phi^2} \\
&+ \frac{2\eta^\star}{(\eta^{\star 2}-d^{\star 2}\cos^2\theta)}\frac{\partial U^\star}{\partial\eta^\star} - \frac{2d^{\star 2}\sqrt{\eta^{\star 2}-d^{\star 2}}\sin\theta\,\cos\theta}{(\eta^{\star 2}-d^{\star 2}\cos^2\theta)^2}\frac{\partial W^\star}{\partial\eta^\star} \\
&+ \frac{\cot\theta}{(\eta^{\star 2}-d^{\star 2}\cos^2\theta)}\frac{\partial U^\star}{\partial\theta} + \frac{2\,\eta^\star\sqrt{\eta^{\star 2}-d^{\star 2}}}{(\eta^{\star 2}-d^{\star 2}\cos^2\theta)^2}\frac{\partial W^\star}{\partial\theta} \\
&- \frac{2\csc\theta\cot\theta}{\sqrt{\eta^{\star 2}-d^{\star 2}}\sqrt{\eta^{\star 2}-d^{\star 2}\cos^2\theta}}\frac{\partial V^\star}{\partial\phi} + \Bigg\{\frac{3\,\eta^{\star 2}-d^{\star 2}(1+\sin^2\theta)}{(\eta^{\star 2}-d^{\star 2}\cos^2\theta)^2} \\
&- \frac{3\,\eta^{\star 2}(\eta^{\star 2}-d^{\star 2})}{(\eta^{\star 2}-d^{\star 2}\cos^2\theta)^3} - \frac{3\;d^{\star 4}\sin^2\theta\cos^2\theta}{(\eta^{\star 2}-d^{\star 2}\cos^2\theta)^3} \\
&- \frac{\csc^2\theta}{(\eta^{\star 2}-d^{\star 2}\cos^2\theta)}\Bigg\}U^\star - \frac{2\,d^{\star 2}\eta^\star\sin\theta\cos\theta}{\sqrt{\eta^{\star 2}-d^{\star 2}}(\eta^{\star 2}-d^{\star 2}\cos^2\theta)^2}W^\star\Bigg]
\end{aligned}
\tag{A.27}
$$

The ϕ–component of Navier-Stoke's equations is written as ,

$$
\begin{aligned}
&\frac{\partial V^\star}{\partial t^\star} + \frac{U^\star}{\sqrt{\eta^{\star 2}-d^{\star 2}\cos^2\theta}}\frac{\partial V^\star}{\partial\theta} + \frac{V^\star\csc\theta}{\sqrt{\eta^{\star 2}-d^{\star 2}}}\frac{\partial V^\star}{\partial\phi} \\
&\quad + \frac{W^\star\sqrt{\eta^{\star 2}-d^{\star 2}}}{\sqrt{\eta^{\star 2}-d^{\star 2}\cos^2\theta}}\frac{\partial V^\star}{\partial\eta^\star} + \frac{U^\star V^\star\cot\theta}{\sqrt{\eta^{\star 2}-d^{\star 2}\cos^2\theta}} \\
&\quad + \frac{\eta^\star V^\star W^\star}{\sqrt{\eta^{\star 2}-d^{\star 2}\cos^2\theta}\sqrt{\eta^{\star 2}-d^{\star 2}}} = -\frac{\csc\theta}{\rho^\star\sqrt{\eta^{\star 2}-d^{\star 2}}}\frac{\partial P^\star}{\partial\phi} \\
&\quad + \nu^\star\Bigg[\frac{(\eta^{\star 2}-d^{\star 2})}{(\eta^{\star 2}-d^{\star 2}\cos^2\theta)}\frac{\partial^2 V^\star}{\partial\eta^{\star 2}} + \frac{2\eta^\star}{(\eta^{\star 2}-d^{\star 2}\cos^2\theta)}\frac{\partial V^\star}{\partial\eta^\star} \\
&\quad + \frac{1}{(\eta^{\star 2}-d^{\star 2}\cos^2\theta)}\frac{\partial^2 V^\star}{\partial\theta^2} + \frac{\csc^2\theta}{(\eta^{\star 2}-d^{\star 2})}\frac{\partial^2 V^\star}{\partial\phi^2} \\
&\quad + \frac{\cot\theta}{(\eta^{\star 2}-d^{\star 2}\cos^2\theta)}\frac{\partial V^\star}{\partial\theta} + \Bigg(\frac{1}{(\eta^{\star 2}-d^{\star 2}\cos^2\theta)} \\
&\quad - \frac{\csc^2\theta}{(\eta^{\star 2}-d^{\star 2}\cos^2\theta)} - \frac{\eta^{\star 2}}{(\eta^{\star 2}-d^{\star 2}\cos^2\theta)(\eta^{\star 2}-d^{\star 2})}\Bigg)V^\star \\
&\quad + \frac{2\csc\theta\cot\theta}{\sqrt{\eta^{\star 2}-d^{\star 2}}\sqrt{\eta^{\star 2}-d^{\star 2}\cos^2\theta}}\frac{\partial U^\star}{\partial\phi} \\
&\quad + \frac{2\eta^\star\csc\theta}{(\eta^{\star 2}-d^{\star 2})\sqrt{\eta^{\star 2}-d^{\star 2}\cos^2\theta}}\frac{\partial W^\star}{\partial\phi}\Bigg]
\end{aligned}
\tag{A.28}
$$

The $\eta^\star$–component of Navier-Stokes equations in prolate spheroidal coordinates is

written as ,

$$\begin{aligned}
&\frac{\partial W^\star}{\partial t^\star}+\frac{U^\star}{\sqrt{\eta^{\star 2}-d^{\star 2}\cos^2\theta}}\frac{\partial W^\star}{\partial\theta}+\frac{V^\star\csc\theta}{\sqrt{\eta^{\star 2}-d^{\star 2}}}\frac{\partial W^\star}{\partial\phi}\\
&\quad+\frac{\sqrt{\eta^{\star 2}-d^{\star 2}}}{\sqrt{\eta^{\star 2}-d^{\star 2}\cos^2\theta}}W^\star\frac{\partial W^\star}{\partial\eta^\star}-\frac{\eta^\star\sqrt{\eta^{\star 2}-d^{\star 2}}}{(\eta^{\star 2}-d^{\star 2}\cos^2\theta)^{3/2}}U^{\star 2}\\
&\quad+\frac{d^{\star 2}\cos\theta\sin\theta}{(\eta^{\star 2}-d^{\star 2}\cos^2\theta)^{3/2}}W^\star U^\star-\frac{\eta^\star V^{\star 2}}{\sqrt{\eta^{\star 2}-d^{\star 2}}\sqrt{\eta^{\star 2}-d^{\star 2}\cos^2\theta}}\\
&=-\frac{\sqrt{\eta^{\star 2}-d^{\star 2}}}{\rho^\star\sqrt{\eta^{\star 2}-d^{\star 2}\cos^2\theta}}\frac{\partial P^\star}{\partial\eta^\star}+\nu^\star\left[\left(\frac{\eta^{\star 2}-d^{\star 2}}{\eta^{\star 2}-d^{\star 2}\cos^2\theta}\right)\frac{\partial^2 W^\star}{\partial\eta^{\star 2}}\right.\\
&\quad+\frac{2\eta^\star}{(\eta^{\star 2}-d^{\star 2}\cos^2\theta)}\frac{\partial W^\star}{\partial\eta^\star}+\frac{1}{(\eta^{\star 2}-d^{\star 2}\cos^2\theta)}\frac{\partial^2 W^\star}{\partial\theta^2}\\
&\quad+\frac{\cot\theta}{(\eta^{\star 2}-d^{\star 2}\cos^2\theta)}\frac{\partial W^\star}{\partial\theta}+\frac{\csc^2\theta}{(\eta^{\star 2}-d^{\star 2})}\frac{\partial^2 W^\star}{\partial\phi^2}\\
&\quad+\frac{2d^{\star 2}\sqrt{\eta^{\star 2}-d^{\star 2}}\cos\theta\sin\theta}{(\eta^{\star 2}-d^{\star 2}\cos^2\theta)^2}\frac{\partial U^\star}{\partial\eta^\star}-\frac{2\eta^\star\sqrt{\eta^{\star 2}-d^{\star 2}}}{(\eta^{\star 2}-d^{\star 2}\cos^2\theta)^2}\frac{\partial U^\star}{\partial\theta}\\
&\quad-\frac{2\eta^\star\csc\theta}{(\eta^{\star 2}-d^{\star 2})\sqrt{\eta^{\star 2}-d^{\star 2}\cos^2\theta}}\frac{\partial V^\star}{\partial\phi}+\left\{\frac{1}{(\eta^{\star 2}-d^{\star 2}\cos^2\theta)}\right.\\
&\quad-\frac{\eta^{\star 2}}{(\eta^{\star 2}-d^{\star 2})(\eta^{\star 2}-d^{\star 2}\cos^2\theta)}+\frac{(\eta^{\star 2}-d^{\star 2})}{(\eta^{\star 2}-d^{\star 2}\cos^2\theta)^2}\\
&\quad-\frac{3\eta^{\star 2}(\eta^{\star 2}-d^{\star 2})}{(\eta^{\star 2}-d^{\star 2}\cos^2\theta)^3}-\frac{d^{\star 2}(3\sin^2\theta-2)}{(\eta^{\star 2}-d^{\star 2}\cos^2\theta)^2}\\
&\quad\left.\left.-\frac{3d^{\star 4}\sin^2\theta\cos^2\theta}{(\eta^{\star 2}-d^{\star 2}\cos^2\theta)^3}\right\}W^\star-\frac{2\eta^\star\sqrt{\eta^{\star 2}-d^{\star 2}}\cot\theta}{(\eta^{\star 2}-d^{\star 2}\cos^2\theta)^2}U^\star\right]
\end{aligned}\tag{A.29}$$

A.1.2 Oblate Spheroidal Coordinates System

The oblate spheroidal coordinate system is shown in §5.1. We transform the general orthogonal coordinates into oblate spheroidal coordinates. Using (A.19)–(A.22) we obtain the continiuty and Navier-Stoke's equations in oblate spheroidal coordinates shown here. The scale factors were derived as follows,

$$h_{\eta^\star}=\sqrt{\frac{\eta^{\star 2}-d^{\star 2}\sin^2\theta}{\eta^{\star 2}-d^{\star 2}}}\,,\tag{A.30}$$

$$h_\theta = \sqrt{\eta^{\star 2} - d^{\star 2}\sin^2\theta}\,, \tag{A.31}$$

$$h_\phi = \eta^\star \sin\theta\,, \tag{A.32}$$

The continuity equation for incompressible fluid flow in oblate spheroidal coordinates is ,

$$\begin{aligned}
&\left(-\frac{d^{\star 2}\cos\theta\sin\theta}{(\eta^{\star 2} - d^{\star 2}\sin^2\theta)^{3/2}} + \frac{\cot\theta}{\sqrt{\eta^{\star 2} - d^{\star 2}\sin^2\theta}}\right)U^\star + \frac{\csc\theta}{\eta^\star}\frac{\partial V^\star}{\partial\phi} \\
&+ \frac{1}{\sqrt{\eta^{\star 2} - d^{\star 2}\sin^2\theta}}\frac{\partial U^\star}{\partial\theta} + \left(\frac{\eta^\star\sqrt{\eta^{\star 2} - d^{\star 2}}}{(\eta^{\star 2} - d^{\star 2}\sin^2\theta)^{3/2}}\right. \\
&\left.+ \frac{\sqrt{\eta^{\star 2} - d^{\star 2}}}{\eta^\star\sqrt{\eta^{\star 2} - d^{\star 2}\sin^2\theta}}\right)W^\star + \sqrt{\frac{\eta^{\star 2} - d^{\star 2}}{\eta^{\star 2} - d^{\star 2}\sin^2\theta}}\frac{\partial W^\star}{\partial\eta^\star} = 0
\end{aligned} \tag{A.33}$$

The θ component of the Navier Stokes equations in Oblate Spheroidal coordinates is written as below ,

$$\begin{aligned}
&\frac{\partial U^\star}{\partial t^\star} + \frac{U^\star}{\sqrt{\eta^{\star 2} - d^{\star 2}\sin^2\theta}}\frac{\partial U^\star}{\partial\theta} + \frac{V^\star\csc\theta}{\eta^\star}\frac{\partial U^\star}{\partial\phi} + \frac{W^\star\sqrt{\eta^{\star 2} - d^{\star 2}}}{\sqrt{\eta^{\star 2} - d^{\star 2}\sin^2\theta}}\frac{\partial U^\star}{\partial\eta^\star} \\
&\quad - \frac{V^{\star 2}\cot\theta}{\sqrt{\eta^{\star 2} - d^{\star 2}\sin^2\theta}} + \frac{U^\star W^\star\eta^\star\sqrt{\eta^{\star 2} - d^{\star 2}}}{(\eta^{\star 2} - d^{\star 2}\sin^2\theta)^{3/2}} + \frac{W^{\star 2}d^{\star 2}\cos\theta\sin\theta}{(\eta^{\star 2} - d^{\star 2}\sin^2\theta)^{3/2}} \\
&\quad = -\frac{1}{\rho^\star\sqrt{\eta^{\star 2} - d^{\star 2}\sin^2\theta}}\frac{\partial P^\star}{\partial\theta} + \nu^\star\left[\frac{(\eta^{\star 2} - d^{\star 2})}{(\eta^{\star 2} - d^{\star 2}\sin^2\theta)}\frac{\partial^2 U^\star}{\partial\eta^{\star 2}}\right. \\
&\quad + \frac{1}{(\eta^{\star 2} - d^{\star 2}\sin^2\theta)}\frac{\partial^2 U^\star}{\partial\theta^2} + \frac{\csc^2\theta}{\eta^{\star 2}}\frac{\partial^2 U^\star}{\partial\phi^2} + \frac{2\eta^{\star 2} - d^{\star 2}\sin^2\theta}{\eta^\star(\eta^{\star 2} - d^{\star 2}\sin^2\theta)}\frac{\partial U^\star}{\partial\eta^\star} \\
&\quad + \frac{2d^{\star 2}\sqrt{\eta^{\star 2} - d^{\star 2}}\sin\theta\cos\theta}{(\eta^{\star 2} - d^{\star 2}\sin^2\theta)^2}\frac{\partial W^\star}{\partial\eta^\star} + \frac{\cot\theta}{(\eta^{\star 2} - d^{\star 2}\sin^2\theta)}\frac{\partial U^\star}{\partial\theta} \\
&\quad + \frac{2\sqrt{\eta^{\star 2} - d^{\star 2}}}{\eta^\star(\eta^{\star 2} - d^{\star 2}\sin^2\theta)}\frac{\partial W^\star}{\partial\theta} - \frac{2\csc\theta\cot\theta}{\eta^\star\sqrt{\eta^{\star 2} - d^{\star 2}\sin^2\theta}}\frac{\partial V^\star}{\partial\phi} \\
&\quad + \frac{\left(-\eta^{\star 2} + 2d^{\star 2}\sin^2\theta - 2d^{\star 2}\sin^4\theta\right)}{\sin^2\theta\left(\eta^{\star 2} - d^{\star 2}\sin^2\theta\right)^2}U^\star \\
&\quad \left. + \frac{2d^{\star 2}\sin\theta\cos\theta\sqrt{\eta^{\star 2} - d^{\star 2}}}{\eta^\star(\eta^{\star 2} - d^{\star 2}\sin^2\theta)^2}W^\star\right]
\end{aligned} \tag{A.34}$$

The ϕ–component of Navier-Stoke's equations is written as ,

$$\begin{aligned}
&\frac{\partial V^\star}{\partial t^\star}+\frac{U^\star}{\sqrt{\eta^{\star 2}-d^{\star 2}\sin^2\theta}}\frac{\partial V^\star}{\partial\theta}+\frac{V^\star\csc\theta}{\eta^\star}\frac{\partial V^\star}{\partial\phi}\\
&\quad+\frac{W^\star\sqrt{\eta^{\star 2}-d^{\star 2}}}{\sqrt{\eta^{\star 2}-d^{\star 2}\sin^2\theta}}\frac{\partial V^\star}{\partial\eta^\star}+\frac{U^\star V^\star\cot\theta}{\sqrt{\eta^{\star 2}-d^{\star 2}\sin^2\theta}}\\
&\quad+\frac{\sqrt{\eta^{\star 2}-d^{\star 2}}V^\star W^\star}{\eta^\star\sqrt{\eta^{\star 2}-d^{\star 2}\sin^2\theta}}=-\frac{\csc\theta}{\rho^\star\eta^\star}\frac{\partial P^\star}{\partial\phi}\\
&\quad+\nu^\star\Bigg[\frac{(\eta^{\star 2}-d^{\star 2})}{(\eta^{\star 2}-d^{\star 2}\sin^2\theta)}\frac{\partial^2 V^\star}{\partial\eta^{\star 2}}+\frac{\left(2\eta^{\star 2}-d^{\star 2}\right)}{\eta^\star(\eta^{\star 2}-d^{\star 2}\sin^2\theta)}\frac{\partial V^\star}{\partial\eta^\star}\\
&\quad+\frac{1}{(\eta^{\star 2}-d^{\star 2}\sin^2\theta)}\frac{\partial^2 V^\star}{\partial\theta^2}+\frac{\csc^2\theta}{\eta^{\star 2}}\frac{\partial^2 V^\star}{\partial\phi^2}\\
&\quad+\frac{\cot\theta}{(\eta^{\star 2}-d^{\star 2}\sin^2\theta)}\frac{\partial V^\star}{\partial\theta}-\frac{\left(\eta^{\star 2}-2d^{\star 2}\sin^2\theta\right)}{\eta^{\star 2}\sin^2\theta\left(\eta^{\star 2}-d^{\star 2}\sin^2\theta\right)}V^\star\\
&\quad+\frac{2\csc\theta\cot\theta}{\eta^\star\sqrt{\eta^{\star 2}-d^{\star 2}\sin^2\theta}}\frac{\partial U^\star}{\partial\phi}\\
&\quad+\frac{\csc\theta\left(2\eta^{\star 2}-d^{\star 2}\sin^2\theta\right)\sqrt{\eta^{\star 2}-d^{\star 2}}}{\eta^{\star 2}\left(\eta^{\star 2}-d^{\star 2}\sin^2\theta\right)^{3/2}}\frac{\partial W^\star}{\partial\phi}\Bigg]
\end{aligned}\tag{A.35}$$

The $\eta^\star$–component of Navier-Stokes equations in Oblate spheroidal coordinates is ,

$$\begin{aligned}
&\frac{\partial W^\star}{\partial t^\star}+\frac{U^\star}{\sqrt{\eta^{\star 2}-d^{\star 2}\sin^2\theta}}\frac{\partial W^\star}{\partial\theta}+\frac{V^\star\csc\theta}{\eta^\star}\frac{\partial W^\star}{\partial\phi}\\
&\quad+\frac{\sqrt{\eta^{\star 2}-d^{\star 2}}}{\sqrt{\eta^{\star 2}-d^{\star 2}\sin^2\theta}}W^\star\frac{\partial W^\star}{\partial\eta^\star}-\frac{\eta^\star\sqrt{\eta^{\star 2}-d^{\star 2}}}{(\eta^{\star 2}-d^{\star 2}\sin^2\theta)^{3/2}}U^{\star 2}\\
&\quad-\frac{d^{\star 2}\cos\theta\sin\theta}{(\eta^{\star 2}-d^{\star 2}\sin^2\theta)^{3/2}}W^\star U^\star-\frac{\sqrt{\eta^{\star 2}-d^{\star 2}}V^{\star 2}}{\eta^\star\sqrt{\eta^{\star 2}-d^{\star 2}\sin^2\theta}}\\
&\quad=-\frac{\sqrt{\eta^{\star 2}-d^{\star 2}}}{\rho^\star\sqrt{\eta^{\star 2}-d^{\star 2}\sin^2\theta}}\frac{\partial P^\star}{\partial\eta^\star}+\nu^\star\Bigg[\left(\frac{\eta^{\star 2}-d^{\star 2}}{\eta^{\star 2}-d^{\star 2}\sin^2\theta}\right)\frac{\partial^2 W^\star}{\partial\eta^{\star 2}}\\
&\quad+\frac{2\eta^{\star 2}-d^{\star 2}}{\eta^\star(\eta^{\star 2}-d^{\star 2}\sin^2\theta)}\frac{\partial W^\star}{\partial\eta^\star}+\frac{1}{(\eta^{\star 2}-d^{\star 2}\sin^2\theta)}\frac{\partial^2 W^\star}{\partial\theta^2}\\
&\quad+\frac{\cot\theta}{(\eta^{\star 2}-d^{\star 2}\sin^2\theta)}\frac{\partial W^\star}{\partial\theta}+\frac{\csc^2\theta}{\eta^{\star 2}}\frac{\partial^2 W^\star}{\partial\phi^2}\\
&\quad-\frac{2d^{\star 2}\sqrt{\eta^{\star 2}-d^{\star 2}}\cos\theta\sin\theta}{(\eta^{\star 2}-d^{\star 2}\sin^2\theta)^2}\frac{\partial U^\star}{\partial\eta^\star}-\frac{2\eta^\star\sqrt{\eta^{\star 2}-d^{\star 2}}}{(\eta^{\star 2}-d^{\star 2}\sin^2\theta)^2}\frac{\partial U^\star}{\partial\theta}
\end{aligned}$$

$$
\begin{aligned}
&- \frac{2\sqrt{\eta^{\star 2} - d^{\star 2}}\csc\theta}{\eta^{\star 2}\sqrt{\eta^{\star 2} - d^{\star 2}\sin^2\theta}}\frac{\partial V^\star}{\partial \phi} + \Bigg\{ \frac{-2\eta^{\star 6} + 4\eta^{\star 4} d^{\star 2}\left(4 - \sin^2\theta\right)}{\eta^{\star 2}\left(\eta^{\star 2} - d^{\star 2}\sin^2\theta\right)^3} \\
&+ \frac{-2\eta^{\star 2} d^{\star 4}\sin^2\theta + d^{\star 4}\sin^4\theta - \left(2\cos\theta - \sin^2\theta\right)\eta^{\star 4} d^{\star 2}}{\eta^{\star 2}\left(\eta^{\star 2} - d^{\star 2}\sin^2\theta\right)^3} \\
&+ \frac{\sin^2\theta\left(2\cos^2\theta - 2\cos\theta + 1\right)\eta^{\star 2} d^{\star 2}}{\eta^{\star 2}\left(\eta^{\star 2} - d^{\star 2}\sin^2\theta\right)^3} \Bigg\} W^\star - \frac{2\eta^\star\sqrt{\eta^{\star 2} - d^{\star 2}}\cot\theta}{(\eta^{\star 2} - d^{\star 2}\sin^2\theta)^2} U^\star \Bigg]
\end{aligned}
\tag{A.36}
$$

Appendix B

Series solution and comparisons of flow profiles of the laminar boundary-layer of prolate spheroid

This Appendix is related to Chapter 2 of this thesis. In Appendix B.1 we present the series solution for the laminar boundary layer equations of the rotating prolate spheroids. Values of quantities $F_n'(0)$, $G_n'(0)$, $H_n(\infty)$ for n=1,3,5,7 are presented in Appendix B.2. In Appendix B.3 comparison of flow profiles due to the numerical and series solutions are shown at various latitudes and eccentricities.

B.1 Details of the series solution for the prolate family

$$F_1^2 + H_1 F_1' - G_1^2 = F_1'' \tag{B.1}$$

$$\begin{aligned} 4F_1F_3 + H_1F_3' + H_3F_1' - 2G_1G_3 + \\ \left(\frac{1}{3} - \frac{e^2}{2(1-e^2)}\right)G_1^2 + \frac{e^2}{2(1-e^2)}\left(F_1^2 + H_1F_1'\right) = F_3'' \end{aligned} \tag{B.2}$$

$$\begin{aligned} 6F_1F_5 + 3F_3^2 + H_1F_5' + H_3F_3' + H_5F_1' - 2G_1G_5 - \\ G_3^2 + \left(\frac{2}{3} - \frac{e^2}{(1-e^2)}\right)G_1G_3 + \left(\frac{1}{45} + \frac{e^2(8-5e^2)}{24(1-e^2)^2}\right)G_1^2 - \\ \frac{e^2(4-e^2)}{24(1-e^2)^2}\left(F_1^2 + H_1F_1'\right) + \\ \frac{e^2}{2(1-e^2)}\left(4F_1F_3 + H_1F_3' + H_3F_1'\right) = F_5'' \end{aligned} \tag{B.3}$$

$$\begin{aligned} 8F_1F_7 + 8F_3F_5 + H_1F_7' + H_3F_5' + H_5F_3' + H_7F_1' - \\ 2G_1G_7 - 2G_3G_5 + \left(\frac{-e^2}{2(1-e^2)} + \frac{1}{3}\right)G_3^2 + \\ \left(\frac{2}{3} - \frac{e^2}{1-e^2}\right)G_1G_5 + \left(\frac{2}{45} + \frac{(8-5e^2)e^2}{12(1-e^2)^2}\right)G_1G_3 + \\ \left(\frac{2}{945} - \frac{e^2(16-2e^2+e^4)}{240(1-e^2)^3}\right)G_1^2 + \\ \frac{e^2(16+28e^2+e^4)}{720(1-e^2)^3}\left(F_1^2 + H_1F_1'\right) - \\ \frac{e^2(4-e^2)}{24(1-e^2)^2}\left(4F_1F_3 + H_1F_3' + H_3F_1'\right) + \\ \frac{e^2}{2(1-e^2)}\left(6F_1F_5 + 3F_3^2 + H_1F_5' + H_3F_3' + H_5F_1'\right) = F_7'' \end{aligned} \tag{B.4}$$

$$2F_1G_1 + H_1G_1' = G_1'' \tag{B.5}$$

$$\begin{aligned} 4F_1G_3 + 2F_3G_1 + H_1G_3' + H_3G_1' + \\ \left(\frac{e^2}{1-e^2} - \frac{1}{3}\right) F_1G_1 + \frac{e^2}{2(1-e^2)} H_1G_1' = G_3'' \end{aligned} \tag{B.6}$$

$$\begin{aligned} 6F_1G_5 + 4F_3G_3 + 2F_5G_1 + H_1G_5' + H_3G_3' + H_5G_1' + \\ \left(\frac{2e^2}{(1-e^2)} - \frac{1}{3}\right) F_1G_3 + \left(\frac{e^2}{(1-e^2)} - \frac{1}{3}\right) F_3G_1 - \\ \left(\frac{e^2(2-e^2)}{4(1-e^2)^2} + \frac{1}{45}\right) F_1G_1 + \frac{e^2}{2(1-e^2)} \left(H_3G_1' + H_1G_3'\right) - \\ \frac{e^2(4-e^2)}{(24(1-e^2)^2)} H_1G_1' = G_5'' \end{aligned} \tag{B.7}$$

$$\begin{aligned} 8F_1G_7 + 6F_3G_5 + 4F_5G_3 + 2F_7G_1 + H_1G_7' + H_3G_5' + \\ H_5G_3' + H_7G_1' + \left(\frac{3e^2}{1-e^2} - \frac{1}{3}\right) F_1G_5 + \\ \left(\frac{2e^2}{1-e^2} - \frac{1}{3}\right) F_3G_3 + \left(\frac{e^2}{1-e^2} - \frac{1}{3}\right) F_5G_1 - \\ \left(\frac{e^2(5-2e^2)}{6(1-e^2)^2} + \frac{1}{45}\right) F_1G_3 - \left(\frac{e^2(2-e^2)}{4(1-e^2)^2} + \frac{1}{45}\right) F_3G_1 + \\ \left(\frac{e^2(32+11e^2+2e^4)}{360(1-e^2)^3} - \frac{2}{945}\right) F_1G_1 + \\ \frac{e^2}{2(1-e^2)} \left(H_1G_5' + H_5G_1'\right) + \\ \left(\frac{e^2(16+28e^2+e^4)}{720(1-e^2)^3}\right) H_1G_1' + \frac{e^2}{2(1-e^2)} H_3G_3' - \\ \frac{e^2(4-e^2)}{24(1-e^2)^2} \left(H_3G_1' + H_1G_3'\right) = G_7'' \end{aligned} \tag{B.8}$$

$$2F_1 + H_1' = 0 \tag{B.9}$$

$$4F_3 + H_3' + \left(\frac{e^2}{1-e^2} - \frac{1}{3}\right) F_1 = 0 \tag{B.10}$$

$$6F_5 + H_5' - \left(\frac{e^2(2+e^2)}{3(1-e^2)^2} + \frac{1}{45}\right) F_1 + \left(\frac{e^2}{1-e^2} - \frac{1}{3}\right) F_3 = 0 \tag{B.11}$$

$$\begin{aligned} 8F_7 + H_7' + \left(\frac{e^2(2+11e^2+2e^4)}{15(1-e^2)^3} - \frac{2}{945}\right) F_1 - \\ \left(\frac{e^2(2+e^2)}{3(1-e^2)^2} + \frac{1}{45}\right) F_3 + \left(\frac{e^2}{1-e^2} - \frac{1}{3}\right) F_5 = 0 \end{aligned} \tag{B.12}$$

B.2 Values of quantities in the series solution for prolate spheroids

e	n	$F_n(0;e)$	$F_n'(0;e)$	$G_n(0;e)$	$G_n'(0;e)$	$H_n(\infty;e)$
0.0	1	0.00000	0.51023	1.00000	-0.61592	-0.88447
	3	0.00000	-0.22129	-0.16667	0.24764	0.16074
	5	0.00000	0.02071	0.00833	-0.02569	0.00084
	7	0.00000	-0.00189	-0.00020	0.00181	0.00085

e	n	$F_n(0;e)$	$F_n'(0;e)$	$G_n(0;e)$	$G_n'(0;e)$	$H_n(\infty;e)$
0.1	1	0.00000	0.51023	1.00000	-0.61592	-0.88447
	3	0.00000	-0.22009	-0.16667	0.24600	0.16236
	5	0.00000	0.01979	0.00833	-0.02447	0.00007
	7	0.00000	-0.00160	-0.00020	0.00147	0.00103

e	n	$F_n(0;e)$	$F_n'(0;e)$	$G_n(0;e)$	$G_n'(0;e)$	$H_n(\infty;e)$
0.2	1	0.00000	0.51023	1.00000	-0.61592	-0.88447
	3	0.00000	-0.21633	-0.16667	0.24085	0.16743
	5	0.00000	0.01684	0.00833	-0.02057	-0.00243
	7	0.00000	-0.00064	-0.00020	0.00031	0.00168

e	n	$F_n(0;e)$	$F_n'(0;e)$	$G_n(0;e)$	$G_n'(0;e)$	$H_n(\infty;e)$
0.3	1	0.00000	0.51023	1.00000	-0.61592	-0.88447
	3	0.00000	-0.20953	-0.16667	0.23153	0.17663
	5	0.00000	0.01126	0.00833	-0.01318	-0.00737
	7	0.00000	0.00138	-0.00020	-0.00219	0.00313

e	n	$F_n(0;e)$	$F_n'(0;e)$	$G_n(0;e)$	$G_n'(0;e)$	$H_n(\infty;e)$
0.4	1	0.00000	0.51023	1.00000	-0.61592	-0.88447
	3	0.00000	-0.19864	-0.16667	0.21660	0.19135
	5	0.00000	0.00175	0.00833	-0.00048	-0.01630
	7	0.00000	0.00537	-0.00020	-0.00735	0.00633

e	n	$F_n(0;e)$	$F_n'(0;e)$	$G_n(0;e)$	$G_n'(0;e)$	$H_n(\infty;e)$
0.5	1	0.00000	0.51023	1.00000	-0.61592	-0.88447
	3	0.00000	-0.18166	-0.16667	0.19332	0.21431
	5	0.00000	-0.01455	0.00833	0.02147	-0.03278
	7	0.00000	0.01373	-0.00020	-0.01858	0.01392

e	n	$F_n(0;e)$	$F_n'(0;e)$	$G_n(0;e)$	$G_n'(0;e)$	$H_n(\infty;e)$
0.6	1	0.00000	0.51023	1.00000	-0.61592	-0.88447
	3	0.00000	-0.15442	-0.16667	0.15597	0.25114
	5	0.00000	-0.04445	0.00833	0.06211	-0.06573
	7	0.00000	0.03360	-0.00020	-0.04619	0.03436

e	n	$F_n(0;e)$	$F_n'(0;e)$	$G_n(0;e)$	$G_n'(0;e)$	$H_n(\infty;e)$
0.7	1	0.00000	0.51023	1.00000	-0.61592	-0.88447
	3	0.00000	-0.10708	-0.16667	0.09107	0.31516
	5	0.00000	-0.10737	0.00833	0.14869	-0.14204
	7	0.00000	0.09208	-0.00020	-0.12947	0.10254

B.3 Comparison of profiles due to numerical and series solutions for prolate spheroids

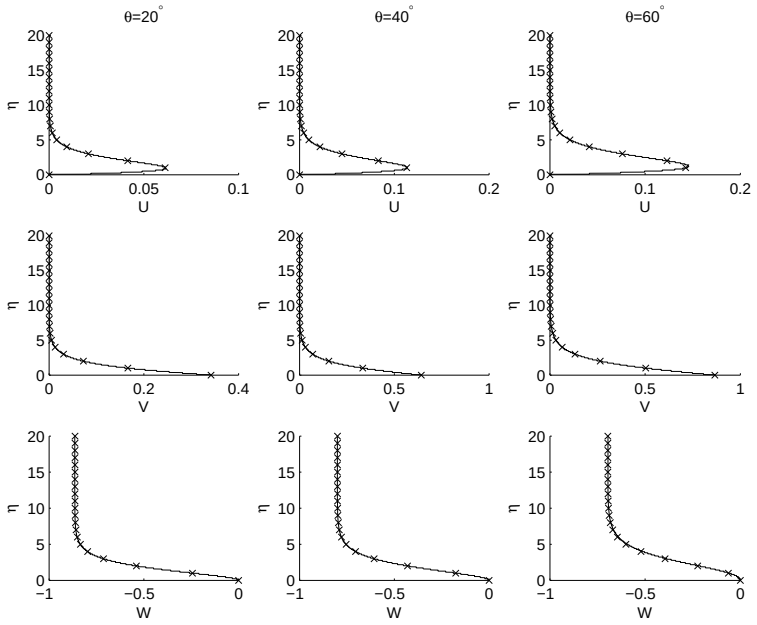

Figure B.1: Comparison of the numerical (solid line) and series solutions (cross points) at $\theta = 20°$, $40°$ $60°$ for $e = 0.3$.

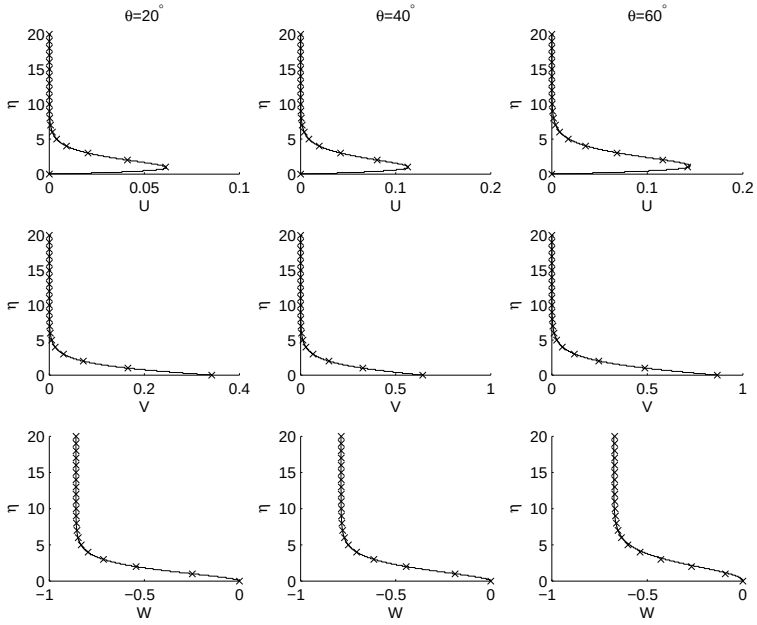

Figure B.2: Comparison of the numerical (solid line) and series solutions (cross points) at $\theta = 20°$, $40°$, $60°$ for $e = 0.5$.

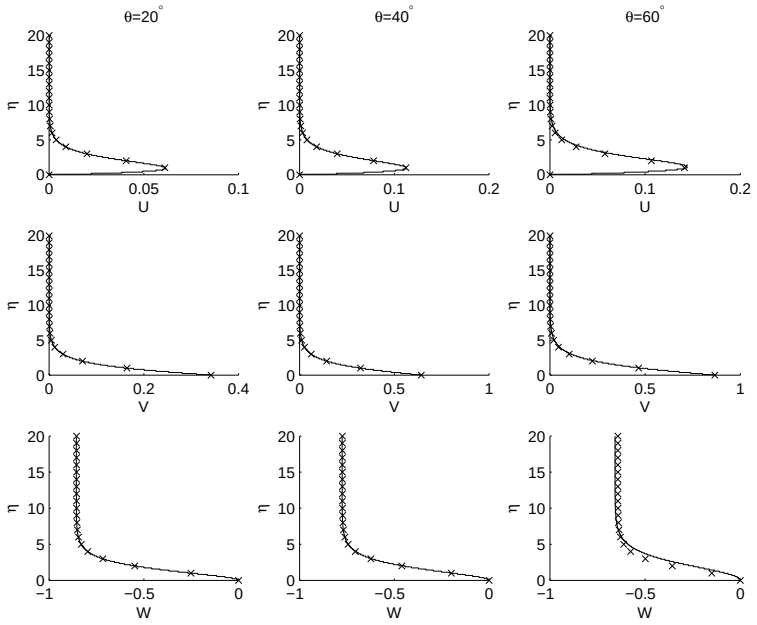

Figure B.3: Comparison of the numerical (solid line) and series solutions (cross points) at $\theta = 20°$, $40°$, $60°$ for $e = 0.6$.

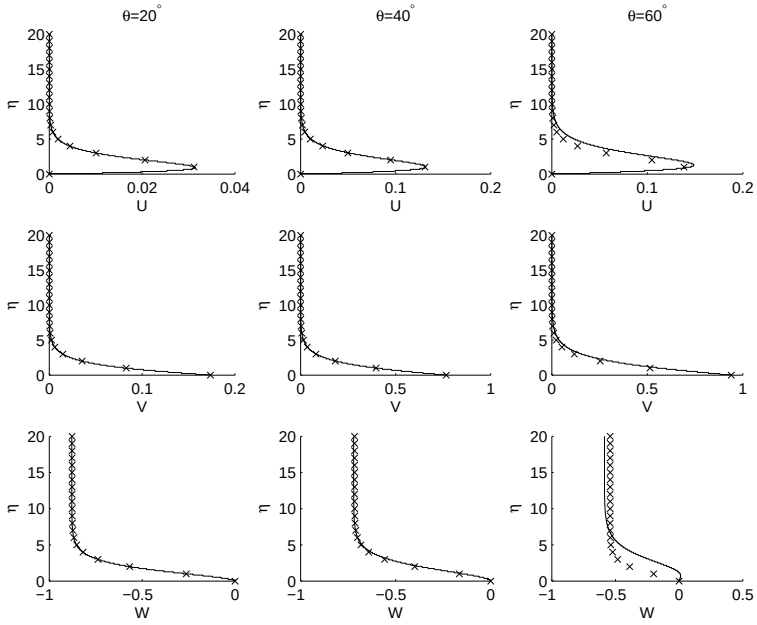

Figure B.4: Comparison of the numerical (solid line) and series solutions (cross points) at $\theta = 10°$, $50°$, $70°$ for $e = 0.6$.

Appendix C

Dimensional perturbation equations and miscellaneous neutral curves of prolate spheroid

In this Appendix we present the dimensional perturbation equations of the boundary-layer over prolate spheroids in Appendix C.1. In Appendix C.2 miscellaneous neutral curves of convective instability are presented in (R_S, n)- and (R_S, ϵ)-planes. Critical Reynolds numbers at each latitude and each value of e are shown in Appendix C.3. Finally, related to Chapter 4, some miscellaneous neutral curves and miscellaneous curves of growth rates for prolate spheroids are shown in Appendix C.4.

C.1 Dimensional perturbation equations of rotating prolate spheroids

$$\frac{\sqrt{\eta^{\star 2}-d^{\star 2}}}{\sqrt{\eta^{\star 2}-d^{\star 2}\cos^2\theta}}\frac{dw^\star}{d\eta^\star}+\left(\frac{\eta^\star\sqrt{\eta^{\star 2}-d^{\star 2}}}{(\eta^{\star 2}-d^{\star 2}\cos^2\theta)^{3/2}}\right.$$
$$\left.+\frac{\eta^\star}{\sqrt{\eta^{\star 2}-d^{\star 2}\cos^2\theta}\sqrt{\eta^{\star 2}-d^{\star 2}}}\right)w^\star+\left(\frac{d^{\star 2}\sin\theta\cos\theta}{(\eta^{\star 2}-d^{\star 2}\cos^2\theta)^{3/2}}\right.$$
$$\left.+\frac{\cot\theta}{\sqrt{\eta^{\star 2}-d^{\star 2}\cos^2\theta}}+\frac{\mathrm{i}\alpha^\star\sqrt{\eta_\circ^{\star 2}-d_\circ^{\star 2}\cos^2\theta}}{\sqrt{\eta^{\star 2}-d^{\star 2}\cos^2\theta}}\right)u^\star$$
$$+\frac{\mathrm{i}\beta^\star\sqrt{\eta_\circ^{\star 2}-d_\circ^{\star 2}}}{\sqrt{\eta^{\star 2}-d^{\star 2}}}\,v^\star\;=\;0 \tag{C.1}$$

$$\frac{\sqrt{\eta^{\star 2}-d^{\star 2}}\;W^\star}{\sqrt{\eta^{\star 2}-d^{\star 2}\cos^2\theta}}\frac{du^\star}{d\eta^\star}+\left[\mathrm{i}\left(\alpha^\star\frac{\sqrt{\eta_\circ^{\star 2}-d_\circ^{\star 2}\cos^2\theta}}{\sqrt{\eta^{\star 2}-d^{\star 2}\cos^2\theta}}U^\star+\beta^\star\frac{\sqrt{\eta_\circ^{\star 2}-d_\circ^{\star 2}}}{\sqrt{\eta^{\star 2}-d^{\star 2}}}V^\star\right.\right.$$
$$\left.\left.-\gamma^\star\right)+\frac{1}{\sqrt{\eta^{\star 2}-d^{\star 2}\cos^2\theta}}\frac{\partial U^\star}{\partial\theta}+\frac{\eta^\star\sqrt{\eta^{\star 2}-d^{\star 2}}}{(\eta^{\star 2}-d^{\star 2}\cos^2\theta)^{3/2}}W^\star\right]\;u^\star$$
$$-\frac{2V^\star\cot\theta}{\sqrt{\eta^{\star 2}-d^{\star 2}\cos^2\theta}}v^\star+\left(\frac{\eta^\star\sqrt{\eta^{\star 2}-d^{\star 2}}U^\star}{(\eta^{\star 2}-d^{\star 2}\cos^2\theta)^{3/2}}-\frac{2d^{\star 2}\sin\theta\cos\theta\;W^\star}{(\eta^{\star 2}-d^{\star 2}\cos^2\theta)^{3/2}}\right.$$
$$\left.+\frac{\sqrt{\eta^{\star 2}-d^{\star 2}}}{\sqrt{\eta^{\star 2}-d^{\star 2}\cos^2\theta}}\frac{\partial U^\star}{\partial\eta^\star}\right)w^\star\;=\;\frac{-\mathrm{i}\alpha^\star\sqrt{\eta_\circ^{\star 2}-d_\circ^{\star 2}\cos^2\theta}\;p^\star}{\rho^\star\sqrt{\eta^{\star 2}-d^{\star 2}\cos^2\theta}}$$
$$+\nu^\star\left[\left(\frac{\eta^{\star 2}-d^{\star 2}}{\eta^{\star 2}-d^{\star 2}\cos^2\theta}\right)\frac{d^2u^\star}{d\eta^{\star 2}}+\frac{2\eta^\star}{(\eta^{\star 2}-d^{\star 2}\cos^2\theta)}\frac{du^\star}{d\eta^\star}\right.$$
$$+\left\{-\left(\alpha^{\star 2}\frac{\eta_\circ^{\star 2}-d_\circ^{\star 2}\cos^2\theta}{\eta^{\star 2}-d^{\star 2}\cos^2\theta}+\beta^{\star 2}\frac{\eta_\circ^{\star 2}-d_\circ^{\star 2}}{\eta^{\star 2}-d^{\star 2}}\right)+\mathrm{i}\alpha^\star\left(\frac{\sqrt{\eta_\circ^{\star 2}-d_\circ^{\star 2}\cos^2\theta}}{(\eta^{\star 2}-d^{\star 2}\cos^2\theta)}\cot\theta\right.\right.$$
$$\left.+\frac{d_\circ^{\star 2}\sin\theta\cos\theta}{(\eta^{\star 2}-d^{\star 2}\cos^2\theta)\sqrt{\eta_\circ^{\star 2}-d_\circ^{\star 2}\cos^2\theta}}\right)+\frac{3\eta^{\star 2}-d^{\star 2}(1+\sin^2\theta)}{(\eta^{\star 2}-d^{\star 2}\cos^2\theta)^2}$$
$$\left.-\frac{3\eta^{\star 2}(\eta^{\star 2}-d^{\star 2})}{(\eta^{\star 2}-d^{\star 2}\cos^2\theta)^3}-\frac{3d^{\star 4}\sin^2\theta\cos^2\theta}{(\eta^{\star 2}-d^{\star 2}\cos^2\theta)^3}-\frac{\csc^2\theta}{(\eta^{\star 2}-d^{\star 2}\cos^2\theta)}\right\}u^\star$$
$$-\frac{2d^{\star 2}\sqrt{\eta^{\star 2}-d^{\star 2}}\sin\theta\cos\theta}{(\eta^{\star 2}-d^{\star 2}\cos^2\theta)^2}\frac{dw^\star}{d\eta^\star}-\frac{2\mathrm{i}\beta^\star\sqrt{\eta_\circ^{\star 2}-d_\circ^{\star 2}}\cot\theta}{\sqrt{\eta^{\star 2}-d^{\star 2}}\sqrt{\eta^{\star 2}-d^{\star 2}\cos^2\theta}}\;v^\star$$

$$+\left(2\mathrm{i}\alpha^\star\frac{\eta^\star\sqrt{\eta^{\star2}-d^{\star2}}\sqrt{\eta_\circ^{\star2}-d_\circ^{\star2}\cos^2\theta}}{(\eta^{\star2}-d^{\star2}\cos^2\theta)^2}\right.$$
$$\left.-\frac{2d^{\star2}\eta^\star\sin\theta\cos\theta}{\sqrt{\eta^{\star2}-d^{\star2}}(\eta^{\star2}-d^{\star2}\cos^2\theta)^2}\right)w^\star\Bigg] \tag{C.2}$$

$$\frac{\sqrt{\eta^{\star2}-d^{\star2}}W^\star}{\sqrt{\eta^{\star2}-d^{\star2}\cos^2\theta}}\frac{dv^\star}{d\eta^\star}+\Bigg[\mathrm{i}\Bigg(\alpha^\star\frac{\sqrt{\eta_\circ^{\star2}-d_\circ^{\star2}\cos^2\theta}}{\sqrt{\eta^{\star2}-d^{\star2}\cos^2\theta}}U^\star+\beta^\star\frac{\sqrt{\eta_\circ^{\star2}-d_\circ^{\star2}}}{\sqrt{\eta^{\star2}-d^{\star2}}}V^\star$$
$$-\gamma^\star\Bigg)+\frac{U^\star\cot\theta}{\sqrt{\eta^{\star2}-d^{\star2}\cos^2\theta}}+\frac{\eta^\star}{\sqrt{\eta^{\star2}-d^{\star2}}\sqrt{\eta^{\star2}-d^{\star2}\cos^2\theta}}W^\star\Bigg]\,v^\star$$
$$+\left(\frac{V^\star\cot\theta}{\sqrt{\eta^{\star2}-d^{\star2}\cos^2\theta}}+\frac{1}{\sqrt{\eta^{\star2}-d^{\star2}\cos^2\theta}}\frac{\partial V^\star}{\partial\theta}\right)u^\star+\left(\frac{\sqrt{\eta^{\star2}-d^{\star2}}}{\sqrt{\eta^{\star2}-d^{\star2}\cos^2\theta}}\frac{\partial V^\star}{\partial\eta^\star}\right.$$
$$\left.+\frac{\eta^\star}{\sqrt{\eta^{\star2}-d^{\star2}}\sqrt{\eta^{\star2}-d^{\star2}\cos^2\theta}}V^\star\right)w^\star\;=\;\frac{-\mathrm{i}\beta^\star\sqrt{\eta_\circ^{\star2}-d_\circ^{\star2}}}{\rho^\star\sqrt{\eta^{\star2}-d^{\star2}}}\;p^\star$$
$$+\nu^\star\Bigg[\left(\frac{\eta^{\star2}-d^{\star2}}{\eta^{\star2}-d^{\star2}\cos^2\theta}\right)\frac{d^2v^\star}{d\eta^{\star2}}+\frac{2\eta^\star}{(\eta^{\star2}-d^{\star2}\cos^2\theta)}\frac{dv^\star}{d\eta^\star}$$
$$+\Bigg\{-\left(\alpha^{\star2}\frac{\eta_\circ^{\star2}-d_\circ^{\star2}\cos^2\theta}{\eta^{\star2}-d^{\star2}\cos^2\theta}+\beta^{\star2}\frac{\eta_\circ^{\star2}-d_\circ^{\star2}}{\eta^{\star2}-d^{\star2}}\right)+\mathrm{i}\alpha^\star\Bigg(\frac{\sqrt{\eta_\circ^{\star2}-d_\circ^{\star2}\cos^2\theta}}{(\eta^{\star2}-d^{\star2}\cos^2\theta)}\cot\theta$$
$$+\frac{d_\circ^{\star2}\sin\theta\cos\theta}{(\eta^{\star2}-d^{\star2}\cos^2\theta)\sqrt{\eta_\circ^{\star2}-d_\circ^{\star2}\cos^2\theta}}\Bigg)-\frac{\cot^2\theta}{(\eta^{\star2}-d^{\star2}\cos^2\theta)}$$
$$-\frac{\eta^{\star2}}{(\eta^{\star2}-d^{\star2})(\eta^{\star2}-d^{\star2}\cos^2\theta)}\Bigg\}v^\star+\frac{2\mathrm{i}\beta^\star\sqrt{\eta_\circ^{\star2}-d_\circ^{\star2}}}{\sqrt{\eta^{\star2}-d^{\star2}}\sqrt{\eta^{\star2}-d^{\star2}\cos^2\theta}}\cot\theta\;u^\star$$
$$+2\mathrm{i}\beta^\star\frac{\eta^\star\sqrt{\eta_\circ^{\star2}-d_\circ^{\star2}}}{(\eta^{\star2}-d^{\star2})\sqrt{\eta^{\star2}-d^{\star2}\cos^2\theta}}\;w^\star \tag{C.3}$$

$$\frac{\sqrt{\eta^{\star2}-d^{\star2}}\;W^\star}{\sqrt{\eta^{\star2}-d^{\star2}\cos^2\theta}}\frac{dw^\star}{d\eta^\star}+\Bigg[\mathrm{i}\Bigg(\alpha^\star\frac{\sqrt{\eta_\circ^{\star2}-d_\circ^{\star2}\cos^2\theta}}{\sqrt{\eta^{\star2}-d^{\star2}\cos^2\theta}}U^\star+\beta^\star\frac{\sqrt{\eta_\circ^{\star2}-d_\circ^{\star2}}}{\sqrt{\eta^{\star2}-d^{\star2}}}V^\star$$
$$-\gamma^\star\Bigg)+\frac{\sqrt{\eta^{\star2}-d^{\star2}}}{\sqrt{\eta^{\star2}-d^{\star2}\cos^2\theta}}\frac{\partial W^\star}{\partial\eta^\star}+\frac{d^{\star2}\cos\theta\sin\theta}{(\eta^{\star2}-d^{\star2}\cos^2\theta)^{3/2}}U^\star\Bigg]\;w^\star$$
$$+\Bigg(\frac{1}{\sqrt{\eta^{\star2}-d^{\star2}\cos^2\theta}}\frac{\partial W^\star}{\partial\theta}-\frac{2\eta^\star\sqrt{\eta^{\star2}-d^{\star2}}}{(\eta^{\star2}-d^{\star2}\cos^2\theta)^{3/2}}U^\star$$
$$+\frac{d^{\star2}\cos\theta\sin\theta\;W^\star}{(\eta^{\star2}-d^{\star2}\cos^2\theta)^{3/2}}\Bigg)u^\star-\frac{2\eta^\star V^\star}{\sqrt{\eta^{\star2}-d^{\star2}}\sqrt{\eta^{\star2}-d^{\star2}\cos^2\theta}}v^\star$$
$$=\frac{-\sqrt{\eta^{\star2}-d^{\star2}}}{\rho^\star\sqrt{\eta^{\star2}-d^{\star2}\cos^2\theta}}\frac{dp^\star}{d\eta^\star}+\nu^\star\Bigg[\left(\frac{\eta^{\star2}-d^{\star2}}{\eta^{\star2}-d^{\star2}\cos^2\theta}\right)\frac{d^2w^\star}{d\eta^{\star2}}$$

$$
\begin{aligned}
&+\frac{2\eta^{\star}}{(\eta^{\star 2}-d^{\star 2}\cos^2\theta)}\frac{dw^{\star}}{d\eta^{\star}}+\Bigg\{-\left(\alpha^{\star 2}\frac{\eta_{\circ}^{\star 2}-d_{\circ}^{\star 2}\cos^2\theta}{\eta^{\star 2}-d^{\star 2}\cos^2\theta}+\beta^{\star 2}\frac{\eta_{\circ}^{\star 2}-d_{\circ}^{\star 2}}{\eta^{\star 2}-d^{\star 2}}\right)\\
&+\mathrm{i}\alpha^{\star}\left(\frac{\sqrt{\eta_{\circ}^{\star 2}-d_{\circ}^{\star 2}\cos^2\theta}}{(\eta^{\star 2}-d^{\star 2}\cos^2\theta)}\cot\theta+\frac{d_{\circ}^{\star 2}\sin\theta\cos\theta}{(\eta^{\star 2}-d^{\star 2}\cos^2\theta)\sqrt{\eta_{\circ}^{\star 2}-d_{\circ}^{\star 2}\cos^2\theta}}\right)\\
&+\frac{1}{\eta^{\star 2}-d^{\star 2}\cos^2\theta}-\frac{\eta^{\star 2}}{(\eta^{\star 2}-d^{\star 2})(\eta^{\star 2}-d^{\star 2}\cos^2\theta)}+\frac{(\eta^{\star 2}-d^{\star 2})}{(\eta^{\star 2}-d^{\star 2}\cos^2\theta)^2}\\
&-\frac{3\eta^{\star 2}(\eta^{\star 2}-d^{\star 2})}{(\eta^{\star 2}-d^{\star 2}\cos^2\theta)^3}-\frac{d^{\star 2}(3\sin^2\theta-2)}{(\eta^{\star 2}-d^{\star 2}\cos^2\theta)^2}-\frac{3d^{\star 4}\sin^2\theta\cos^2\theta}{(\eta^{\star 2}-d^{\star 2}\cos^2\theta)^3}\Bigg\}w^{\star}\\
&+\frac{2d^{\star 2}\sqrt{\eta^{\star 2}-d^{\star 2}}\cos\theta\sin\theta}{(\eta^{\star 2}-d^{\star 2}\cos^2\theta)^2}\frac{du^{\star}}{d\eta^{\star}}-\Bigg(\frac{2\mathrm{i}\alpha^{\star}\eta^{\star}\sqrt{\eta_{\circ}^{\star 2}-d_{\circ}^{\star 2}\cos^2\theta}\sqrt{\eta^{\star 2}-d^{\star 2}}}{(\eta^{\star 2}-d^{\star 2}\cos^2\theta)^2}\\
&+\frac{2\cot\theta\eta^{\star}\sqrt{\eta^{\star 2}-d^{\star 2}}}{(\eta^{\star 2}-d^{\star 2}\cos^2\theta)^2}\Bigg)u^{\star}-\frac{2\mathrm{i}\beta^{\star}\eta^{\star}\sqrt{\eta_{\circ}^{\star 2}-d_{\circ}^{\star 2}}}{(\eta\star^2-d^{\star 2})\sqrt{\eta^{\star 2}-d^{\star 2}\cos^2\theta}}v^{\star}\Bigg]
\end{aligned}
\tag{C.4}
$$

C.2 The nuetral curves of convective instability for rotating prolate spheroids in terms of spin Reynolds numbers

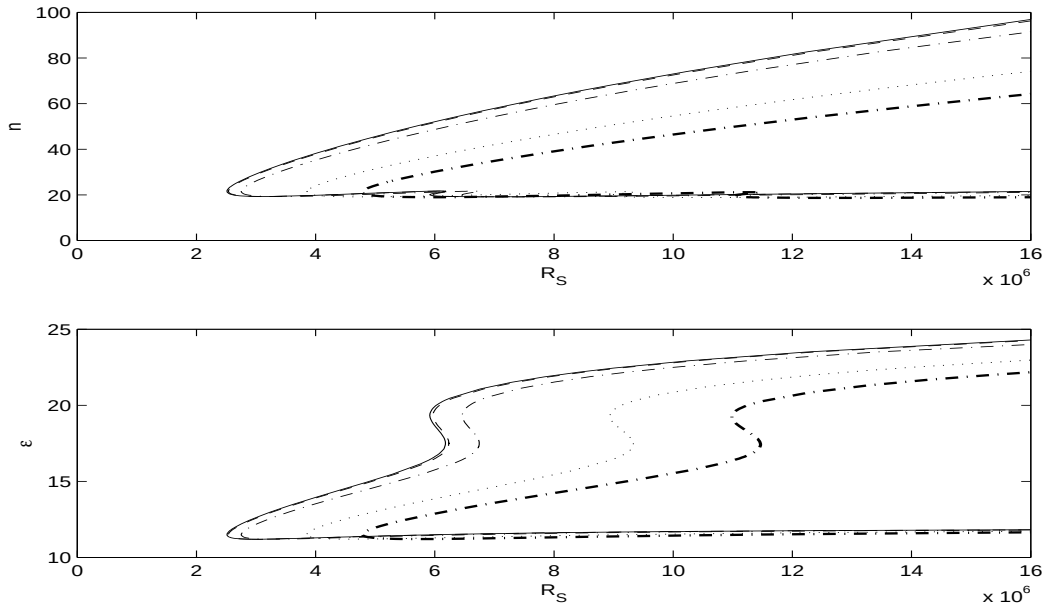

Figure C.1: Neutral curves in (R_S, n)- and (R_S, ϵ)-planes at latitude 10° for $e = 0$(–), 0.1 (-.), 0.3(−−), 0.6 (· · ·) & 0.7 (**-.**)

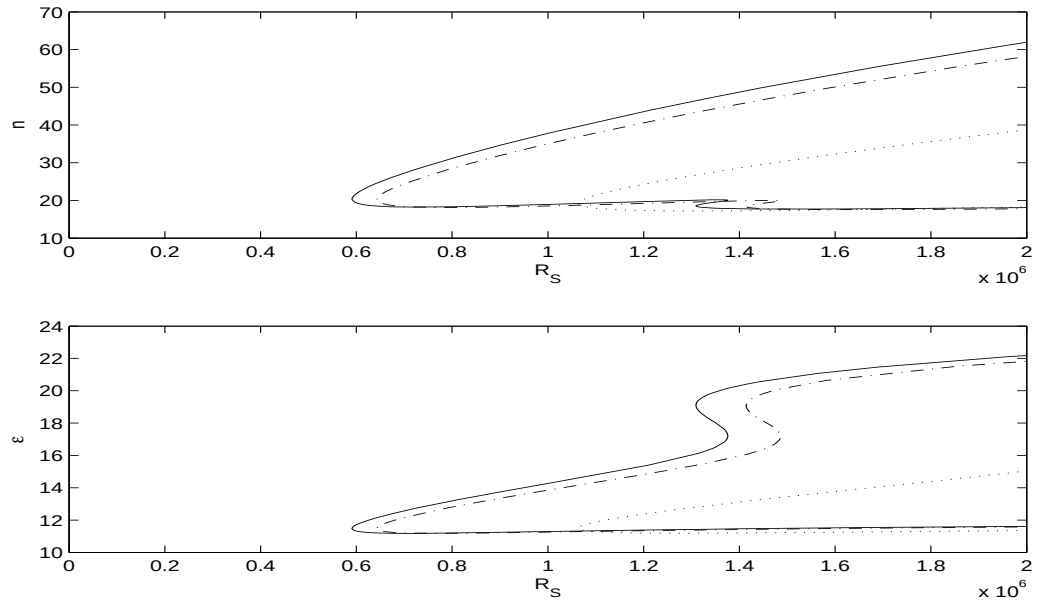

Figure C.2: Neutral curves in (R_S, n)- and (R_S, ϵ)-planes at latitude 20° for $e = 0$(–), 0.3 (-.) & 0.7 (· · ·)

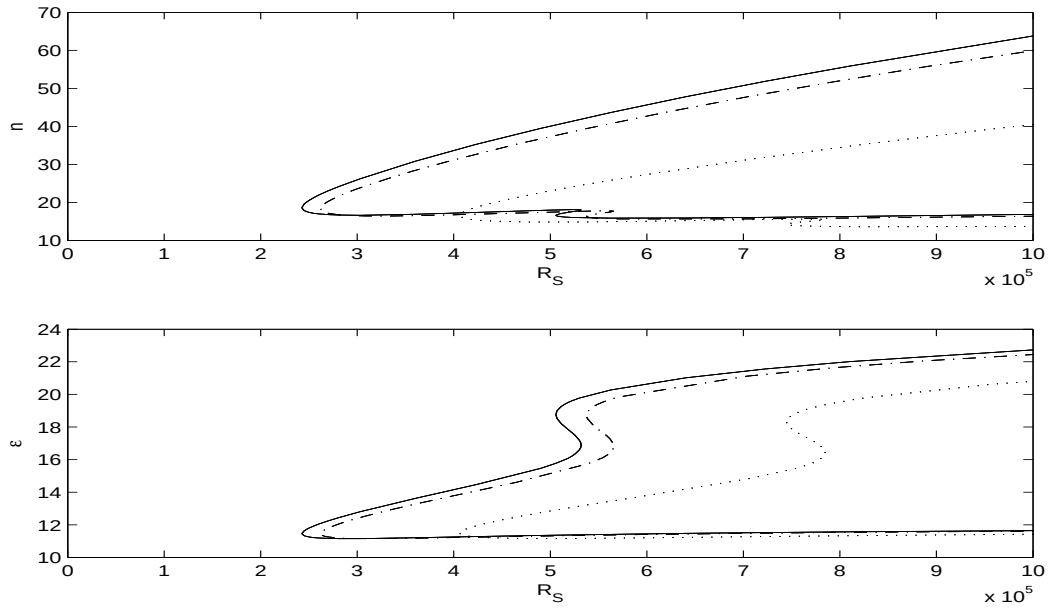

Figure C.3: Neutral curves in (R_S, n)- and (R_S, ϵ)-planes at latitude 30° for $e = 0$(–), 0.3 (-.) & 0.7 ($\cdots$)

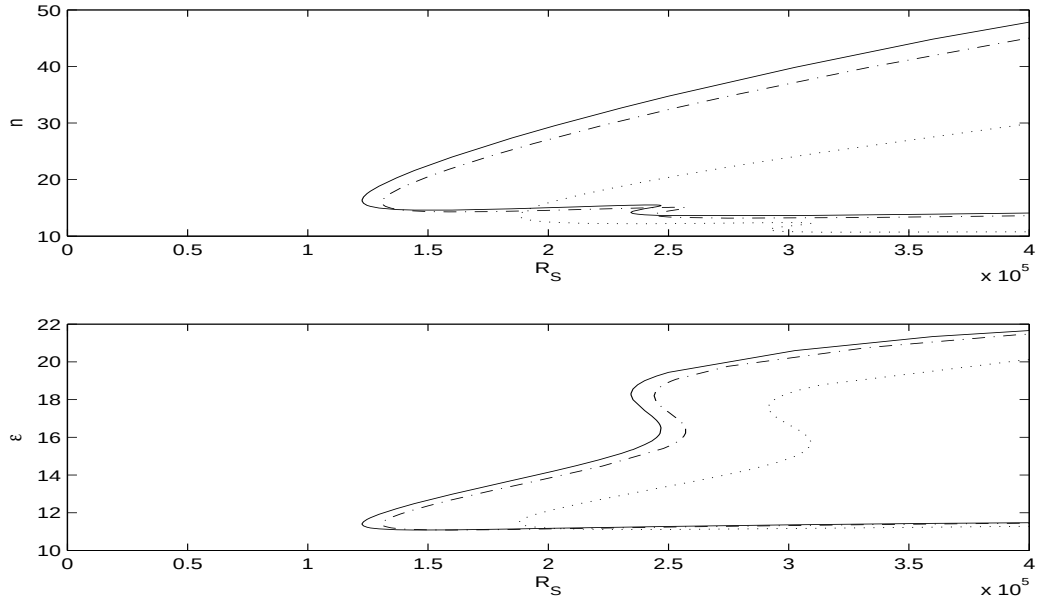

Figure C.4: Neutral curves in (R_S, n)- and (R_S, ϵ)-planes at latitude 40° for $e = 0$(–), 0.3 (-.) & 0.7 ($\cdots$)

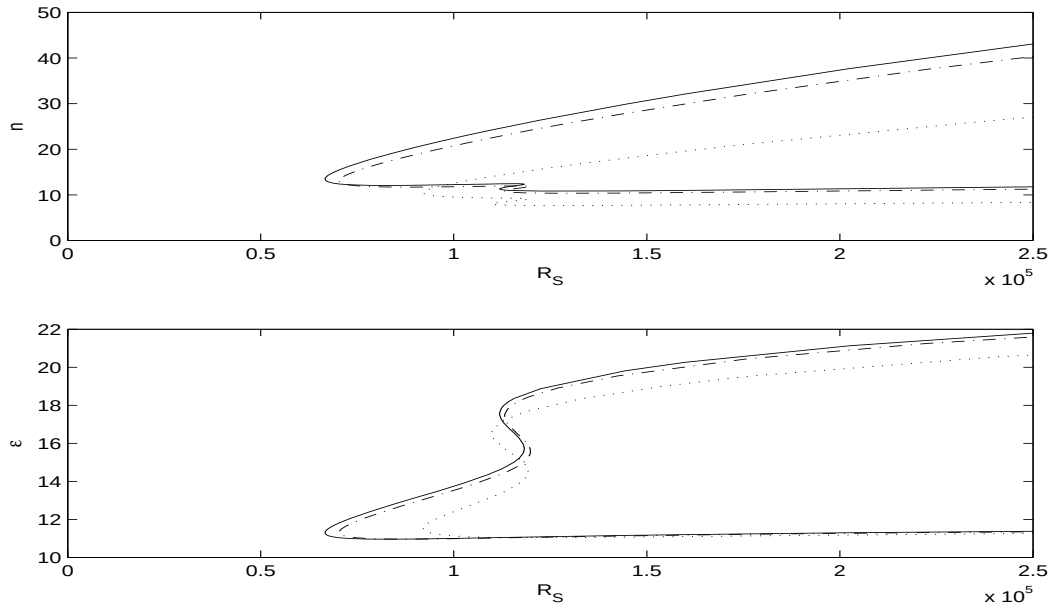

Figure C.5: Neutral curves in (R_S, n)- and (R_S, ϵ)-planes at latitude 50° for $e = 0$(–), 0.3 (-.) & 0.7 ($\cdots$)

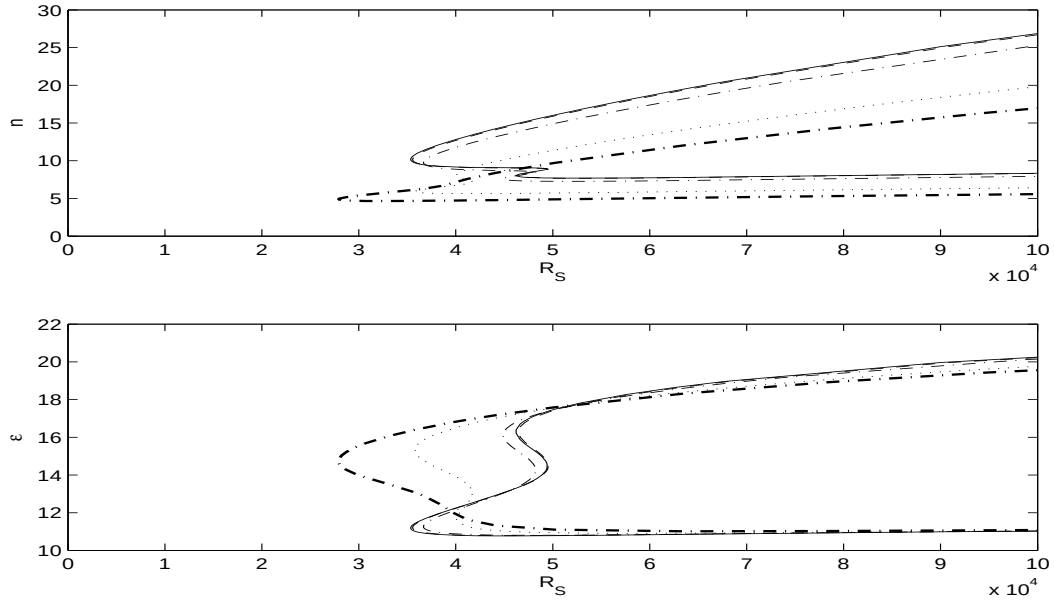

Figure C.6: Neutral curves in (R_S, n)- and (R_S, ϵ)-planes at latitude 60° for $e = 0$(–), 0.1 (-.), 0.3(––), 0.6 ($\cdots$) & 0.7 (**-.**)

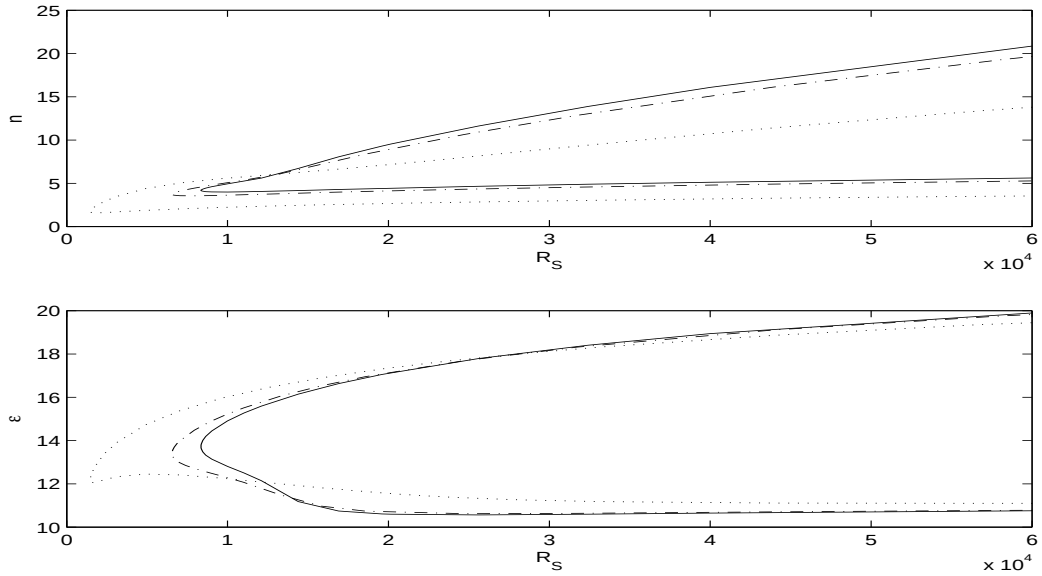

Figure C.7: Neutral curves in (R_S, n)- and (R_S, ϵ)-planes at latitude 70° for $e = 0$(–), 0.3 (-.) & 0.7 ($\cdots$)

C.3 Critical Reynolds numbers for prolate spheroids

e	θ	R_I	R_{II}	R_{SI}	R_{SII}
0.0	10	1585.3	2432.5	2.51×10^6	5.92×10^6
0.0	20	768.8	1144.3	5.91×10^5	1.31×10^6
0.0	30	492.9	711.2	2.43×10^5	5.06×10^5
0.0	40	350.1	484.2	1.23×10^5	2.34×10^5
0.0	50	258.3	334.5	6.67×10^4	1.12×10^5
0.0	60	188.0	215.0	3.53×10^4	4.62×10^4
0.0	70	-	91.4	-	8.35×10^3

Table C.1: The critical Reynolds numbers R and R_S for the onset of stationary ($c = 1$) crossflow (type I) and streamline curvature (type II) modes of convective instability for $e = 0.0$, - indicates that a crossflow lobe is not seen.

e	θ	R_I	R_{II}	R_{SI}	R_{SII}
0.1	10	1585.0	2431.4	2.54×10^6	5.97×10^6
0.1	20	768.4	1143.2	5.96×10^5	1.32×10^6
0.1	30	492.5	710.1	2.45×10^5	5.09×10^5
0.1	40	349.6	482.9	1.23×10^5	2.35×10^5
0.1	50	257.5	332.4	6.70×10^4	1.12×10^5
0.1	60	187.6	214.5	3.55×10^4	4.65×10^4
0.1	70	-	89.9	-	8.16×10^3

Table C.2: The critical Reynolds numbers R and R_S for the onset of stationary ($c = 1$) crossflow (type I) and streamline curvature (type II) modes of convective instability for $e = 0.1$, - indicates that a crossflow lobe is not seen.

e	θ	R_I	R_{II}	R_{SI}	R_{SII}
0.2	10	1584.1	2429.4	2.61×10^6	6.15×10^6
0.2	20	767.2	1140.0	6.13×10^5	1.35×10^6
0.2	30	491.1	706.3	2.51×10^5	5.20×10^5
0.2	40	348.0	478.7	1.26×10^5	2.39×10^5
0.2	50	256.0	328.7	6.83×10^4	1.13×10^5
0.2	60	185.8	210.0	3.60×10^4	4.59×10^4
0.2	70	-	85.2	-	7.56×10^3

Table C.3: The critical Reynolds numbers R and R_S for the onset of stationary ($c = 1$) crossflow (type I) and streamline curvature (type II) modes of convective instability for $e = 0.2$, - indicates that a crossflow lobe is not seen.

e	θ	R_I	R_{II}	R_{SI}	R_{SII}
0.3	10	1582.6	2424.8	2.75×10^6	6.46×10^6
0.3	20	765.1	1134.4	6.43×10^5	1.41×10^6
0.3	30	488.5	699.6	2.62×10^5	5.38×10^5
0.3	40	345.1	471.3	1.31×10^5	2.44×10^5
0.3	50	252.9	320.9	7.03×10^4	1.13×10^5
0.3	60	182.7	202.2	3.67×10^4	4.49×10^4
0.3	70	-	77.3	-	6.56×10^3

Table C.4: The critical Reynolds numbers R and R_S for the onset of stationary ($c = 1$) crossflow (type I) and streamline curvature (type II) modes of convective instability for $e = 0.3$, - indicates that a crossflow lobe is not seen.

e	θ	R_I	R_{II}	R_{SI}	R_{SII}
0.4	10	1580.2	2418.0	2.97×10^6	6.96×10^6
0.4	20	761.8	1125.5	6.91×10^5	1.51×10^6
0.4	30	484.5	689.3	2.79×10^5	5.66×10^5
0.4	40	340.7	460.0	1.38×10^5	2.52×10^5
0.4	50	248.3	309.4	7.34×10^4	1.14×10^5
0.4	60	177.8	190.5	3.77×10^4	4.32×10^4
0.4	70	-	66.1	-	5.20×10^3

Table C.5: The critical Reynolds numbers R and R_S for the onset of stationary ($c = 1$) crossflow (type I) and streamline curvature (type II) modes of convective instability for $e = 0.4$, - indicates that a crossflow lobe is not seen.

e	θ	R_I	R_{II}	R_{SI}	R_{SII}
0.5	10	1576.6	2407.8	3.31×10^6	7.73×10^6
0.5	20	756.7	1112.1	7.63×10^5	1.65×10^6
0.5	30	473.8	658.5	2.99×10^5	5.78×10^5
0.5	40	334.1	443.7	1.49×10^5	2.62×10^5
0.5	50	241.4	292.9	7.77×10^4	1.14×10^5
0.5	60	170.7	174.0	3.89×10^4	4.04×10^4
0.5	70	-	52.5	-	3.68×10^3

Table C.6: The critical Reynolds numbers R and R_S for the onset of stationary ($c = 1$) crossflow (type I) and streamline curvature (type II) modes of convective instability for $e = 0.5$, - indicates that a crossflow lobe is not seen.

e	θ	R_I	R_{II}	R_{SI}	R_{SII}
0.6	10	1570.8	2391.9	3.86×10^6	8.94×10^6
0.6	20	749.0	1092.0	8.77×10^5	1.86×10^6
0.6	30	469.5	651.2	3.44×10^5	6.63×10^5
0.6	40	324.5	420.3	1.64×10^5	2.76×10^5
0.6	50	231.7	269.8	8.38×10^4	1.14×10^5
0.6	60	160.2	152.0	4.01×10^4	3.61×10^4
0.6	70	-	38.7	-	2.34×10^3

Table C.7: The critical Reynolds numbers R and R_S for the onset of stationary ($c = 1$) crossflow (type I) and streamline curvature (type II) modes of convective instability for $e = 0.6$, - indicates that a crossflow lobe is not seen.

e	θ	R_I	R_{II}	R_{SI}	R_{SII}
0.7	10	1561.8	2366.9	4.78×10^6	1.10×10^7
0.7	20	736.7	1059.9	1.06×10^6	2.20×10^6
0.7	30	455.3	616.4	4.06×10^5	7.45×10^5
0.7	40	309.6	400.0	1.88×10^5	3.14×10^5
0.7	50	216.8	247.0	9.21×10^4	1.20×10^5
0.7	60	-	119.4	-	2.79×10^4
0.7	70	-	27.4	-	1.47×10^3

Table C.8: The critical Reynolds numbers R and R_S for the onset of stationary ($c = 1$) crossflow (type I) and streamline curvature (type II) modes of convective instability for $e = 0.7$, - indicates that a crossflow lobe is not seen.

C.4 Miscellaneous neutral curves and growth rates of prolate spheroids

Here we show the neutral curves and growth rates for traveling disturbances at various latitudes and various values of eccentricity of prolate spheroid, which are related to Chapter 4.

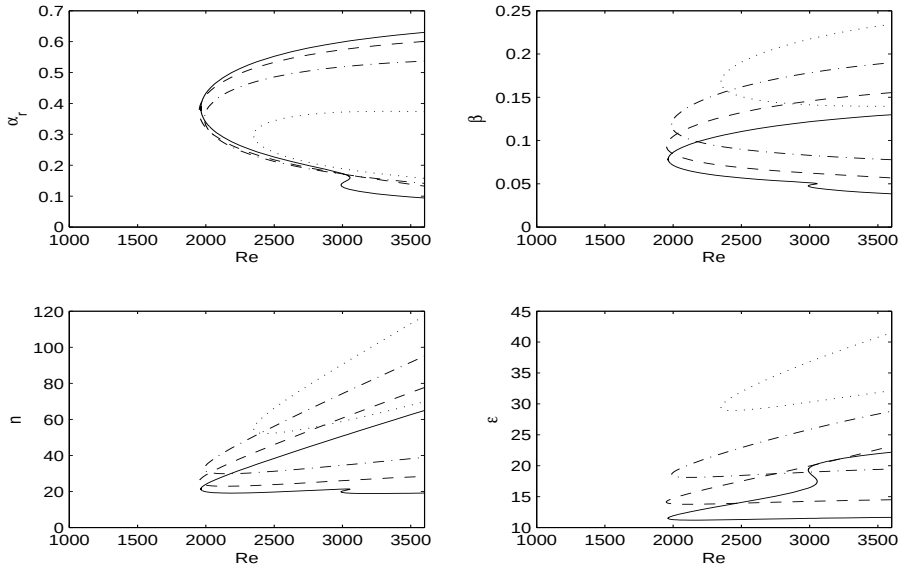

Figure C.8: Neutral curves for traveling disturbances with c=0.7 ($\cdots$), 0.8 (-.), 0.9 ($--$), 1.0 (–) at $\theta = 10°$ for $e = 0.6$.

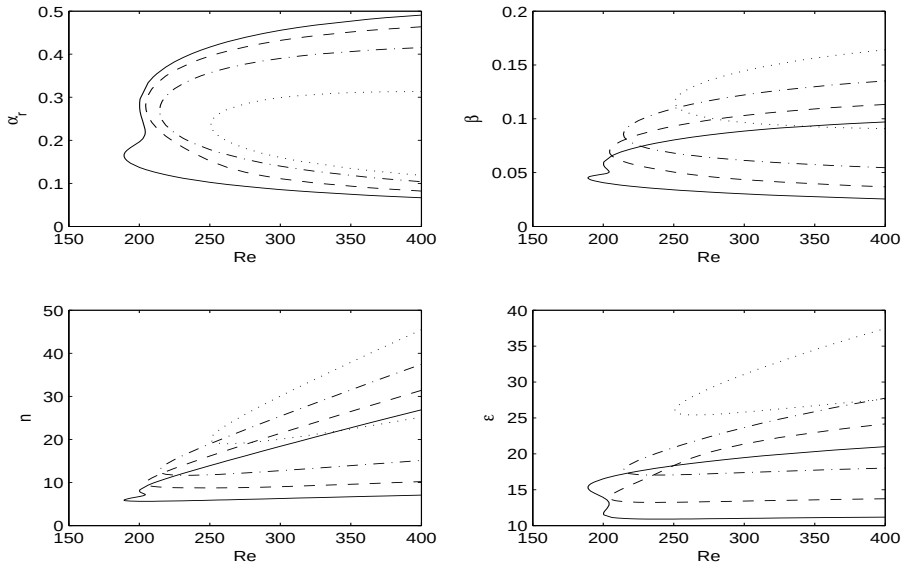

Figure C.9: Neutral curves for traveling disturbances with c=0.7 ($\cdots$), 0.8 (-.), 0.9 ($--$), 1.0 (–) at $\theta = 60°$ for $e = 0.6$.

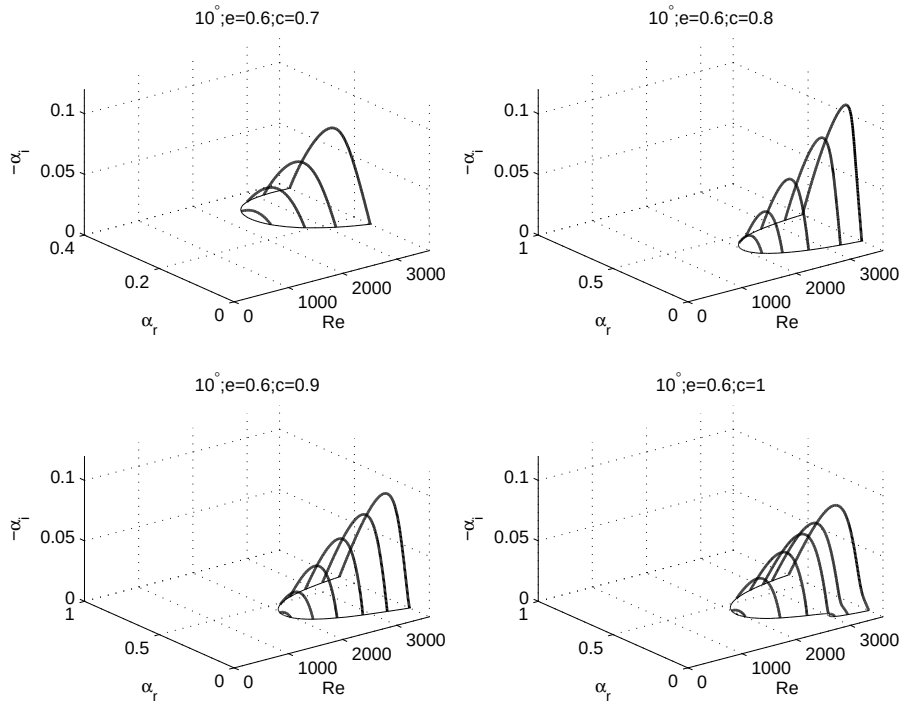

Figure C.10: Linear convective growth rates for travelling-mode disturbances with $c = 0.7$–1 for $\theta = 10°, e = 0.6$.

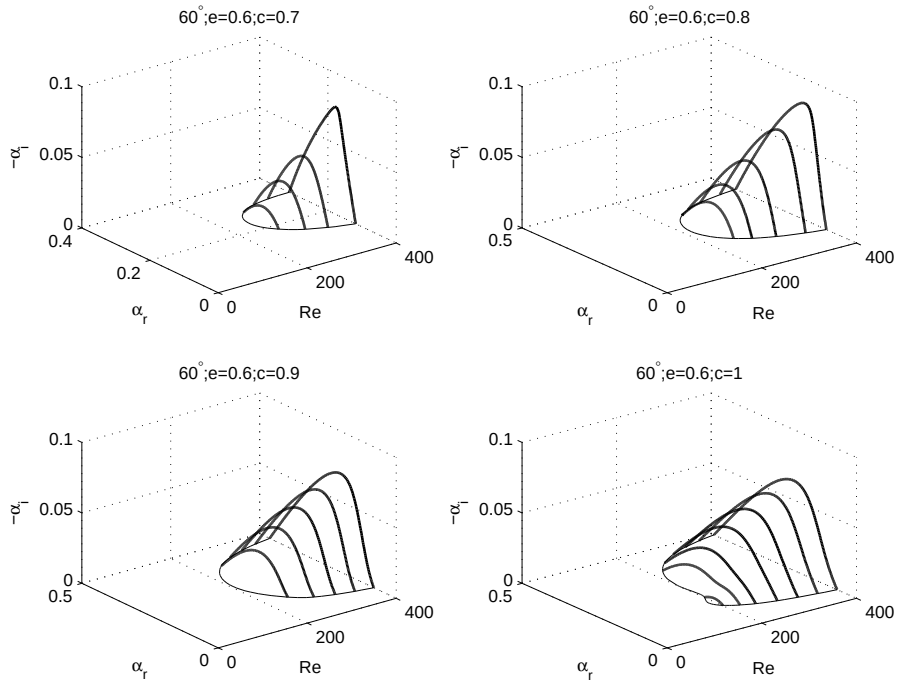

Figure C.11: Linear convective growth rates for travelling-mode disturbances with $c = 0.7$–1 for $\theta = 60°, e = 0.6$.

Appendix D

Series solution and comparisons of flow profiles of the laminar boundary-layer of oblate spheroid

This Appendix is related to Chapter 5. In Appendix D.1 we present the series solution to the laminar boundary layer equations of rotating oblate spheroid. Values of quantities $F_n'(0)$, $G_n'(0)$, $H_n(\infty)$ for n=1,3,5,7 are presented in Appendix D.2. In Appendix D.3 comparison of flow profiles due to the numerical and series solutions are shown at various latitudes and eccentricities.

D.1 Details of the series solution for the oblate family

$$F_1^2 + \sqrt{1-e^2}H_1F_1' - G_1^2 = (1-e^2)F_1'' \quad \text{(D.1)}$$

$$4F_1F_3 + \sqrt{1-e^2}\,(H_1F_3' + H_3F_1') - 2G_1G_3 + \left(\frac{1}{3} + \frac{e^2}{2}\right)G_1^2 - \frac{e^2}{2}\left(F_1^2 + \sqrt{1-e^2}H_1F_1'\right) = (1-e^2)F_3'' \quad \text{(D.2)}$$

$$6F_1F_5 + 3F_3^2 + \sqrt{1-e^2}(H_1F_5' + H_3F_3' + H_5F_1') - 2G_1G_5 - G_3^2 + \left(\frac{2}{3} + e^2\right)G_1G_3 + \left(\frac{1}{45} - \frac{e^2}{3} + \frac{e^4}{8}\right)G_1^2 + \left(\frac{e^2}{6} - \frac{e^4}{8}\right)\left(F_1^2 + \sqrt{1-e^2}H_1F_1'\right) - \frac{e^2}{2}\left(4F_1F_3 + \sqrt{1-e^2}\,(H_1F_3' + H_3F_1')\right) = (1-e^2)F_5'' \quad \text{(D.3)}$$

$$8F_1F_7 + 8F_3F_5 + \sqrt{1-e^2}\,(H_1F_7' + H_3F_5' + H_5F_3' + H_7F_1') - 2G_1G_7 - 2G_3G_5 + \left(\frac{e^2}{2} + \frac{1}{3}\right)G_3^2 + \left(\frac{2}{3} + e^2\right)G_1G_5 + \left(\frac{2}{45} - \frac{2e^2}{3} + \frac{e^4}{4}\right)G_1G_3 + \left(\frac{2}{945} + \frac{e^2}{15} - \frac{e^4}{8} + \frac{e^6}{16}\right)G_1^2 + \left(\frac{-e^2}{45} + \frac{e^4}{12} - \frac{e^6}{16}\right)\left(F_1^2 + \sqrt{1-e^2}H_1F_1'\right) + \left(\frac{e^2}{6} - \frac{e^4}{8}\right)\left(4F_1F_3 + \sqrt{1-e^2}\,(H_1F_3' + H_3F_1')\right) - \frac{e^2}{2}\left(6F_1F_5 + 3F_3^2 + \sqrt{1-e^2}\,(H_1F_5' + H_3F_3' + H_5F_1')\right) = (1-e^2)F_7'' \quad \text{(D.4)}$$

$$2F_1G_1 + \sqrt{1-e^2}H_1G_1' = (1-e^2)G_1'' \tag{D.5}$$

$$4F_1G_3 + 2F_3G_1 + \sqrt{1-e^2}\,(H_1G_3' + H_3G_1') - \left(e^2 + \frac{1}{3}\right)F_1G_1 - \frac{e^2\sqrt{1-e^2}}{2}H_1G_1' = (1-e^2)G_3'' \tag{D.6}$$

$$6F_1G_5 + 4F_3G_3 + 2F_5G_1 + \sqrt{1-e^2}\,(H_1G_5' + H_3G_3' + H_5G_1') - \left(2e^2 + \frac{1}{3}\right)F_1G_3 - \left(e^2 + \frac{1}{3}\right)F_3G_1 + \left(\frac{e^2}{2} - \frac{e^4}{4} - \frac{1}{45}\right)F_1G_1 - \frac{e^2\sqrt{1-e^2}}{2}\,(H_3G_1' + H_1G_3') + \left(\frac{e^2}{6} - \frac{e^4}{8}\right)\sqrt{1-e^2}H_1G_1' = (1-e^2)G_5'' \tag{D.7}$$

$$8F_1G_7 + 6F_3G_5 + 4F_5G_3 + 2F_7G_1 + \sqrt{1-e^2}\Big(H_1G_7' + H_3G_5' + H_5G_3' + H_7G_1'\Big) - \left(3e^2 + \frac{1}{3}\right)F_1G_5 - \left(2e^2 + \frac{1}{3}\right)F_3G_3 - \left(e^2 + \frac{1}{3}\right)F_5G_1 - \left(\frac{e^4}{2} - \frac{5e^2}{6} + \frac{1}{45}\right)F_1G_3 - \left(\frac{e^4}{4} - \frac{e^2}{2} + \frac{1}{45}\right)F_3G_1 - \left(\frac{2}{945} + \frac{4e^2}{45} - \frac{5e^4}{24} + \frac{e^6}{8}\right)F_1G_1 - \frac{e^2\sqrt{1-e^2}}{2}\,(H_1G_5' + H_5G_1') - \sqrt{1-e^2}\left(\frac{e^2}{45} - \frac{e^4}{12} + \frac{e^6}{16}\right)H_1G_1' - \frac{e^2\sqrt{1-e^2}}{2}H_3G_3' + \sqrt{1-e^2}\left(\frac{e^2}{6} - \frac{e^4}{8}\right)(H_3G_1' + H_1G_3') = (1-e^2)G_7'' \tag{D.8}$$

$$2F_1 + \sqrt{1-e^2}H_1' = 0 \tag{D.9}$$

$$4F_3 + \sqrt{1-e^2}H_3' - \left(\frac{1}{3} + e^2\right)F_1 = 0 \tag{D.10}$$

$$6F_5 + \sqrt{1-e^2}H_5' + \left(\frac{2e^2}{3} - e^4 - \frac{1}{45}\right)F_1 - \left(\frac{1}{3} + e^2\right)F_3 = 0 \tag{D.11}$$

$$8F_7 + \sqrt{1-e^2}H_7' - \left(\frac{2}{945} + \frac{2e^2}{15} - e^4 + e^6\right)F_1 - \left(\frac{1}{45} - \frac{2e^2}{3} + e^4\right)F_3 - \left(\frac{1}{3} + e^2\right)F_5 = 0 \tag{D.12}$$

D.2 Values of quantities in the series solution for oblate spheroids

e	n	$F_n(0;e)$	$F_n'(0;e)$	$G_n(0;e)$	$G_n'(0;e)$	$H_n(\infty;e)$
0.0	1	0.00000	0.51023	1.00000	-0.61592	-0.88447
	3	0.00000	-0.22129	-0.16667	0.24764	0.16074
	5	0.00000	0.02071	0.00833	-0.02569	0.00084
	7	0.00000	-0.00189	-0.00020	0.00181	0.00085

e	n	$F_n(0;e)$	$F_n'(0;e)$	$G_n(0;e)$	$G_n'(0;e)$	$H_n(\infty;e)$
0.1	1	0.00000	0.51280	1.00000	-0.61902	-0.88447
	3	0.00000	-0.22363	-0.16667	0.25050	0.15892
	5	0.00000	0.02173	0.00833	-0.02702	0.00166
	7	0.00000	-0.00217	-0.00020	0.00218	0.00071

e	n	$F_n(0;e)$	$F_n'(0;e)$	$G_n(0;e)$	$G_n'(0;e)$	$H_n(\infty;e)$
0.2	1	0.00000	0.52075	1.00000	-0.62862	-0.88447
	3	0.00000	-0.23084	-0.16667	0.25927	0.15339
	5	0.00000	0.02481	0.00833	-0.03104	0.00406
	7	0.00000	-0.00296	-0.00020	0.00321	0.00035

e	n	$F_n(0;e)$	$F_n'(0;e)$	$G_n(0;e)$	$G_n'(0;e)$	$H_n(\infty;e)$
0.3	1	0.00000	0.53487	1.00000	-0.64566	-0.88447
	3	0.00000	-0.24354	-0.16667	0.27461	0.14391
	5	0.00000	0.03001	0.00833	-0.03777	0.00787
	7	0.00000	-0.00415	-0.00020	0.00474	-0.00004

e	n	$F_n(0;e)$	$F_n'(0;e)$	$G_n(0;e)$	$G_n'(0;e)$	$H_n(\infty;e)$
0.4	1	0.00000	0.55671	1.00000	-0.67203	-0.88447
	3	0.00000	-0.26298	-0.16667	0.29785	0.13004
	5	0.00000	0.03745	0.00833	-0.04731	0.01285
	7	0.00000	-0.00557	-0.00020	0.00652	-0.00026

e	n	$F_n(0;e)$	$F_n'(0;e)$	$G_n(0;e)$	$G_n'(0;e)$	$H_n(\infty;e)$
0.5	1	0.00000	0.58917	1.00000	-0.71121	-0.88447
	3	0.00000	-0.29140	-0.16667	0.33138	0.11111
	5	0.00000	0.04743	0.00833	-0.05991	0.01868
	7	0.00000	-0.00700	-0.00020	0.00824	-0.00008

e	n	$F_n(0;e)$	$F_n'(0;e)$	$G_n(0;e)$	$G_n'(0;e)$	$H_n(\infty;e)$
0.6	1	0.00000	0.63779	1.00000	-0.76990	-0.88447
	3	0.00000	-0.33311	-0.16667	0.37978	0.08612
	5	0.00000	0.06059	0.00833	-0.07611	0.02508
	7	0.00000	-0.00828	-0.00020	0.00962	0.00061

e	n	$F_n(0;e)$	$F_n'(0;e)$	$G_n(0;e)$	$G_n'(0;e)$	$H_n(\infty;e)$
0.7	1	0.00000	0.71447	1.00000	-0.86246	-0.88447
	3	0.00000	-0.39715	-0.16667	0.45267	0.05355
	5	0.00000	0.07847	0.00833	-0.09736	0.03181
	7	0.00000	-0.00933	-0.00020	0.01057	0.00169

e	n	$F_n(0;e)$	$F_n'(0;e)$	$G_n(0;e)$	$G_n'(0;e)$	$H_n(\infty;e)$
0.8	1	0.00000	0.85038	1.00000	-1.02658	-0.89006
	3	0.00000	-0.50695	-0.16667	0.57491	0.03294
	5	0.00000	0.10557	0.00833	-0.12790	0.07658
	7	0.00000	-0.01050	-0.00020	0.01149	-0.07727

D.3 Comparison of profiles due to numerical and series solutions for oblate spheroids

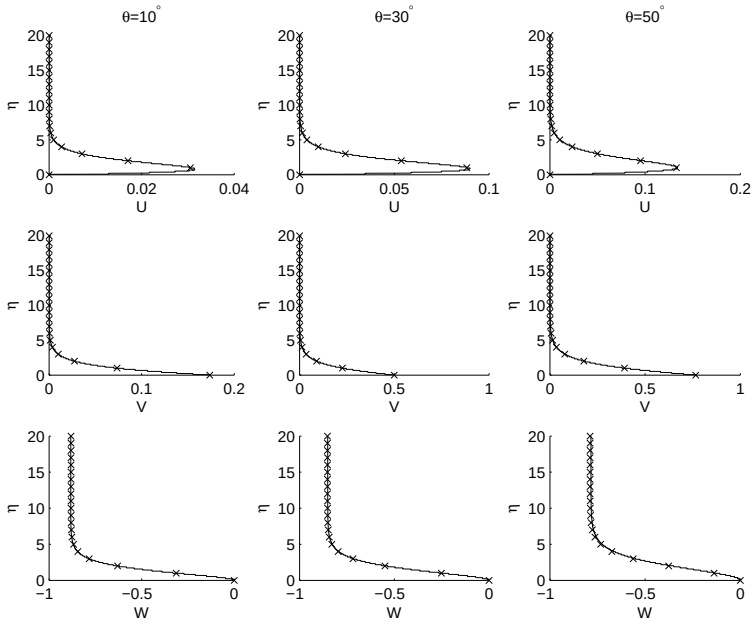

Figure D.1: Comparison of the numerical (solid line) and series solutions (cross points) at $\theta = 10°$, $30°$ $50°$ for $e = 0.5$.

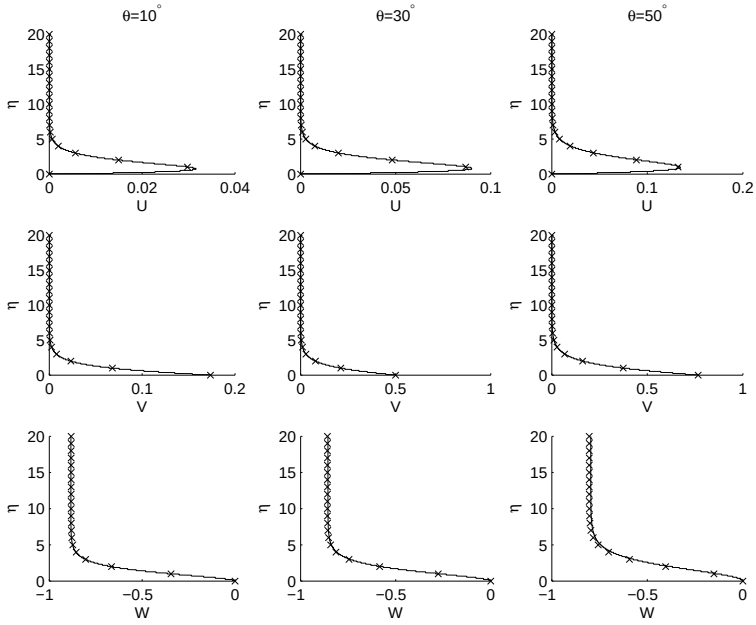

Figure D.2: Comparison of the numerical (solid line) and series solutions (cross points) at $\theta = 10°$, $30°$ $50°$ for $e = 0.6$.

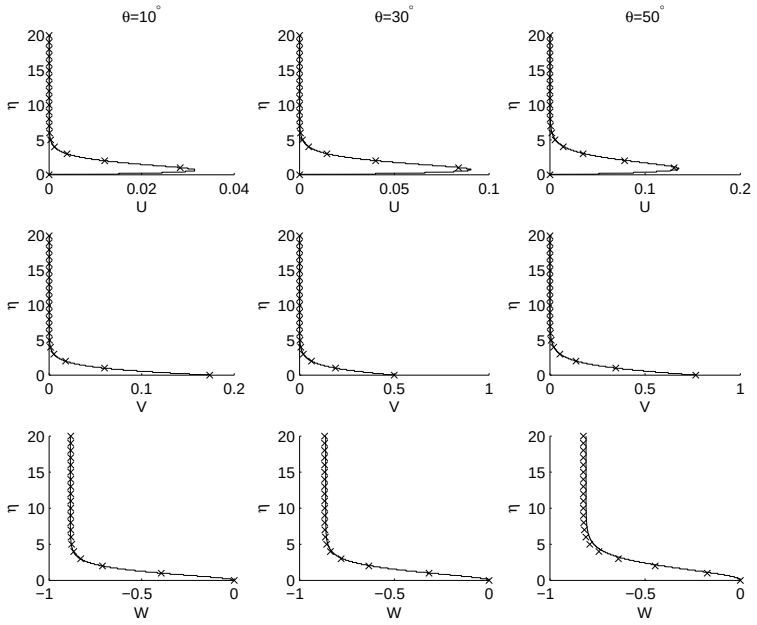

Figure D.3: Comparison of the numerical (solid line) and series solutions (cross points) at $\theta = 10°$, $30°$ $50°$ for $e = 0.7$.

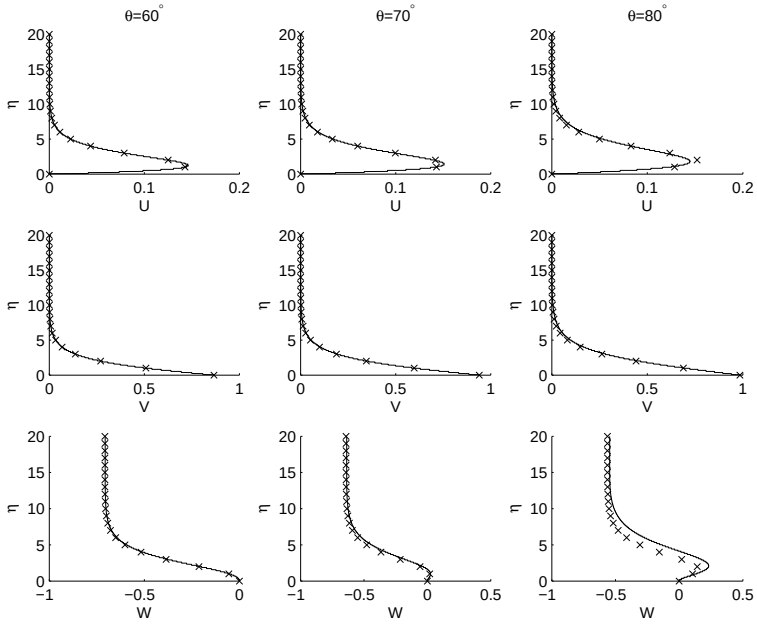

Figure D.4: Comparison of the numerical (solid line) and series solutions (cross points) at $\theta = 60°$, $70°$ $80°$ for $e = 0.1$.

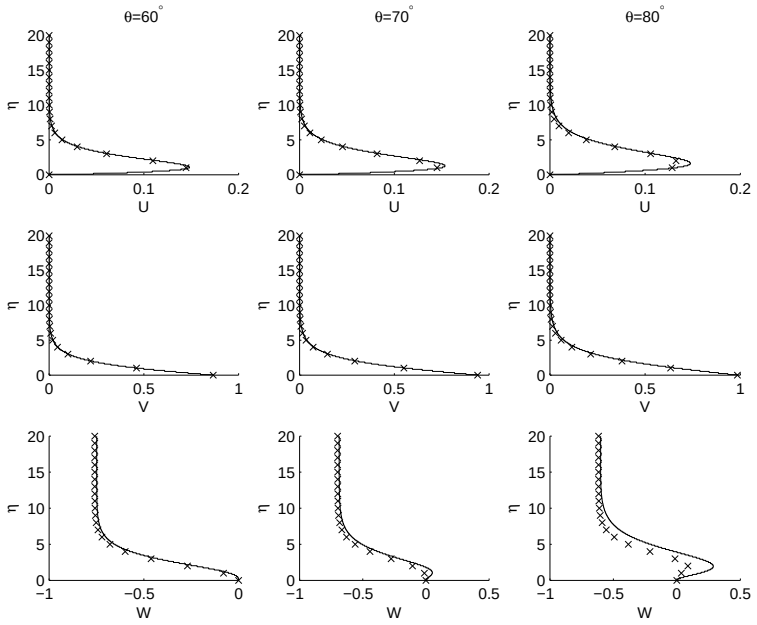

Figure D.5: Comparison of the numerical (solid line) and series solutions (cross points) at $\theta = 60°$, $70°$ $80°$ for $e = 0.6$.

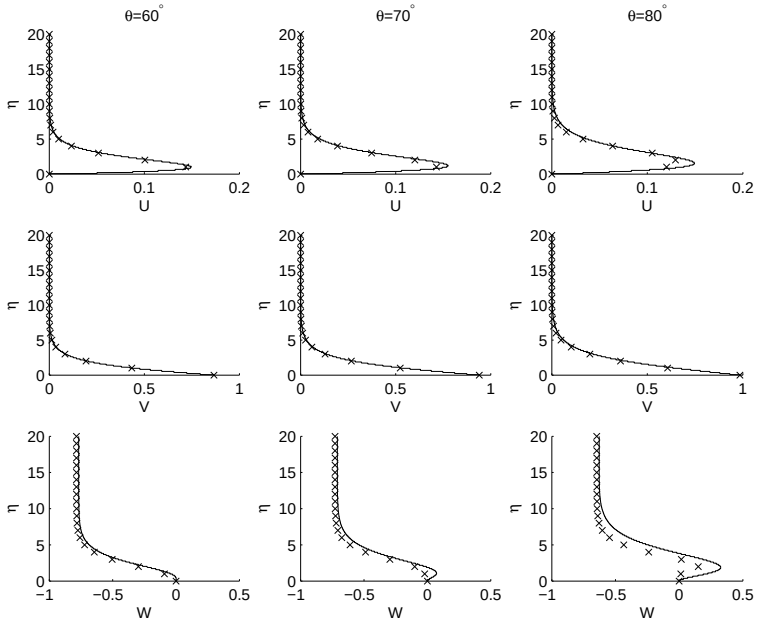

Figure D.6: Comparison of the numerical (solid line) and series solutions (cross points) at $\theta = 60°$, $70°$ $80°$ for $e = 0.7$.

Appendix E

Dimensional perturbation equations and miscellaneous neutral curves of oblate spheroid

In this Appendix we present the dimensional perturbation equations of the boundary-layer over oblate spheroids in E.1. In Appendix E.2 critical Reynolds numbers at all latitudes and each value of e are shown. In Appendix E.3 miscellaneous neutral curves of convective instability for oblate spheroids, are presented in (R_S, n)- and (R_S, ϵ)-planes. Comparisons of neutral curves of both types of spheroids are shown in Appendix E.4.

E.1 Dimensional perturbation equations of rotating oblate spheroids

Dimensional perturbed continuity equation is,

$$\frac{\sqrt{\eta^{\star 2}-d^{\star 2}}}{\sqrt{\eta^{\star 2}-d^{\star 2}\sin^2\theta}}\frac{dw^\star}{d\eta^\star}+\Bigg(\frac{\eta^\star\sqrt{\eta^{\star 2}-d^{\star 2}}}{(\eta^{\star 2}-d^{\star 2}\sin^2\theta)^{3/2}}+\frac{\sqrt{\eta^{\star 2}-d^{\star 2}}}{\eta^\star\sqrt{\eta^{\star 2}-d^{\star 2}\sin^2\theta}}\Bigg)w^\star+\Bigg(-\frac{d^{\star 2}\sin\theta\cos\theta}{(\eta^{\star 2}-d^{\star 2}\sin^2\theta)^{3/2}}+\frac{\cot\theta}{\sqrt{\eta^{\star 2}-d^{\star 2}\sin^2\theta}}+\frac{\mathrm{i}\alpha^\star\sqrt{\eta_\circ^{\star 2}-d_\circ^{\star 2}\sin^2\theta}}{\sqrt{\eta^{\star 2}-d^{\star 2}\sin^2\theta}}\Bigg)u^\star+\frac{\mathrm{i}\beta^\star\eta_\circ^\star}{\eta^\star}\,v^\star\;=\;0 \tag{E.1}$$

The θ–component of the dimensional perturbation equations is,

$$\frac{\sqrt{\eta^{\star 2}-d^{\star 2}}\;W^\star}{\sqrt{\eta^{\star 2}-d^{\star 2}\sin^2\theta}}\frac{du^\star}{d\eta^\star}+\Bigg[\mathrm{i}\Bigg(\alpha^\star\frac{\sqrt{\eta_\circ^{\star 2}-d_\circ^{\star 2}\sin^2\theta}}{\sqrt{\eta^{\star 2}-d^{\star 2}\sin^2\theta}}U^\star+\beta^\star\frac{\eta_\circ^\star}{\eta^\star}V^\star-\gamma^\star\Bigg)+\frac{1}{\sqrt{\eta^{\star 2}-d^{\star 2}\sin^2\theta}}\frac{\partial U^\star}{\partial\theta}+\frac{\eta^\star\sqrt{\eta^{\star 2}-d^{\star 2}}}{(\eta^{\star 2}-d^{\star 2}\sin^2\theta)^{3/2}}W^\star\Bigg]\,u^\star-\frac{2V^\star\cot\theta}{\sqrt{\eta^{\star 2}-d^{\star 2}\sin^2\theta}}v^\star+\Bigg(\frac{\eta^\star\sqrt{\eta^{\star 2}-d^{\star 2}}U^\star}{(\eta^{\star 2}-d^{\star 2}\sin^2\theta)^{3/2}}+\frac{2d^{\star 2}\sin\theta\cos\theta\;W^\star}{(\eta^{\star 2}-d^{\star 2}\sin^2\theta)^{3/2}}+\frac{\sqrt{\eta^{\star 2}-d^{\star 2}}}{\sqrt{\eta^{\star 2}-d^{\star 2}\sin^2\theta}}\frac{\partial U^\star}{\partial\eta^\star}\Bigg)w^\star\;=\;\frac{-\mathrm{i}\alpha^\star\sqrt{\eta_\circ^{\star 2}-d_\circ^{\star 2}\sin^2\theta}\;p^\star}{\rho^\star\sqrt{\eta^{\star 2}-d^{\star 2}\sin^2\theta}}+\nu^\star\Bigg[\Bigg(\frac{\eta^{\star 2}-d^{\star 2}}{\eta^{\star 2}-d^{\star 2}\sin^2\theta}\Bigg)\frac{d^2u^\star}{d\eta^{\star 2}}+\frac{(2\eta^{\star 2}-d^{\star 2})}{\eta^\star(\eta^{\star 2}-d^{\star 2}\sin^2\theta)}\frac{du^\star}{d\eta^\star}+\Bigg\{-\Bigg(\alpha^{\star 2}\frac{\eta_\circ^{\star 2}-d_\circ^{\star 2}\sin^2\theta}{\eta^{\star 2}-d^{\star 2}\sin^2\theta}+\beta^{\star 2}\frac{\eta_\circ^\star}{\eta^\star}\Bigg)+\mathrm{i}\alpha^\star\Bigg(\frac{\sqrt{\eta_\circ^{\star 2}-d_\circ^{\star 2}\sin^2\theta}}{(\eta^{\star 2}-d^{\star 2}\sin^2\theta)}\cot\theta-\frac{d_\circ^{\star 2}\sin\theta\cos\theta}{(\eta^{\star 2}-d^{\star 2}\sin^2\theta)\sqrt{\eta_\circ^{\star 2}-d_\circ^{\star 2}\sin^2\theta}}\Bigg)+\frac{3\eta^{\star 2}-d^{\star 2}(2-\sin^2\theta)}{(\eta^{\star 2}-d^{\star 2}\sin^2\theta)^2}-\frac{3\eta^{\star 2}(\eta^{\star 2}-d^{\star 2})}{(\eta^{\star 2}-d^{\star 2}\sin^2\theta)^3}-\frac{3d^{\star 4}\sin^2\theta\cos^2\theta}{(\eta^{\star 2}-d^{\star 2}\sin^2\theta)^3}-\frac{\csc^2\theta}{(\eta^{\star 2}-d^{\star 2}\sin^2\theta)}\Bigg\}u^\star+\frac{2d^{\star 2}\sqrt{\eta^{\star 2}-d^{\star 2}}\sin\theta\cos\theta}{(\eta^{\star 2}-d^{\star 2}\sin^2\theta)^2}\frac{dw^\star}{d\eta^\star}$$

$$
\begin{aligned}
&- \frac{2\mathrm{i}\beta^\star\eta_\circ\cot\theta}{\eta^\star\sqrt{\eta^{\star2}-d^{\star2}\sin^2\theta}}\,v^\star + \Bigg(2\mathrm{i}\alpha^\star\frac{\eta^\star\sqrt{\eta^{\star2}-d^{\star2}}\sqrt{\eta_\circ^{\star2}-d_\circ^{\star2}\sin^2\theta}}{(\eta^{\star2}-d^{\star2}\sin^2\theta)^2}\\
&+ \frac{2d^{\star2}\sqrt{\eta^{\star2}-d^{\star2}}\sin\theta\cos\theta}{\eta^\star(\eta^{\star2}-d^{\star2}\sin^2\theta)^2}\Bigg)\,w^\star\Bigg] \qquad \text{(E.2)}
\end{aligned}
$$

The ϕ–component of the dimensional perturbation equations is,

$$
\begin{aligned}
&\frac{\sqrt{\eta^{\star2}-d^{\star2}}W^\star}{\sqrt{\eta^{\star2}-d^{\star2}\sin^2\theta}}\frac{dv^\star}{d\eta^\star} + \Bigg[\mathrm{i}\Bigg(\alpha^\star\frac{\sqrt{\eta_\circ^{\star2}-d_\circ^{\star2}\sin^2\theta}}{\sqrt{\eta^{\star2}-d^{\star2}\sin^2\theta}}U^\star + \beta^\star\frac{\eta_\circ^\star}{\eta^\star}V^\star - \gamma^\star\Bigg)\\
&+ \frac{U^\star\cot\theta}{\sqrt{\eta^{\star2}-d^{\star2}\sin^2\theta}} + \frac{\sqrt{\eta^{\star2}-d^{\star2}}}{\eta^\star\sqrt{\eta^{\star2}-d^{\star2}\sin^2\theta}}W^\star\Bigg]\,v^\star\\
&+ \Bigg(\frac{V^\star\cot\theta}{\sqrt{\eta^{\star2}-d^{\star2}\sin^2\theta}} + \frac{1}{\sqrt{\eta^{\star2}-d^{\star2}\sin^2\theta}}\frac{\partial V^\star}{\partial\theta}\Bigg)u^\star\\
&+ \Bigg(\frac{\sqrt{\eta^{\star2}-d^{\star2}}}{\sqrt{\eta^{\star2}-d^{\star2}\sin^2\theta}}\frac{\partial V^\star}{\partial\eta^\star} + \frac{\sqrt{\eta^{\star2}-d^{\star2}}}{\eta^\star\sqrt{\eta^{\star2}-d^{\star2}\sin^2\theta}}V^\star\Bigg)w^\star\\
&= \frac{-\mathrm{i}\beta^\star\eta_\circ^\star}{\rho^\star\eta^\star}\,p^\star + \nu^\star\Bigg[\Bigg(\frac{\eta^{\star2}-d^{\star2}}{\eta^{\star2}-d^{\star2}\sin^2\theta}\Bigg)\frac{d^2v^\star}{d\eta^{\star2}} + \frac{(2\eta^{\star2}-d^{\star2})}{\eta^\star(\eta^{\star2}-d^{\star2}\sin^2\theta)}\frac{dv^\star}{d\eta^\star}\\
&+ \Bigg\{-\Bigg(\alpha^{\star2}\frac{\eta_\circ^{\star2}-d_\circ^{\star2}\sin^2\theta}{\eta^{\star2}-d^{\star2}\sin^2\theta} + \beta^{\star2}\frac{\eta_\circ^{\star2}}{\eta^{\star2}}\Bigg) + \mathrm{i}\alpha^\star\Bigg(\frac{\sqrt{\eta_\circ^{\star2}-d_\circ^{\star2}\sin^2\theta}}{(\eta^{\star2}-d^{\star2}\sin^2\theta)}\cot\theta\\
&- \frac{d_\circ^{\star2}\sin\theta\cos\theta}{(\eta^{\star2}-d^{\star2}\sin^2\theta)\sqrt{\eta_\circ^{\star2}-d_\circ^{\star2}\sin^2\theta}}\Bigg) - \frac{\csc^2\theta}{\eta^{\star2}}\Bigg\}v^\star\\
&+ \frac{2\mathrm{i}\beta^\star\eta_\circ^\star\cot\theta}{\eta^\star\sqrt{\eta^{\star2}-d^{\star2}\sin^2\theta}}\,u^\star + \frac{2\mathrm{i}\beta^\star\eta_\circ^\star\sqrt{\eta^{\star2}-d^{\star2}}}{\eta^{\star2}\sqrt{\eta^{\star2}-d^{\star2}\sin^2\theta}}\,w^\star \qquad \text{(E.3)}
\end{aligned}
$$

The $\eta^\star$–component of the dimensional perturbation equations is,

$$
\begin{aligned}
&\frac{\sqrt{\eta^{\star2}-d^{\star2}}\;W^\star}{\sqrt{\eta^{\star2}-d^{\star2}\sin^2\theta}}\frac{dw^\star}{d\eta^\star} + \Bigg[\mathrm{i}\Bigg(\alpha^\star\frac{\sqrt{\eta_\circ^{\star2}-d_\circ^{\star2}\sin^2\theta}}{\sqrt{\eta^{\star2}-d^{\star2}\sin^2\theta}}U^\star + \beta^\star\frac{\eta_\circ^\star}{\eta^\star}V^\star - \gamma^\star\Bigg)\\
&+ \frac{\sqrt{\eta^{\star2}-d^{\star2}}}{\sqrt{\eta^{\star2}-d^{\star2}\sin^2\theta}}\frac{\partial W^\star}{\partial\eta^\star} - \frac{d^{\star2}\cos\theta\sin\theta}{(\eta^{\star2}-d^{\star2}\sin^2\theta)^{3/2}}U^\star\Bigg]\,w^\star\\
&+ \Bigg(\frac{1}{\sqrt{\eta^{\star2}-d^{\star2}\sin^2\theta}}\frac{\partial W^\star}{\partial\theta} - \frac{2\eta^\star\sqrt{\eta^{\star2}-d^{\star2}}}{(\eta^{\star2}-d^{\star2}\sin^2\theta)^{3/2}}U^\star\\
&- \frac{d^{\star2}\cos\theta\sin\theta\;W^\star}{(\eta^{\star2}-d^{\star2}\sin^2\theta)^{3/2}}\Bigg)u^\star - \frac{2\sqrt{\eta^{\star2}-d^{\star2}}V^\star}{\eta^\star\sqrt{\eta^{\star2}-d^{\star2}\sin^2\theta}}v^\star\\
&= \frac{-\sqrt{\eta^{\star2}-d^{\star2}}}{\rho^\star\sqrt{\eta^{\star2}-d^{\star2}\sin^2\theta}}\frac{dp^\star}{d\eta^\star} + \nu^\star\Bigg[\Bigg(\frac{\eta^{\star2}-d^{\star2}}{\eta^{\star2}-d^{\star2}\sin^2\theta}\Bigg)\frac{d^2w^\star}{d\eta^{\star2}}
\end{aligned}
$$

$$+\frac{2(\eta^{\star 2}-d^{\star 2})}{\eta^{\star}(\eta^{\star 2}-d^{\star 2}\sin^2\theta)}\frac{dw^{\star}}{d\eta^{\star}}+\Bigg\{-\left(\alpha^{\star 2}\frac{\eta_{\circ}^{\star 2}-d_{\circ}^{\star 2}\sin^2\theta}{\eta^{\star 2}-d^{\star 2}\sin^2\theta}+\beta^{\star 2}\frac{\eta_{\circ}^{\star 2}}{\eta^{\star 2}}\right)$$
$$+\mathrm{i}\alpha^{\star}\left(\frac{\sqrt{\eta_{\circ}^{\star 2}-d_{\circ}^{\star 2}\sin^2\theta}}{(\eta^{\star 2}-d^{\star 2}\sin^2\theta)}\cot\theta-\frac{d_{\circ}^{\star 2}\sin\theta\cos\theta}{(\eta^{\star 2}-d^{\star 2}\sin^2\theta)\sqrt{\eta_{\circ}^{\star 2}-d_{\circ}^{\star 2}\sin^2\theta}}\right)$$
$$-\left(\frac{(\eta^{\star 2}-d^{\star 2})(2\eta^{\star 2}-d^{\star 2}\sin^2\theta)}{\eta^{\star 2}(\eta^{\star 2}-d^{\star 2}\sin^2\theta)^2}+\frac{d^{\star 2}\sin^2\theta}{(\eta^{\star 2}-d^{\star 2}\sin^2\theta)^2}\right)\Bigg\}w^{\star}$$
$$-\frac{2d^{\star 2}\sqrt{\eta^{\star 2}-d^{\star 2}}\cos\theta\sin\theta}{(\eta^{\star 2}-d^{\star 2}\sin^2\theta)^2}\frac{du^{\star}}{d\eta^{\star}}-\Bigg(\frac{2\mathrm{i}\alpha^{\star}\eta^{\star}\sqrt{\eta_{\circ}^{\star 2}-d_{\circ}^{\star 2}\sin^2\theta}\sqrt{\eta^{\star 2}-d^{\star 2}}}{(\eta^{\star 2}-d^{\star 2}\sin^2\theta)^2}$$
$$+\frac{2\eta^{\star}\cot\theta\sqrt{\eta^{\star 2}-d^{\star 2}}}{(\eta^{\star 2}-d^{\star 2}\sin^2\theta)^2}\Bigg)u^{\star}-\frac{2\mathrm{i}\beta^{\star}\eta_{\circ}^{\star}\sqrt{\eta^{\star 2}-d^{\star 2}}}{\eta^{\star 2}\sqrt{\eta^{\star 2}-d^{\star 2}\sin^2\theta}}v^{\star}\Bigg] \tag{E.4}$$

E.2 Critical Reynolds numbers for oblate spheroids

e	θ	Re_I	Re_{II}	R_{SI}	R_{SII}
0.0	10	1585.3	2432.5	2.51×10^6	5.92×10^6
0.0	20	768.8	1144.3	5.91×10^5	1.31×10^6
0.0	30	492.9	711.2	2.43×10^5	5.06×10^5
0.0	40	350.1	484.2	1.23×10^5	2.34×10^5
0.0	50	258.3	334.5	6.67×10^4	1.12×10^5
0.0	60	188.0	215.0	3.53×10^4	4.62×10^4
0.0	70	-	91.4	-	8.35×10^3

Table E.1: The critical Reynolds numbers Re and R_S for the onset of stationary ($c = 1$) crossflow (type I) and streamline curvature (type II) modes of convective instability for $e = 0.0$, - indicates that a crossflow lobe is not seen.

e	θ	Re_I	Re_{II}	R_{SI}	R_{SII}
0.1	10	1585.5	2432.65	2.51×10^6	5.92×10^6
0.1	20	769.04	1145.0	5.91×10^5	1.31×10^6
0.1	30	493.34	712.4	2.43×10^5	5.08×10^5
0.1	40	350.61	485.56	1.23×10^5	2.36×10^5
0.1	50	258.8	336.02	6.70×10^4	1.13×10^5
0.1	60	188.57	216.52	3.56×10^4	4.69×10^4
0.1	70	-	92.95	-	8.64×10^3

Table E.2: The critical Reynolds numbers Re and R_S for the onset of stationary ($c = 1$) crossflow (type I) and streamline curvature (type II) modes of convective instability for $e = 0.1$, - indicates that a crossflow lobe is not seen.

e	θ	Re_I	Re_{II}	R_{SI}	R_{SII}
0.2	10	1586.2	2434.25	2.52×10^6	5.93×10^6
0.2	20	770.12	1147.66	5.93×10^5	1.32×10^6
0.2	30	494.64	716.0	2.45×10^5	5.13×10^5
0.2	40	352.09	489.72	1.24×10^5	2.10×10^5
0.2	50	260.38	340.5	6.77×10^4	1.16×10^5
0.2	60	190.25	221.14	3.62×10^4	4.89×10^4
0.2	70	-	97.8	-	9.56×10^3

Table E.3: The critical Reynolds numbers Re and R_S for the onset of stationary ($c = 1$) crossflow (type I) and streamline curvature (type II) modes of convective instability for $e = 0.2$, - indicates that a crossflow lobe is not seen.

e	θ	Re_I	Re_{II}	R_{SI}	R_{SII}
0.3	10	1587.26	2436.85	2.52×10^6	5.94×10^6
0.3	20	771.8	1151.98	5.96×10^5	1.33×10^6
0.3	30	496.82	721.94	2.47×10^5	5.21×10^5
0.3	40	354.63	496.86	1.26×10^5	2.47×10^5
0.3	50	263.12	348.28	6.92×10^4	1.21×10^5
0.3	60	193.13	229.3	3.73×10^4	5.26×10^4
0.3	70	-	106.32	-	1.13×10^4

Table E.4: The critical Reynolds numbers Re and R_S for the onset of stationary ($c = 1$) crossflow (type I) and streamline curvature (type II) modes of convective instability for $e = 0.3$, - indicates that a crossflow lobe is not seen.

e	θ	Re_I	Re_{II}	R_{SI}	R_{SII}
0.4	10	1588.68	2440.0	2.52×10^6	5.95×10^6
0.4	20	774.12	1157.9	6.0×10^5	1.34×10^6
0.4	30	499.9	730.44	2.50×10^5	5.34×10^5
0.4	40	358.27	507.14	1.28×10^5	2.57×10^5
0.4	50	267.14	359.84	7.14×10^4	1.29×10^5
0.4	60	197.31	241.4	3.89×10^4	5.83×10^4
0.4	70	-	119.23	-	1.42×10^4

Table E.5: The critical Reynolds numbers Re and R_S for the onset of stationary ($c = 1$) crossflow (type I) and streamline curvature (type II) modes of convective instability for $e = 0.4$, - indicates that a crossflow lobe is not seen.

e	θ	Re_I	Re_{II}	R_{SI}	R_{SII}
0.5	10	1590.21	2443.25	2.53×10^6	5.97×10^6
0.5	20	777.06	1165.26	6.04×10^5	1.36×10^6
0.5	30	503.96	741.64	2.54×10^5	5.5×10^5
0.5	40	363.13	521.1	1.32×10^5	2.72×10^5
0.5	50	272.58	375.84	7.43×10^4	1.41×10^5
0.5	60	203.08	258.7	4.12×10^4	6.69×10^4
0.5	70	-	-	-	-

Table E.6: The critical Reynolds numbers Re and R_S for the onset of stationary ($c = 1$) crossflow (type I) and streamline curvature (type II) modes of convective instability for $e = 0.5$, - indicates that a crossflow lobe is not seen.

e	θ	Re_I	Re_{II}	R_{SI}	R_{SII}
0.6	10	1591.5	2445.6	2.53×10^6	5.98×10^6
0.6	20	780.48	1173.46	6.09×10^5	1.86×10^6
0.6	30	508.98	755.46	2.59×10^5	5.71×10^5
0.6	40	369.43	539.38	1.64×10^5	2.91×10^5
0.6	50	279.75	397.52	7.83×10^4	1.58×10^5
0.6	60	210.82	283.23	4.44×10^4	8.02×10^4
0.6	70	146.2	164.25	2.14×10^4	2.70×10^4

Table E.7: The critical Reynolds numbers Re and R_S for the onset of stationary ($c = 1$) crossflow (type I) and streamline curvature (type II) modes of convective instability for $e = 0.6$, - indicates that a crossflow lobe is not seen.

e	θ	Re_I	Re_{II}	R_{SI}	R_{SII}
0.7	10	1591.51	2444.5	2.53×10^6	5.98×10^6
0.7	20	783.9	1181.04	6.14×10^5	1.39×10^6
0.7	30	514.9	771.66	2.65×10^5	5.95×10^5
0.7	40	377.27	562.58	1.42×10^5	3.16×10^5
0.7	50	289.12	427.1	8.36×10^4	1.83×10^5
0.7	60	221.14	317.8	4.89×10^4	1.01×10^5
0.7	70	157.25	203.38	2.47×10^4	4.14×10^4

Table E.8: The critical Reynolds numbers Re and R_S for the onset of stationary ($c = 1$) crossflow (type I) and streamline curvature (type II) modes of convective instability for $e = 0.7$, - indicates that a crossflow lobe is not seen.

e	θ	Re_I	Re_{II}	R_{SI}	R_{SII}
0.8	10	1586.9	2430.5	2.52×10^6	5.91×10^6
0.8	20	785.85	1182.64	6.18×10^5	1.41×10^6
0.8	30	521.08	787.92	2.72×10^5	6.21×10^5
0.8	40	386.75	591.04	1.50×10^5	3.49×10^5
0.8	50	301.33	467.5	9.08×10^4	2.19×10^5
0.8	60	235.25	370.54	5.53×10^4	2.37×10^5
0.8	70	172.09	266.81	2.96×10^4	7.12×10^4
0.8	80	-	95.7	2.96×10^4	9.16×10^3

Table E.9: The critical Reynolds numbers Re and R_S for the onset of stationary ($c = 1$) crossflow (type I) and streamline curvature (type II) modes of convective instability for $e = 0.8$, - indicates that a crossflow lobe is not seen.

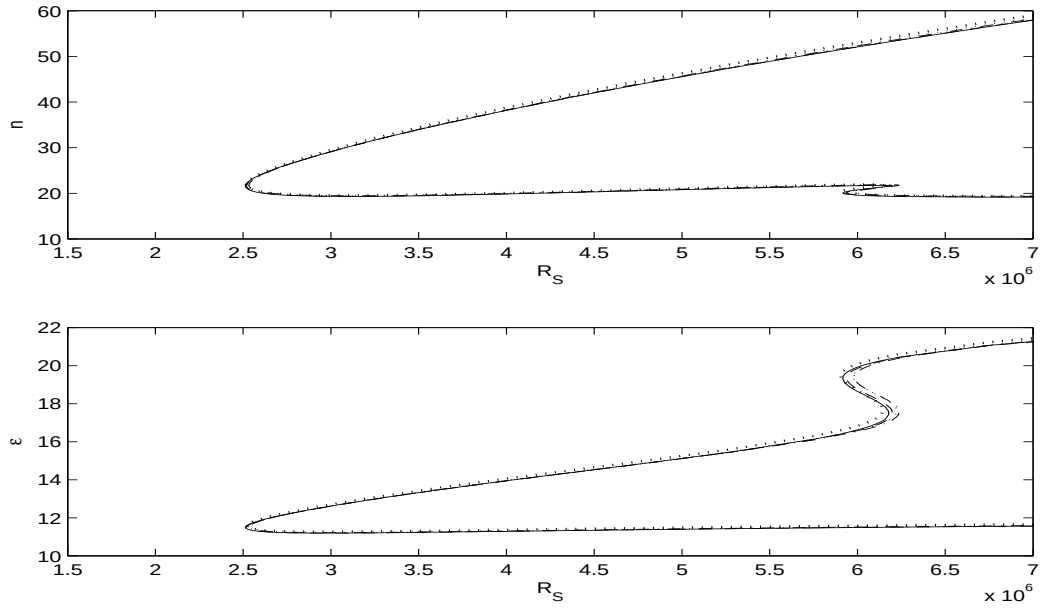

Figure E.1: Neutral curves in (R_S, n)- and (R_S, ϵ)-planes at latitude 10° for $e = 0$ (–), 0.3 (−−), 0.6 (-.), 0.7 (. . .) & 0.8 (...)

E.3 The neutral curves of convective instability for rotating oblate spheroids in terms of spin Reynolds numbers

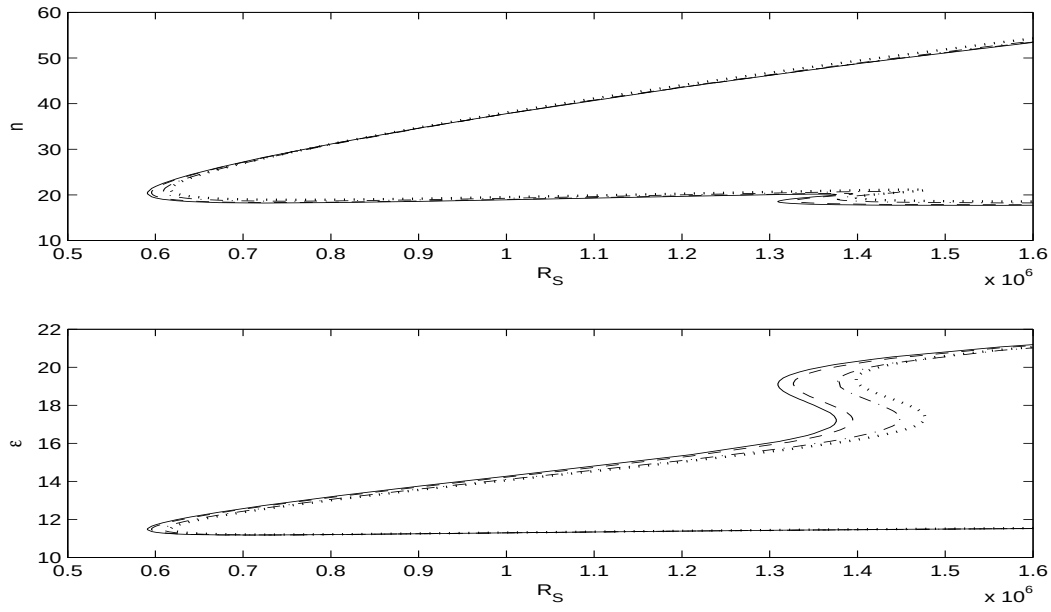

Figure E.2: Neutral curves in (R_S, n)- and (R_S, ϵ)-planes at latitude 20° for $e = 0$ (–), 0.3 (−−), 0.6 (-.), 0.8 (...)

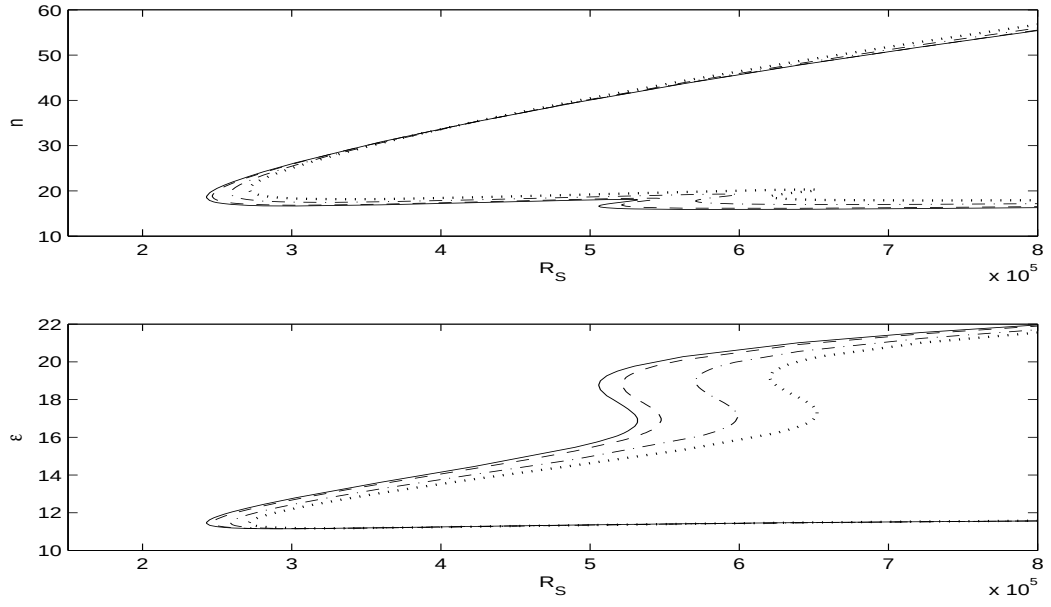

Figure E.3: Neutral curves in (R_S, n)- and (R_S, ϵ)-planes at latitude 30° for $e = 0$ (–), 0.3 (−−), 0.6 (-.), 0.8 (...)

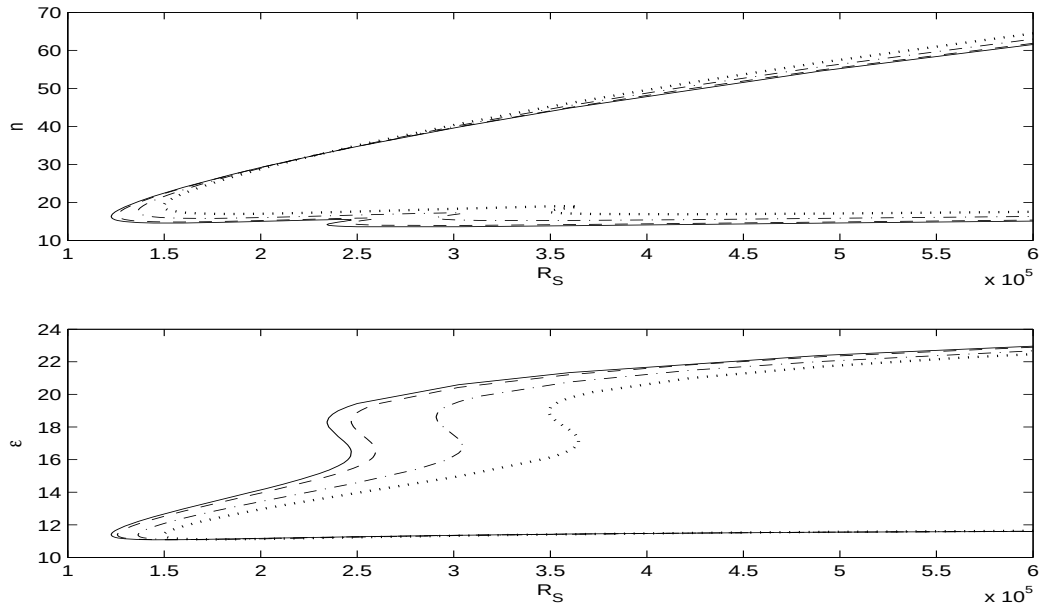

Figure E.4: Neutral curves in (R_S, n)- and (R_S, ϵ)-planes at latitude 40° for $e = 0$ (–), 0.3 (−−), 0.6 (-.), 0.8 (...)

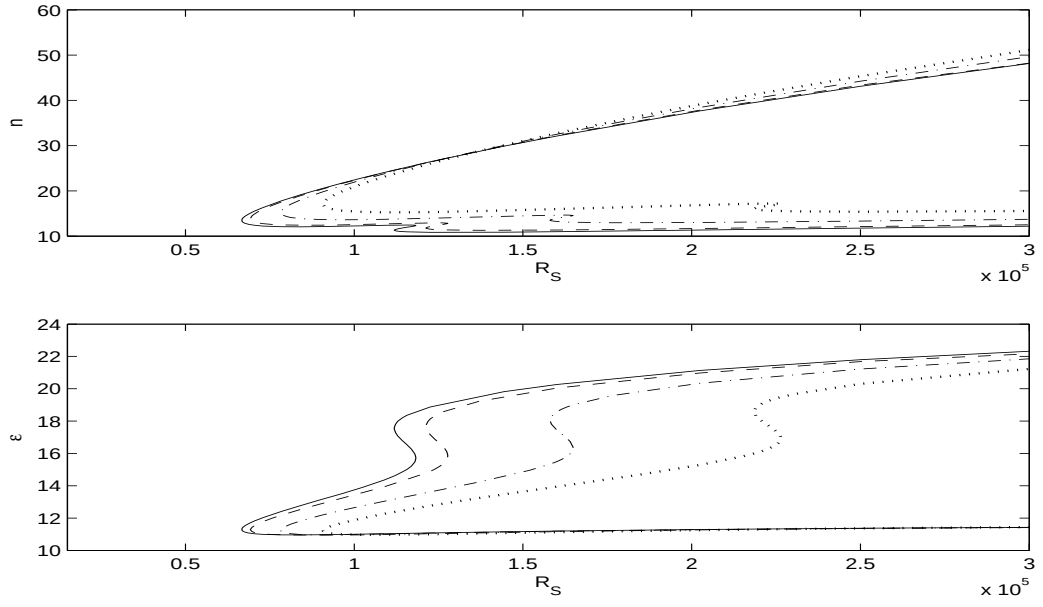

Figure E.5: Neutral curves in (R_S, n)- and (R_S, ϵ)-planes at latitude 50° for $e = 0$ (–), 0.3 (−−), 0.6 (-.), 0.8 (...)

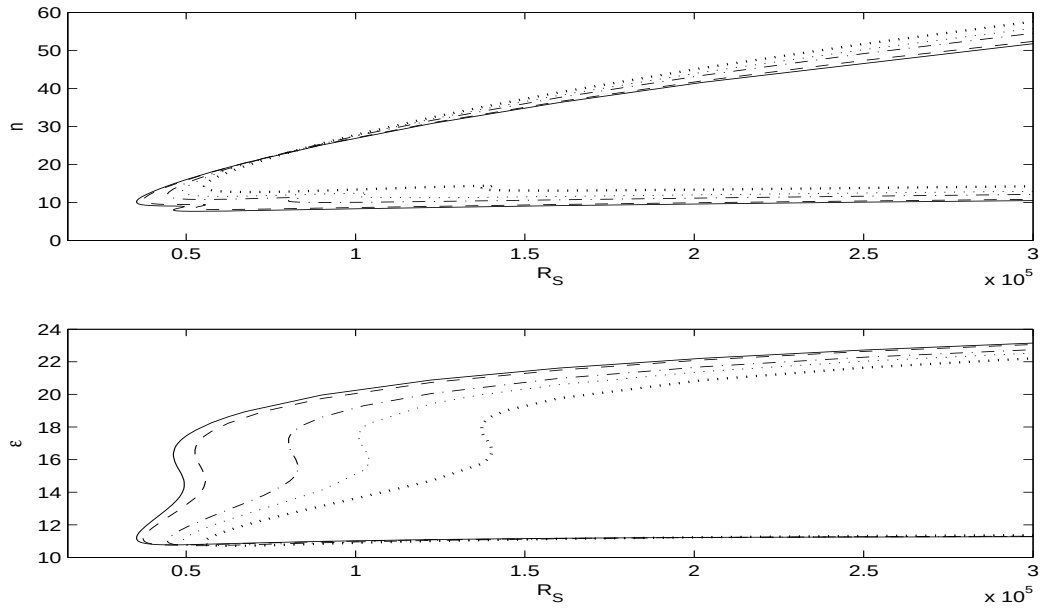

Figure E.6: Neutral curves in (R_S, n)- and (R_S, ϵ)-planes at latitude 60° for $e = 0$ (–), 0.3 (−−), 0.6 (-.), 0.7 (. . .) & 0.8 (...)

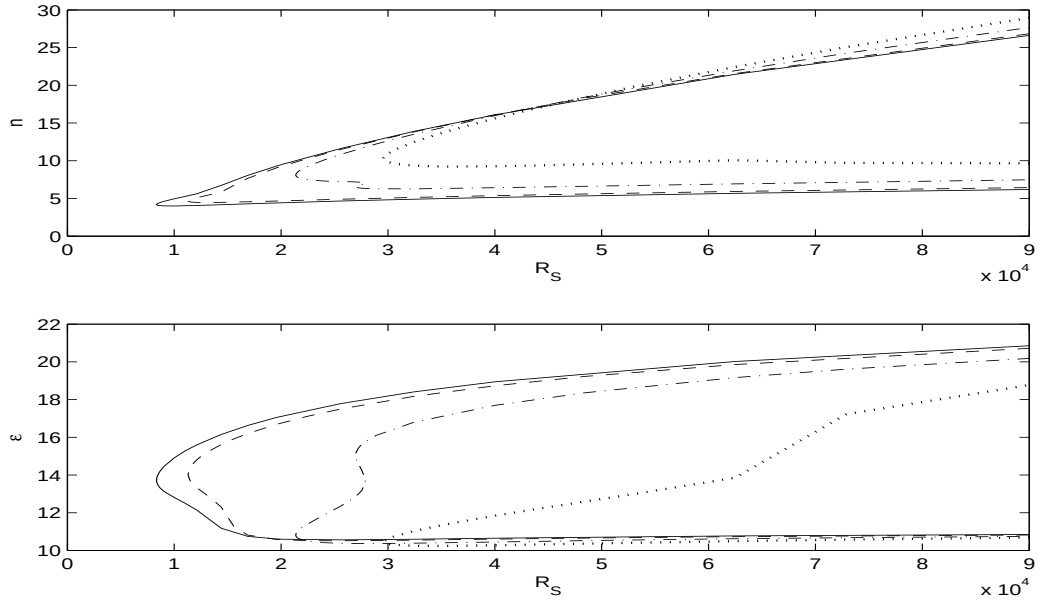

Figure E.7: Neutral curves in (R_S, n)- and (R_S, ϵ)-planes at latitude 70° for $e = 0$ (–), 0.3 (−−), 0.6 (-.), 0.8 (...)

E.4 Neutral curves for the prolate spheroids and oblate spheroids in the same plane

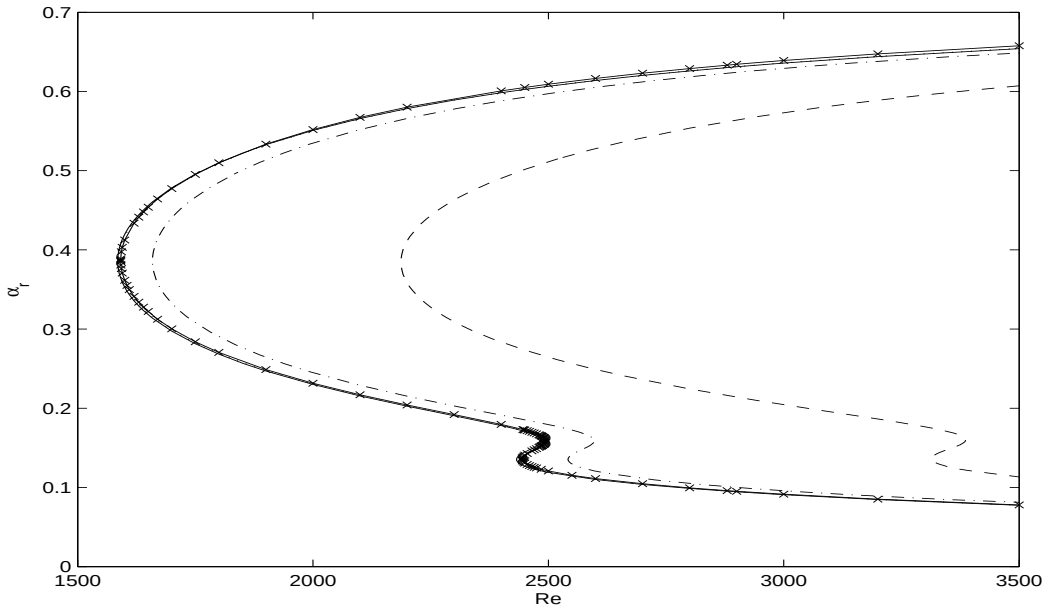

Figure E.8: Neutral curves in the (Re, α)-plane at latitude 10° for prolate spheroids at $e = 0$ (–), 0.3 (-.) & 0.7 (−−) and oblate spheroids at $e = 0.3$ $(\cdots)$ & 0.7 (-x).

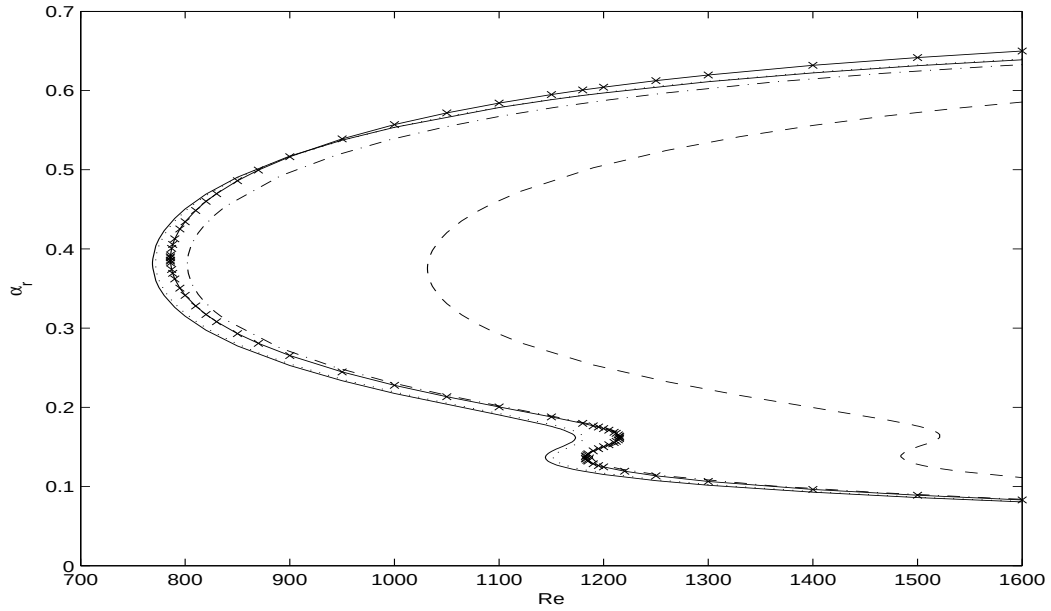

Figure E.9: Neutral curves in the (Re, α)-plane at latitude 20° for prolate spheroids at $e = 0$ (–), 0.3 (-.) & 0.7 (−−) and oblate spheroids at $e = 0.3$ $(\cdots)$ & 0.8 (-x).

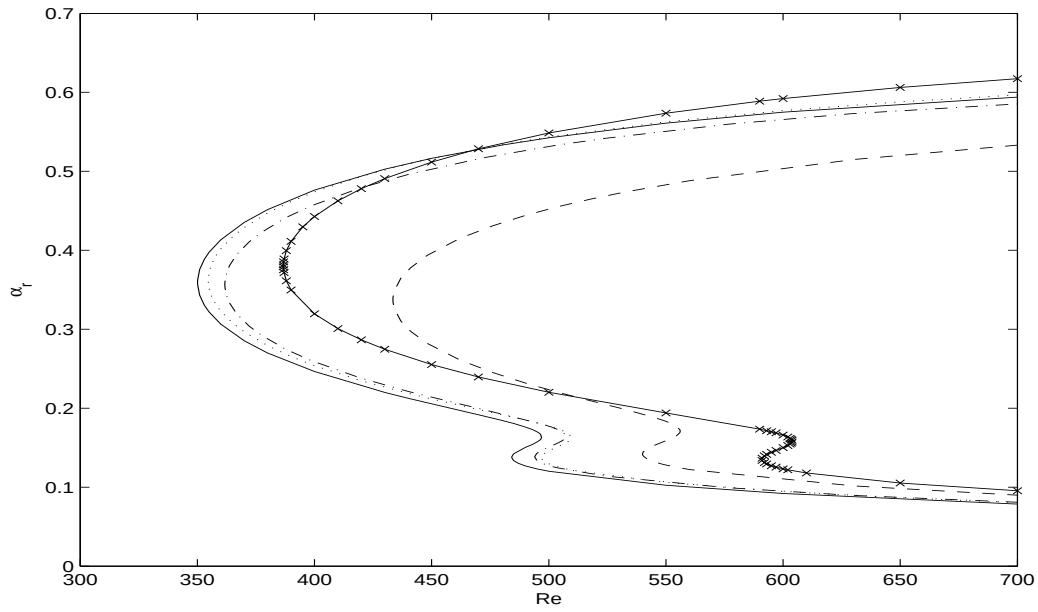

Figure E.10: Neutral curves in the (Re, α)-plane at latitude 40° for prolate spheroids at $e = 0$ (–), 0.3 (-.) & 0.7 (−−) and oblate spheroids at $e = 0.3$ $(\cdots)$ & 0.8 (-x).

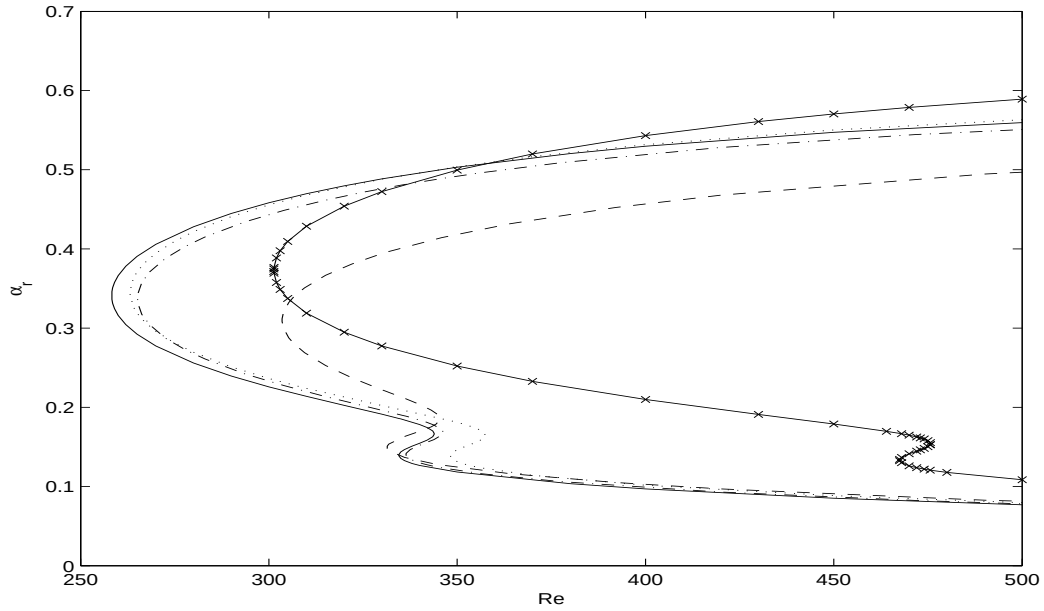

Figure E.11: Neutral curves in the (Re, α)-plane at latitude 50° for prolate spheroids at $e = 0$ (–), 0.3 (-.) & 0.7 (−−) and oblate spheroids at $e = 0.3$ $(\cdots)$ & 0.8 (-x).

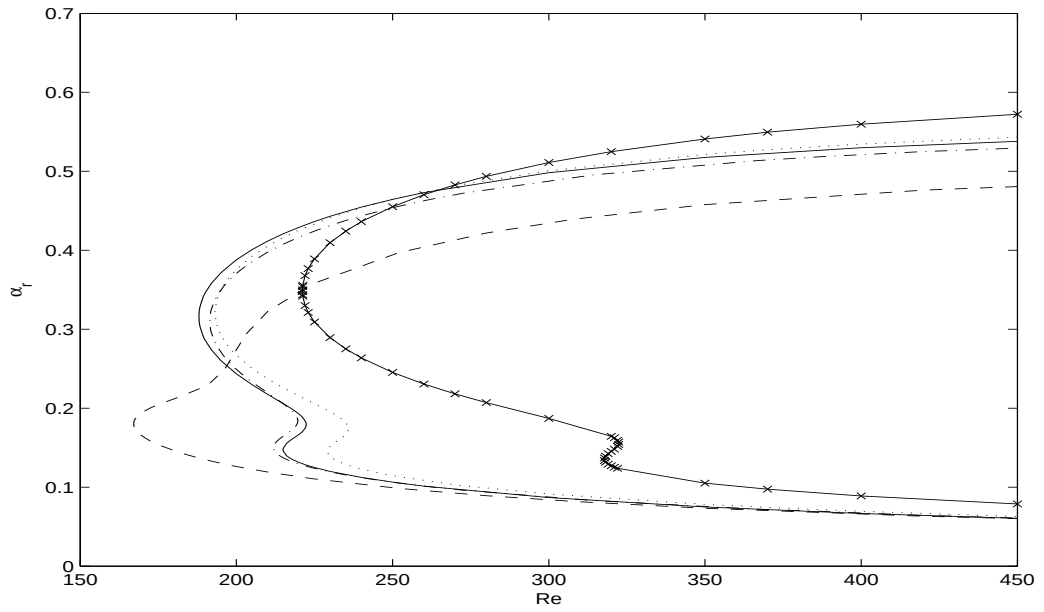

Figure E.12: Neutral curves in the (Re, α)-plane at latitude 60° for prolate spheroids at $e = 0$ (–), 0.3 (-.) & 0.7 (−−) and oblate spheroids at $e = 0.3$ $(\cdots)$ & 0.7 (-x).

Bibliography

Balakumar P & Malik M. R. 1991 'Waves produced from a harmonic point source in a supersonic boundary layer.' *AIAA* Pap. No. 91

Banks, W. H. H. 1965 The boundary layer on a rotating sphere. *Q. J. Mech. Appl. Math.* **18**, 443–454.

Banks, W. H. H. 1976 The laminar boundary layer on a rotating sphere. *Acta Mech.* **24**, 273–287.

Bers, A. 1975 Linear waves and instabilities. In *Physique des Plasmas* (ed. C. DeWitt, J. Peyraud), Gordon & Breach, Chap. 4.

Berzins, M., Dew, P. M. & Furzeland R. M. 1989 Developing software for time-dependent problems using the method of lines and differential-algebraic integrators. *Appl. Numer. Math.* **5**, 375–397.

Briggs, R. J. 1964 *Electron-stream interaction with plasmas.* MIT Press, Chap. 2.

Chomaz, J-M., Huerre, P. & Reddekopp, L. G. 1991 A frequency selection criterion in spatially developing flows. *Stud. App. Math.* **84**, 119–144.

Cooper, A. J. & Crighton, D. G. 2000 Global modes and superdirective acoustic radiation in low-speed axisymmetric jets. *Eur. J. Mech. B - Fluids* **19**, 559–574.

Corke, T. C. & Knasiak, K. F. 1998 'Stationary travelling cross-flow mode interactions on a rotating disk.' *J. Fluid Mech.* **355**, 285–315.

Davies, C. & Carpenter, P. W. 2001 Global behaviour corresponding to the absolute instability of the rotating-disk boundary layer. *Submitted to JFM.*

El-Shaarawi, M. A. I., El-Refaie, M. F. & El-Bedeawi, S. A. 1985 Numerical solution of laminar boundary layer flow about a rotating sphere in an axial stream. *Trans. ASME, J. Fluids Engng.* **107**, 97–104.

El-Shaarawi, M. A. I., Kemry, M. M. & El-Bedeawi, S. A. 1987 Experiments on laminar flow about a rotating sphere in an air sphere. *Proc. Instn. Mech. Engrs* **201**, No C6 427–438.

Evans, H. 1968 *Laminar Boundary Layers.* Addison–Wesley.

Fadnis B. S. 1954 'Boundary layer on rotating spheroids.' *ZAMP.* **5**, 156–163

Fage, A. 1936 Experiments on a Sphere at Critical Reynolds Numbers. *Aero. Res. Council London*, R & M 1766.

Faller, A. J. 1991 'Instability and transition of disturbed flow over a rotating disk.' *J. Fluid Mech.* **230**, 245-70.

Furuta, T., Jimbo, T., Okazaki, M. & Toei, R. 1975 Mass transfer to a rotating sphere in an axial stream. *J. Chem. Engr of Japan* **8**(6), 457.

Garrett, S. J. 2002 'The stability and transition of the boundary layer on rotating bodies.' PhD thesis, Cambridge University.

Garrett, S. J. & Peake, N. 2002 The stability and transition of the boundary layer on a rotating sphere. *J. Fluid Mech.* **456**, 199–218.

Garrett, S. J. & Peake, N. 2004 'The stability of the boundary layer on a rotating sphere in a uniform axial flow.' *European J. Mech., B.*, **23**, 241–253.

Garrett, S. J. & Peake, N. 2007 'The absolute instability of the boundary layer on a rotating cone.' *European. J. Mech. B.* **26**, 344–53.

Garrett, S. J. 2010a 'Vortex-speed selection in the rotating-disk boundary layer.' *Journal of Algorithms & Computational Technology*, Vol. **4**, No. 1., invited paper.

Garrett, S. J. 2010b 'Linear growth rates of type I & II convective modes within the rotating-cone boundary layer.' *Fluid Dyn. Res.* , **42**, 025504.

Garrett, S. J. 2010c 'Vortex-speed selection within the boundary-layer flow over a rotating sphere placed in an enforced axial flow', *European J. Mech. B.*, in press.

Garrett, S. J., Hussain, Z. & Stephen, S. O. 2009a 'The crossflow instability of the boundary layer on a rotating cone.' *J. Fluid Mech.* **622**, 209–32.

Garrett, S. J., Hussain, Z. & Stephen, S. O. 2009b 'Boundary-layer transition on broad cones rotating in an imposed axial flow.' *AIAA Journal*, to appear.

Gray, W. E. 1952 The nature of the boundary layer at the nose of a swept back wing. *Unpublished, Min. Aviation, Lond.*

Gregory, N., Stuart, J. T. & Walker, W. S. 1955 On the stability of three-dimensional boundary layers with application to the flow due to a rotating disk. *Phil. Trans. R. Soc. Lond. A* **248**, 155–199.

Howarth, L. 1951 Note on the boundary layer on a rotating sphere. *Phil. Mag.* **42**, 1308–1315.

Huerre, P. & Monkewitz, P. A. 1985 Absolute and convective instabilities in free shear layers. *J. Fluid Mech.* **159**, 151–168.

Huerre, P. & Monkewitz, P. A. 1990 Local and global instabilities in spatially developing flows. *Ann. Rev. Fluid Mech.* **22**, 473–537.

Kappesser, R., Greif, R. & Cornet, I. 1973 Mass transfer on rotating cones. *Appl. Sci. Res.* **28**, 442–452.

Kármán, T. von. 1921 Uber laminare und turbulente Reiburg. *Z. Angew. Math. Mech.* **1**, 233–252.

Keller, H. B. 1970 A new difference scheme for parabolic problems. *Numerical Solution of Partial Differential Equations* (ed J Bramble) **22**, 273–287, Acadmic Press.

Kobayashi, R., Kohama, Y. & Takamadate, Ch. 1980 Spiral vortices in the boundary layer transition regime on a rotating disk. *Acta Mech.* **35**, 71–82.

Kobayashi, R. 1981 Linear stability theory of boundary layer along a cone rotating in axial flow. *Bull. Japan Soc. Mech. Engrs.* **24**, 934–940.

Kobayashi, R. & Izumi, H. 1983 Boundary-layer transition on a rotating cone in still fluid. *J. Fluid Mech.* **127**, 353–364.

Kobayashi, R. & Kohama, Y. 1984 Spiral vortices in boundary-layer transition on a rotating cone. In *Laminar Turbulent Transition* IUTAM Symposium Novosibirsk, USSR, pp. 573–580. Springer-Verlag Berlin Heidelberg.

Kobayashi, R., Kohama, Y. & Kurosawa, M. 1983 Boundary-layer transition on a rotating cone in axial flow. *J. Fluid Mech.* **127**, 341–352.

Kobayashi, R., Kohama, Y., Arai, T. & Ukaku, M. 1987 The boundary-layer transition on a rotating cone in axial flow with free-stream turbulence. *JSME Intern. J.* **30**, 423–429.

Kobayashi, R., Arai, T. & Nakajima, M. 1988 Boundary layer transition and separation on spheres rotating in axial flow. *Exp. Thermal and Fluid Sci.* **1**, 99–104.

Kobayashi, R. & Arai, T. 1990 Spiral vortex behaviour in transition region and separation of three-dimensional boundary layers on spheres rotating in axial flow. In *Laminar Turbulent Transition* (eds. D. Arnal, R. Michel), IUTAM Symposium Toulouse, France, pp. 551–557. Springer-Verlag Berlin Heidelberg.

Kobayashi, R. 1994 Review: Laminar-to-turbulent transition of three-dimensional boundary layers on rotating bodies.

Kobayashi, R. & Izumi, H. 1983 'Boundary-layer transition on a rotating cone in still fluid.' *J. Fluid Mech.* **127**, 353-64.

Kobayashi, R., Kohama, Y. & Kurosawa, M. 1983 'Boundary-layer transition on a rotating cone in axial flow.' *J. Fluid Mech.* **127**, 341-52.

Kohama, Y. 1984a Behaviour of spiral vortices on a rotating cone in axial flow. *Acta Mech.* **50**, 105–117.

Kohama, Y. 1984b Study on boundary-layer transition of a rotating disk. *Acta Mech.* **50**, 193–199.

Kohama, Y. 1985 'Turbulent transition process of the spiral vortices appearing in the laminar boundary layer of a rotating cone.' *Phys.-Chem. Hydrodyn.* **6(5)**, 659.

Kohama, Y. P. 2000 'Three-dimensional boundary layer transition study' *Current Science* Vol. **79**, No. 6, 800–807.

Kohama, Y. & Kobayashi, R. 1983 Boundary-layer transition and the behaviour of spiral vortices on rotating spheres. *J. Fluid Mech.* **137**, 153–164.

Kreith, F., Ellis, D. & Giesing, J. 1962 An experimental investigation of the flow engendered by a rotating cone. *Appl. Sci. Res.* **A11**, 430–440.

Kupfer, K., Bers, A. & Ram, A. K. 1987 The cusp map in the complex-frequency plane for absolute instabilities. *Phys. Fluids* **30**, 3075–3082.

Lingwood, R. J. 1995a Absolute instability of the boundary layer on a rotating disk. *J. Fluid Mech.* **299**, 17–33.

Lingwood, R. J. 1995b *Stability and transition of the boundary layer on a rotating disk.* PhD Thesis, Cambridge University.

Lingwood, R. J. 1996 An experimental study of absolute instability of the rotating-disk boundary-layer flow. *J. Fluid Mech.* **314**, 373–405.

Lingwood, R. J. 1997a Absolute instability of the Ekman layer and related flows. *J. Fluid Mech.* **331**, 405–428.

Lingwood, R. J. 1997b On the impulse response for swept boundary-layer flows. *J. Fluid Mech.* **344**, 317 - 334

Luthander, S. & Rydberg, A. 1935 Experimentelle untersuchungen über den luftwiderstand bei einer um eine mit der windrichtung parallelen achse rotieren kugel. *Physik. Z.* **36**, 552–558.

Malik, M. R. 1986 The neutral curve for stationary disturbances in rotating-disk flow. *J. Fluid Mech.* **164**, 275–287.

Malik, M. R., Wilkinson, S. P. & Orszag, S. A. 1981 Instability and transition in rotating disk flow. *AIAA J.* **19**, 1131–1138.

Mangler, W. 1945 Boundary layers on Bodies of Revolution in Symmetrical Flow. *Ber. Aerodyn Versuchsanst. Goett.*, Report 45/A/17.

Manohar, R. 1967 The boundary on a rotating sphere. *Z. angew. Math. Phys.* **18**, 320.

Monkewitz, P. A., Huerre, P. & Chomaz, J. M. 1993 Global linear stability analysis of weakly non-parallel shear flows. J. Fluid Mech. **251**, 1–20.

Morse, P. M. 1953 Methods of theoretical Physics, McGraw–Hill.

Nicholson, W. K. 1995 *Linear algebra with applications.* PWS Publishing Company, §§6.3 & 8.2.

Niew, T. R. 1993 *The stability of the flow in a laminar separation bubble.* PhD Thesis, Cambridge University.

Nigam, S.D. 1954 'Note on the boundary layer on a rotating sphere.' *Z. angew. Math. Phys.'* **5**, 151–155

Noordzij, P. & Rotte, J. W. 1967 Mass transfer coefficients to a rotating and to a vibrating sphere. *Chem. Engng Sci.* **22**, 1475.

Noordzij, P. & Rotte, J. W. 1968 Mass transfer coefficient for simultaneously rotating and translating sphere. *Chem. Engng Sci.* **23**, 657.

Owen, J.M. & Rogers, R.H. 1989 Flow and heat transfer in rotating-disc systems, vol. 1 Rotor-stator systems (Research Studies, Taunton, Sommerset, U.K).

Pier, B. & Huerre, P. 2001 Nonlinear self-sustained structures and fronts in spatially developing wake flows. *J. Fluid Mech.* **435**, 145–174 .

Pier, B. 2002 Fully nonlinear waves and transition in the boundary layer over a rotating disk. In *Advances in turbulence* IX (eds. I.P. Castro & P.W. Hancock), Ninth European Turbulence Conference, Barcelona. CIMNE.

Press, W. H., Teukolshy, S. A., Vetterling, W. T. & Flannery, B. P. 1992 *Numerical Recipes.* Cambridge University Press, §§2.6, 9.4, 12.1, 13.4, 16.1 & 17.1.

Ralston, A. & Wilf, H. S. 1960 *Mathematical Methods for Digital Computers.* Wiley, New York.

Reed, H.L. & Saric, W.S. 1989 Stability of three-dimensional boundary layers *Annu. Rev. Fluid Mech.* **21**, 235.

Salzberg, F. & Kezios, S. P. 1965 Mass transfer from a rotating cone in axisymmetric flow. *J. Heat Transfer* **87**, 469–476.

Samad, A. & Garrett, S.J. 2010 On the laminar boundary-layer flow over rotating spheroids. *Int. J. Eng. Sci*, In Press.

Saric, W.S., Reed, H.L. & White, E.B. 2003 Stability and transition of three-dimensional boundary layers, *Annu. Rev. Fluid Mech.* **35**, 413.

Sawatzki, O. 1970 Das Strömungsfeld un eine rotiernde kugel. *Acta Mech.* **9**, 159–214.

Soward, A. M. & Jones, C. A. 1983 The linear stability of the flow in the narrow gap between two concentric rotating spheres. *Q. J. Mech. Appl. Math.* **36**, 19–42.

Smith, N.H. 1947 Exploratory investigation of laminar-boundary-layer oscillations on a rotating disk, National Advisory Committee for aeronautics, Technical Note no. 1227, Washington DC, USA.

Strykowshi, P. J. & Niccum, D. L. 1991 The stability of countercurrent mixing layers in circular jets. *J. Fluid Mech.* **227**, 309–343.

Tanaka, H. & Tago, O. 1975 Mass transfer from a rotating sphere in air stream. *Kagaku Kögaku* **37**, 151.

Taniguchi, H., Kobayashi, R. & Fukunishi, Y. 1998 Stability of the boundary layer on a sphere rotating in still fluid. *Acta Mech.* **129**, 243–253.

Taylor, M. J. & Peake, N. 1998 The long-time behaviour of incompressible swept-wing boundary layers subject to impulsive forcing. *J. Fluid Mech.* **355**, 359–381.

Taylor, M. J. & Peake, N. 1999 The long-time impulse response of compressible swept-wing boundary layers. *J. Fluid Mech.* **379**, 333–350.

Tein, C. L. 1960 Heat transfer by laminar flow from a rotating cone. *ASME Journal of Heat Transfer* **82**, 252–253.

Tein, C. L. & Campbell, D. T. 1963 Heat and mass transfer from rotating cones. *J. Fluid Mech.* **17**, 105–112.

Theodorsen, T. & Regier, A. 1944 Experiments on drag of revolving disks,

cylinders and streamline rods at high speeds, National Advisory Committee for aeronautics, Washington DC, USA., Report no. 793, **13**, 744-803

Turkyilmazoglu, M., & Gajjar, J.S.B. 1998 'Absolute and convective instability in the incompressible boundary layer on a rotating disk.' Report no. CLSCM, University of Manchester.

Wazzan, A. R., Okamura, T. T. & Smith, A. M. O. 1968 The stability of water flow over heated and cooled flat plates. *J. Heat Transfer* **90**, 109–114.

White, F. M. 1991 *Viscous fluid flow.* McGraw-Hill.

Wilkinson, S. P. & Malik, M. R. 1985 Stability experiments in the flow over a rotating disk. *AIAA J.* **21**, 588–595.

Wimmer, M. 1988 Viscous flows and instabilities near rotating bodies, *Prog. Aerospace Sci.* **25**, 43.

Wu, C. S. 1959 The three dimensional incompressible laminar boundary layer on a rotating cone. *Applied Scientific Research*, Sect. A, **8** pp 140–146